TESTING BOTH MODES OF GALAXY FORMATION: A CLOSER LOOK AT GALAXY MERGERS AND GAS ACCRETION

by

YUJIN YANG

—————

A DISSERTATION SUBMITTED TO THE FACULTY OF THE

DEPARTMENT OF ASTRONOMY

IN PARTIAL FULFILLMENT OF THE REQUIREMENTS
FOR THE DEGREE OF

DOCTOR OF PHILOSOPHY

IN THE GRADUATE COLLEGE

THE UNIVERSITY OF ARIZONA

2 0 0 8

THE UNIVERSITY OF ARIZONA
GRADUATE COLLEGE

As members of the Dissertation Committee, we certify that we have read the dissertation prepared by Yujin Yang entitled "Testing both Modes of Galaxy Formation: A Closer Look at Galaxy Mergers and Gas Accretion " and recommend that it be accepted as fulfilling the dissertation requirement for the Degree of Doctor of Philosophy.

_____ Date: 8 August 2008
Ann Zabludoff

_____ Date: 8 August 2008
Daniel Eisenstein

_____ Date: 8 August 2008
Romeel Davé

_____ Date: 8 August 2008
George Rieke

_____ Date: 8 August 2008
Arjun Dey

Final approval and acceptance of this dissertation is contingent upon the candidate's submission of the final copies of the dissertation to the Graduate College.

I hereby certify that I have read this dissertation prepared under my direction and recommend that it be accepted as fulfilling the dissertation requirement.

_____ Date: 8 August 2008
Dissertation Director: Ann Zabludoff

Statement By Author

This dissertation has been submitted in partial fulfillment of requirements for an advanced degree at The University of Arizona and is deposited in the University Library to be made available to borrowers under rules of the Library.

Brief quotations from this dissertation are allowable without special permission, provided that accurate acknowledgment of source is made. Requests for permission for extended quotation from or reproduction of this manuscript in whole or in part may be granted by the head of the major department or the Dean of the Graduate College when in his or her judgment the proposed use of the material is in the interests of scholarship. In all other instances, however, permission must be obtained from the author.

Signed: Yujin Yang

Acknowledgments

It's been quite a long journey to become an astronomer and I am indebted to so many people. It is a sincere pleasure to acknowledge them. First and foremost, my thesis advisor, Ann Zabludoff, probably the most optimistic and enthusiastic person I've even known. Ann was always supportive and rooting for me even when I feel most pessimistic about the research and myself. She taught me to see the glass as half-full, not as half-empty and encouraged me to always aim high when setting up research and career goals. I am also grateful to her for training me how to write papers and proposals, and telling me that it's always good to find mistakes before publishing whenever I made numerous mistakes. Special thanks to Dennis Zaritsky for setting up high standards and teaching me to be most skeptical when we got the results that we wanted. To Romeel Davé and Daniel Eisenstein, for showing examples of the great theorists who understand the observation better than any observer. I am greatly indebted to Christy Tremonti who has been instrumental in large parts of this work and always available for my questions. Deciphering her IDL codes was hundred times more helpful than any paper or IDL tips. Her hard-working, amazing insights on so many areas, and the scrutiny and tenacity in doing research was truly a great example for me starting as a post-doc.

I had the privilege to share the office and classes with Fu-Yan Bian, Jennifer Donley, Kristian Finlator, András Gáspár, Nadya Gorlova, Dennis Just, Wilson Liu, Ivelina Momcheva, Jeremiah Murphy, Moire Prescott, Wiphu Rujopakarn, Nick Siegler, Suresh Sivanandam, Amy Stutz, and more.

I also thank Korean friends in the Steward who provide one of a few social, but most refreshing life. Ryeojin for sharing her dreams and warm dinners. Hee-Jong has been a good friend, officemate, and colleague. Discussions and debates over lunch was always fun and memorable. Her ever-lasting passion for astronomy, persistence, and modesty have been good examples. Miju has been an inspiration at the most stressful times of writing this thesis by encouraging me and making me laugh all the time. Special thanks to Serena Kim and Xiaohui Fan for sharing advices and experiences and for the wonderful parties in Korean/Chinese holidays (especially the hot drinks!).

Next, I owe my gratitude to the Seoul National University Astronomy Department at the very beginning of this journey: Seung Soo Hong, Hyung Mok Lee, Bon-Chul Koo, Changbom Park, and Yong-Sun Park. Especially, my undergraduate advisor, Prof. Myung Gyoon Lee influenced to become an observer by providing the first research project and showed me the joy of doing science.

I also like to thank all the friends who have shared the passion for the US national parks from Olympics to Acadia NPs every summer, aka, Gang-Sang summer school members: Ji-Hoon, Min-Suk, Jaiyul, Eun-Joo, Guembong, and Sungryong. Without their company, the joy would have been tainted.

DEDICATION

This dissertation is dedicated to my parents, sister, and aunt for their unconditional love and support.

TABLE OF CONTENTS

TABLE OF CONTENTS — *Continued*

TABLE OF CONTENTS — *Continued*

LIST OF FIGURES

LIST OF FIGURES — *Continued*

LIST OF TABLES

ABSTRACT

This thesis focuses primarily on how two important processes — galaxy mergers and gas accretion from the surrounding intergalactic medium — affect the evolution of galaxies. Using post-starburst, or E+A, galaxies as a marker sample that undergoes a rapid transition from gas-rich star-forming galaxies to quiescent, passively-evolving E/S0s, we study what triggers E+A evolution and what E+A galaxies will become after the fading of their young stellar population. With high resolution *HST* WFPC2/ACS imaging, we investigate their small and large scale properties, including their detailed morphologies, bulge fractions, color gradients, scaling relationships, and newly formed star-clusters. 70% of E+A galaxies show disturbances and tidal features indicating a merger origin and all their properties are either consistent with those of E/S0s or, if left to evolve passively, will become like those of early-types.

Using cosmological simulations, we study hydrogen and helium gravitational cooling radiation from gas accretion by young galaxies, finding that observing optically thin cooling lines such as He II $\lambda1640$ and H I Hα is critical in understanding the nature of galaxies forming via gas-accretion. To obtain an unbiased sample of Lyα blobs that will allow us to follow-up their optically thin Hα lines in the *NIR*, we conduct a blind, wide-field, narrow-band imaging survey for Lyα blobs. After searching over 4.82 deg^2, we discover four blobs that we spectroscopically confirm to lie at $z = 2.3$. The properties of these blobs are diverse: two blobs are X-ray-detected and have broad optical emission lines (e.g., C IV) characteristic of AGN. The other 50% of blobs are not X-ray or optically-detected as AGN down to similar limits. The number density of the four blobs is extremely low, $\sim 3 \times 10^{-6}\, h_{70}^3\, \mathrm{Mpc}^{-3}$, comparable to that of galaxy clusters at similar red-

shifts. The two X-ray undetected blobs are separated by only 70″ (550 kpc) and have almost identical redshifts (corresponding to $\lesssim$ 360 kpc along the line-of-sight), suggesting that they are part of the same system. Given the rarity of the blobs and our discovery of a close pair, we speculate that blobs occupy the highest density regions and thus may be precursors of today's rich cluster galaxies.

CHAPTER 1

INTRODUCTION

This thesis focuses primarily on how two important processes — *galaxy-galaxy mergers* and *gas accretion from the surrounding intergalactic medium* — affect the evolution of galaxies. We target two classes of objects that are markers for each process: post-starburst or "E+A" galaxies (galaxies in late-to-early type transitions through mergers), and extended Lyα nebulae or "Lyα blobs" (the possible progenitors of the brightest cluster galaxies forming via gas accretion). Ultimately, we plan to use our work here to 1) construct a detailed timeline of how the stellar, gaseous, and nuclear components of galaxies evolve through galaxy-galaxy mergers onto the red sequence and 2) identify unambiguous observational signatures of gas accretion by distant forming galaxies.

1.1 Constructing a Detailed Timeline for E/S0 Evolution through the Post-Starburst Phase

The observed bimodality of galaxy properties — less clustered, blue, star-forming galaxies versus more clustered, red, and dead spheroids — implies that blue galaxies must transform into red galaxies over a short timescale to preserve the gap between the two galaxy populations. Spectroscopic surveys have identified at least one set of candidates for such a transformation: post-starburst, or "E+A" galaxies whose spectra have deep Balmer absorption lines but no significant [O II] emission, indicating that star formation ceased abruptly in these galaxies within the last $\sim$ Gyr (Zabludoff et al., 1996; Poggianti et al., 1999; Goto et al., 2003; Blake et al., 2004; Tran et al., 2003, 2004; Yan et al., 2008). Because their spectra are a superposition of a young stellar population (represented by A stars) and an old

population (characterized by K stars), these galaxies are also known as "K+A" or "k+a" galaxies (Franx et al., 1989; Dressler et al., 1999; Poggianti et al., 1999). In general, E+A galaxies lack significant amounts of H I gas (Chang et al., 2001) and have hot, pressure-supported kinematics (Norton et al., 2001), suggesting that these galaxies are indeed evolving — somehow — from late to early types.

However, due to a lack of spatial resolution in previous studies, we do not yet know 1) what triggers E+A evolution, 2) whether their detailed properties, e.g., their bulge fractions, color gradients, and internal kinematics, are consistent with late-to-early type evolution, and 3) what E+A galaxies will become after the fading of their young stellar population.

To answer these questions, we must identify morphological features on small and large scales and ask how well E+As match the full range of E/S0 properties. First, do the morphologies of E+A galaxies reveal recent disturbances and/or tidal features that would suggest which mechanism or mechanisms triggered their starburst? Second, are the global morphologies (e.g., bulge-to-total light ratios and concentration) of the E+A sample consistent with those of E/S0s? Third, E/S0s in the local universe become redder toward their center; these negative color gradients originate from metallicity gradients (Peletier et al., 1990). In contrast, E+As exhibit a wide range of color morphologies (Yamauchi et al., 2005). Can the color profiles of E+As evolve into those of typical early types? Fourth, the number of globular clusters per unit luminosity is higher in early types than in late types (Harris & van den Bergh, 1981). If E+As are in transition from late to early types, one should find new star clusters formed during the starburst. Are there such clusters, and, if so, do their colors and numbers coincide with the expected evolution of the globular cluster systems of present-day E/S0s? Lastly, early-type galaxies lie on the Fundamental Plane (FP), an empirical scaling re-

lation between effective radius, central velocity dispersion, and mean surface brightness with remarkably small scatter (Djorgovski & Davis, 1987; Dressler, 1987). Will E+As lie on the same FP once they evolve?

To determine the origin and end-products of E+As, we present *HST* WFPC2 and ACS observations of the 21 E+A galaxies from the Las Campanas Redshift Survey (LCRS; Zabludoff et al., 1996) (Chapters 2-3). High resolution *HST* observations enable us to study the detailed morphologies, color profiles, and newly formed star cluster populations of E+As at the sub-kpc scale. Using existing kinematic data (Norton et al., 2001) and our *HST* photometry, we also also determine the various scaling relations of E+As. We will show that the properties of many E+As are consistent with the galaxy-galaxy interaction scenario and with final evolution into the properties of red sequence galaxies.

The strong correlation between black hole mass and galaxy bulge velocity dispersion ($M_\bullet - \sigma_B$; Ferrarese & Merritt, 2000; Gebhardt et al., 2000) suggests there is a connection — perhaps causal — between the small-scale physics of black hole (BH) growth and the large-scale physics that organizes the host galaxy morphology, kinematics, and stellar populations during and after the merger. Among the best candidates for such a mechanism are galaxy-galaxy mergers. Recent numerical simulations including BHs suggest that collisions between galaxies trigger an inflow of gas that causes a strong circumnuclear starburst and fuels BH accretion. A powerful quasar outflow removes the gas from the inner region of the merger remnant, quenching the star formation on a relatively short timescale ($\sim$1 Gyr; Springel et al., 2005a,b). Given that E+A galaxies are undergoing large-scale transitions via mergers from gas-rich disky systems to bulge-dominated systems, E+A galaxies are plausible test cases for this scenario. As a first step, we investigate the nuclear properties of E+A galaxies with blue cores (Chapter 4).

1.2 Searching for Galaxies Forming via Gas-accretion

The other important process governing galaxy evolution is gas-accretion from the surrounding intergalactic medium (IGM). Although mergers are clearly important in the evolution of some galaxies (see above), all the mass in galaxies must have entered the galaxy population by accretion (presumably at high redshifts). Mergers only redistribute this mass from smaller to larger systems. Furthermore, numerical simulations predict that galaxies grow primarily by smooth gas accretion rather than by cannibalism of smaller objects (Murali et al., 2002; Kereš et al., 2005). How galaxies obtain that gas from the IGM may play a critical role in shaping the observed bi-modality of galaxy properties (Kereš et al., 2005; Dekel & Birnboim, 2006).

Despite the importance of gas accretion, a direct observation of galaxy formation via gas accretion has yet to be made. Theoretical studies predict 1) that galaxies forming via gas accretion should lie not only at the highest redshifts ($z \sim 7$), but also at more accessible distances ($z \sim 2 - 3$) and 2) that accreting gas should channel some of its gravitational cooling radiation into atomic emission lines such as Lyα (Haiman, Spaans, & Quataert, 2000; Fardal et al., 2001). These predictions have coincided with the discovery of Lyα nebulae, the so-called "Lyα blobs," mysterious, extended sources at $z \sim 2 - 5$ with typical sizes of $\sim 10''$ and line luminosities of $L_{\mathrm{Ly}\alpha} \sim 10^{44}$ ergs s^{-1} (e.g., Keel et al., 1999; Steidel et al., 2000; Francis et al., 2001; Palunas et al., 2004; Dey et al., 2005; Smith & Jarvis, 2007).

To test whether these objects are galaxies forming via gas accretion and to explore the details of that accretion presents two challenges. First, we need to constrain their basic properties, including how common they are, how they are spatially distributed, and how diverse their possible power sources may be. Despite intense interest, these characteristics, for even the brightest Lyα blobs, are

poorly constrained due to the absence of an appropriate sample. Giant, luminous blobs (Steidel et al., 2000) appear to be rare at $z = 3 - 5$ (Saito et al., 2006), so an efficient, large-volume survey is required to detect any. Furthermore, the survey must be blind to be representative of blob statistics and must include ancillary data (in the X-ray, other optical bands, etc.) to better constrain possible sources of blob emission. To date most Lyα blobs have been discovered by targeting two previously known over-dense regions (Steidel et al., 2000; Francis et al., 2001; Palunas et al., 2004; Matsuda et al., 2004). Matsuda et al. (2004) discovered 33 additional Lyα blobs in the proto-cluster region at $z = 3.1$ where the two giant Steidel et al. blobs reside, and spectroscopic follow-up confirms that the blobs are located in three filamentary structures traced by compact Lyα-emitting galaxies (Matsuda et al., 2005). Palunas et al. (2004) report that four Lyα blobs are associated with an over-dense region of Lyα emitters around the galaxy cluster J2142-4420 at $z = 2.38$. The first and only study of the environment of a Lyα blob found without any prior knowledge of its surroundings (Dey et al., 2005) shows it to lie in a $3\times$ over-dense region traced by Lyα-emitting galaxies (Prescott et al., 2008). Although these results suggest that bright Lyα blobs occupy higher density regions, we still lack an unbiased, statistical measurement of how frequent and clustered they truly are.

Second, while the emission from these blobs could be from accreting gas, it could also arise from other interesting sources, including collisionally ionized gas in galactic superwinds (Taniguchi & Shioya, 2000), or gas photoionized by young stellar populations (Matsuda et al., 2007) or by active galactic nuclei (Haiman & Rees, 2001). This uncertainty in blob origin has arisen because of the ambiguities associated with interpreting their optically thick Lyα emission. For example, even the most general classes of Lyα blob models — infall (due to gas accretion) vs.

outflow (arising from AGN or stellar winds) — cannot be tested with Lyα emission measurements alone. Because Lyα is a resonant line and typically optically thick in the surrounding intergalactic medium, studies even of the same blob's kinematics can lead to radically different conclusions. On one hand, Wilman et al. (2005) argue that integrated field unit spectra from a blob are consistent with a simple model where the Lyα emission is absorbed by a foreground slab of neutral gas swept out by a galactic scale outflow. In contrast, Dijkstra et al. (2006) claim that the same data can be explained by the infall of the surrounding intergalactic medium. Even worse, Verhamme et al. (2006) claim that the same symmetric Lyα profiles are most consistent with static surrounding gas.

In order to overcome these two challenges, we have developed an extensive observational and theoretical program, searching for new and unambiguous signatures of gas accretion in a new, large, and unbiased sample of blobs. Using numerical simulations, we study hydrogen and helium gravitational cooling radiation (Chapter 5). In particular, we focus on the He II $\lambda 1640$ cooling radiation because unlike H I $\lambda 1216$ cooling lines, He II $\lambda 1640$ is optically thin, less sensitive to the UV background, and less contaminated by the recombination lines from star-forming galaxies, making it an ideal diagnostic line to uncover the processes by which galaxies acquire their baryons.

In the observational side, we have undertaken a two-stage program. In the first stage of our program, we survey for Lyα blobs at $z \sim 2.3$ using our custom narrow-band filter in order to obtain an environmentally unbiased sample of blobs. We choose this redshift for three reasons: 1) numerical simulations predict that cooling radiation becomes stronger (Fardal et al. 2002, Furlanetto et al 2005) at times later than z=3, 2) because the Lyα line at $z = 2.3$ is blueward of Hβ (4868Å) and [O III] (5007Å), the only contaminating sources in our survey
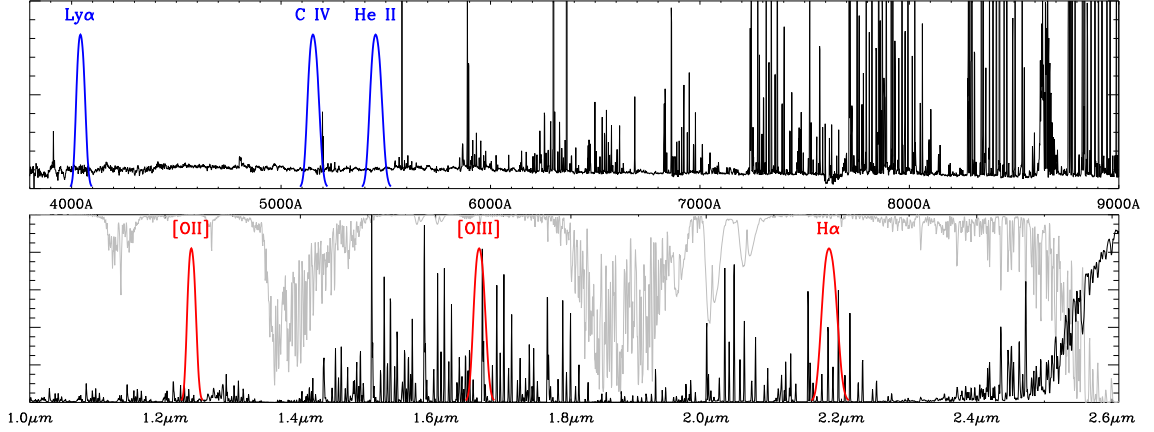
Figure 1.1 — Wavelength ranges of the detectable C IV, He II $\lambda1640$, [O II] $\lambda3727$, [O III] $\lambda5007$, and Hα lines that correspond to the Lyα filter at $z = 2.3$, relative to the sky spectrum or transmission. Note that all emission lines will be in a sufficiently clean region of the sky spectrum or transmission to allow their detection.

will be (obvious) [O II] (3727Å) emitters at $z = 0.07$, and most importantly, 3) at $z = 2.3$, we avoid bright sky lines (or atmospheric absorption) not only in the Lyα band, but also in the C IV $\lambda1549$, He II $\lambda1640$, and Hα bands, which are important diagnostics in the planned spectroscopic follow-ups (Fig. 1.1).

To acquire a new unbiased sample of Lyα blobs, we have conducted two complimentary narrow-band imaging surveys. The Bok+90Prime survey specifically targets rare, luminous Lyα blobs ($L_{\mathrm{Ly}\alpha} \gtrsim 2 \times 10^{43}$ ergs s^{-1}) with its shallow, but ultra-wide, imaging, and our deeper, but smaller sky coverage, CTIO/KPNO-4m + MOSAIC survey targets the presumably more common intermediate size ($A_{iso} \gtrsim 20$ arcsec^2) and luminosity ($L_{\mathrm{Ly}\alpha} \gtrsim 4 \times 10^{42}$ ergs s^{-1}) Lyα blobs whose properties may overlap those of Lyα emitters. Because these intermediate blobs are slightly more extended than compact Lyα emitters and have very low surface brightnesses, the CTIO/KPNO survey is designed to be very deep (10 hrs per

Table 1.1.   Narrow-band Imaging Survey for Lyα Blobs

	Wide-field Survey	Deep Survey
Target	bright blobs	intermediate blobs
	$L_{\mathrm{Ly}\alpha} \sim 10^{44}\,\mathrm{ergs\,s^{-1}}$	$L_{\mathrm{Ly}\alpha} < 10^{43}\,\mathrm{ergs\,s^{-1}}$
	$A_{\mathrm{iso}} \sim 50\square''$	$A_{\mathrm{iso}} \sim 20\square''$
Telescope	Bok2.3m+90Prime	KPNO/CTIO-4m+MOSAIC
Fields	NOAO Bootes/Cetus/COSMOS	CDF-S/CDF-N/COSMOS
Exposure	6 – 20 hours	~ 10 hours
	45 nights (2007-08)	11 nights (2007)
Area	6+4+2 $\square°$	$3 \times (35' \times 35')$

field). Table 1.1 summarizes our survey strategies. We have now completed this first stage of our program and this thesis will discuss the initial results from the ultra-wide FOV Bok+90Prime survey (Chapter 6).

In the second stage, we plan to compare the center of the Lyα line with that of the optically thin Hα λ6563 (hereafter, Hα) line to determine whether a blob's gas is infalling or outflowing. We will discuss this part of project in the Future Directions section (Chapter 7).

This thesis is organized as follows. In Chapters 2 – 4, we focus on galaxy evolution driven by galaxy mergers, which transform late-type galaxies into quiescent, gas-poor early-types. In Chapter 2, we characterize the detailed morphologies of the five bluest post-starburst galaxies in the LCRS sample using *HST/WFPC2* high-resolution images. We explore the evidence suggesting that

galaxy-galaxy tidal interactions or mergers trigger the starbursts in E+A galaxies.

Chapter 3 expands our morphological study to the full LCRS post-starburst sample to answer whether these galaxies are evolving onto the red sequence. We study their small and large scale features, including their global morphologies (e.g., *B/T* and *C-A*), color profiles, scaling relationships (e.g., the Fundamental Plane relation), and the star cluster systems, and compare them with those of E/S0s. Chapter 4 describes our discovery of low-luminosity AGNs or LINERs in the four E+As with compact blue cores, which will provide a chance to explore how the evolution of black holes and AGN may be tied to that of galactic bulges. The presence of LINERs in these E+As suggests that any rapid growth phase of the central black hole ended in rough concert with the cessation of star formation.

In Chapters 5 – 6, we describe our observational and theoretical efforts to identify the signatures gas accretion by galaxies forming at high redshift. In Chapter 5, using cosmological simulations, we characterize the hydrogen and helium gravitational cooling lines arising from accreting gas. This theoretical work motivated our observational program to obtain a new, large, unbiased sample of Lyα blobs, which are the best candidates for galaxies forming via gas-accretion. In Chapter 6, we present the first results from our blind survey for Lyα blobs, including their number density, environment, and possible energy sources. In Chapter 7, we summarize the results and discuss the issues that we plan to follow-up in the future.

CHAPTER 2

E+A GALAXIES AND THE FORMATION OF EARLY TYPE GALAXIES AT $z \sim 0$

2.1 Introduction

If galaxies evolve morphologically from late to early types, then some may be now changing from star-forming, gas-rich, disk-dominated objects into quiescent, gas-poor spheroidals. Spectroscopic surveys have identified at least one set of candidates for such a transformation: "E+A" galaxies[1], whose spectra have deep Balmer absorption lines but no significant [OII] emission, indicating that star formation ceased abruptly in these galaxies within the last $\sim$ Gyr. In general, E+A galaxies lack significant amounts of HI gas (Chang et al., 2001) and have hot, pressure-supported kinematics (Norton et al., 2001), suggesting that these galaxies are indeed evolving — somehow — from late to early types. However, we do not yet know whether their current *morphologies* are consistent with late-to-early type evolution or what drives E+A evolution.

While the mechanism (or mechanisms) that causes galaxies to pass through an E+A phase is not understood, there are several clues. First, E+A spectra suggest a recent burst of star formation that required the rapid consumption or dispersal of a gas reservoir. Second, although they were first studied in distant clusters (Dressler & Gunn, 1983), E+As — at least at low redshifts ($z \sim 0.1$) — lie mostly in low density environments (Zabludoff et al., 1996; Quintero et al., 2004). Third, in low-resolution POSS images, some E+As have features suggestive of tidal tails (Zabludoff et al., 1996). Could E+As be the result of disk galaxy merg-

---

[1]Because their spectra are a superposition of a young stellar population (represented by A stars) and an old population (characterized by K stars), these galaxies became known as "E (for elliptical) + A" galaxies (Dressler & Gunn, 1983) or, more straightforwardly, "K+A" or "k+a" galaxies (Franx et al., 1989; Dressler et al., 1999; Poggianti et al., 1999).

ers, which are both common in the field and known to enhance star formation? In the merger hypothesis, E+As are further along the "Toomre sequence" (Toomre, A., 1977) and thus more relaxed than systems like the Antennae, whose morphology and kinematics are in such disarray that it is nearly impossible to constrain its endproduct. E+As may thus teach us considerably more about the endpoints of galaxy-galaxy mergers.

We cannot test this picture of E+A formation, or whether the E+A phase is a bona fide late-to-early type transition, without detailed morphological information. Simulations predict that well-evolved major mergers have a hybrid morphology, including fading, low surface brightness tidal tails at large radii, a more relaxed spheroid-dominated core, and a population of young star clusters (Barnes, 1988; Barnes & Hernquist, 1996; Ashman & Zepf, 1992; Mihos & Hernquist, 1994). Identifying such low surface brightness or small scale features, even at low redshifts, requires spatial resolution on the order of 100 pc and low sky background levels. Therefore, Hubble Space Telescope imaging of nearby E+As is required.

In this paper, we present the detailed *HST*/WFPC2 morphologies of the five bluest E+A galaxies in the Zabludoff et al. (1996) sample. We review the sample and the data reduction methods in §2.2. We describe the qualitative morphologies of these galaxies in §2.3.1, discussing the observed tidal features and the implications for E+A origin. We address the question of whether E+As are consistent with evolution into early types by fitting two-dimensional, surface brightness models to each image and deriving structural parameters such as bulge-to-disk ratio, effective radius, and central surface density (§2.3.2). In §2.3.4, we examine the color gradients in the E+As and compare them with the expectations from disk merger models. We compare the results with the fundamental plane for

early type galaxies and with the surface brightness profiles of the nearby elliptical galaxies in §2.3.5 and §2.3.6, respectively. In §2.3.7, we search for star clusters in the E+As and ask whether their properties are consistent with late-to-early type galaxy evolution. We discuss the implications of our results for higher redshift galaxy surveys in §2.3.8, cautioning that bulge-to-disk decompositions, quantitative measures of asymmetry, and tests to uncover tidal features may mislead. Section 2.4 summarizes our results.

2.2 Observations and Data Reduction

Our *HST* imaging sample is a subset of the 20 nearby E+A galaxies[2] that were spectroscopically identified from 11,113 galaxy spectra in the Las Campanas Redshift Survey (LCRS) with redshifts between 0.07 and 0.18 (Zabludoff et al., 1996). These E+As are selected by requiring that their spectra have strong Balmer absorption features (average equivalent width $\langle H \rangle$ of Hβ, Hγ and H$\delta > 5.5$Å) and little if any [OII] emission (EW[OII] < 2.5 Å). Three-quarters of the E+As in the sample are in the field, well outside rich cluster environments. The number of each E+A (e.g., EA1) is from Zabludoff et al. (1996) and increases with increasing 4000Å break (D_{4000}) strength. D_{4000} is related to the galaxy's color — bluer galaxies have smaller D_{4000}. EA1 through EA5, the focus of our *HST* study, have the smallest D_{4000}'s, and therefore are more dominated by the young stellar population than the other E+As. This dominance can arise either because they have had the most recent or strongest bursts. For the remainder of this paper, we refer to each galaxy by its assigned number. Table 2.1 summarizes the basic data of five galaxies: coordinates, redshift, and environment. Throughout this paper, we assume $H_0 = 70$ km s^{-1} Mpc^{-1}, $\Omega_{\mathrm{M}} = 0.3$, and $\Omega_{\Lambda} = 0.7$.

[2]One (EA20) of the original 21 galaxies turned out to be misclassified as an E+A due to noise in the region of one of the spectral line diagnostics (Norton et al., 2001).

We obtained high resolution images of the five nearby ($z \sim 0.08 - 0.12$) E+A galaxies with the *Hubble Space Telescope* Wide Field Planetary Camera 2 (WFPC2). Because our sample is at relatively low redshift (typically $z \sim 0.1$, for which $0.5'' =$ ~ 1 kpc), it is possible to study the LCRS sample in ways that are not possible for the more classic E+As discovered in distant clusters. We take advantage of this benefit to obtain spatially-resolved spectroscopy (Norton et al., 2001) and sub-kpc imaging here. We observed the sample using the F702W ($\lambda_{\mathrm{eff}} = 6997\text{Å}$) and F439W ($\lambda_{\mathrm{eff}} = 4292\text{Å}$) filters and obtained three CR-split 700s exposures for each object. Stacked images were generated by summing the three individual images for each galaxy and filter. The pointing was identical for each image, so no shifting or interpolation was required. We rejected CR events by comparing deviant pixels within the stack to a WFPC2 noise model.

We adopt photometric zero points of the *HST*/WFPC2 from Holtzman et al. (1995) after correcting for the gain=7.0 and the nominal infinite aperture. Our values are the same as given in the *HST Data Handbook*. For the Planetary Camera, F439W and F702W magnitude zero points are 20.884 and 22.428, respectively. We adopt Galactic extinction corrections from Schlegel et al. (1998), assuming an $R_V = 3.1$ extinction curve. A_{F702W} and A_{F439W} are calculated from the relative extinction table in the Appendix (Schlegel et al., 1998). The value for F439W is not available in the Appendix, so we use the extinction appropriate for the Landolt B magnitude.

To compare the magnitudes of galaxies within certain filters across a range of redshifts, or to photometric models, we apply K-corrections. In principle, the K-correction can be calculated by using the spectral energy distribution (SED) of an object with full spectral coverage and high S/N. Unfortunately, flux-calibrated spectra with full spectral coverage and high S/N are not available for our sample.

The SEDs of E+As strongly depend both on the stellar mass formed during the starburst and on the time elapsed since the burst. To account for this variation in stellar populations, we examine both extremes — a pure A type and a pure K type stellar spectrum. We use A dwarf and K giant templates from the Gunn-Stryker spectrophotometric atlas (Gunn & Stryker, 1983), which covers the wavelength range 3130 to 10800 Å. We artificially redshift the template spectra to $(1 + z)$ and measure the magnitude differences in the F702W and F439W filters using the CALCPHOT routine within the IRAF/SYNPHOT package. In the F702W band the difference between the corrections for the two populations is within $\sim 0.19 - 0.31$ magnitudes. In contrast, the difference in the corrections is larger than 0.62 magnitudes for F439W because the F439W filter band includes the Balmer jump. A slight shift of the spectra can cause a large change in measured brightness. We list both sets of corrections in Table 2.3, but adopt the correction calculated for an A star with the justification that these are the bluest, most A-like, of the E+As in the Zabludoff et al. (1996) sample. Because the K correction is the major source of uncertainty in our error budget, the global photometric quantities, especially colors, possibly harbor significant systematic errors. The sense of any relative colors within a galaxy is not affected, although the numerical values may be.

2.3 Results and Discussion

The *HST* images provide a wealth of information on the small and large scale structure of these galaxies. With the goal of understanding the origin of the E+A phenomenon and into what these systems will evolve, we investigate the morphologies of these systems, their color profiles, their location on the Fundamental Plane (Jørgensen et al., 1996) of elliptical galaxies, and their relationship to "core" and "power-law" ellipticals (Faber et al., 1997). We also discover a population

of associated point sources (possibly young star clusters). Finally, we review the implications of our results, obtained for low-redshift E+As, for the identification and study of such systems at higher redshifts. The reader is referred to Tables 2-5 for a summary of the quantitative results discussed in this section.

2.3.1   Morphologies: First Impressions

Figure 2.1 shows the WFPC2 mosaic and PC images of our five E+A galaxies at different contrast levels. The full mosaic images ($80'' \times 80''$) are in the left column. The center of each E+A is located in the PC, which is in the upper right corner of each mosaic. Tidal features that extend into the other CCDs are evident in EA1-3. The middle and right columns contain the F702W ($24'' \times 24''$) and F439W ($12'' \times 12''$) PC images, respectively, on a logarithmic flux scale. *HST*/WFPC2 observations are relatively insensitive in the bluer band so that the signal in the F439W images typically extends out only to ~ 3 kpc, 25% of the red coverage, and even there it is of low signal-to-noise.

These five E+As exhibit a variety of morphologies ranging from a highly complex system (EA1) to what could visually be classified as a barred S0 galaxy (EA5), even though they have been uniformly selected using spectroscopic criteria, i.e., "k+a" type spectra from the LCRS.

EA1 stands apart from the other four E+As. It is composed of two components that are separated spatially by ~ 3 kpc and another companion with a projected separation of 14 kpc (assuming the companion is at the redshift of EA1). The association is supported by an asymmetric feature emanating from the companion that could be tidal material and a faint bridge that appears to connect it to EA1.

EA2 and EA3 also exhibit highly disturbed morphologies, although EA3 could be visually classified as a normal face-on spiral galaxy in the low contrast PC image. This ambiguity in visual classification is discussed in more detail in §2.3.8.
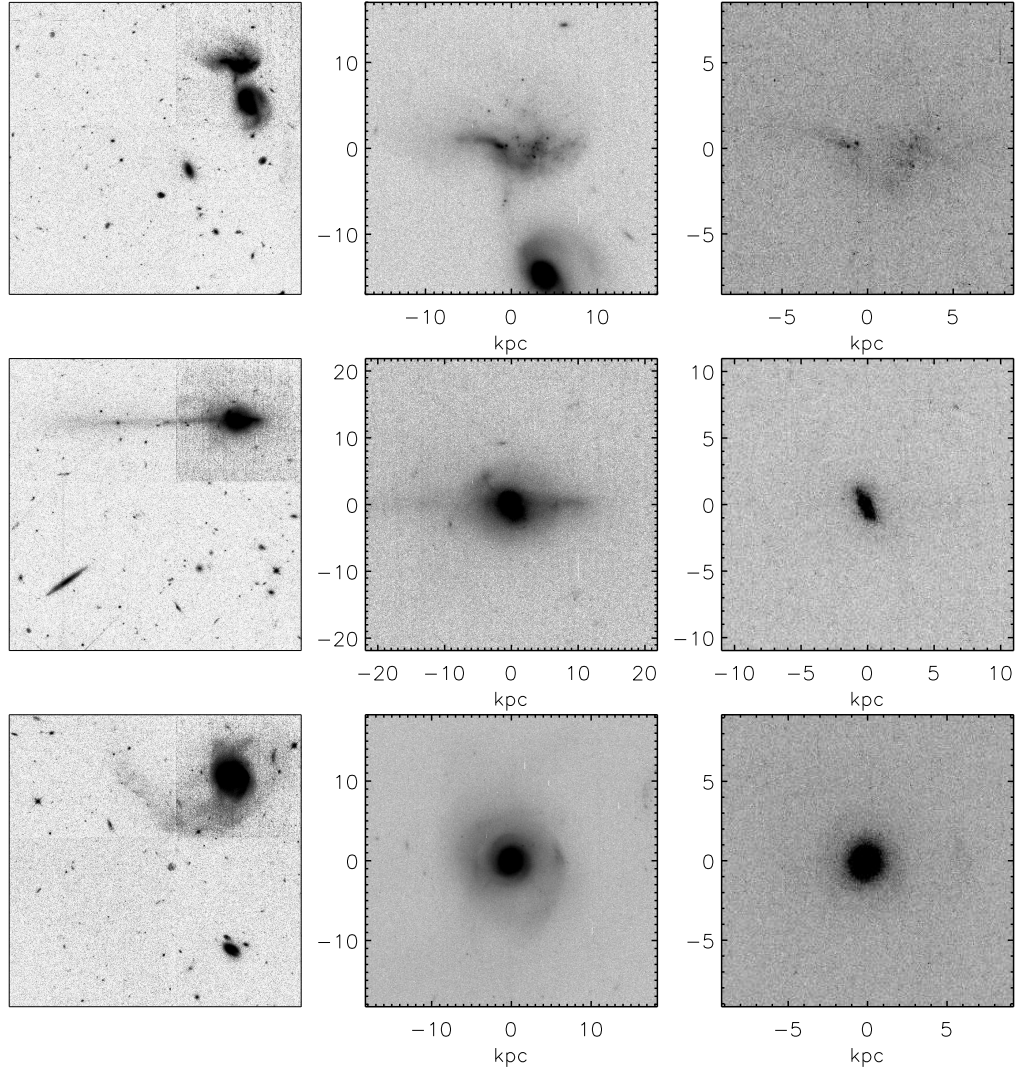
Figure 2.1 — *HST* WFPC2 images of five E+A galaxies. From top to bottom, EA1 to EA5. (*left column*) WFPC2 mosaic images in high contrast. Notice the dramatic tidal tails. (*middle column*) High resolution F702W band PC images in low contrast. (*right column*) Central regions in F439W band. The size of each field is $\sim 80''$, $24''$, and $12''$ (left to right), and the pixel scale in the middle and right columns is $0''.046/$pixel.
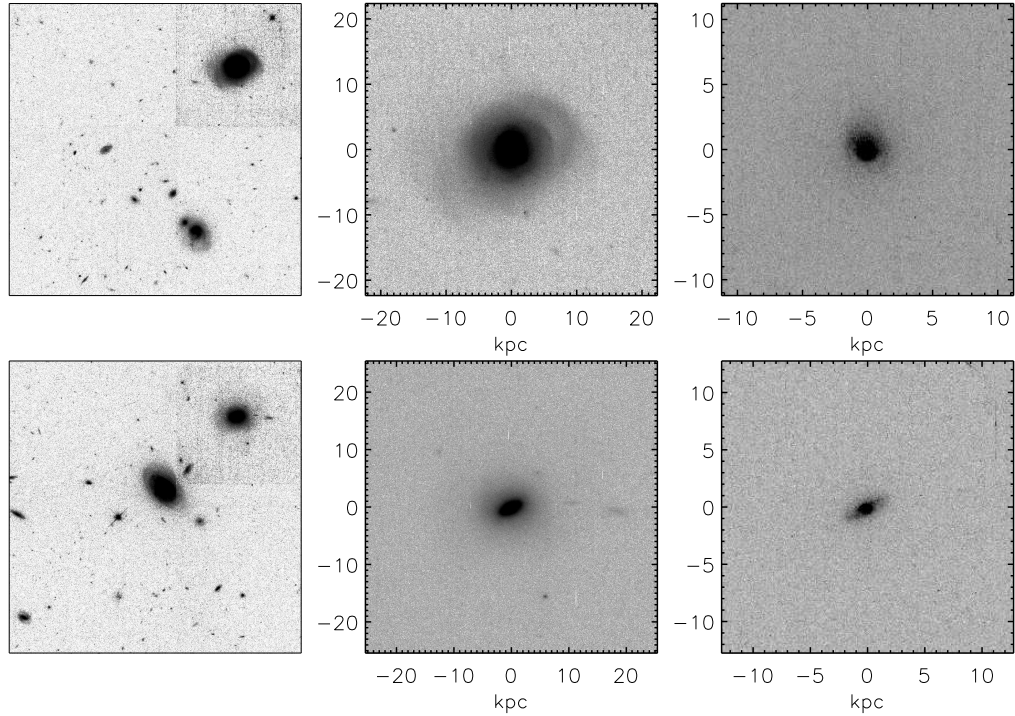
Figure 2.1 — Continued.

EA2 has tidal tail that extends to at least 50 kpc.

EA4 and EA5 appear less disturbed, although EA4 has somewhat irregular outer isophotes, some lopsidedness (in the F439W filter image), and shell-like structures closer to the center that are visible in the PC image. The mechanism or mechanisms responsible for the spectral E+A phenomenon produce a variety of morphologies. Whether all of these systems will evolve into a somewhat more homogeneous population — for example, early-type galaxies — is yet unclear.

2.3.2 Morphologies : Bulge-Disk Decompositions

While EA2-5 appear to have significant spheroidal components, EA3 and EA4, at least, also seem to have a flattened, or perhaps disk-like, morphology. Under-standing the fate of these systems requires a quantitative estimate of the relative

importance of the dynamically hot and cold stellar components.

Measuring the surface brightness profile for asymmetric, disturbed systems is challenging. To mitigate potential systematic problems, we use two different algorithms. First, to obtain photometric parameters, r_e and μ_e, we use the two-dimensional image fitting algorithm GALFIT (Peng et al., 2002) designed to extract structural parameters directly from the galaxy image. GALFIT assumes a two-dimensional model profile for the galaxy. The functional form of the models we choose to fit include combinations of an $r^{1/4}$-law, a Sérsic $r^{1/n}$-law, an exponential disk profile, and a spatially constant sky background. We fit the following: the (x, y) position of the center, M_{tot} (the total magnitude of the component), r_e (the effective radius), n (the Sérsic index), q (the axis ratio defined as b/a), the major axis position angle, and c (the diskiness/boxiness index, where $c > 0$ indicates boxy). This index c plays the same role as the $\cos 4\theta$ Fourier coefficient term used often in isophote analysis (Rix & Zaritsky, 1995). As GALFIT explores parameter space, it convolves the model image with a point-spread function (PSF) and compares it to the data for each parameter set. The model PSFs are generated for each galaxy by the TinyTim (Krist & Hook, 1999) software for the WFPC2. Although convolution is computer intensive, the advantage of the convolution process is that it preserves the noise characteristics of the images and can be applied to low signal-to-noise images.

Because GALFIT begins with a very specific, smooth model, which may be a poor representation of such distorted galaxies, we also measure surface brightness profiles using the IRAF/ELLIPSE algorithm. This approach allows the center, major axis position angle, and ellipticity of each ellipse to change, but does not enforce a model radial profile. To accurately recover the surface brightness profiles without recourse to *ad hoc* models, we applied 20 iterations of Richardson-

Lucy deconvolution (Richardson, 1972; Lucy, 1974). Lauer et al. (1998) showed that the WFPC2 PSF can depress the brightness profile as far out as $0''5$ from the galaxy center. Richardson-Lucy deconvolution allows the intrinsic brightness profile to be recovered to the few percent level down to $r \sim 0''05$, with adequate exposure levels ($S/N \sim 50$ in the galaxy center). With reduced S/N and only 20 deconvolution cycles, the central ($r = 0$) point in the profile may remain slightly-depressed, dependent on the (unknown) intrinsic structure of the galaxy center.

Because EA1 is too disturbed to be reasonably modeled by a simple disk+bulge model, we restrict our analysis to EA2-5. For each galaxy, we fit three different light distributions: $r^{1/4}$ law, $r^{1/n}$ Sérsic law, and $r^{1/4}$ + exponential disk law. For EA2, we do not fit the $r^{1/4}$ + exponential disk law model because we might be seeing this galaxy close to edge-on (see the linear residuals in Figure 2.2), and it is hard for GALFIT to fit an edge-on disk with an extended tail. The structural parameters and the reduced χ_ν^2's of these three GALFIT models are listed in Tables 2.4 and 2.5. With the exception of one case, $1 < \chi_\nu^2 < 2$. These values of χ_ν^2 are somewhat larger than statistically acceptable, due presumably to the presence of asymmetric components, as can be seen in Figure 2.2.

Of the three profiles we consider, only the Sérsic profile has the flexibility to model either a spheroidal or disk-like system by varying the parameter n. Therefore the best-fit value of n can guide our conclusions about the nature of the galaxy. An exponential disk corresponds to a value of $n = 1$, while the classic de Vaucouleurs profile corresponds to $n = 4$. However, the correspondence between disk system, spheroid, and n is not quite this simple — fitting Sérsic profiles to SDSS galaxies, Blanton et al. (2003) show a peak at $n = 1$ corresponding to disky systems, but no peak at $n = 4$. Instead, spheroidal systems show a range of n values. This result is further complicated when one factors in differences in
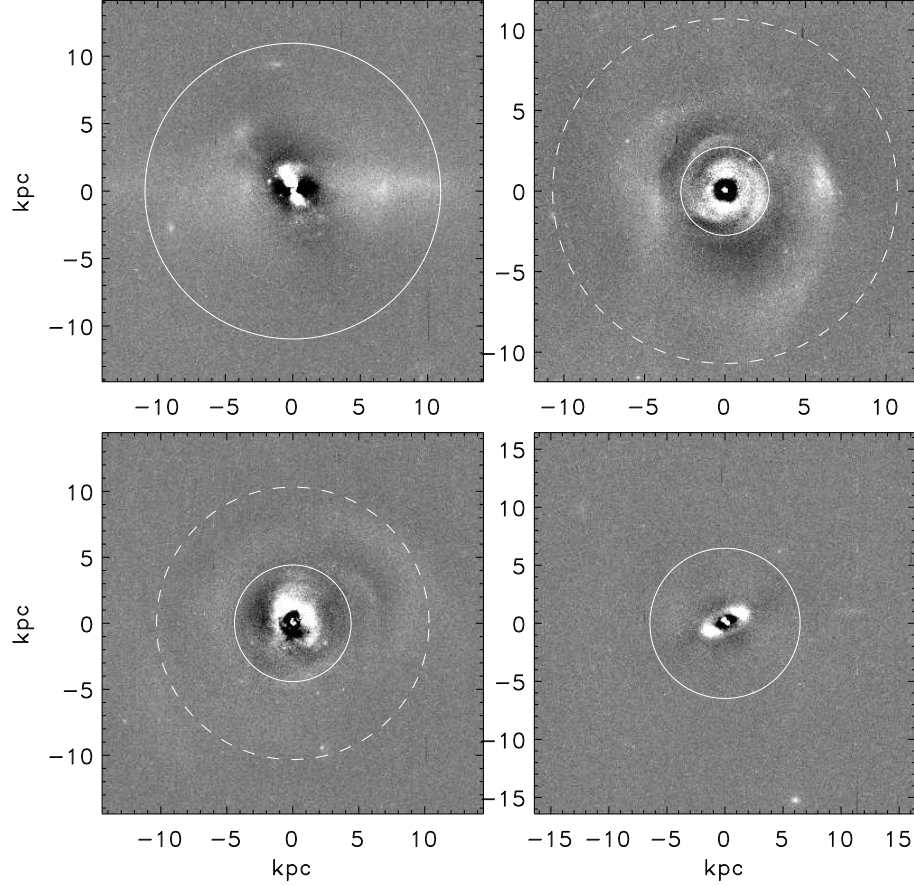
Figure 2.2 — Residual images ($15.5'' \times 15.5''$) obtained by subtracting the smooth and symmetric model images from the data. EA3 and EA4 : $r^{1/4}$ bulge + exponential disk model. EA2 and EA5 : $r^{1/4}$ bulge only. The solid and dashed circles represent $4r_e$ and $3r_d$ (if bulge+disk decomposition was done), respectively. The relative asymmetric light — excess (deficit) — within a $10''$ radius is 16(8)%, 6(5)%, 8(9)% and 9(8)% of the symmetric model components for EA2-5, respectively.

radial ranges fit — for example, fitting the inner slope of cuspy power-law ellipticals (e.g., Lauer et al. 1995) will give a much higher n value than will fits at larger radii.

With these caveats in mind, we find that a single Sérsic profile fit yields $n > 5$ for all our galaxies, demonstrating that the light is dominated by a spheroidal component. Indeed, the high values for n indicate a very high concentration of the light, even more than expected for a classic de Vaucouleurs profile. Such high concentrations are consistent with the idea that central starbursts have raised the central luminosity density (e.g., Mihos & Hernquist 1994). For example, in the case of EA4, masking the inner kpc and refitting the Sersic law results in a value of $n = 3.6$, much more typical of a normal elliptical. This is not always the case, however — in EA3, the high Sérsic value persists even when the nucleus is masked out. For EA3 the fitted value ($n = 8.7$) is unusually high compared to normal ellipticals (e.g., Kelson et al. 2000; Graham et al. 2001; Graham 2002). An additional complication to the interpretation of these fits is that, while the light appears to be dominated by a concentrated spheroid, some of the galaxies appear to contain an additional disk-like component that would affect any dynamical model of a merger and its aftermath.

To determine whether these galaxies do indeed contain a disk component, we also fit models with two components. The resulting radial profiles for EA3 and 4 (Figure 2.3) and the significant decrease in χ^2_ν (an improvement in the fit at the 99% confidence level) demonstrate that a pure spheroid model is not the preferred model for these two systems. To avoid the degeneracies present in fitting disk and bulge simultaneously, we also fit single Sérsic profiles just to the outer parts of the galaxies. Using the effective radii of the bulges calculated from the two-component fit, we mask pixels inside a chosen radius, vary that radius to be $\sim 3 - 5r_e$ and refit a single component. We mark the effective radii and disk scale lengths with circles in Figure 2.2. For EA3, the best-fit Sérsic indicies are $n = 2.5$, 1.6 and 1.3 for masks corresponding to $3r_e$, $4r_e$, and $5r_e$, respectively. For EA4,
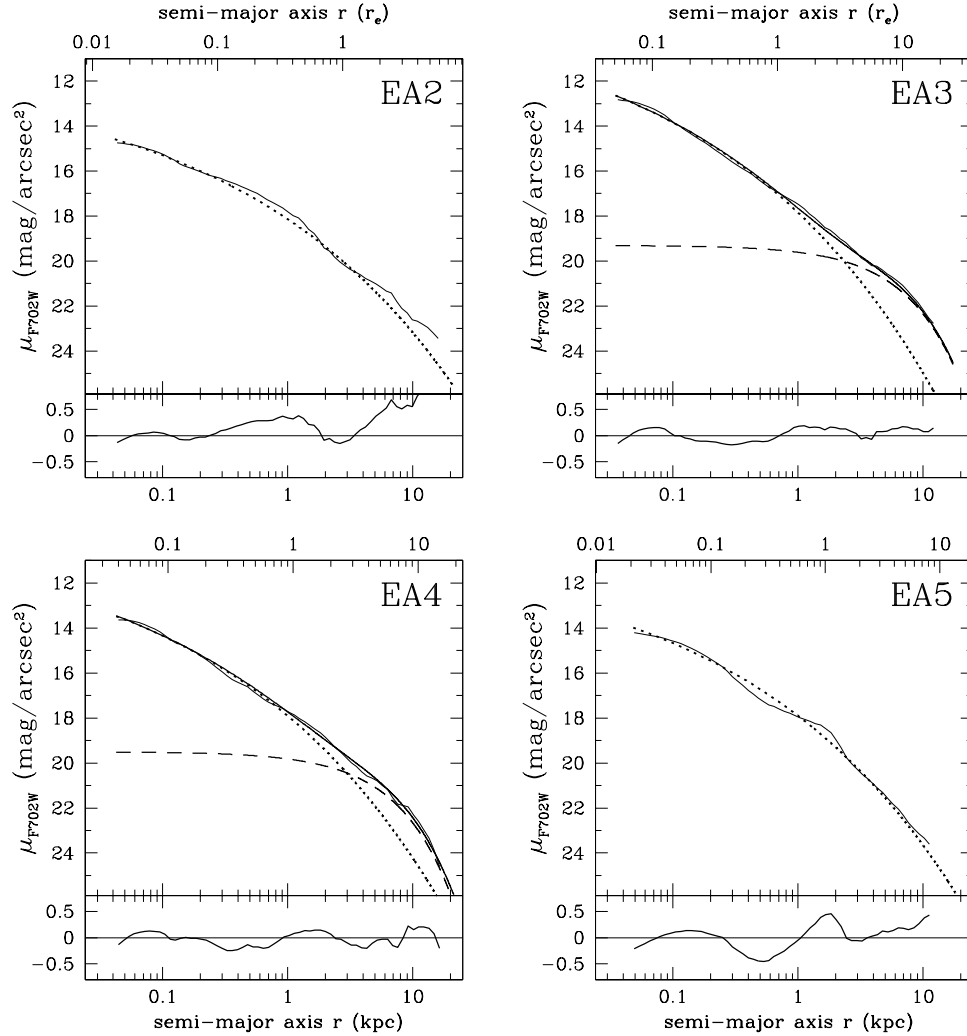
Figure 2.3 — F702W radial surface brightness profiles. The thin solid lines show the radial profiles obtained from ELLIPSE, the dotted lines show the bulge components fitted to the $r^{1/4}$ law, and the dashed lines show the disk/tidal components fitted to the exponential law. The thick solid lines are the superposition of the bulge and disk components. Pure bulge + disk decomposition was done only for EA3 and EA4 (fitting EA5 was more complicated, see text and Figure 2.4). The top axis of each panel is the effective radius r_e of the bulge component of each galaxy. Bottom panels show the difference between the data (ELLIPSE) and fits (GALFIT).

we measure $n = 0.93$ and 0.86 when we apply $3r_e$ and $4r_e$ masks, respectively. In both of these cases, the Sérsic index beyond several r_e is as expected for an exponential disk and the fit spans 4 to 5 disk scale lengths. Although we cannot discriminate tidal material from a possible underlying disk, we conclude that in EA3 and EA4 there is material beyond that described by a spheroid and that it is consistent with an underlying disk. EA3 and EA4 appear to be sufficiently relaxed that no significant dynamical evolution is expected, so they may become S0's. We also hypothesize that their progenitors may have included a disk that was significantly heated but not completely destroyed during an intermediate mass ratio merger (e.g., Naab 2000; Bendo & Barnes 2000).

Even though no disturbed tidal structure is apparent in EA5, the modeling is complicated by the presence of a strong bar-like structure. The presence of a bar-like feature suggests an underlying disk. When viewed at the different contrasts in Figure 2.4, EA5 is composed of at least three distinct components, a extended light distribution in outer part (axis ratio $q \sim 0.8$), a compact and elliptical bar structure ($q \sim 0.4 - 0.5$), and a very bright blue central nucleus. The three-component fit gives the Sérsic index $n = 1.1$ for the central nucleus, $n = 0.5$ (Gaussian) for the bar, and $n = 1.5$ for the outer disk-like region. This three-component Sérsic profile fit (Figure 2.4) is acceptable and suggests the presence of disk. For mask sizes $2.5r_e$, $3r_e$ and $3.5r_e$, the best fit Sérsic indicies n are 2.0, 1.8, and 1.8, respectively. However, unlike for EA3 and EA4, we do this fit in a limited region and cannot conclude that EA5 has a distinct exponential disk component. The presence of a bar-like feature also suggests an underlying disk.

For the E+As that may contain a disk component, we calculate a bulge-to-total light ratio (B/T) to quantify the relative importance of the bulge and disk-like components. B/T for EA3 and EA4 is 0.56 and 0.62, respectively. These values are
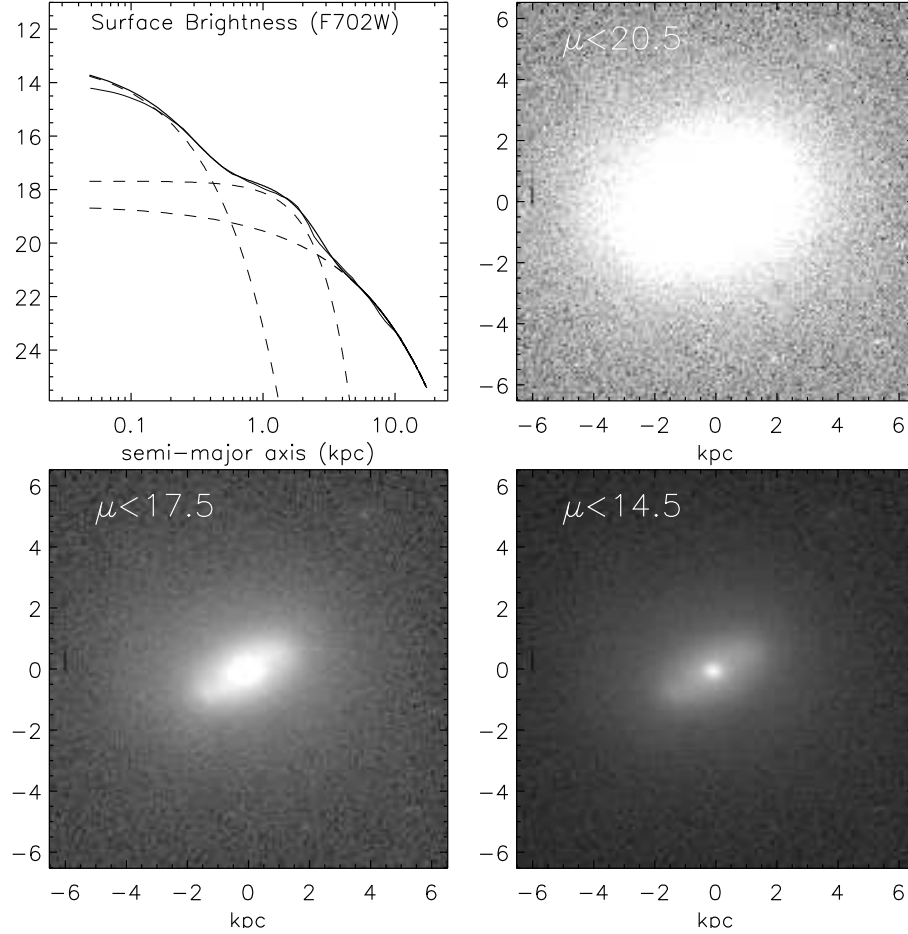
Figure 2.4 — EA5 galaxy in different contrasts. EA5 shows three components — an extended light distribution in the outer part, a bar structure, and a very bright blue central nucleus. (*Upper left panel*) Three-component decomposition of EA5. The dashed lines represent each component. Solid thin and thick lines show the data and the sum of the three model components ($n = 1.1$, 0.5, and 1.5 from inside to outside), respectively.

larger than the typical B/T for Sa galaxies (0.45) and comparable to the median for S0's (0.63; Kent 1985). Despite the complications of fitting EA5, various modes of fitting the galaxy produce B/T ~ 0.7. Unless the bulge and any underlying disk-like component fade at dramatically different rates, which is unlikely given the relatively weak large-scale population gradients in these galaxies (Norton et al., 2001), the descendants of these galaxies must be early type (S0 or E, if the disk-like material is tidal debris that disperses or collapses onto the central component).

Given the asymmetric features, how reliable are these fits? There are several ways to check the results for possible systematic errors. First, we compare the fitted analytical profiles to the radial surface brightness profiles obtained from the isophote fitting procedure. In Figure 2.3, we plot the radial surface brightness profiles of a chosen model for each galaxy: $r^{1/4}$ profile for EA2 and EA5, $r^{1/4}$ + exponential disk profile for EA3 and EA4, and the profiles obtained from the isophote fitting. The differences between the data (ELLIPSE) and models (GAL-FIT) range mostly between ± 0.5 mag/arcsec^2, are not global, and reflect local asymmetric components. Second, we examine the residual images obtained by subtracting the smooth and symmetric models from the data (see Figure 2.2). In all cases we see evidence for components beyond the bulge + disk model. We then calculate how much light remains in the residual images to quantify the goodness of the fit. The relative asymmetric light — excess (deficit) — within a 10″ radius is 16(8)%, 6(5)%, 8(9)%, 9(8)% of the symmetric model components for EA2-5, respectively. Most (50% to 80%) of the under(over)subtracted light comes from the central region within 0.5″, where the even a small amount of fractional deviation from the data can dominate the residual flux over the outer faint parts. Except for EA2, the global under(over)subtractions are roughly the same and localized fluctuations dominate the residuals, so we conclude that our global fits

are reliable. In the case with the most residual light (EA2), 24% of the light cannot be explained by a symmetric model and the positive residuals dominate all over the galaxy. Therefore, we cannot exclude the possibility that we are looking right along the interaction plane (the tidal debris are quite linear). The point sources near the E+A bulges in the residual images are discussed in §2.3.7.

2.3.3 Morphologies: Asymmetric Components

So far we have fit symmetric smooth models with moderate success, but have found that asymmetric features are quite common in our sample. Asymmetry, in particular lopsidedness, has been used to measure disturbances in local "normal" disk galaxies (Rix & Zaritsky, 1995; Zaritsky & Rix, 1997) and correlates with recent star formation (Zaritsky & Rix, 1997; Rudnick & Rix, 1998). There are multiple ways in which one can quantify asymmetry, but here we choose to follow what was done for local spirals by Rix & Zaritsky (1995). This measurement is based on the azimuthal Fourier decomposition of the surface brightness along elliptical isophotes.

For the two most disk-like of the E+As (EA3 and 4), we calculate the Fourier decomposition of the F702W band surface brightness distribution. We use a grid with 24 azimuthal and 36 radial bins from semi-major axes of 4 to 200 pixels. The center of the azimuthal grid is identified as the brightest central point in the galaxy image. Figure 2.5 shows the amplitudes of the various first Fourier terms as a function of radius. In field spirals, $A_1 > 0.2$ is identified as strong lopsidedness, found in $\sim 20\%$ of the cases, and interpreted as the result of a recent interaction (other explanations, such as halo-induced disk sloshing have since been suggested; e.g., Levine & Sparke 1998; Kornreich et al 2002). EA3 has $A_1 \ll 0.2$ at all radii except in the transition region between the inner spiral arms and the tidal tails at $\sim 3-6$ kpc and at large radii where the uncertainties are large.
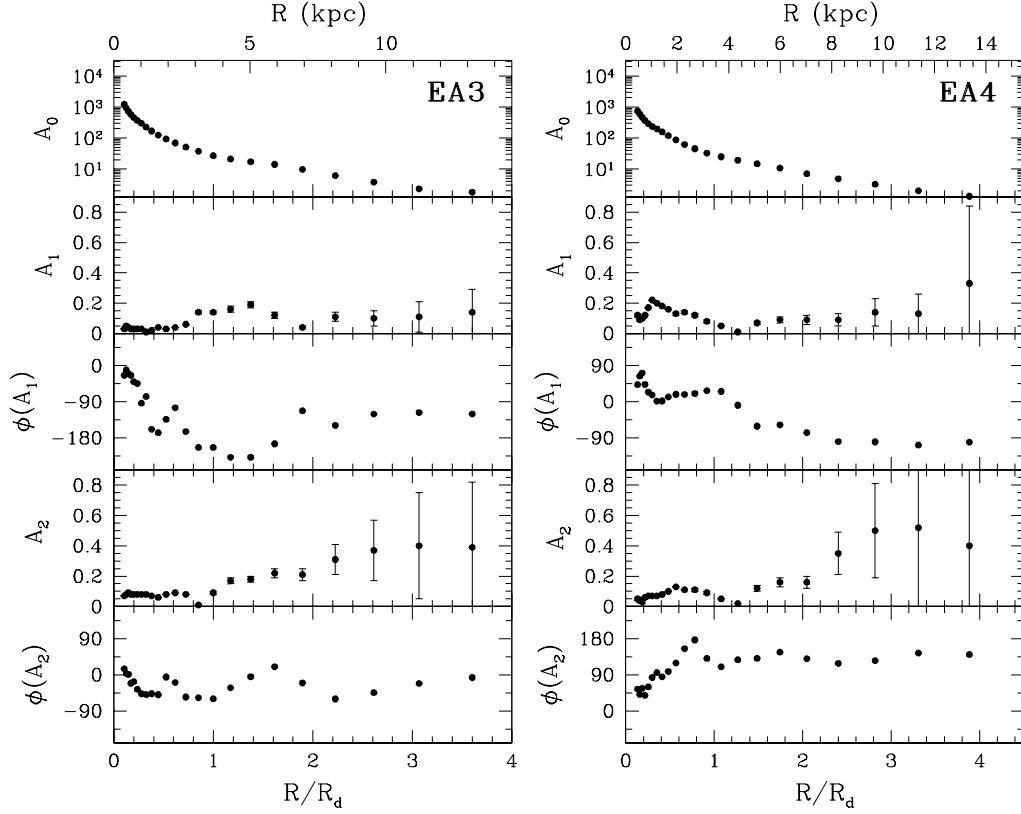
Figure 2.5 — Amplitudes and phases of each Fourier component in the F702W images. Radius is plotted in disk scale units and kpc. A_m and $\phi(A_m)$ are the m-th order Fourier amplitudes and phase angles, respectively. The zeroth order component A_0 has no phase and reflects the mean flux at the given radius. The first order component A_1 denotes the lopsidedness of the galaxy at the given radius.

Although EA4 has large A_1 within 3 kpc, which is consistent with the appearance of the residual image (Figure 2.2), $A_1 < 0.2$ for $1.5 < r_d < 2.5$, the range used in the study of field spirals. The lopsidedness of EA3 and EA4 is consistent with that of normal spiral galaxies despite the cataclysmic event that occurred $\sim$ Gyr ago indicated by the spectra. This result has two possible interpretations: either these galaxies have had sufficient time to relax and "smooth out" interaction-induced

asymmetries (e.g., Mihos 1995), or they are the result of encounters not strong enough to cause major dynamical damage. Of course, the latter possibility runs into the problem of how to trigger such a massive starburst without dynamically disturbing the galaxy.

2.3.4   Color Gradients

The color gradients of E+As are constraints on merger models and clues as to what these galaxies will ultimately become. In Figure 2.6, we show the (F702W $-$ F439W) color profiles of EA2-5, which are obtained by using the results from the ELLIPSE task and include the A-type K-correction. Because of the shallow exposure in F439W band, the color profiles are limited to $r \lesssim 2 - 3$ kpc, which is only 25% of the radial coverage available in the red. To derive the color profiles within the most central region ($< 0.5''$), we use the deconvolved images. However, because deconvolution can produce large artificial fluctuations in low signal-to-noise data, we cannot use the deconvolved F439W profiles in the outer regions of the galaxy. We compromise by using the deconvolved images for $r < 0.5''$ and the non-deconvolved images for $r > 0.5''$.

The overall colors of E+As are relatively blue globally due to the recent star formation (bottom panel of Figure 2.6). The radial extent of the blue colors confirms previous observations (Franx, 1993; Caldwell et al., 1996; Norton et al., 2001) that the recent star formation region is not confined within the innermost regions. However, the color gradients, especially within 1 kpc of the centers, are as diverse as the overall morphologies. While, EA3 and EA5 have blue nuclei and become redder going outward, EA2 becomes bluer with radius, and EA4 shows a relatively flat profile.

The colors are the result of the complicated interplay between age, metallicity and dust. The lack of HI in these systems (Chang et al., 2001; Miller & Owen,
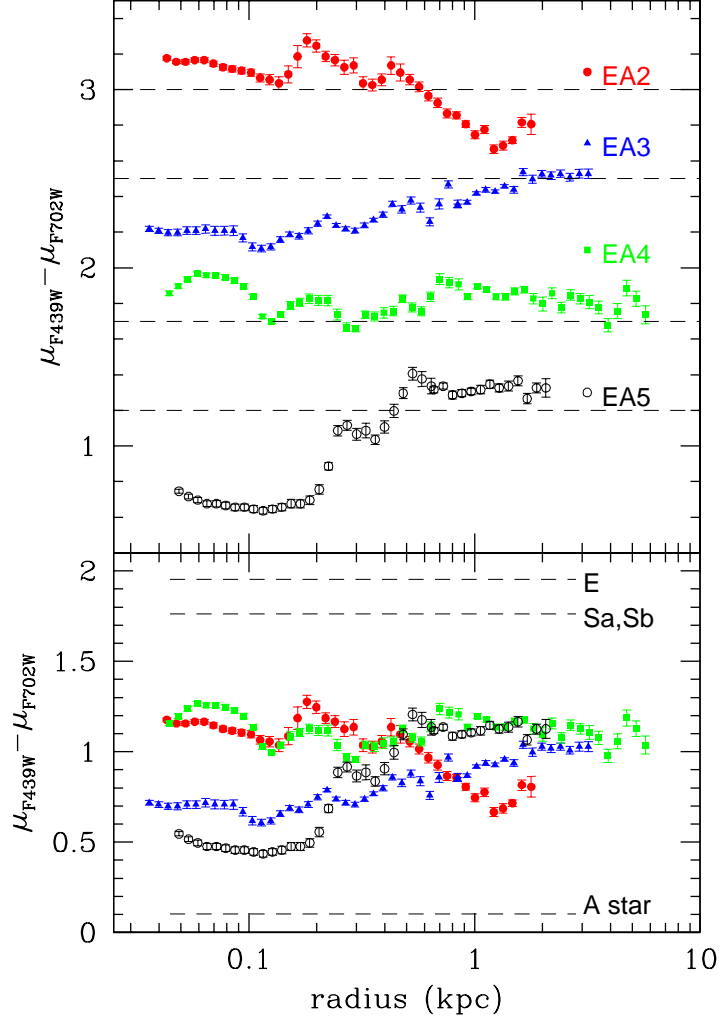
Figure 2.6 — (F702W − F439W) color profiles of four E+A galaxies. The zero point in the color axis is arbitrary in the upper panel. The dashed (F702W − F439W) = 1.0 lines for each color profile are shown for reference. The dashed lines in the lower panel represent the typical colors of elliptical galaxies, spiral galaxies, and A stars. Notice the diversity of the color gradients within 1 kpc, which is reminiscent of their morphological diversity.

2001) and of any patchiness in the images of EA2-5 argue against high levels of dust (but it is still possible that high density pockets of dust are present, particularly toward the nucleus of some of these systems). With the exception of EA1, none of the E+As show the irregular, filamentary structures expected from strong dust lanes. We thus conclude that the variety of color gradients within the inner few hundred parsecs reflects variations of the spatial distribution of the young population, which in some systems appears to be preferentially located near the center of the galaxy and in others appears to avoid the center. Perhaps this reflects differences in the types of encounter involved and its ability to drive true nuclear starbursts — e.g., differences between prograde and retrograde encounters (Barnes & Hernquist, 1996), major versus minor mergers (Hernquist & Mihos, 1995), or differences in the structural properties of the progenitor galaxies (Mihos & Hernquist, 1996).

2.3.5   Relationship to Fundamental Plane

To investigate whether E+As can evolve into E/S0 galaxies, we compare the stellar kinematics and structural parameters of E+As with "normal" early type galaxies. Norton et al. (2001) found that the old component of E+A galaxies is offset (brighter by ~ 0.6 mag) from the the local Faber-Jackson relation. Using the structural parameters that can only be measured using *HST* imaging, we extend this comparison to various projections of the Fundamental Plane (hereafter FP) in Figure 2.7. To compare our results with the FP of Jørgensen et al. (1996), we correct these observables to our adopted cosmology ($H_0 = 70 \, \mathrm{km \, s^{-1} \, Mpc^{-1}}$, $(\Omega_M, \Omega_\Lambda) = (0.3, 0.7)$). Changes in the cosmological parameters only affect zero points in the FP equation. We use velocity dispersions from Norton et al. (2001) for the K-star component and the structural parameters from a single $r^{1/4}$ model
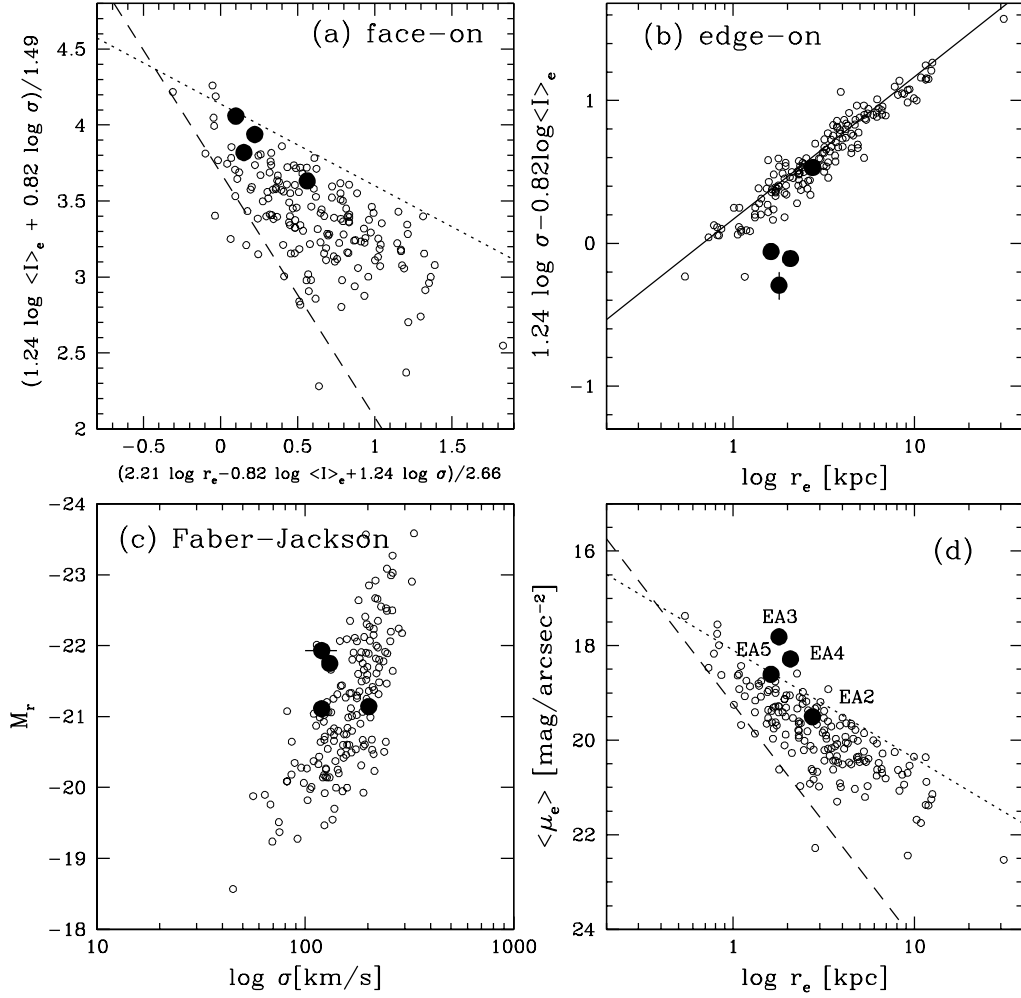
Figure 2.7 — Relative position of four E+A galaxies in the Fundamental Plane (FP). The small open circles are data from Jorgensen et al (1996). (*a*) Face-on view of the FP as in Jorgensen et al (1996). The dashed line indicates the boundary set by the limiting magnitude, but the upper dotted line is not caused by a selection effect. (*b*) Edge-on view of the FP in the longest direction (dashed line in panel (*a*)) of distribution. (*c*) The Faber-Jackson relation. Our galaxies occupy a small region in the parameter space. (*d*) The $r_e - \mu_e$ correlations of early type galaxies and the four E+As. Notice the deviation of EA3 and EA4 from the average relation ($\sim 0.5 - 1.0$ magnitudes brighter than E/S0 galaxies within one effective radius).

[3]. We transform the F702W magnitude to a Gunn r magnitude using the average (F702W − Gunn r) color for galaxies of various Hubble type (Fukugita et al., 1995). The average (r − F702W) colors range from 0.56 for elliptical to 0.51 for Scd galaxies. Even for the extreme case of irregular (Im) galaxies, (r − F702W) is different by only ~ 0.1 magnitude from the average value of 0.54.

We show various projections of the FP in Figure 2.7. Figure 2.7(a) shows the face-on view of the FP given by $x = (2.21\ log\ r_e - 0.82\ log\langle I\rangle_e + 1.24\ log\ \sigma)/2.66$, $y = (1.24\ log\langle I\rangle_e + 0.82\ log\ \sigma)/1.49$ (see Jørgensen et al. (1996)). The dashed line indicates the bound set by the limiting magnitude, but the upper dotted boundary is not caused by a selection effect. Figure 2.7(b) shows the edge-on view of the FP along the long axis of the distribution, given by $y = 1.24\ log\ \sigma - 0.82\ log\langle I\rangle_e$. Figure 2.7(c) shows the Faber-Jackson relation. Figure 2.7(d) shows the correlations between r_e and $\langle \mu_e\rangle$.

The four E+As stand apart from the E/S0s in the edge-on view of the FP, but otherwise populate the same general region of the 3-D volume. The most striking deviation of the E+As among the scaling laws lies in the $\mu_e - r_e$ correlation. EA2-5 are more than a half magnitude brighter than the median E/S0 galaxies with the same effective radii. Especially, EA3 and EA4 have a large excess surface brightness over the dotted boundary of E/S0 galaxies in the FP. We measure the excess brightness to be 0.86 and 0.54 mag relative to the dotted upper boundary of the $\mu_e - r_e$ projection for EA3 and 4, respectively. As seen Figure 2.7(c), although EA2-5 have intermediate luminosities ($-22 < M_r < -20$) in comparison to E and S0 galaxies, they have a large mean surface brightness within the effective radius.

Will E+As fade onto the locus of E/S0's after a few Gyr? We estimate the

---

[3]There is an issue as to which structural parameters (for the entire galaxy or the bulge only) one should use to construct the FP for S0 or disk galaxies. However, we opt to use the (r_e, μ_e) from a single $r^{1/4}$ profile, because we are comparing with Jørgensen et al. (1996), who also used single de Vaucouleurs profiles for S0's.

amount of fading within an effective radius using STARBURST99 models (Leitherer et al., 1999). Assuming solar metallicity, a Salpeter IMF, an underlying 5 Gyr-old population (not evolving), and a single instantaneous starburst with a mass fraction of 50%, the E+As will fade ~ 0.5 magnitudes during the first Gyr after the burst. This degree of fading places EA2, EA4, and EA5 on the E/S0 locus, but not EA3. This model is oversimplified, however. The evolutionary tracks in the $\mu_e - r_e$ projection will proceed from upper-left to lower-right, because of the decline of the mean surface brightness within r_e both due to fading and the inclusion of the larger fraction of the galaxy. But, calculating these effects requires a detailed knowledge of the spatial distribution of the young and old populations.

2.3.6 Comparison with to "Core" and "Power-law" Ellipticals

Does the consistency in global surface brightness profiles between E+As and normal early-type galaxies (as discussed in §2.3.5) extend to the innermost radii? The recently discovered dichotomy in the central surface brightness profiles ("core" vs. "power-law"; Lauer et al. 1995; Faber et al. 1997) of normal early-type provides a framework for this comparison. In Figure 2.8, we plot the F702W surface brightness profiles for our E+As and the F555W profiles of Faber et al. (1997) sample (assuming $V - R = 0.5$ and adjusting for differences in adopted cosmology). The apparent lack of any central "break" and associated transition to a shallow cusp in the E+A profiles leads us to classify the E+As as "power-law" galaxies. Not only are the profiles shapes consistent, but the total luminosities of these E+As lie within the range spanned by normal power-law early-types, and any fading will place them even more securely in that range.

Although the profile shapes and total luminosities of E+As are consistent with those of power-law early-types, Figure 2.8 shows that the E+A surface brightness are generally higher. EA2 is consistent with the highest surface brightness normal
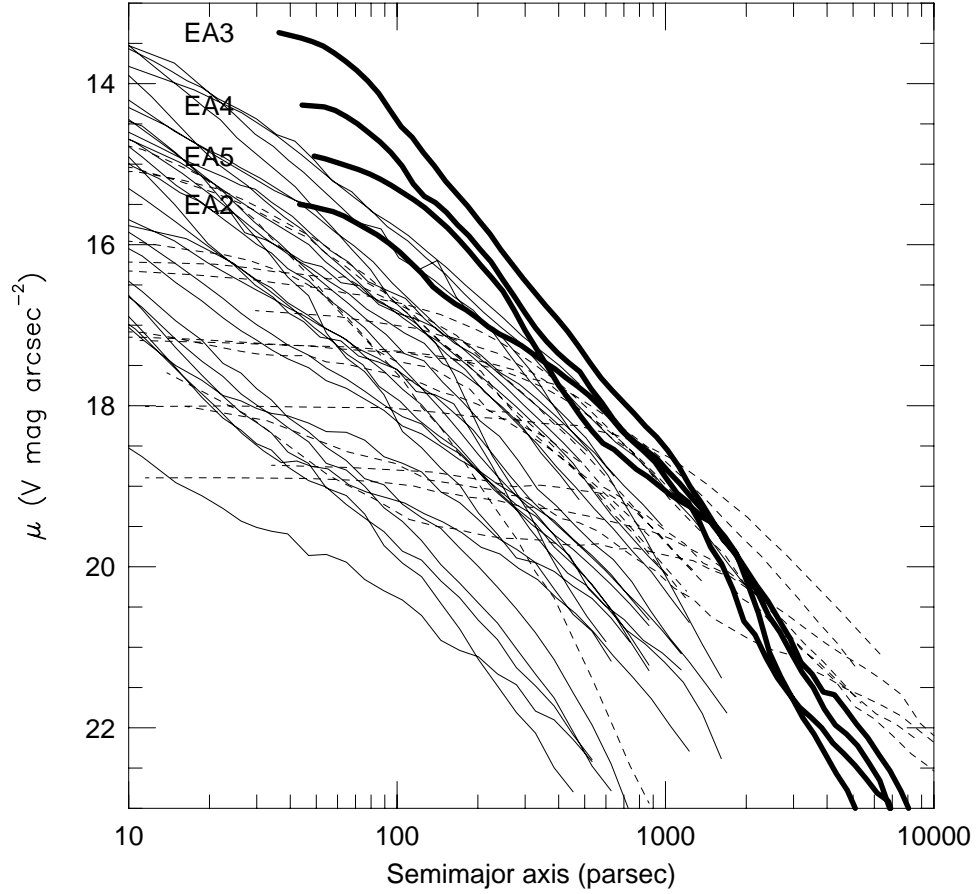
Figure 2.8 — The F702W surface brightness plots of the sample E+A galaxies versus those of normal early-type galaxies (Faber et al., 1997). (The present figure is an adaptation of Faber et al.'s Figure 1.) The E+As are matched to the Faber et al. (1997) scale by assuming $V - R = 0.5$ mag and adopting $H_0 = 70$. Power-law galaxies are plotted as solid lines; core galaxies are plotted as dashed lines. E+A galaxies (thick solid lines) have profiles like those of normal power-law early-type galaxies, but scaled-up in surface brightness.

power-law galaxies, and the other three E+As have even higher surface brightness. If fading of the young stellar population does not significantly alter the profile shape, then these galaxies will retain their power-law profiles. While we cannot be certain that the profiles will remain unchanged, the current inner profiles and total luminosities are consistent with E+A evolution into normal power-law early-type galaxies.

2.3.7 Discovery of Young Star Clusters

A specific type of asymmetric small-scale feature is the compact sources most visible in the residual images. We identify a set of these sources using SExtractor (Bertin & Arnouts, 1996) to analyze both the combined and residual images. Because we expect stellar clusters to be unresolved at these distances (one pixel corresponds to $\sim 65 - 95$ pc at $z = 0.07 - 0.12$), confusion between real sources and hot pixels or background fluctuations is a serious problem. After testing various detection criteria and comparing visually, we decided to consider an object real only if it has at least three adjacent pixels that are each at a flux level 3 times above the local background rms. To estimate the local background level, we use a background mesh size for SExtractor of $\sim 4 - 8$ pixels, depending on the image. The residual images are used to detect compact sources close to the galaxy center, where the rapidly varying galaxy light complicates detections in the original images.

Using these criteria, we detect 35, 9, 29, 10 and 1 point-like sources within the PC images of EA1-5, respectively. These objects may be foreground stars, background compact sources, giant HII regions, or star clusters. Unfortunately, due to the insensitivity of the F439W band, we are able to obtain colors for only a few of the objects. The lack of emission lines in the spectra of these E+A galaxies (Zabludoff et al., 1996; Norton et al., 2001) suggests that these galaxies are not
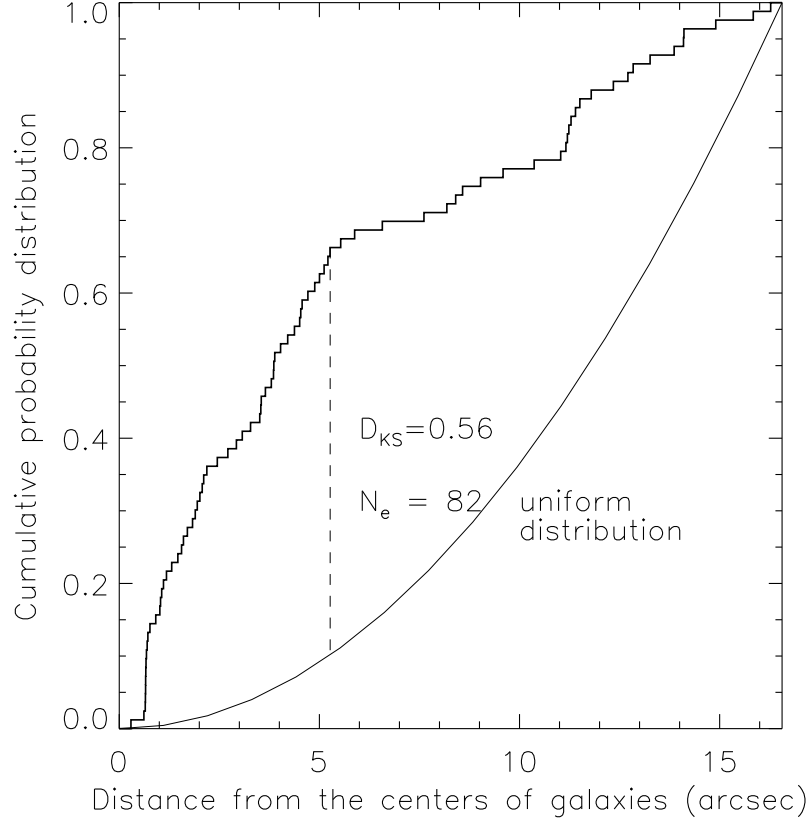
Figure 2.9 — Cumulative distribution of the angular distances of the candidate clusters from the center of the E+As. Thin solid line represents a uniform (or random) distribution, $P(<r) \propto r^2$.

littered with giant HII regions. The spatial distribution of the compact objects suggests that the majority of these sources are associated with the E+As. For example, in EA1 almost all of the point sources are located around EA1 and its companion, and three of them lie in the bridge-like structure connecting the two galaxies. In EA2, some objects lie in the elongated tidal tails. In EA3, five to six unresolved objects surround the nucleus of EA3 and form a concentric circle. We apply a Kolmogorov-Smirnoff (K-S) one-sample test to find the probability that the radial distributions of the compact sources are drawn from a random distribu-

tion. We show the cumulative distribution of the angular distances from the center of each galaxy in Figure 2.9. There is almost zero probability that the sources follow the random distribution, indicating that the detected compact sources are truly associated with the E+A galaxies. Because of the post-starburst nature of E+A galaxies and the discovery of numerous young clusters in ongoing mergers (e.g., Holtzman et al. 1992; Whitmore et al. 1993), it is likely that the majority of these objects are relatively young star clusters.

Like the morphological diversity of the E+As themselves, the number of cluster candidates varies widely among EA1-5. In particular, the difference between EA3 and EA5 is remarkable because these otherwise appear to have comparable masses (the velocity dispersions of their old populations are the same and the luminosity ratio is ~ 0.5). The principal difference between these systems is that EA5 is more distant. To determine whether the distance difference is responsible for the difference in detected sources, we model the detectability of the point sources as a function of distance. For a given size (half-light radius) and brightness, we generate two dimensional surface brightness distributions of the model clusters for a King profile (King, 1966) with concentration $c = 0.5 - 2.5$. We convolve the model profiles with the PC PSF generated from the TinyTim software (Krist & Hook, 1999). All models and PSFs are constructed at a resolution of 1/10th of a PC pixel, re-binned to the original image size, and smeared using the pixel smearing kernel. After adding the Poisson noise and sky background, we attempt to detect the cluster using the same detection criteria that we apply to the original images. The position on the PC and the spectral variation of the PSF do not affect our detection threshold.

The number of detected pixels above 3σ is nearly insensitive to the size of the sources and the shape of the profile in the subpixel regime. In other words,

the images of point sources give us little or no information about their spatial structures, but they can be detected if they are sufficiently bright. We adopt the detection limit as the magnitude at which the number of detected pixels above 3σ drops below three pixels. The number of compact sources above EA5's detection limit ($M_R < -12.5 \pm 0.25$) and well outside the E+A are 6 to 16 for EA3 and is 1 for EA5. The uncertainty in the detection limit arises from uncertainties in the aperture correction and photometry. Assuming EA5 has the same number of the compact sources as EA3, we would expect to detect 3 to 8 sources in EA5 after rough scaling of the projected area occupied by the detections around each galaxy. The statistics of our sample thus preclude us from distinguishing between the cluster populations of EA3 and EA5. If the difference is significant, it might reflect a difference in the starburst (strength or progenitors) or an age difference. The latter possibility is consistent with the observation that EA5 has the reddest D_{4000} and is the most symmetric among our sample.

Matching the observed colors of the cluster candidates with the predictions of stellar population synthesis models can help break the degeneracy between the age and starburst strength of our post-merger E+As. We show the evolution of the color and brightness of a simple stellar population based on Starburst99 models (Leitherer et al., 1999) in Figure 2.10. Because of the unknown SEDs of our sources, the K correction of the observed colors is problematic. To avoid applying an uncertain K correction, we calculate the redshifted (F439W-F702W) colors from the model spectra provided from Starburst99. Superposed on the various models, we show the range of the colors observed and the corresponding range of ages for each of the five point-like sources in EA1 with $\sigma(\mathrm{F439W} - \mathrm{F702W}) < 0.25$ and sufficient S/N. They are identified by eye in the F439W band and are not located in the crowded region. Because the absence of the O, B stellar signa-
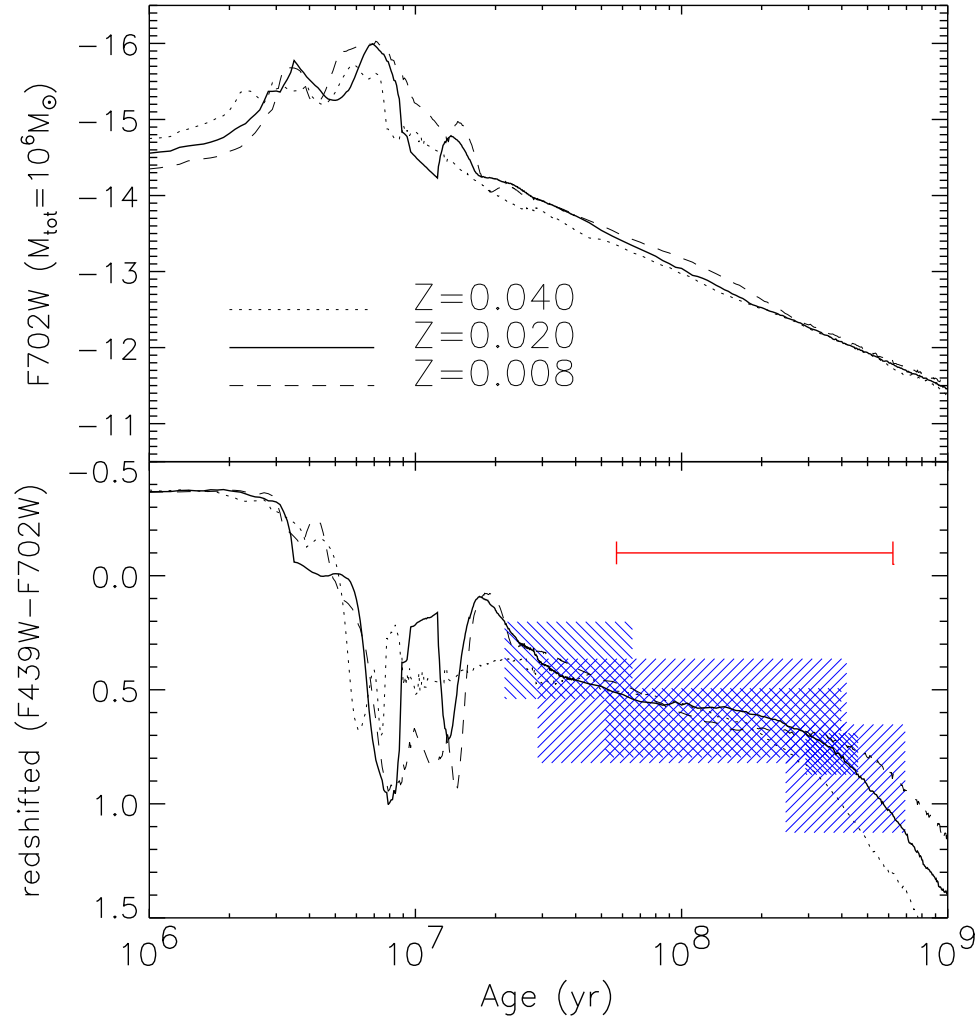
Figure 2.10 — The evolution of the redshifted (F439W-F702W) color and F702W magnitude of a simple stellar population calculated from the models of Starburst99 (Leitherer et al., 1999). Evolution is shown for a single starburst, Salpeter initial mass function (Salpeter, 1955), and three different metallicities. The shaded regions represent the range of colors observed and the corresponding range of ages for each cluster candidate in EA1. These candidates are identified in both the F702W and F439W image. The horizontal line in the bottom panel indicates the 95% confidence level of the estimated single age of the clusters — the time elapsed since the starburst.

tures (Zabludoff et al., 1996; Norton et al., 2001) suggest that the ages of the clusters are older than 10^7 yr, we rule out the solutions in the double trough of the model. Assuming a Salpeter IMF that extends from 1 to 100 $M_\odot$, solar metallicity ($Z = 0.020$), and an instantaneous starburst, we estimate the ages of the candidate clusters to be between ~ 30 Myr and 500 Myr.

We applied the following statistical test to constrain the time since the starburst under the assumption that all the candidate clusters formed at the same time and have a spread of estimated age due to photometric errors. For each model age, we draw a thousand samples of five clusters each with colors scattered according to a Gaussian of dispersion 0.2 mag. We calculate the percentage of simulations that have a median color as far from the true color as the observed median color. If that number is 5% or less, the model is rejected. Because of the slow evolution of colors in the relevant age range, we can constrain the age of clusters (time elapsed since the starburst) to only $\sim 35 - 450$ Myr at the 95% confidence level (see the horizontal line in Figure 2.10). While our constraint on the age is drawn from only a few cluster candidates, this range is as good as the typical age ranges that Leonardi & Rose (1996) derived using CaII and $H\delta/\lambda4045$ indices from the integrated spectra of E+A galaxies. Because any reddening by the host galaxy will make the sources look older, our estimated ages are upper limits on the true ages. However, it is unlikely that the reddening affects our results seriously because the five sources are at large radii, where the extinction should be minor compared to the galaxy center. To improve upon the age estimate, in particular to reduce contamination, to correct the reddening, and to get more precise ages for the sources, ideally we would need deep multicolor photometry to produce a two-color diagram like Fig. 6 in Harris et al. (2001). However, we can see from the present analysis that we would benefit from just more clusters with

colors. We conclude that the derived ages are consistent with what we expect on the basis of the integrated galaxy spectra, again supporting the claim that these are stellar clusters associated with the E+A phenomenon, and suggesting that this is part of a population of clusters formed during the E+A phase.

We compare the R band cluster luminosities of EA1, EA3, the Milky Way globular clusters (Harris, 1996) and the clusters in starbursting, merging systems (e.g., NGC3597, Carlson et al 1999). If the compact sources in the E+As are clusters, they are much brighter ($M_R \sim -13$) than Galactic globular clusters ($M_R > -11$) and similar to clusters in galaxies with on-going starburst. The latter agreement supports the interpretation that we have identified the bright end of a population (e.g., $M_R \sim -14$ in NGC3597) of star clusters formed during a starburst that occurred < 1 Gyr ago. A fading of several magnitudes is required for these systems to resemble the massive end of the Milky Way cluster population.

2.3.8 Implications for High Redshift Interacting Galaxies

The difficulty we have experienced in determining whether these E+As have a disk component, have tidal components, and are asymmetric suggests that at high redshift these galaxies might be classified as "normal" morphologically. For example, the tidal tails that connect onto what may be a disk would naturally be interpreted as spiral arms if one is not able to trace the tails out to large radii. To better understand this effect, we rebin the F702W band image of EA3 and fade it artificially according to our adopted cosmology to mimic its appearance at higher redshift (Figure 2.11). The rebined images are convolved with the PSF, and the sky background and noise proportional to the exposure time are added to the redshifted images. For each image, we assume the same exposure time (2100s) and average sky brightness. The tidal features are lost at a redshift over ~ 0.5 (see also Mihos 1995; Hibbard & Vacca 1997), and EA3 appears to be a
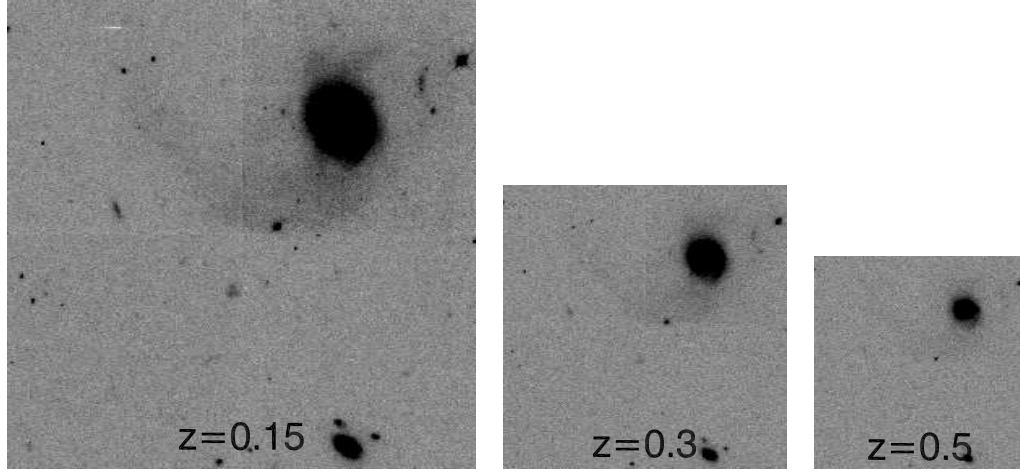
Figure 2.11 — Artificially redshifted images of EA3. We rebin the F702W band image of EA3 and fade it artificially to mimic what it would look like at higher redshifts. The rebined images are convolved with the PSF, and then the sky background and noise proportional to the exposure time are added to the redshifted images.

normal spiral or S0 galaxy. The mean surface brightness of the tidal tails of EA3 is $\sim 24-25 \, \mathrm{mag} \, \mathrm{arcsec}^{-2}$. This exercise suggests that some of the disky E+A galaxies found frequently in distant clusters might be misclassified as non-interacting disk galaxies and nevertheless have tidal features like EA2-4. The lack of apparent tidal features and of asymmetry at high redshift should not be interpreted directly as an absence of interactions.

2.4 Summary

Using *HST* imaging, we have obtained high resolution images of five E+A galaxies. Our results, when coupled with studies of E+A kinematics, star formation histories, and gas content, argue that E+As are in transition between late and early types, a missing link in the evolution of galaxies. Our principal findings

are:

1. Four (EA1-4) of the five E+As are morphologically disturbed (with tidal tails and shell-like structures), consistent with being relics of galaxy-galaxy inter-actions. The dramatic tidal features found in EA1, 2, and 3 further confirm that galaxy-galaxy mergers are at least one mechanism that triggers the starburst that leads to the E+A phase.

2. E+As have diverse morphologies. Even in this small sample, one highly disturbed galaxy cannot be morphologically classified (EA1) and one regular galaxy could plausibly be classified as a barred S0 galaxy (EA5). Two other galax-ies (EA3 and 4) seem to contain disk components. The striking aspect of this mor-phological variety is that all of these galaxies have been selected on the basis of their very similar spectra.

3. The bulge fractions of these systems are consistent with elliptical and S0 galaxies. E+As have a central structure consistent with "normal" power-law early type galaxies (Faber et al., 1997), although at present the E+As have significantly higher surface brightnesses. This is the first direct confirmation that power-law elliptical galaxies can be formed from gas-rich mergers.

4. E+As are blue due to recent star formation, but their color gradients in the central region are as diverse as their morphologies. Two galaxies (EA3 and 5) have extremely blue cores that redden toward the outer regions, one (EA4) has a relatively flat profile, and one (EA2) has a redder core within a few kpc. The red core is particularly puzzling from the standpoint of merger models that pre-dict gas inflow into the center and a subsequent starburst. It is possible that the red color arises from dust extinction, but we see no evidence for the filamentary structure usually associated with dust lanes.

5. E+As stand apart from the E/S0s in the Fundamental Plane mainly due to

their high central surface brightness. Fading of the young stellar population and a corresponding increase in r_e (if the young population is more concentrated than the underlying population) will cause the systems to migrate toward the locus of E/S0s in time. Without a detailed knowledge of the distribution of young and old stars it is not possible to model this evolution precisely.

6. We find compact sources associated with E+A galaxies. Although some of these sources could be foreground stars, giant HII regions, or background objects, we conclude that the majority are star clusters that formed during the starburst phase, such as those found in nearby starburst galaxies. These systems are similar in luminosity to the brightest clusters in NGC 3597 (Carlson et al., 1999) and have ages consistent with that expected for the time elapsed since the starburst (several 10^8 yrs). They are much brighter ($M_R \sim -13$) than Galactic globular clusters, but will fade over a Hubble time to be consistent with the most massive Milky Way clusters. Further study of these systems might provide the elusive chronometer for lifting the age/burst-strength degeneracy for post-merger galaxies.

One valuable lesson of our work is that despite the recent interactions that at least some of these E+As have experienced, one of the standard tests for interactions (the lopsidedness measure based on the azimuthal Fourier decomposition of the isophotes) fails to identify these systems as having experienced a recent interaction. The tidal features are sufficiently faint and the inner surface brightness profiles sufficiently regular that the galaxies are measured to be symmetric. Such indicators should therefore be used with caution on large-scale surveys and at high-redshifts because they obviously miss at least some recently interacting systems. Furthermore, in a system that one does not suspect to be interacting, the tidal tails can easily be misidentified as spiral arms.

This work described the observations of the five bluest E+A galaxies in LCRS

sample with *HST*/WFPC2. To confirm the various results presented here and determine whether this subset was biased by the color selection requires a study of the remainder of the LCRS sample. We are currently obtaining *HST*/ACS imaging of those galaxies.

Table 2.1.   Properties of galaxies

ID	R.A. (1950.0)	Dec. (1950.0)	z	$kpc/''$	f_A [a]	$\langle V_{rot}\rangle$ [a] Old	$\langle V_{rot}\rangle$ [a] Young	σ (kms^{-1}) [a] Old	σ (kms^{-1}) [a] Young	cluster ?
EA1	10 58 48.97	-11 54 9.80	0.0746	1.417	0.80	24^{+57}_{-54}	19^{+17}_{-17}	35^{+39}_{-35}	23^{+53}_{-23}	N
EA2	2 15 43.24	-44 46 36.70	0.0987	1.823	0.42	23^{+16}_{-20}	22^{+24}_{-25}	202^{+17}_{-16}	193^{+32}_{-46}	N
EA3	12 6 31.34	-12 5 55.40	0.0810	1.527	0.59	23^{+17}_{-23}	25^{+18}_{-17}	120^{+22}_{-20}	56^{+35}_{-32}	N
EA4	3 58 23.42	-44 43 40.29	0.1012	1.864	0.56	$1^{+\ 8}_{-\ 9}$	35^{+15}_{-16}	$131^{+\ 9}_{-\ 9}$	246^{+24}_{-25}	Y
EA5	1 56 0.12	-44 51 49.00	0.1172	2.119	0.42	33^{+24}_{-25}	52^{+34}_{-18}	$120^{+\ 7}_{-\ 8}$	94^{+34}_{-41}	N

[a]Data from Norton et al. (2001)

Table 2.2.   Magnitudes and colors of E+A galaxies

ID	F439W $m\,(< 4.5'')$	F439W M	F702W $m\,(< 4.5'')$	F702W M	F439W$-$F702W $(r < r_e)$
EA1	17.95 ± 0.02	-19.97	17.18 ± 0.01	-20.40	—
EA2	18.09 ± 0.02	-20.50	16.44 ± 0.01	-21.70	1.10 ± 0.01
EA3	16.75 ± 0.01	-21.52	15.34 ± 0.01	-22.49	0.80 ± 0.01
EA4	17.47 ± 0.01	-21.17	15.86 ± 0.01	-22.31	1.18 ± 0.01
EA5	18.58 ± 0.04	-20.51	16.83 ± 0.01	-21.67	0.99 ± 0.01

Table 2.3.   K corrections for A dwarf and K giant

		A dwarf		K giant	
ID	z	K(F439W)	K(F702W)	K(F439W)	K(F702W)
EA1	0.0746	0.136 ±0.035	-0.148 ±0.022	0.755 ±0.123	0.042 ±0.032
EA2	0.0987	0.233 ±0.038	-0.192 ±0.028	0.991 ±0.168	0.065 ±0.038
EA3	0.0810	0.157 ±0.036	-0.160 ±0.024	0.823 ±0.136	0.048 ±0.034
EA4	0.1012	0.246 ±0.039	-0.196 ±0.029	1.016 ±0.172	0.068 ±0.039
EA5	0.1172	0.340 ±0.042	-0.225 ±0.033	1.176 ±0.192	0.084 ±0.043

Table 2.4.   Structural parameters

	$r^{1/4}$-Law			Sérsic $r^{1/n}$-Law			
ID	r_e (kpc)	μ_e	χ^2_ν	r_e (kpc)	μ_e	n	χ^2_ν
EA2	2.74 ± 0.14	19.99 ± 0.09	1.72	4.49 ± 0.98	21.10 ± 0.39	6.22 ± 0.53	1.62
EA3	1.79 ± 0.07	18.56 ± 0.07	2.08	3.74 ± 0.64	20.19 ± 0.28	8.73 ± 0.45	1.51
EA4	2.07 ± 0.07	19.22 ± 0.06	1.61	2.43 ± 0.24	19.61 ± 0.17	5.10 ± 0.25	1.56
EA5	1.62 ± 0.06	18.85 ± 0.07	1.49	2.39 ± 0.38	19.70 ± 0.31	6.40 ± 0.56	1.45

Table 2.5.　Bulge-disk decompositions

	Bulge		Disk			
ID	r_e (kpc)	μ_e	r_d (kpc)	μ_d	χ^2_ν	B/T
EA3	0.69 $\pm$ 0.03	17.02 $\pm$ 0.05	3.57 $\pm$ 0.22	19.30 $\pm$ 0.14	1.58	0.56
EA4	1.11 $\pm$ 0.05	18.11 $\pm$ 0.05	3.44 $\pm$ 0.16	19.50 $\pm$ 0.12	1.48	0.62
EA5	1.14 $\pm$ 0.03	18.23 $\pm$ 0.04	4.01 $\pm$ 0.45	21.00 $\pm$ 0.21	1.45	0.70

CHAPTER 3

THE DETAILED EVOLUTION OF E+A GALAXIES INTO EARLY TYPES

3.1   Introduction

If some galaxies evolve from star-forming, gas-rich, disk-dominated galaxies (late-types) into quiescent, gas-poor, spheroid-dominated galaxies (early-types), we should find objects caught in the midst of this transformation. The best candidates are the so-called "E+A", "K+A", or "post-starburst" galaxies (Dressler & Gunn, 1983; Couch & Sharples, 1987) due to their combination of late- and early-type characteristics, including both a significant young stellar population (age $\lesssim 1$ Gyr) and a lack of on-going star formation. These galaxies have been spectroscopically identified by their strong Balmer absorption lines and absence of emission lines (e.g., [O II] and Hα) in various environments and at all redshifts (Zabludoff et al., 1996; Poggianti et al., 1999; Goto et al., 2003; Blake et al., 2004; Tran et al., 2003, 2004).

While the cause of the abrupt end of their star formation is poorly understood, there is strong evidence that galaxy-galaxy tidal interactions or mergers trigger the starburst in many cases. First, most E+A galaxies reside in low-density environments, such as poor groups, that are similar to those of star-forming galaxies (Zabludoff et al., 1996; Quintero et al., 2004; Blake et al., 2004; Balogh et al., 2005; Goto, 2005; Hogg et al., 2006; Yan et al., 2008). Therefore, many E+As must arise from a process common in the field, such as galaxy-galaxy interactions, instead of a mechanism limited to denser, hotter environments, such as ram pressure stripping (Gunn & Gott, 1972) or strangulation (Balogh et al., 2000). Second, a significant fraction of E+As have tidal features (Zabludoff et al., 1996; Yang et al., 2004; Blake et al., 2004; Tran et al., 2003, 2004; Goto, 2005). Third, optical and *NIR*

colors show that the spectral signatures of E+As require enhanced recent star formation, rather than simply a truncation of star formation in a normal spiral galaxies (Balogh et al., 2005).

What will E+A galaxies become? In general, E+As are bulge-dominated, highly-concentrated (Quintero et al., 2004; Tran et al., 2004; Blake et al., 2004; Goto, 2005; Balogh et al., 2005), relatively gas-poor (Chang et al., 2001; Buyle et al., 2006), and kinematically hot systems (Norton et al., 2001). Therefore, in a statistical sense, E+As are likely to become E/S0 galaxies. However, due to a lack of spatial resolution in previous studies, we do not know whether the detailed properties of individual E+As, e.g., their bulge fractions, color gradients, internal kinematics, and newly formed stellar clusters, are consistent with their presumed evolution into early type galaxies. Using *HST/WFPC2*, Yang et al. (2004) showed that their morphological features are consistent with a transition from late to early types, but their sample contained only the five bluest E+As galaxies from the Las Campanas Redshift Survey (LCRS; Zabludoff et al. (1996)) and thus was not representative. As a result, we still do not know whether the entire population of E+As will evolve into E/S0s, whether there is a distinguishable subclass of E+As that evolves into E/S0s, or whether E+As evolve into typical E/S0s.

To answer these questions, we must understand how well E+As match the *full* range of E/S0 properties. Most fundamentally, are the global morphologies (e.g., bulge-to-total light ratios and concentration) of the whole LCRS E+A sample consistent with those of E/S0s? Second, E/S0s in the local universe become redder toward their center; these negative color gradients originate from metallicity gradients (Peletier et al., 1990). In contrast, E+As exhibit a wide range of color morphologies (Yang et al., 2004; Yamauchi et al., 2005). Can the color profiles of E+As evolve into those of the typical early types? Third, the number of

globular clusters per unit luminosity is higher in early types than in late types (Harris & van den Bergh, 1981). If E+As are in transition from late to early types, one should find new star clusters formed during the starburst. Are there such clusters, and, if so, do their colors and numbers coincide with the expected evolution of the globular cluster systems of present-day E/S0s? Fourth, early-type galaxies lie on the Fundamental Plane (FP), an empirical scaling relation between the effective radius, the central velocity dispersion, and the mean surface brightness, with remarkably small scatter (Djorgovski & Davis, 1987; Dressler, 1987). Will E+As lie on the same FP once they evolve?

To determine whether E+As evolve into objects that are indistinguishable from the bulk of E/S0s, we present *HST/ACS* observations of the 15 remaining E+A galaxies from the Zabludoff et al. (1996) sample. We combine these with the previous *HST/WFPC2* observations of five blue E+As (Yang et al., 2004) and of one serendipitously discovered E+A (Yang et al., 2006). The resulting high resolution imaging of the 21 confirmed E+A galaxies in the LCRS sample enables us to study the detailed color morphologies and the properties of the newly formed star cluster candidates at the sub-kpc scale. The detailed morphologies, color profiles, and cluster populations of many E+As are consistent with the galaxy-galaxy interaction scenario. We discuss how these features will evolve and then relate this evolution to the properties of E/S0s. Using existing kinematic data (Norton et al., 2001) and our *HST* photometry, we also address whether or not the various scaling relations of E+As are consistent with those of E/S0s.

This paper is organized as follows. We describe our E+A galaxy sample and the *HST/ACS* data reduction in §3.2. In §3.3, we examine the general morphology of E+As, including a discussion of tidal features (§3.3.1), surface brightness profiles (§3.3.2), structural parameters (§3.3.3), and concentration/asymmetry mea-

sures (§3.3.4). The color profiles, including a class of E+As with luminous blue cores (Yang et al., 2006), are presented in §3.4. We compare the scaling relations of E+As with those of E/S0s in §3.5. We present the properties of the newly-formed young star clusters in §3.6. We summarize in §3.7.

3.2 Observations and Data Reduction

3.2.1 LCRS E+A Sample

Our *HST* imaging sample consists of 21 nearby E+A galaxies spectroscopically identified from the 11,113 galaxy spectra of the Las Campanas Redshift Survey (LCRS; Shectman et al., 1996) with redshifts between 0.07 and 0.18 (Zabludoff et al., 1996). These E+As are required to have strong Balmer absorption features (average equivalent width $\langle H\beta\gamma\delta \rangle > 5.5$Å) and little if any [O II] emission (EW[O II] < 2.5 Å). Three-quarters of this sample are in the field, well outside rich cluster environments. The number of each E+A (e.g., EA01) is adopted from Zabludoff et al. (1996) and increases with increasing 4000 Å break (D_{4000}) strength. D_{4000} is related to the galaxy's color — bluer galaxies have smaller D_{4000}. For the remainder of this paper, we refer to each galaxy by its assigned number.

There have been two changes to the original sample since published. One of the original galaxies (EA20) was misclassified as an E+A due to noise in the region of the spectral line diagnostics (Norton et al., 2001). On the other hand, the morphologically disturbed companion galaxy of EA01 lies at the same redshift and also has an E+A spectrum (Yang et al., 2006). We include it in our sample and refer to it as EA01B, and to the original EA01 as EA01A. The EA01AB system is the first known binary E+A system and provides additional evidence that the E+A phase of galaxy evolution can be triggered by galaxy-galaxy interactions.

This LCRS sample is the most extensively studied E+A sample, with data

that includes measurements of internal kinematics (Norton et al., 2001), H I content (Chang et al., 2001; Buyle et al., 2006), radio-continuum emission (Chang et al., 2001; Miller & Owen, 2001), *NIR* fluxes and morphologies (Galaz, 2000), *HST* optical morphologies (Yang et al., 2004), and spectral diagnostics of nuclear activity (Yang et al., 2006). Table 3.1 summarizes the basic data and inferred properties from the various studies. Throughout this paper, we adopt $H_0 = 70 \text{ km s}^{-1} \text{ Mpc}^{-1}$, $\Omega_{\text{M}} = 0.3$, and $\Omega_{\Lambda} = 0.7$.

3.2.2 *HST ACS* Observations

By combining the observations of six E+As with *HST/WFPC2*, EA01AB through EA05 (Yang et al., 2004, 2006), with the new *ACS/WFC* imaging of the remaining 15 E+As, we now have data for the complete LCRS sample. The *ACS/WFC* imaging is in the F435W and F625W bands, which closely match the Johnson B and the SDSS r bands, respectively. We chose these filters to match the two *WFPC2* filters (F439W and F702W) used by Yang et al. (2004). Hereafter, we will refer to magnitudes in each of these filters as B_{435}, R_{625}, B_{439}, and R_{702}, respectively.

The F625W band images consist of three cosmic ray split exposures, one short (200s) and two long (350s) exposures, while the F435W band images consist of only two exposures. The exposure time for each split in F435W ranges from 500 to 550 sec depending on the galaxy's location on the sky. These uneven exposure times per pointing and the number of splits were adopted to obtain both B_{435} and R_{625} band exposures within an orbit, thereby maximizing the efficiency of our *HST* program by avoiding unnecessary readout overheads.

The images are bias-subtracted and flat-fielded with the standard *ACS* calibration pipeline. We determine the offsets and rotations between the exposures by cross-correlating the bright field stars and then "drizzle" the individual frames into the geometrically corrected output frame using the Pyraf/Multidrizzle pack-

age. We use an output pixel scale of $0.05''$per pixel and the square interpolation kernel for the drizzle.

We reject cosmic-rays using the standard Multidrizzle routine for the R_{625} band images, which have three exposures, and the LACOSMIC algorithms (van Dokkum, 2001) and Multidrizzle together for the B_{435} band images. Because there are only two images and each exposure is moderately deep, our B_{435} band images do have coincident cosmic ray hits in the exposures. To address this problem, we identify cosmic rays in the individual images using LACOSMIC, fix the flagged pixels by interpolating across neighboring pixels, and then apply the standard drizzle process. We apply LACOSMIC in a conservative way to retain real objects (e.g., star clusters) and visually check the rejected cosmic rays within a $20''$ radius from each E+A.

We use the Vega photometric system calibrated with the *ACS WFC* zero points, 25.779 (B_{435}) and 25.731 (R_{625}) from Sirianni et al. (2005), and correct for Galactic extinction using the reddening laws (Sirianni et al., 2005) $A_{F625W} = 2.633\,E(B-V)$ and $A_{F435W} = 4.103\,E(B-V)$ for an Sc type spectral energy distribution (SED). The color excess, $E(B-V)$, at each position is obtained from the Schlegel et al. (1998) maps. Because the LCRS sample is at high galactic latitude, the extinction correction is almost negligible for our sample. We do not include the errors from the extinction correction in our error budget.

3.2.3 Magnitude Transformation and K-correction

To compare our photometric measurements with our previous *WFPC2* imaging, and with the color gradients (Johnson B and Cousins R) and the Fundamental Plane data (Johnson B and Gunn r) of early type galaxies in the literature, we establish the magnitude transformation relation between the ground, *WFPC2,* and *ACS/WFC* photometric systems using synthetic photometry of K+A type tem-

plates as outlined by Sirianni et al. (2005). Because the spectra of post-starburst galaxies depend strongly on burst strength and time elapsed since the burst, we build a library of K+A type spectra using stellar population synthesis models (Bruzual & Charlot, 2003, BC03). The model stellar populations are composed of a young burst population (A–type) and an old underlying population (K–type). We assume that the old stellar population started forming 5 or 10 Gyr ago and has since experienced an exponentially declining star formation rate (τ = 2 Gyr). Superposed is a young stellar population with burst mass fraction, f_{burst}, which represents the fraction by mass of all stars formed in a brief, $\Delta t_{\mathrm{burst}}$ = 20–300 Myr, burst. We allow the burst mass fractions to range from 0.02 to 1.0. We also vary the metallicities of the old and young stellar populations between $Z = 0.004$ and $Z = 0.02$. The purpose of this analysis is *not* to reconstruct the star formation history (SFH) of our galaxies, but to generate a grid of SEDs that covers the wide range of observed spectral parameters and broad-band colors.

Using this grid of SEDs and the IRAF/Synphot routine, we measure the Johnson B, B_{435}, B_{439}, Cousins R, Gunn r, R_{702} and R_{625} magnitudes over time until 2 Gyr after the end of burst (well beyond when the galaxy would be classified as an E+A). We derive transformation equations by fitting to the data across the model grid using the following linear relations,

$$\mathrm{TCOL} = c_0 + c_1\,\mathrm{SCOL} + c_2\,\mathrm{SCOL}^2 \tag{3.1}$$

where TCOL and SCOL represent the target and source color (e.g., TCOL = B_{435} − R_{625} and SCOL = B_{439} − R_{702}). In Table 3.2, we list the conversion parameters for the WFPC2, ACS, Landolt (i.e., Johnson B + Cousins R) and Thuan-Gunn systems.

To compare the properties of E+As across a range of redshift ($z = 0 - 0.15$), one should apply *K*-corrections. In principle, the *K*-correction can be derived

from the known SED of the object for an arbitrary redshift and filter. If SEDs are not available, but there are enough measurements of the broadband magnitudes, one can reconstruct the galaxy SED and calculate the *K*-correction (e.g., Blanton et al., 2003). However, neither flux-calibrated spectra nor multiple broadband colors are available for our sample.

Therefore, we adopt an alternative approach using the synthetic photometry of the described model K+A SED library. The procedure is similar to what we use to derive the magnitude transformation equations. Using the grid of SEDs, we redshift the rest frame spectra to the appropriate E+A redshift, z, measure the observed B^z_{435} and R^z_{625} magnitudes, and calculate the differences from the corresponding rest frame magnitudes (i.e., *K*-corrections) as a function of $B^z_{435} - R^z_{625}$ color. For each E+A, we determine the *K*-correction at the measured ($B^z_{435} - R^z_{625}$) color and use the range of model values as an error estimate for the *K*-correction.

3.3 Morphology

3.3.1 Qualitative Description

We show images of the six *WFPC2* E+A galaxies in Figure 3.1. The leftmost panels are high contrast images in R and reveal low surface brightness features. The middle panels are the R band images (the B band images are far more shallow). Figure 3.2 shows the *ACS* data for the remaining 15 E+As. The leftmost panels are the same as Figure 3.1. The middle panels here are the two-color composite images from the B and R bands. We adopt a color scheme employing the arcsinh stretch from Lupton et al. (2004). We bound each image with 4 arcsec tickmarks and include a 4 kpc horizontal scalebar. The right panels of both figures are the R band residual images resulting from the subtraction of best-fit models (see §3.3.2).

High resolution *HST* images enable us to identify a wealth of small and large
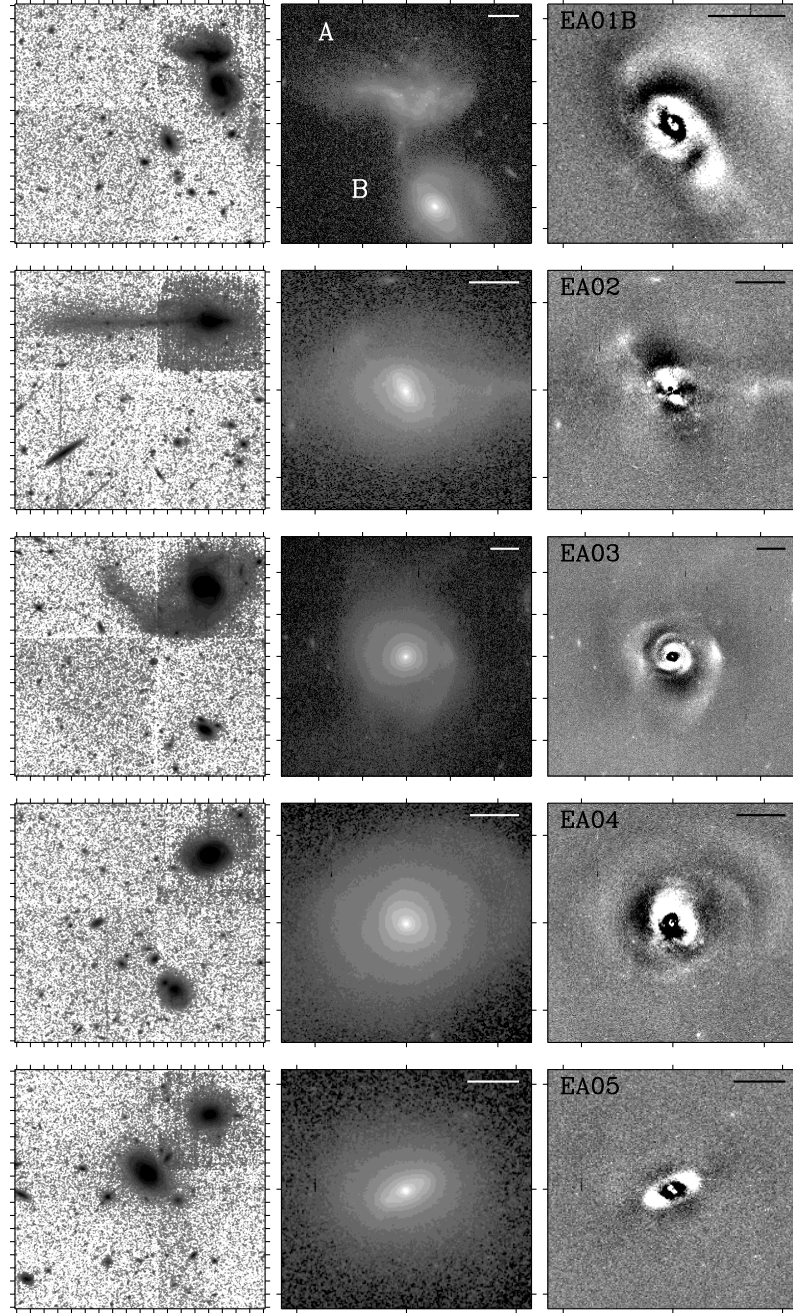
Figure 3.1 — (*Left*) High-contrast R band (R_{702}) images show the low surface brightness tidal features. (*Middle*) R band images for the *WFPC2* sample (EA01AB – EA05). (*Right*) Residual R band images subtracted from the smooth symmetric model components. We bound each image with 4 arcsec tickmarks and include a 4 kpc horizontal scalebar. Note the diverse morphologies of E+A galaxies: tidal and disturbed features, dusty galaxies, blue-cores, bars, and even compact star clusters. Because EA01A is too disturbed to be modeled by axisymmetric models, we restrict our analysis to EA01B and show the residual image only for EA01B in the top panel.
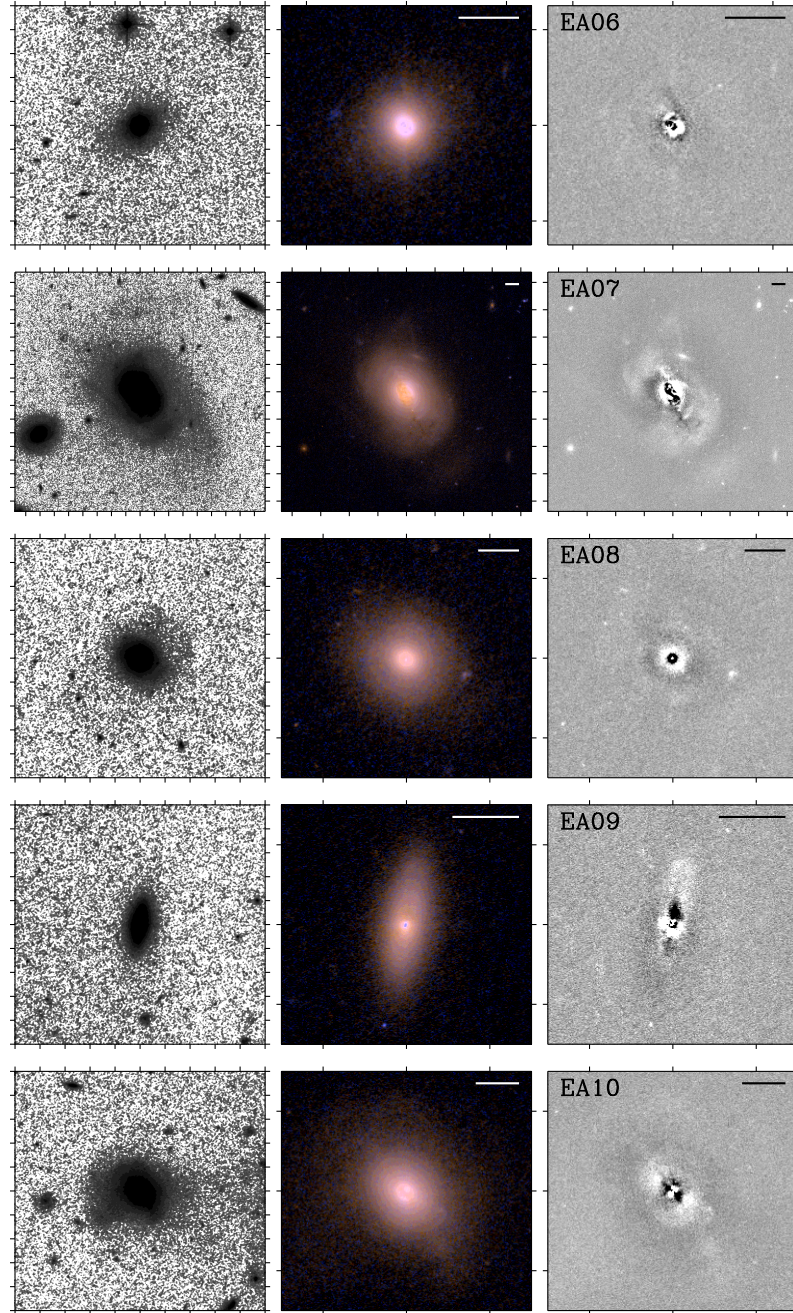
Figure 3.2 — (*Left*) Same as for Fig 3.1, except these are *ACS* images of EA06–20. (*Middle*) Two-color composite images from the B and R bands. (*Right*) Same as for Fig 3.1, except for the *ACS* images.
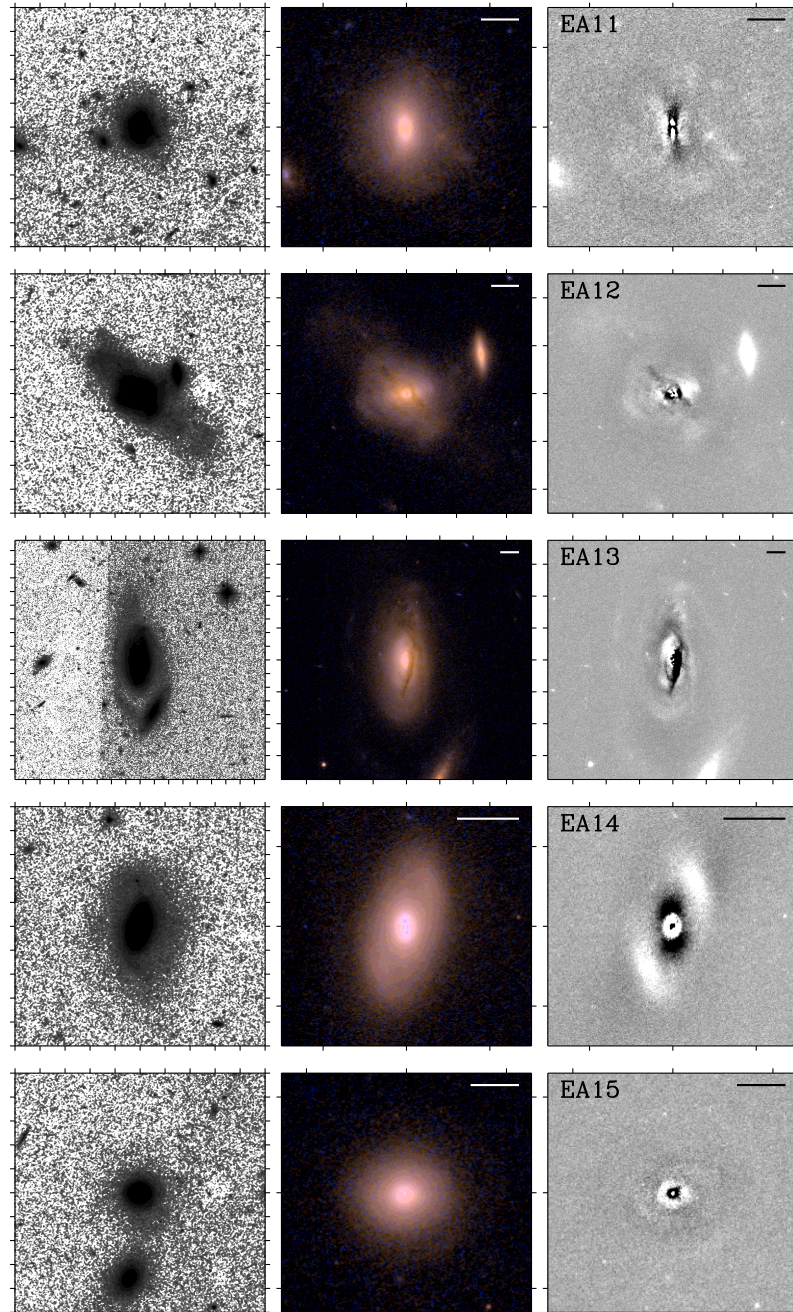
Figure 3.2 — Continued.
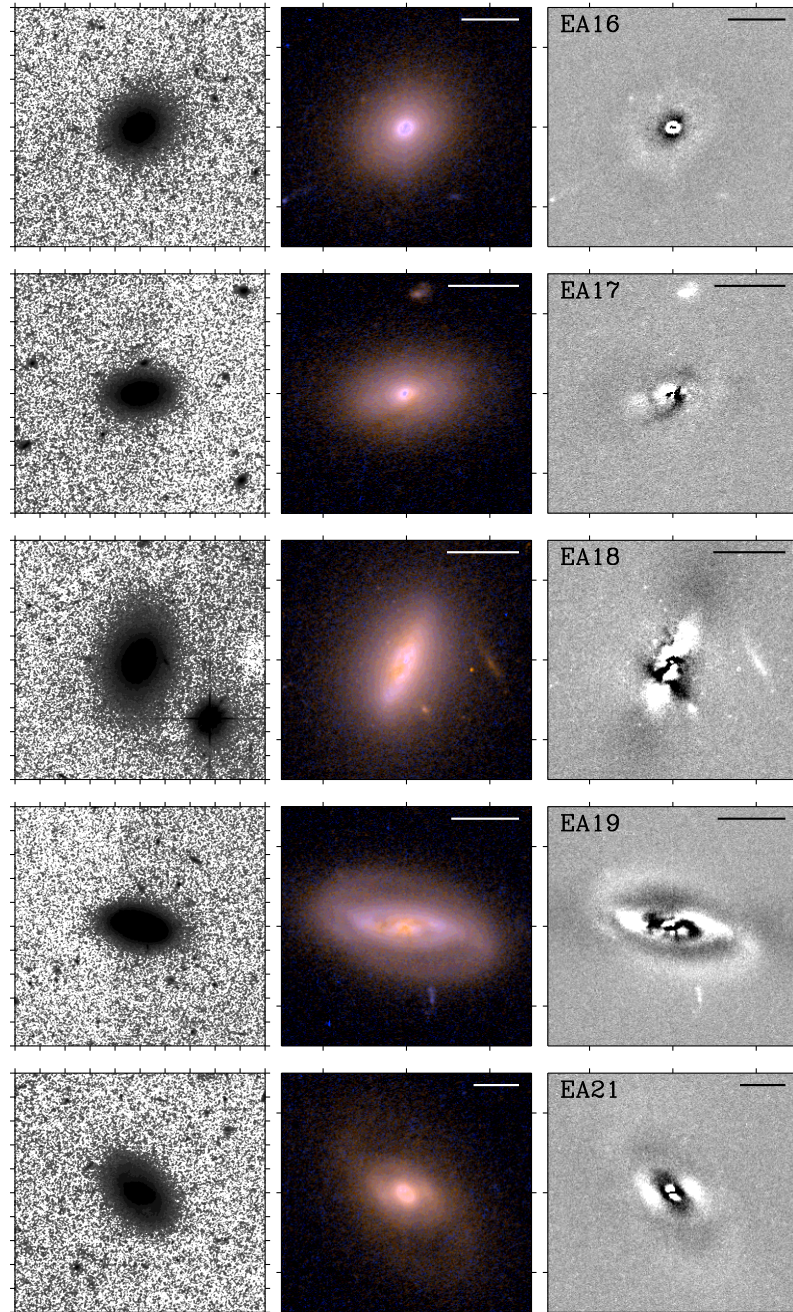
Figure 3.2 — Continued.

scale features. Readers are referred to Appendix A for detailed descriptions of the morphological features. Here we briefly describe our findings. First, the morphologies of E+As are extremely diverse, including train-wrecks, barred galaxies, blue-cores, and relaxed-looking disky galaxies. Given that our E+A sample was selected using uniform spectroscopic criteria, it is striking that the morphologies are so varied. Second, more than half (55%) of the E+As have tidal and/or disturbed features brighter than our detection limit ($\mu_R < 25.1 \pm 0.5$ mag arcsec^{-2}), supporting the picture that galaxy-galaxy interactions/mergers are responsible for E+A phase. Five E+As also have apparent companion galaxies within ~ 30 kpc that appear to be interacting with the E+A. Third, six E+As (30%) exhibit distinct compact blue cores with a characteristic size of $\sim 0.5''$. Fourth, seven E+As show dust features, such as lanes and filamentary structures, in the two-color composites or the residual images. Only three of those have color profiles that are seriously affected by these dust lanes (§3.4).

3.3.2 Surface Photometry and Model Fitting

To compare E+A morphologies with those of early- and late-type galaxies in a quantitative way, we fit models to the surface photometry. First, to obtain the surface brightness profiles (and the color profiles in §3.4), we extract the one-dimensional azimuthally-averaged light profiles of the galaxies using the IRAF/ELLIPSE task. Because a large fraction of E+As are disturbed and have asymmetric features, we allow the model to follow the light distribution as closely as possible. Thus, we allow the center, major axis position angle, and ellipticity of each ellipse to change freely, but we force ellipses to not overlap by fitting over a limited radial range along the major axis. The only difference from our analysis of the previous WFPC2 imaging is that we forego point-spread function deconvolution because the errors in the drizzled ACS images are correlated.
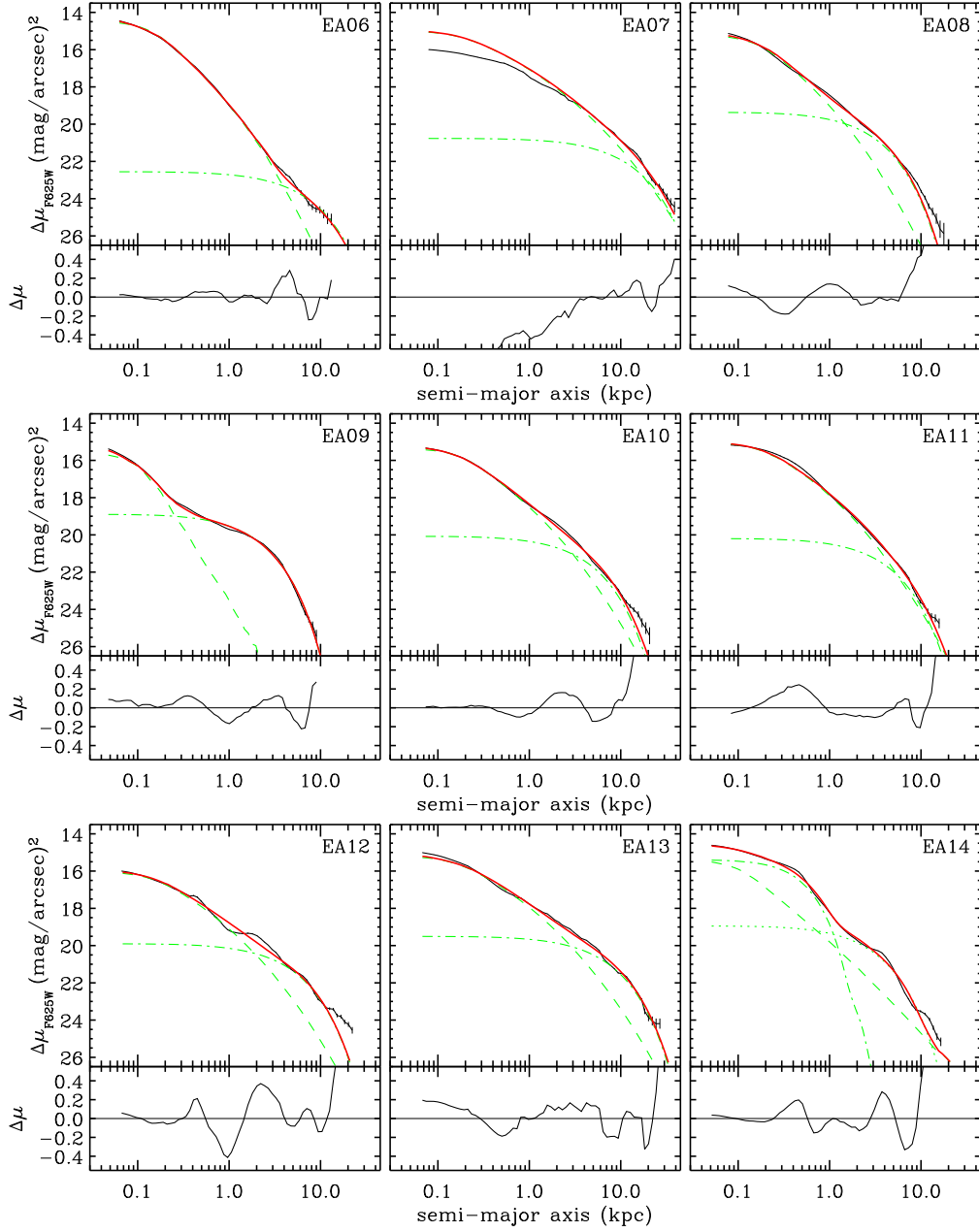
Figure 3.3 — E+A surface brightness profiles. The data are extracted using the ELLIPSE task (dark solid line) and the model profiles with GALFIT (gray solid line). The dashed and dot-dashed lines are the bulge and disk components from GALFIT, respectively. For the barred galaxies (EA14 and 21), we show the three components fits (Sérsic + Sérsic + disk; Appendix A). The differences between the data and the model are shown in the bottom panels. The large excess of light at large radii ($r \geqslant 10$kpc) in some E+As (EA08, 10, 11, 12, 18) is mainly due to low surface brightness tidal features.
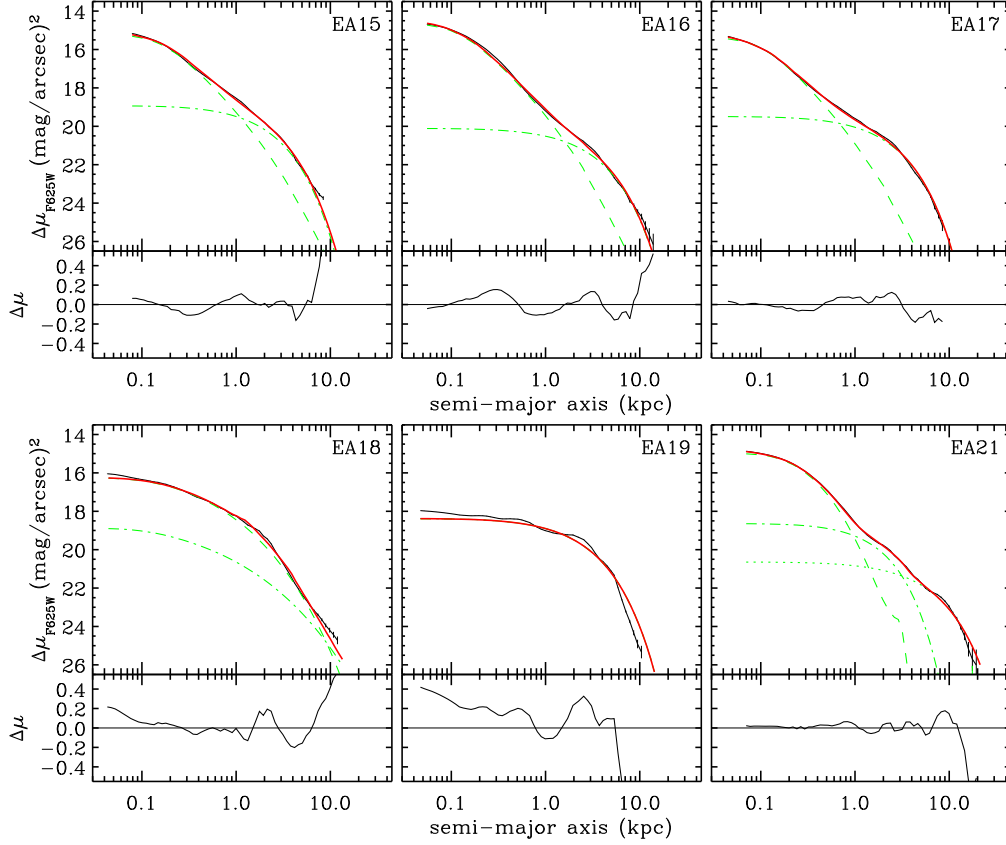
Figure 3.3 — Continued.

To obtain global photometric parameters, such as effective radius r_e, effective surface brightness μ_e, and Sérsic index n, we use the two-dimensional image fitting algorithm GALFIT (Peng et al., 2002). GALFIT assumes a two-dimensional model profile for the galaxy with the following free parameters: the (x, y) position of the center, M_{tot} (the total magnitude of the component), r_e (the effective radius), n (the Sérsic index), q (the axis ratio defined as b/a), the major axis position angle, and c (the diskiness/boxiness index, where $c > 0$ indicates boxy). This index c plays the same role as the $\cos 4\theta$ Fourier coefficient term used often in isophote analysis (Jedrzejewski, 1987). As GALFIT explores parameter space,

it convolves the model image with a point-spread function (PSF) and compares it to the data for each parameter set.

We use three types of model profiles with a pre-determined fixed sky background: 1) $r^{1/4}$-law bulge plus an exponential disk, 2) single de Vaucouleurs $r^{1/4}$-law profile, and 3) single Sérsic $r^{1/n}$-law profile. Therefore, for each galaxy, we have three sets of structural parameters, unless bulge/disk decomposition proves to be impossible (e.g., EA01A and 19). Bulge-disk decomposition (model 1) is useful for determining whether there is a disk and for measuring a bulge fraction (B/T). Model 2 is used mostly to compare the morphologies of E+As with those of normal ellipticals or S0 galaxies, and we use the derived parameters to place E+As on the Fundamental Plane (§3.5). Model 3 is flexible enough to distinguish early type galaxies ($n > 3$) from disk-dominated late type galaxies ($n \sim 1$). We determine the adopted sky value using median values from 40×40 pixel regions that appear free from tidal features or other large scale sources. The GALFIT input PSFs are evaluated using unsaturated stars in the ACS field with S/N higher than 100 as identified by the IRAF/DAOPHOT package. Because the number of available stars is often too small ($N < 5$) in each E+A field, we generate the time- and spatially-averaged PSFs using all of the stars ($N \sim 90$) in our *HST* observations. We fit the galaxy images with all three profiles and determine which profiles are the best fits based on the χ^2 values and visual inspection of the residual images.

We plot the light profiles derived from the ELLIPSE fit and the best fitting model profiles from GALFIT in Figure 3.3. As expected, the 1–D and 2–D fits do not always agree, especially when there are a significant changes in PA or ellipticity, but generally they are consistent to within ~0.2 mag. Because systematic errors, such as that introduced by the fixed sky value, dominate, we run GALFIT

with various plausible fitting input parameters and take the full range of fitting results as representative of the final errors. Therefore, the errors given in Table 3.4 and 3.5 are conservative estimates of the true uncertainties.

3.3.3   Light Profiles

3.3.3.1   Bulge-disk Decomposition

In Figure 3.4a, we show the distribution of the R band bulge fractions (B/T) of the 15 E+As for which the bulge-disk decomposition is reliable (red shaded histogram). The decompositions are not reliable in other cases, for example, in those galaxies (EA07, 18, 19) where a large portion of the bulge is masked by dust lanes and in strongly disturbed systems (EA01A, EA02, EA12) where the distinction between bulge and disk is meaningless. Except for two disky E+As (EA09 and EA17), most (13/15) of the remaining E+As have B/T's greater than the median for Sa's (0.45; Kent, 1985). The median B/T of E+As (0.59) is consistent with that of S0 galaxies (0.63; Kent, 1985). E+A galaxies are mostly bulge-dominated systems, confirming previous studies using bulge-disk decomposition (e.g., Yang et al., 2004; Blake et al., 2004; Balogh et al., 2005).

3.3.3.2   Sérsic Profile

The Sérsic index n is often used to quantify galaxy morphology (e.g., Blanton et al., 2003) because $r^{1/n}$ profiles are flexible enough to represent a wide range of profiles, from those of disk galaxies ($n = 1$) to those of spheroidals ($n = 4$). E+A galaxies in the SDSS have large Sérsic indices (median $n = 3$), and therefore their luminosity is centrally concentrated (Quintero et al., 2004). We fit single Sérsic profiles to all of our E+A galaxies, and present the results in Table 3.4. This model generally results in larger χ_ν^2 values than those obtained with bulge+disk decomposition, but both sets of models are statistically acceptable.

In Figure 3.4b, we plot the distribution of the Sérsic index n in the R band for 20 E+As, the entire sample except for EA01A, which is too disturbed to fit. Most E+As (17/20) have very high Sérsic index, $n \gtrsim 5$, even higher than the $n = 4$ de Vaucouleurs profile of normal ellipticals, indicating that the galaxy's luminosity is highly concentrated, presumably due to recent centralized star formation. The exceptions are the three dusty galaxies (EA07, EA18, EA19) with $n = 1 - 3$, where we hypothesize that the dust lanes partially mask the bulge component. High central concentrations do not necessarily mean that the galaxies are bulge-dominated systems. For example, two of our most disky systems, EA09 and EA17, with $B/T = 0.17$ and 0.35, respectively, have unusually high Sérsic indices ($n > 10$).

What causes the Sérsic index of E+As to be even larger than those of early-types (e.g., Kelson et al., 2000; Graham et al., 2001; Graham, 2002)? We consider three possibilities: 1) we are being misled by the comparison across different studies because the derived Sérsic indices are strongly dependent on the fitted radial range, the choice of fitting method (1D vs. 2D), and the depth of the images, 2) the index is dominated by the presence of an additional, highly concentrated, central source, and 3) misidentification of a disk or tidal feature as the shallow wing of the Sérsic profile is creating the apparently large central concentration. For the remainder of this discussion, we presume that the first possibility is not the origin of these results, although a more thorough cross-comparison among samples is warranted.

To test the degree to which the central regions of E+As affect the Sérsic fits, we mask the centers with a 3 pixel radius mask and repeat the fitting. In Figure 3.4c, we plot the Sérsic indices before and after masking. Most (65%) of the galaxies have a smaller n after masking, which suggests that a central concen-
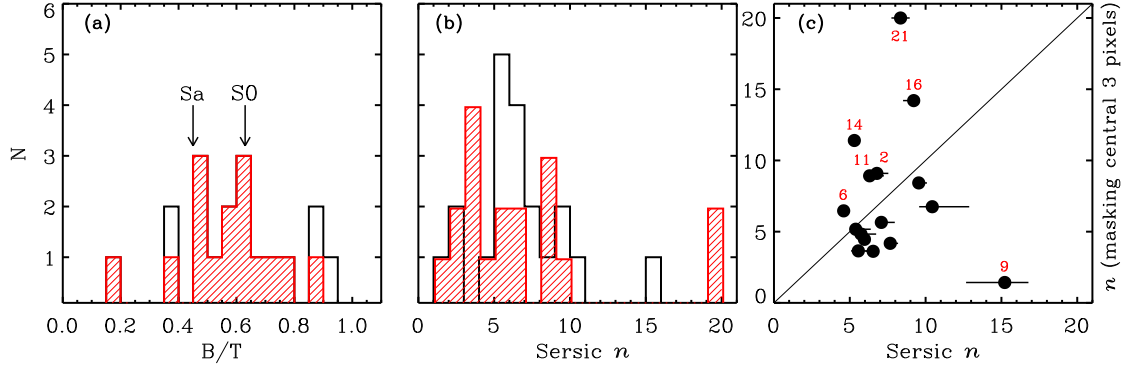
Figure 3.4 — (*a*) Distribution of R band bulge fractions (B/T) of 15 E+As where the bulge-disk decomposition is reliable (shaded histogram). Except for two disky E+As (EA09 and EA17), most E+As (13/15) have B/T's greater than the median for Sa galaxy bulges (0.45). The median B/T of E+As (0.59) is roughly consistent with that of S0 galaxies (0.63). (*b*) Distribution of Sérsic indices n in the R band for 20 E+As (except EA01A) using a single Sérsic fit (solid) and Sérsic + disk fit (shaded). Most E+As (17/20) have very high Sérsic index ($n \gtrsim 5$), even higher than the $n = 4$ of de Vaucouleurs profiles of normal ellipticals, indicating that the galaxy luminosity is highly concentrated. (*c*) Sérsic indices before and after masking the galaxy center. Most galaxies (65%) have a smaller n after masking, suggesting that the central pixels play a role in the large derived n values.

tration does play a role in causing the high n's. This conclusion is supported by positive central residuals in the model subtracted images (Fig. 3.1 and 3.2). EA09 is a special case because the bulge is so small that this masking leaves only the disk component. However, Sérsic indices in six E+As actually increase after the masking. The E+As with a larger resulting n after masking generally have ring-like substructures in the residual images and negative central residuals. We conclude that substructures near the center, e.g., bright nuclei, bars, and rings, play an important role in generating the highly concentrated light of most E+As.

The last of our three possibilities is that disk or tidal features are fitted as the shallow wings of the Sérsic profiles. To examine the Sérsic index of the bulge component alone, we fit a Sérsic+disk model. In Figure 3.4b, we show the resulting distribution of Sérsic indices for the bulge components (red shaded histogram) compared with the original, single-component values. The Sérsic index of the bulge itself is more consistent with that of normal bulges ($n \simeq 3 - 5$); however, some bulges still have large Sérsic indices ($n > 5$). We conclude that both the central substructures and disk-like features are responsible for the unusually high Sérsic indices in E+As. In any case, our E+As are more consistent with $n \sim 4$ than $n \sim 1$.

3.3.4   Concentration and Asymmetry, Residuals

So far, we have derived structural parameters by fitting smooth symmetric models to the images, even though asymmetric features are quite common in the residual images (Fig. 3.1 and 3.2). To quantify the asymmetric features and measure morphologies in a model-independent way, we calculate nonparametric measures of the galaxy morphologies: the concentration index C (Abraham et al., 1994) and the rotational asymmetry index A (Schade et al., 1995). In previous work (Yang et al., 2004), we used the azimuthal Fourier decomposition method (e.g., Rix & Zaritsky, 1995) to investigate asymmetric features of the disk-like components, such as the lopsideness in two face-on disky E+As (EA03 and EA04). We use CA indices in this paper, because a large comparison sample for the azimuthal Fourier decomposition is not available.

To determine the C and A indices (collectively referred to as CA), we follow the methodology described by Conselice et al. (2000) and Bershady et al. (2000). First, the Petrosian radius r_p is determined from the growth curve for circular apertures requiring that $\eta \equiv I(r_p)/\langle I(r_p)\rangle = 0.2$, where $I(r)$ is the surface bright-

ness at the radius r and $\langle I(r) \rangle$ is the mean surface brightness within r (Petrosian, 1976). We calculate the CA indices for image pixels within the "total" aperture defined to be twice the Petrosian radius. We measure the asymmetry index A by subtracting the galaxy image rotated by $180°$ from the original image and correcting for the contribution to the asymmetry arising from background noise:

$$A \equiv min\left(\frac{\sum |I_0 - I_{180}|}{\sum |I_0|}\right) - \frac{\sum |B_0 - B_{180}|}{\sum |I_0|}, \tag{3.2}$$

where I and B represent the image pixels within a circular aperture of radius $2r_p$ and the background region, respectively. We choose a rotational center that minimizes A by searching over sub-pixel grids with 0.1 pixel resolution. The concentration index C is defined by

$$C \equiv 5\log\left(\frac{r_{80}}{r_{20}}\right), \tag{3.3}$$

where r_{20} and r_{80} are the radii containing 20% and 80% of the total flux, respectively. Galaxies with a de Vaucouleurs profile ($n = 4$) or a pure exponential disk profile have $C = 4.50$ or 2.79, respectively.

In Figure 3.5, we show the CA classification diagram, which is frequently used for the morphological classification of high-z galaxies (e.g. Abraham et al., 1996), for our 21 E+As and for 113 local galaxies with various Hubble types drawn from the Frei et al. (1996) catalog. The CA indices of the Frei sample were measured in exactly the same way as those of the E+As. Although the CA diagram is not an ideal classification tool (e.g., see Conselice et al., 2000), it is quite useful in distinguishing early from late type galaxies. In Figure 3.5, intermediate spirals occupy a wide space in the CA plane, but early-types are segregated from late-types. The CA indices have low sensitivity to S/N and spatial resolution, within certain limits. For example, Lotz et al. (2004) show that CA indices can be robustly measured within $\Delta C \lesssim 0.1$ and $\Delta A \lesssim 0.05$ for images with an average $\langle S/N \rangle \gtrsim$

5 and a spatial resolution of ~ 500 pc per pixel or better (see also Conselice et al., 2000). Because our *HST* images satisfy these criteria ($\langle S/N \rangle \gtrsim 7$ within r_p and a spatial resolution $\lesssim 100$ pc per pixel), a direct comparison between the E+As at $z \sim 0.1$ with the local Frei sample is valid.

E+As populate a wide range in the CA plane, as already suggested by their morphological diversity. We overlay a dashed line providing a rough division of the CA plane into regions of early- and late-types. Most of the dusty E+As (EA07, 12, 13, 18, 19) and the train-wreck E+A (EA01A) lie below the dividing line and have large asymmetry and/or low concentration, presumably due to extinction. The remaining E+As are located above the line, but populate a unique part of the CA plane where there is both high concentration $C \gtrsim 4.3$ and moderately large asymmetry $A \gtrsim 0.04$. These E+As have concentration indices greater than or equal to those of early types ($\langle C \rangle = 4.4 \pm 0.3$), as expected from their B/T fractions and high Sérsic index n's, but they have a considerably larger A than ellipticals ($\langle A \rangle = 0.02 \pm 0.02$).

Where in radius does the largest contribution to the A parameter come from? Faint tidal features do not contribute significantly to A because 1) the total aperture size is not large enough to enclose features at such large radii and 2) the asymmetry is normalized using the total galaxy luminosity (eq. 3.2), so little weight is placed on low surface brightness tidal features. In the local galaxy sample, small scale features such as spiral arms and flocculence in the disk are the main contributors to A (Conselice et al., 2000). However, such features are not visible in the disks of our E+As (except for in EA03 and EA19), which are smooth (see also the *NIR* imaging from Balogh et al., 2005). Therefore, the large asymmetry of E+As is probably due to relic structures within a few effective radii arising from the starburst and/or recent galaxy-galaxy interaction. Yamauchi et al. (2005)
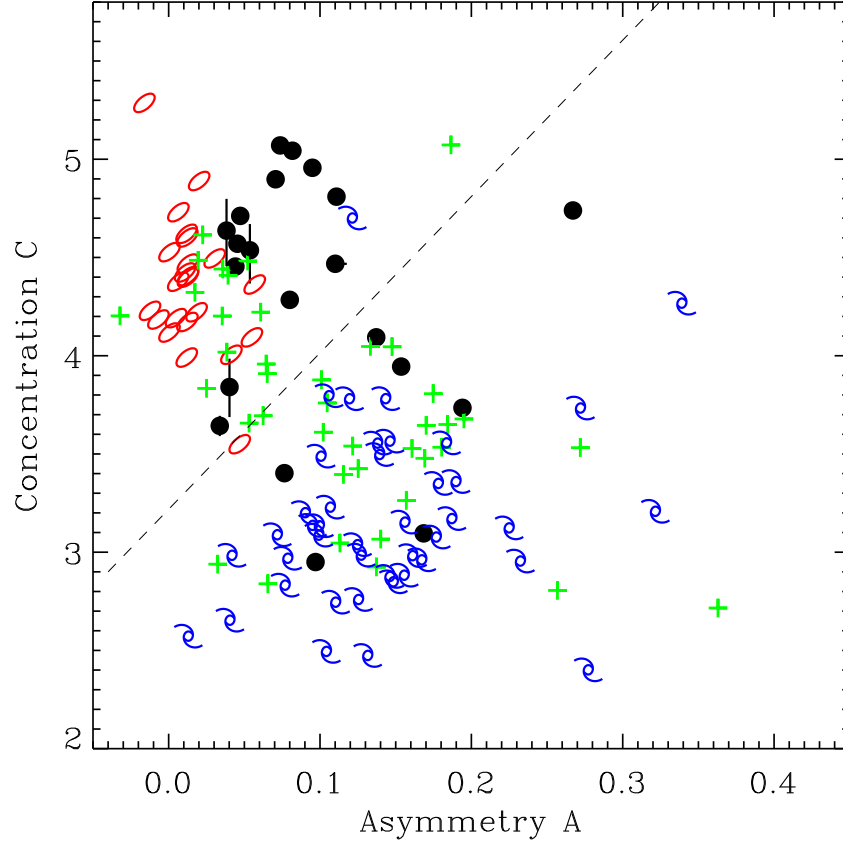
Figure 3.5 — CA classification diagram for our 21 E+As as well as 113 local galaxies with various Hubble types drawn from the Frei et al. (1996) catalog. The ellipses, crosses and spirals represent early-types ($T \leqslant 0$), intermediate spirals, and late-type spirals ($T \geqslant 5$), respectively. E+As are represented with filled circles. We overlay a dashed line providing a rough division of the $C - A$ plane into regions of early- and late-types. E+As populate the CA plane widely, as suggested by their morphological diversity. Two-thirds of E+As occupy a unique part of the plane: high concentration ($C \gtrsim 4.3$) and moderately large asymmetry ($A \gtrsim 0.04$). These E+As have concentrations consistent with those of early type galaxies ($\langle C \rangle = 4.4 \pm 0.3$) or even higher, as expected from their B/T fractions and high Sérsic indices n. However, they have considerably larger asymmetry than ellipticals ($\langle A \rangle = 0.02 \pm 0.02$) due to disturbances in their centers, presumably arising from the starburst and/or recent galaxy-galaxy interaction.

reached a similar conclusion from their analysis of 22 SDSS E+As.

To further investigate the nature of the asymmetry, we compare the asymmetry profiles, i.e., the asymmetry index interior to radius r, $A(< r)$, of E+As and late-type spirals ($T \geqslant 5$). Except for three E+A galaxies (EA01B, 03, 11), E+As have decreasing or flat $A(r)$ profiles. Conversely, the late-type galaxies tend to have increasing asymmetry profiles, because spiral arms and flocculence in the disk are increasingly included as the aperture increases. We conclude that the asymmetry in E+As originates mostly in the central parts (within a few r_e), presumably due to unrelaxed structures or residual dust from the starburst and/or recent merger. These E+As would be classified as "normal" elliptical galaxies or early-type spirals if they were observed at high redshift, unless the disturbances in their innermost regions (within a few kpc) or the low surface brightness features with $\mu \simeq 24 - 25$ could be clearly identified. In Table 3.3, we list the aperture sizes (r_p), CA indices, and relevant aperture magnitudes.

3.4   Color Profiles

The radial color profile of a galaxy depends on its dust content and the spatial distributions, ages, and metallicities of its stellar populations, which in turn depend on the evolutionary history of the galaxy. For example, if galaxy-galaxy interactions are responsible for an E+A's recent starburst, the young stellar population is expected to be centrally concentrated (e.g., Mihos & Hernquist, 1994; Bekki et al., 2005) and to produce a positive color gradient, i.e., a redder color with increasing radius. On the other hand, if the E+A arises from a truncation of continuous star formation, due to a mechanism such as ram pressure stripping in the cluster environment, then it may have a uniform color profile (see the extensive discussions in Caldwell et al., 1999; Rose et al., 2001).

Current observational evidence supports the model of centralized star formation in E+A galaxies. Using long slit spectroscopy, Norton et al. (2001) find that young stars are more centrally concentrated than older ones in our E+As. Even for E+As in clusters, Bartholomew et al. (2001) show that on average they become slightly bluer toward the center than normal early-type galaxies. Recently, Yamauchi et al. (2005) found that a substantial fraction of SDSS E+As have such a positive color gradient. However, these studies are somewhat limited due to the galaxies' small angular extent and/or the effects of ground-based seeing. In this section, we present high resolution internal color distributions of our E+As and show that indeed a significant fraction have positive color gradients and sometimes distinct blue cores. Then, we investigate whether the color profiles of E+As can evolve into those of early-type galaxies.

3.4.1 Positive Color Gradients in E+A Galaxies

We show the $(B_{435}-R_{625})$ radial color profiles of 20 E+As in Figure 3.6, excluding EA01A because it is so irregular. To enable direct comparison between the profiles, the $(B_{439}-R_{702})$ colors were transformed into $(B_{435}-R_{625})$, and all colors were K-corrected with respect to $z = 0.1$ to minimize the K-correction uncertainties. We refer to these colors as $(B - R)^{0.1}$. Note that we do not apply different K-corrections along the color gradients because these corrections are small (typically 0.02 mag) compared to the overall K-correction values. We measure the radial color profiles using the surface brightness profiles obtained with the ELLIPSE task. Before fitting ellipses to the isophotes, we correct for the different point spread functions in the B and R bands by convolving the sharper R band images to match the B band images. The smoothing kernel is determined using unsaturated stars in both images. We extract surface brightness profiles in the R band as described in §3.3.3, and then extract the B band profiles using the same
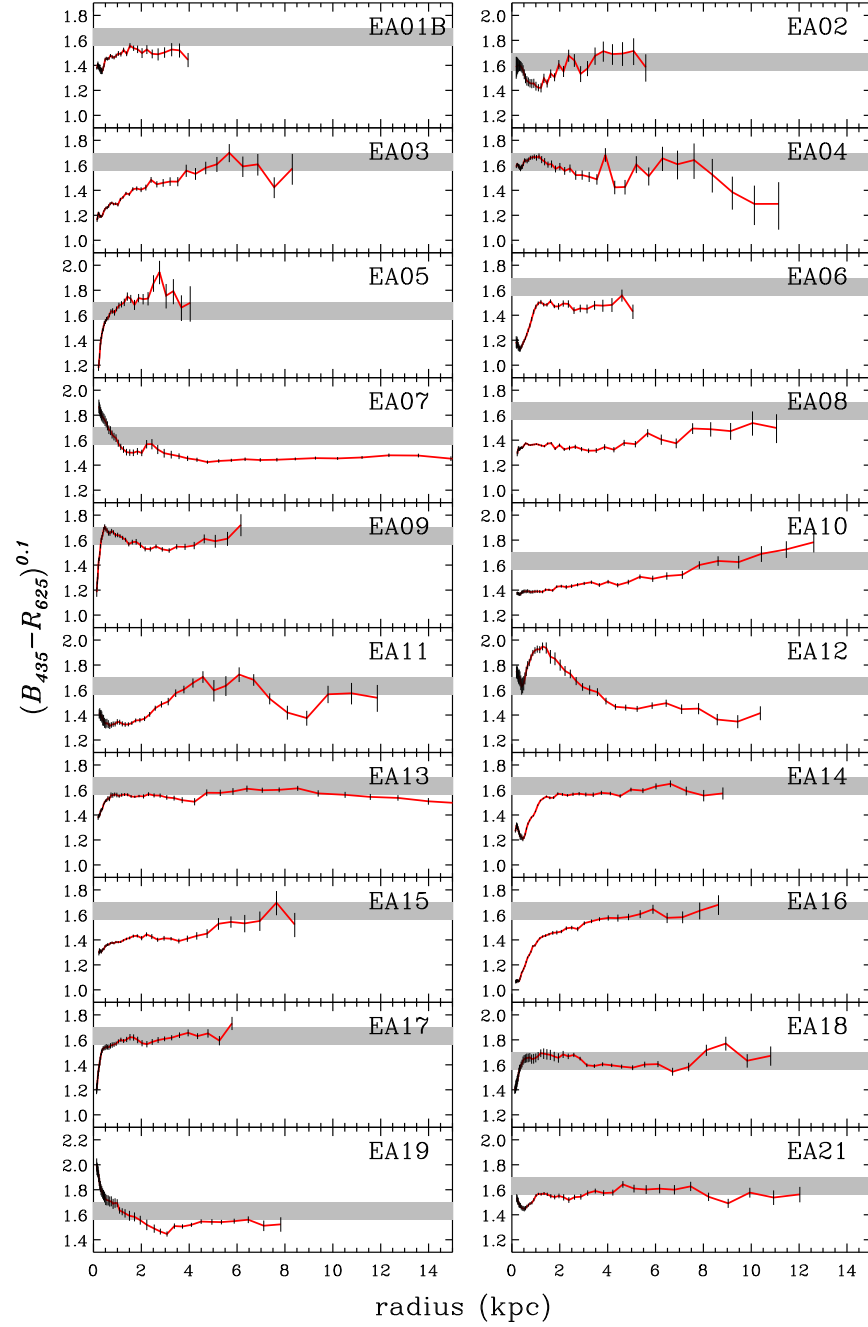
Figure 3.6 — Redshifted radial $(B_{435}-R_{625})^{0.1}$ color profiles of the 20 E+As. All the colors are *K*-corrected to $z = 0.1$. The color profiles are as diverse as the morphologies of E+As, ranging from negative color gradients (EA02, 04, 07, 12, 19) to positive color gradients including compact blue cores (EA05, 06, 09, 14, 16, 17). The large fraction (70%) of positive color gradients suggests that many E+As had a central burst of star formation and therefore that the E+A phase is triggered by galaxy interactions/mergers that funnel gas toward the center of the remnant. The shaded region indicates the $(B_{435}-R_{625})^{0.1}$ colors of a 5–10 Gyr old SSP with metallicity $Z = 0.004$ ($1/5Z_{\odot}$). The color of an SSP with solar metallicity is redder and varies from 1.86 to 2.04 between 5 and 10 Gyr. Recent star formation is not limited to the central region, as evidenced by the fact that the color is bluer than the shaded region at most radii.
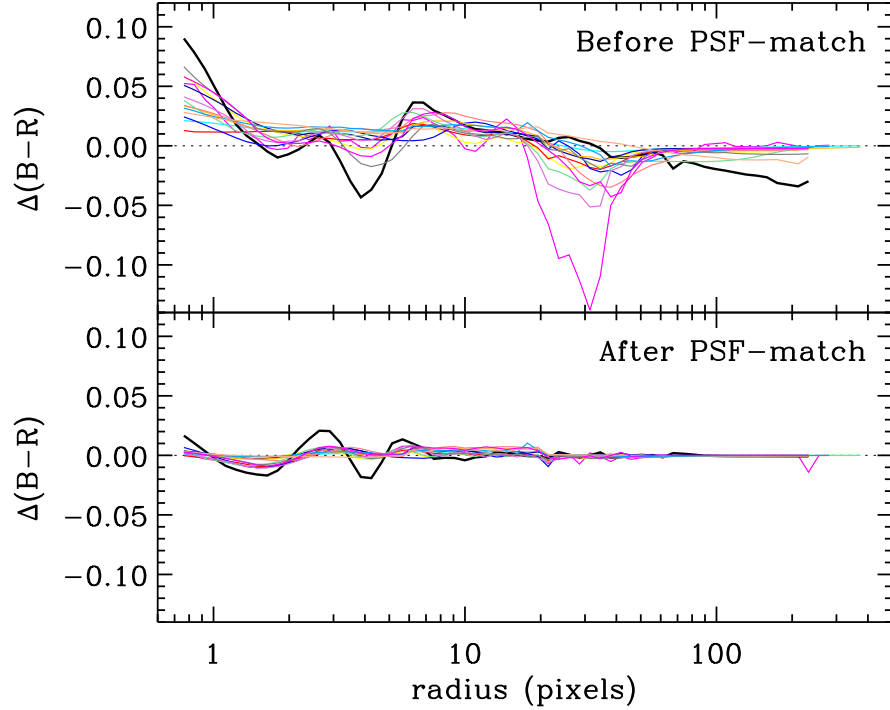
Figure 3.7 — Effect of the PSF correction. (*Top*) Measured color profiles for model galaxies with a uniform color distribution, i.e., a zero color gradient, without convolving the PSF-matching kernels with the R band images. The non-zero color gradients arising due to differences in the PSF function are clear over the entire range of radii depending on the model galaxy. (*Bottom*) Color profiles extracted after the PSF-matching. The measured color profiles deviate from the flat profiles by no more than ~ 0.02 magnitudes. Our color gradient measurement is valid even in the innermost region.

isophotes as in the R band analysis.

Note that this PSF-matching is critical in order to investigate the innermost color profiles of E+A galaxies and to identify color structures such as blue cores that can be as small as a kpc (see also Menanteau et al. (2004) for a comprehensive treatment of PSF issues). Figure 3.7 shows the effect of this PSF correction. Assuming an intrinsically uniform color distribution, i.e., a zero color gradient, we

generate model B and R images with the best fitting GALFIT models for our 20 E+As, and then convolve these with the appropriate B and R PSF's to generate the "observed" B and R images. In the upper panel, we plot the observed color profiles when we do not match PSFs. We plot the measured color profiles after PSF-matching in the lower panel. The improvement is obvious and the measured color profiles deviate from the intrinsic flat profile by no more than ~ 0.02 magnitudes. The extracted profiles tend to be biased toward redder cores, but the effect is negligible.

We find that all E+As have globally blue colors, except within dusty regions, and so conclude that recent star formation extends across the face of these galaxies (consistent with the results of Franx, 1993; Caldwell et al., 1996; Norton et al., 2001). In Figure 3.6, we overlay the model $(B - R)^{0.1}$ colors of 5 to 10 Gyr-old simple stellar populations which are consistent with those of early type galaxies for comparison.

While E+As are relatively blue overall, their internal color variations are surprisingly diverse, as suggested by their morphological diversity (see Table 3.6). Twelve E+As (57%) have positive color gradients, i.e., they become redder with increasing radius, while five E+As (20%; EA02, 04, 07, 12, 19) have negative color gradients. The remaining five E+As have relatively flat color profiles or a mixture of positive and negative color gradients. Half of the E+As with positive gradients exhibit blue cores, which we discuss below. This diversity echoes the variation in Hδ absorption line strength profiles observed in cluster E+As (Pracy et al., 2005). We list the overall color morphologies of E+A galaxies in Table 3.6 within broad categories: positive (including blue core), negative, or flat color gradient.

Among the E+As with negative color gradients, three (EA07, 12, 19) show clear dust signatures, such as dust lanes and irregular filamentary structures in

the two-color composite images. The clear detection of dust features in the *ACS* sample is mainly due to the excellent B band sensitivity, and so we cannot exclude the possibility that similar dust exists in the *WFPC2* sample galaxies with negative color gradients (EA02 and 04). Therefore, although there are other possible explanations, including a truncated IMF during the starburst (see Bekki et al. (2005)), we speculate that the red cores in these galaxies arise from increasing dust extinction toward the center.

To quantify the color gradients, $\Delta(B-R)/\Delta\log r$, we perform linear least-square fits to the radial color profiles. Because of the highly variable color profiles and compact blue cores in some E+As, a single color gradient is obviously not the best representation. Therefore, we measure the color gradients with two piecewise linear fits, allowing the break radius R_{break} between the inner and outer slope to change freely. Our only constraint is $R_{\mathrm{break}} \gtrsim 0.3$ kpc (~ 4 pixels) to prevent measuring break radii that might be seriously affected by the PSF. In Table 3.6, we list the color gradients and break radii from the piecewise linear fits, as well as the color gradient derived from the single line fit. The color gradients are measured in $(B_{435}-R_{625})$ at $z = 0.1$ to minimize the systematic errors that may arise from the *K*-corrections and color transformations. For EA01-05, the WFPC2 sample, we measure the color gradient in $(B_{439}-R_{702})$ at $z = 0.1$ and convert it to $(B_{435}-R_{625})$ at $z = 0.1$ using the relation $\Delta(B_{435}-R_{625}) \simeq c_1\, \Delta(B_{439}-R_{702})$ in Table 3.2. We find that the broken linear fits significantly improve the fits (χ^2s) in all but three E+As (EA01B, 03, 15).

The distribution of color gradients is shown in Figure 3.8, where the solid and hatched histograms indicate the color gradients for single and double line fits, respectively. The range of color gradients for early-type galaxies (E and S0s from Franx et al., 1989; Peletier et al., 1990) is shown for comparison (dashed curve).

The majority of E+As ($\sim 70\%$) have a positive color gradient that deviates from the slightly negative profile typical of early-type galaxies. We conclude that the young stellar populations are more concentrated than the underlying old populations. This conclusion is independent of whether the single or double line fits are used and is qualitatively consistent with that of Yamauchi et al. (2005).

3.4.2 Blue Cores

The most interesting morphological feature in certain E+As is the compact, almost stellar-like, blue core that is distinct from the other parts of the galaxy. We define blue core galaxies as those that have a color variation, $\delta(B-R)$, within the inner 2 kpc region that is greater than 0.3 magnitudes. This definition is comparable to the original criteria adopted by Menanteau et al. (2001), $\delta(V-I)_{\mathrm{obs}} \gtrsim 0.2$, for morphologically selected early-type galaxies. Six E+As (EA05, 06, 09, 14, 16, 17) satisfy our definition and have characteristic core sizes of $R_{\mathrm{break}} = 0.4 - 1.4$ kpc. Within these break radii, the color gradients of blue core galaxies are very steep, $\Delta(B-R)/\Delta \log r > 0.6$. The slopes become relatively flat at radii larger than the break radii. Note that we classified EA01B as one of the blue core galaxies based on its *WFPC2* $(B-R)$ colors in previous work (Yang et al., 2006); however, EA01B is not counted as a blue core galaxy in this paper because its color profile does not have a break radius.

Though the origin of blue cores is not fully understood, they are common in early-type galaxies at higher redshifts ($z \gtrsim 0.5$), when field spheroids are presumably still assembling. For example, 30% of the morphologically-selected elliptical galaxies in the Hubble Deep Field North have color inhomogeneities, mostly due to blue cores (Menanteau et al., 2001). Treu et al. (2005) find that $\sim 8\%$ (14/165) of early-type spheroidals in the Great Observatories Origins Deep Survey North (GOODS-N) have blue cores. Lee et al. (2006) also find "blue clumps" in al-
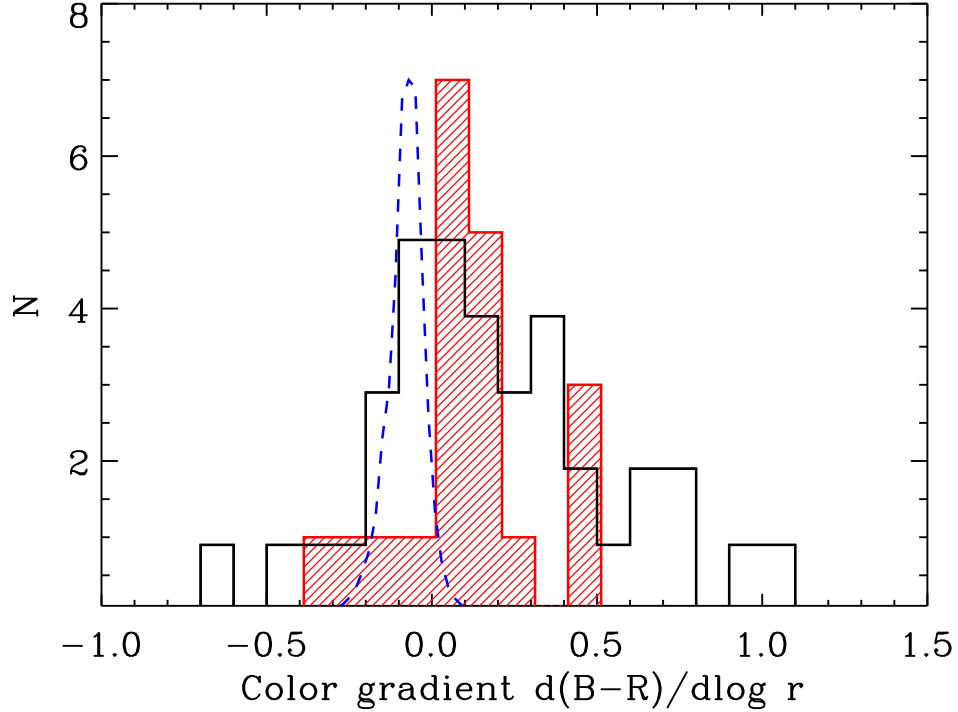
Figure 3.8 — Distribution of the E+A color gradients $\Delta(B - R)/\Delta \log r$. The solid and shaded histograms represent the gradients measured from the two-line fits and single line fits, respectively. Most E+A galaxies have positive color gradients, i.e., the color becomes redder as the radius increases. Note that there are some very steep [$\Delta(B - R)/\Delta \log r > 0.6$] color gradients due to the blue cores. The dashed curve represents the distribution of the color gradients of local E/S0s (Wise & Silva, 1996) with arbitrary normalization. E/S0s have a narrow range of color gradients [$\Delta(B - R)/\Delta \log r = -0.09 \pm 0.06$]. These color gradients are interpreted as being the result of metallicity gradients.

most half of the early-type galaxies with blue colors in the GOODS North and South fields. The blue-core E+As in our sample have relaxed morphologies and bulge fractions of $0.2 - 0.6$. Given that the CA classification scheme identifies these galaxies as early type galaxies, the blue-core E+As would be classified as

early-types if they were observed at high redshift. Therefore, these blue core
E+A galaxies might be the local analog of the blue core spheroids often found at
high redshift. The importance of blue core E+As for better understanding galaxy-
galaxy mergers and the origin of the black hole mass-bulge velocity dispersion
relation for galaxies ($M_{\bullet} - \sigma_B$; Ferrarese & Merritt, 2000; Gebhardt et al., 2000) is
described by Yang et al. (2006).

3.4.3   Evolution of Color Gradient

It is now well established that E/S0s in the local Universe have negative color
gradients [$\Delta(B - R)/\Delta\log r = -0.09 \pm 0.06$ mag dex^{-1} in Fig. 3.8], which origi-
nate from their metallicity gradients; their stellar populations become more metal
rich and redder toward the center (e.g., Tamura et al., 2000). If E+As evolve into
E/S0s, how can their diverse color morphologies converge into such a narrow
range of color gradients within a few Gyr? In particular, is it possible that the
observed positive color gradients invert into the negative color gradients typical
of early-types?

For those E+As whose negative color gradients arise from dust, it is difficult to
determine the underlying color gradients without incorporating radiative trans-
fer calculations (Wise & Silva, 1996). Nor do we know how the dust content will
evolve. However, were the dust in these E+As to disperse somehow, the negative
color gradients [$\Delta(B - R)/\Delta\log r \lesssim -0.3$] would flatten and be more consistent
with those of E/S0s.

For those E+As with positive color gradients — which are most of the sam-
ple — the centralized starburst will naturally lead to metallicity and color gra-
dients if the young stellar populations are more metal rich than the underlying
old populations. Although violent mixing during the merger could dilute any
previously established metallicity gradients, numerical simulations suggest that
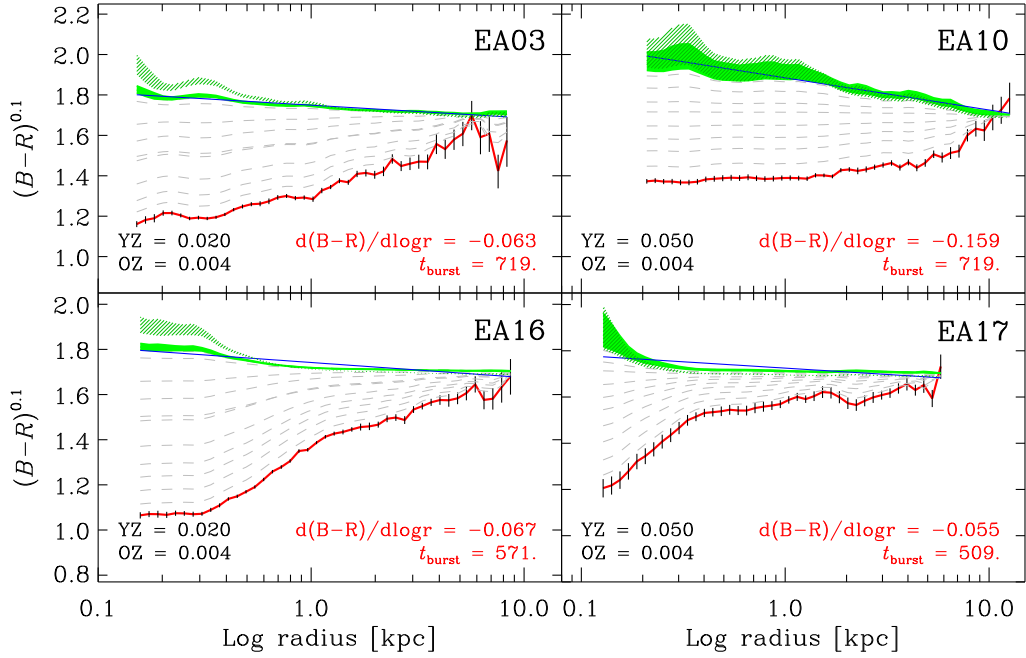
Figure 3.9 — Examples of color gradient evolution for two E+As with positive gradients (EA3 and 10) and for two blue-core E+As (EA16 and 17). The solid and dashed lines represent the current color profiles and the subsequent evolution, respectively. The ranges of color profiles after 5 and 10 Gyr are represented with solid and hatched regions, respectively. We adopt $Z_{\mathrm{young}} = 0.02$ for EA03 and EA16 (*left*), and $Z_{\mathrm{young}} = 0.05$ for EA10 and EA17 (*right*). The chosen burst ages (t_{burst}) can produce the whole range of colors in each galaxy. The positive color gradients in E+As can be inverted within ~ 5 Gyr, evolving into a range $[-0.05 < \Delta(B-R)/\Delta \log r < -0.16]$ consistent with that observed for E/S0s.

metallicity gradients might be regenerated by centralized star formation (Mihos & Hernquist, 1994; Kobayashi, 2004).

To investigate the evolution of the color gradients of E+As quantitatively, we take the current color gradients and evolve the stellar populations using simple assumptions. We assume that the current color gradients are due solely to burst-

strength gradients and that the young populations are coeval, i.e., that the last starburst was instantaneous. We adopt a uniform metallicity ($Z_{\mathrm{old}} = 0.004$) for the old population, and consider $Z_{\mathrm{young}} = 0.02$ and 0.05 for the young population. Then, for each galaxy, we choose a single post-burst age (the time since the starburst ended) that produces the whole range of colors observed in that galaxy, and derive the burst strength profile that reproduces the color profile. As older post-burst ages are selected, the burst strength gradient increases for a given color, and therefore larger metallicity gradients are introduced. We evolve these stellar populations passively for 5 and 10 Gyr ignoring further dynamical evolution, and measure the resulting color gradients.

In Figure 3.9, we show the color gradient evolution for two E+As with positive gradients (EA03 and 10) and for two with blue-cores (EA16 and 17). The solid and the dashed lines represent the current color profiles and their subsequent evolution, respectively. Taking into account measurement errors, we show the range of color profiles after 5 and 10 Gyr with the solid and hatched regions, respectively. We adopt $Z_{\mathrm{young}} = 0.02$ for EA03 and EA16 (left panels), and $Z_{\mathrm{young}} = 0.05$ for EA10 and EA17 (right panels).

In these examples, the positive color gradients can invert within ~ 5 Gyr and evolve to a color gradient range $[-0.05 < \Delta(B - R)/\Delta\log r < -0.16]$ consistent with that of E/S0s. Larger metallicity differences between the old and young stellar populations and older post-burst ages will result in steeper metallicity and color profiles after 5–10 Gyr. While it is hard to predict the true color gradient evolution of the E+As without exact knowledge of the post-burst ages and metallicities, our calculation shows that the current color profiles, most likely arising from a centralized starburst during a galaxy-galaxy tidal interaction or merger, can evolve into those of early-type galaxies.

3.5 E/S0 Scaling Relationships and E+As

In previous sections, we have shown that some aspects of E+A morphology (B/T, concentration C, Sérsic index n) are consistent with those of current early-type galaxies. We have also presented models or arguments in which other aspects now inconsistent with current early-type properties (blue cores, tidal features, and positive color gradients) could, via evolution, become consistent with the properties of current early-type galaxies. To further investigate whether E+A galaxies truly evolve into present-day early-types after a few Gyr, when the discrepant morphological features might disappear, we test whether E+As will eventually lie on the various scaling relationships of early-type galaxies. For example, Tacconi et al. (2002) and Rothberg & Joseph (2006) show that late-stage ultra-luminous infrared galaxy (ULIRG) mergers and optically selected merger remnants (other possible progenitors of present-day E/S0s) are located very close to or on the *K*-band Fundamental Plane (FP) of early type galaxies. We start with the simplest forms of the scaling relations, i.e., the Faber-Jackson relation (FJR; Faber & Jackson, 1976) and the Kormendy relation (KR; Kormendy, 1977).

3.5.1 Faber-Jackson and Kormendy Relations

In Figure 3.10, we show the Faber-Jackson relation ($L - \sigma^4$) and the Kormendy relation ($r_e - \langle \mu_e \rangle$) of E/S0s in comparison to those of E+As. We draw the E/S0 comparison sample from Jørgensen et al. (1996), because their photometric bands (Gunn r and B band) closely match our *HST WFPC2* and *WFC* filters. For the E+As, we adopt the velocity dispersions of the old components (σ_{old}) from Norton et al. (2001). To disentangle the kinematics of the young and old stellar populations, Norton et al. (2001) simultaneously fit the velocity profile and the relative contributions of different stellar components using longslit (1.5″× 6.6″aperture)

spectra. For three E+As (EA06, EA17, and EA18), we have only upper limits on σ_{old}, because a large fraction of the light is contributed by a young A-type population (f_A in N01) and thus the velocity dispersion of the old K-type population is not measured reliably. Although we include these galaxies in Figures 3.10 and 3.12, we exclude them from the following analysis. For the structural parameters, we adopt r_e, $\langle \mu_e \rangle$ and the total magnitude M_{tot} from our de Vaucouleurs fit (Figure 3.11). While a single de Vaucouleurs profile is not an ideal fit/model for complex morphologies (e.g., EA02) and/or for disky systems (EA09 and EA17), we justify the choice of r_e from the $r^{1/4}$ fits as a simple measurement of the half light radius of the galaxy. Indeed, we find that the luminosity within r_e given by the $r^{1/4}$ GALFIT fit agrees with a circular aperture measurement of the half light radius to within 10–20%.

We reproduce Norton et al. (2001)'s result that there is a strong correlation between E+A magnitude and velocity dispersion, and find that it is roughly parallel to the E/S0 Faber-Jackson relation with some offset (left panels in Figure 3.10). This relation implies that E+A galaxies already harbor dynamically relaxed old populations and that they are pressure-supported systems. While Norton et al. (2001) had to perform several steps to transform the LCRS Gunn/Kron-Cousins magnitude into Gunn r magnitude to compare the properties of E+As with those of E/S0s, we determine more directly the relative offsets between the E+As and E/S0s with our *HST* photometry. We measure the offset by fitting the $L \propto \sigma^4$ (i.e., $M_{\mathrm{tot}} \propto 10 \log \sigma$) relation to the E+As and the J96 sample.

On average, E+A galaxies are 1.31 (± 0.73) and 1.64 (± 0.71) mag brighter than the E/S0s in the Gunn r and B bands, respectively. This offset in Gunn r is almost twice as large (~ 0.6 mag) as that derived by Norton et al. (2001). This difference arises not only because we use improved photometry and magnitude transfor-
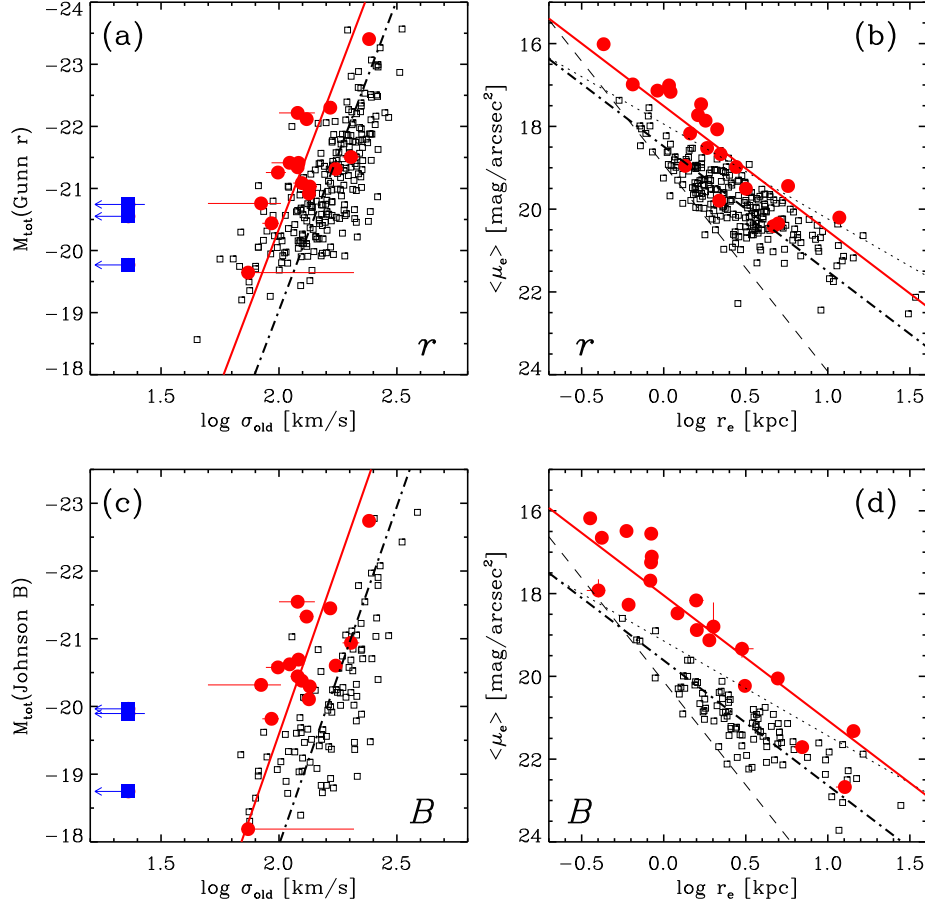
Figure 3.10 — Faber-Jackson and Kormendy relations for E+A galaxies in the *B* (*bottom*) and Gunn *r* bands (*top*). The small squares and large circles represent cluster E/S0s in the J96 sample and our E+As, respectively. The large filled squares are the E+As for which we have only an upper limit on the velocity dispersion of their old stellar population, σ_{old} from N01. In the left panels, the solid and dot-dashed lines represent the best-fit Faber-Jackson relations ($L \propto \sigma^4$) for E+As and E/S0s, respectively. On average, E+A galaxies are 1.31 (± 0.73) and 1.64 (± 0.71) mag brighter than E/S0s in the Gunn *r* and *B* bands. In the right panels, the solid and dot-dashed lines are the Kormendy relations with fixed slope for E+As and E/S0s, respectively. The average offsets between E+As and E/S0s are 0.98 ± 0.45 and 1.57 ± 0.52 mag in *r* and *B*, respectively. The dashed line is the boundary set by the limiting magnitude. The dotted line is the sharp physical boundary that divides the plane into the E/S0s and the so-called *exclusion zone* where dynamically relaxed systems are not allowed (Bender et al., 1992).

mations, but also because the functional forms used to calculate the offset are different.

These offsets can be interpreted as either that E+As have an elevated luminosity for a given velocity dispersion or that they have an unusually low velocity dispersion at a given luminosity. To investigate which interpretation is more correct, we compare E+As to E/S0s on the purely photometric scaling relation, i.e., the Kormendy (1977) relation (hereafter KR), between the effective radius (r_e) and the mean surface brightness within r_e. The right panels in Figure 3.10 show the KRs for the E+As and E/S0s, the latter of which is corrected from the original KR Kormendy (1977) by assuming an average color, $B - r \simeq 1.20$ (Fukugita et al., 1995). The slope of the relation is known to be insensitive to the band. For example, Hamabe & Kormendy (1987) find a slope of 2.98 in the V band compared to 3.02 in the B band.

In the KR plane, most of E+As, except for a few disky ones, have a higher surface brightness than E/S0s at a given effective radius. The average offset between E+As and E/S0s is 0.98 ±0.45 and 1.57 ±0.52 mag in r and B, respectively. The offsets appear to increase as the galaxies become smaller; roughly half of the E+As do not overlap with the B and r band E/S0 loci. The lower boundary (dashed line) of the E/S0 region is set by the limiting magnitude of $M_r \simeq -20.45$. The upper boundary is not due to selection effects (see §3.5.3). Because the surface brightness offsets in the KR are consistent with the magnitude offsets obtained from the FJR, we conclude that elevated luminosities, probably due to the recent star formation, are responsible for the offsets of the E+A scaling relations, rather than unusually low velocity dispersions. While the FJR and KR suggest that roughly one magnitude of fading may bring E+As down to the E/S0 scaling relations, the large scatter makes such an analysis difficult.

3.5.2 Fundamental Plane

The fundamental plane, hereafter FP, is an empirical scaling relation between the effective (or half-light) radius r_e, the central velocity dispersion σ, and the mean surface brightness $\langle I_e \rangle$ within r_e for early type galaxies (Djorgovski & Davis, 1987; Dressler, 1987). Although the physical origin of the FP is not fully understood, both cluster and field early-type galaxies follow this relation with remarkably small scatter (e.g., ~ 0.1 dex in $\log r_e$ in the Gunn r band; J96), and an extension of this formalism appears to fit all spheroids ranging from Galactic dSph galaxies to the intracluster stellar component of galaxy clusters (Zaritsky et al., 2006).

To examine the FP of E+As and compare it with that of E/S0s, we adopt the definition and methodologies of Jørgensen et al. (1996) (see also Kelson et al., 2000). The fundamental plane is defined as

$$\log r_e = \alpha \log \sigma + \beta \log \langle I_e \rangle + \gamma \,, \tag{3.4}$$

where r_e, σ, and $\langle I_e \rangle$ are the effective or half-light radius in kpc, central velocity dispersion in km s^{-1}, and mean surface brightness within r_e in units of $L_\odot \mathrm{pc}^{-2}$. For the E+A structural parameters, we adopt r_e and $\langle \mu_e \rangle$ from the single de Vaucouleurs fits to our *HST* images (Figure 3.11). We transform the mean surface brightness in our *HST* bands into Gunn r and Johnson B using our transformation relations (eq.3.1) and the coefficients in Table 3.2. We convert to units of $L_\odot \mathrm{pc}^{-2}$ using the relation $\langle I_e \rangle = -0.4(\langle \mu_e \rangle - \mathrm{constant})$, where the constants are 26.4 and 27.0 for Gunn r and Johnson B magnitudes, respectively. We do not apply a color-dependent correction to r_e, because the E/S0 FP is only weakly sensitive to color (Pahre et al., 1998; Bernardi et al., 2003).
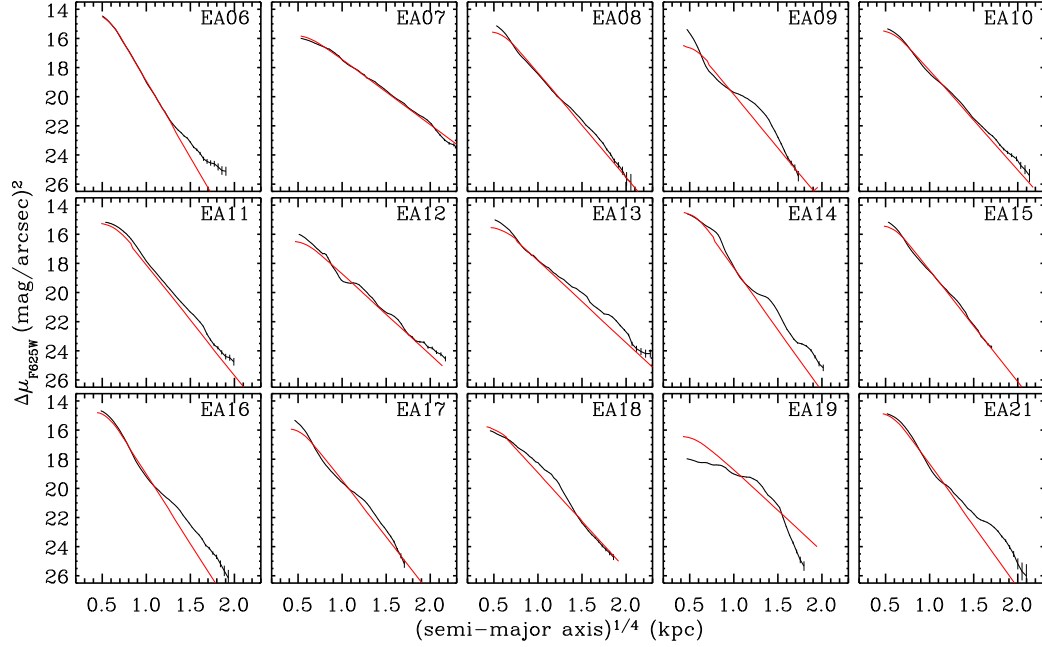
Figure 3.11 — Light profiles of E+As with a single $r^{1/4}$-law fit (dark lines). The thick dot-dashed lines are the best fits. The structural parameters (r_e and $\langle\mu_e\rangle$) from the single de Vaucouleurs profiles fits are used to construct the FP of E+A galaxies.

3.5.3 Location of E+As on the FP

We show the location of our E+As on various projections of the J96 FP in the Gunn r and B bands in Figure 3.12. Figures 3.12a and 3.12c present the face-on view of the E/S0 FP in r and B, respectively. The dashed line is the boundary set by the limiting magnitude of $M_r \simeq -20.45$, which corresponds to the constant magnitude line (dashed line) in 3.10b and 3.10d. The boundary set by the dotted line divides the plane into the E/S0 FP and the so-called *zone of exclusion* (ZOE), where dynamically relaxed systems do not reside (Bender et al., 1992). The physical origin of this boundary is not fully understood, although it might correspond to the upper limit of the velocity dispersion function of early-type galaxies ($\sigma \lesssim 350$ km

s^{-1}; Treu et al., 2006). In the face-on projection, E+As span the same region defined by the normal early-type galaxies in the r band; however, half of our E+As violate the zone of exclusion in the B band. We plot vectors parallel to the FP parameters to find out which parameters drive this shift in the r band. E+As are shifted from the E/S0s along the direction of increasing $\langle I_e \rangle$, as we concluded earlier from the Kormendy relation. Given that E+As already populate the same region as E/S0s in the r band and that the $\langle I_e \rangle$ offset is larger in B, this violation of the ZOE must be due to the temporary increase of the surface brightness caused by the recent starburst.

Figures 3.12b and 3.12d present the edge-on projection of the E/S0 FP, defined as $x = \log r_e$ and $y = \alpha \log \sigma + \beta \log \langle I_e \rangle$, in r and B, respectively. In this projection, E+As are distinct from E/S0s. The existence of a tight correlation among E+As indicates that they follow their own scaling relation. The large offset between the E/S0s and E+As suggests that the E+As' current stellar content is different. Although the mechanisms that trigger the E+A phase and stop star formation are not fully understood, any model must be able to explain the relative tilt and offset of the E+A FP. In the following section, we discuss how the observable properties are related to physical ones, such as mass-to-light ratio M/L, and possible interpretations of the tilt and offset.

3.5.3.1   FP Offsets: Evolution of the FP Zero Points

E+A galaxies stand apart from the E/S0 FP in the edge-on projection (Figures 3.12b and 3.12d). The difficulty in interpreting this difference is that any, or all, of the three plotted parameters or the implicit parameter, M/L, may be evolving as the E+A evolves. The simplest option is to assume that only M/L evolves. In this case, the offset between the two populations can be directly related to a difference

in M/L,

$$\Delta\log\frac{M}{L} = \frac{\Delta\gamma}{\beta}, \tag{3.5}$$

where the FP offset $\Delta\gamma$ is measured from the difference between the intercepts of two parallel lines in Figures 3.12b and 3.12d. We find $\Delta\gamma = -0.47 \pm 0.12$ in the Gunn r band, which implies $\Delta\log\,(M/L) = -0.57 \pm 0.14$. In other words, E+As have, on average, a M/L that is 3.8 times smaller than that of E/S0s. Note that this average offset has a smaller error than the offsets measured from the FJR and KR. However, as we have shown previously in §3.4, the structural properties are affected by the E+A phase (the color gradients are altered, some E+As have blue cores) and so assuming that only M/L evolves cannot be completely correct. Our expectation is that r_e will be smaller in E+As because of the centrally concentrated star formation, and hence that r_e will increase (and $\langle I_e \rangle$ decrease) as the E+A evolves, leading to a complex evolution on the FP. Therefore, the M/L difference discussed above is the minimum amount of fading that E+As should experience to settle onto the E/S0 locus. By examining the tilt of the FP, and other projections of the scaling laws, we explore whether we can proceed beyond this simple model and the potential complexity of evolution on the FP.

3.5.3.2   FP Tilts: Variation of M/L along the FP

Given the range of possible evolutionary paths on the FP, it is rather surprising that there is a tight relation for E+As on the E/S0 FP edge-on projection. Further-more, the difference appears to be both a relative shift and a tilt. To measure the relative tilt of E+As with respect to E/S0s, we find the best-fit plane in the form of equation 3.4 through the E+As using an orthogonal fitting method that mini-mizes the normal distances to the plane. We adopt this fitting method to enable direct comparison with the fits from J96. J96 find $\alpha = 1.24\pm0.07$, $\beta = -0.82\pm0.02$ for Gunn r and $\alpha = 1.20\pm0.06$, $\beta = -0.83\pm0.02$ for Johnson B using 226 and 91
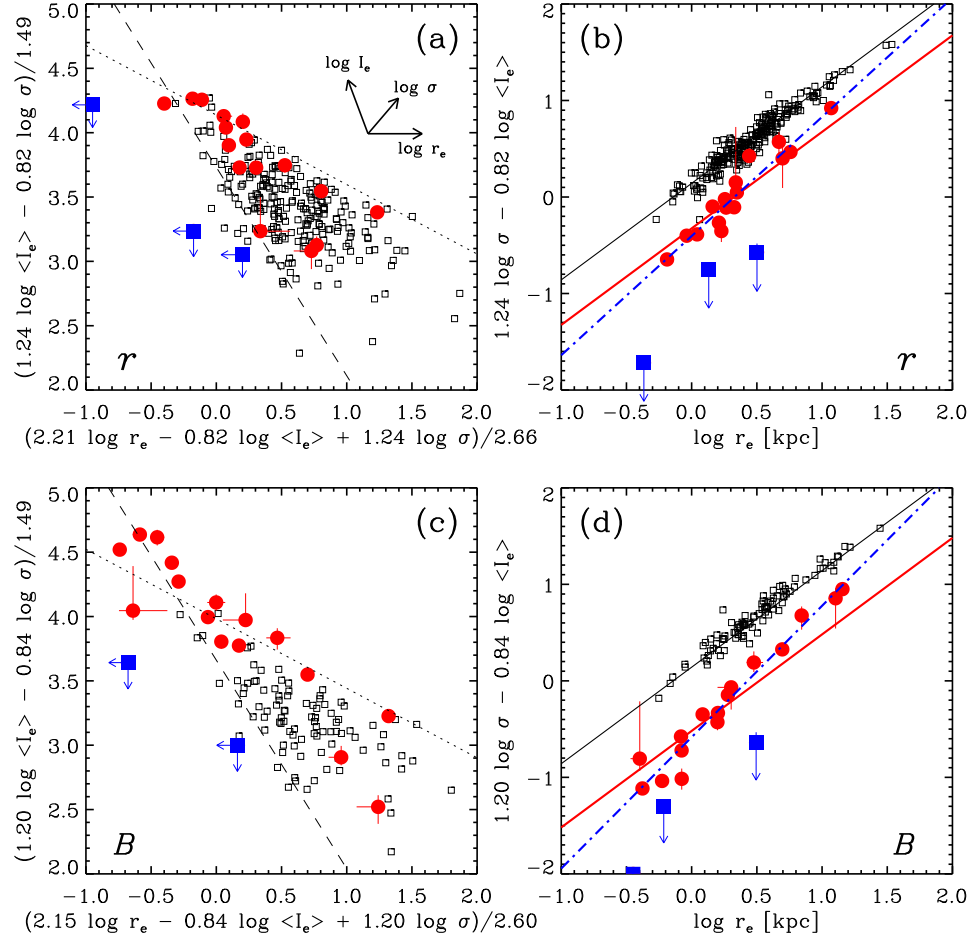
Figure 3.12 — Face-on and edge-on projections of the fundamental plane in the B (*bottom*) and r (*top*) bands. The small squares and large circles represent the E/S0s in the J96 sample and our E+As, respectively. The large filled squares are the three E+As (EA06, EA17, and EA18) that have only upper limits on σ_{old} from N01. Of all the sample galaxies, these three E+As have the largest light fraction contributed by the young A-type population (f_A in N01). (*a*)(*c*) Face-on projection of the FP. The dashed line is the boundary set by the limiting magnitude. The dotted line is the sharp physical boundary that divides the plane into the E/S0 FP and the so-called *exclusion zone* where dynamically relaxed systems are not allowed (Bender et al., 1992). (*b*)(*d*) Edge-on view of the FP. The solid and dot-dashed lines represent the best-fit planes for E+As with and without fixed slopes (α, β), respectively. E+As follow their own scaling relations and have significant offsets from the E/S0s.

cluster galaxies, respectively. Using 16 E+A galaxies[1] and taking an equal weight for each galaxy, we find that the best-fit FPs are

$$r_e \propto \sigma^{1.13\pm0.10} \langle I_e \rangle^{-0.62\pm0.07} 10^{-0.08\pm0.10} \tag{3.6}$$

$$r_e \propto \sigma^{1.09\pm0.08} \langle I_e \rangle^{-0.59\pm0.06} 10^{-0.11\pm0.07} \tag{3.7}$$

for the Gunn r and Johnson B bands, respectively. The errors in α, β, and γ are estimated using the bootstrap method. The rms scatter around these planes is 0.10 and 0.10 in $\log r_e$ for Gunn r and Johnson B, respectively. The parameters (α, β, γ) for Gunn r and Johnson B agree within the uncertainties, because the FP parameters are generally not highly sensitive to the bandpass (J96). Therefore, we adopt the (α, β, γ) derived using the Gunn r data in the following discussion. While $\alpha = 1.13$ for the E+A FP agrees to within the errors with that of the E/S0 FP ($\alpha = 1.24$) (the E+A FP is still viewed edge-on in the projection in Figure 3.12*b*), $\beta = -0.62$ for the E+As is $\sim 3\sigma$ discrepant from that of the E/S0s ($\beta = -0.82$). In the context of interpreting differences between the FPs as primarily due to M/L, the tilt implies a mass dependence. A similar tilt of the FP of merger remnants is observed relative to the K-band E/S0 FP (Fig. 1; Rothberg & Joseph, 2006).

The tight correlation within the E+A FP suggests that M/L is correlated with the structural parameters. The scatter around the plane appears to be comparable to the typical scatter of E/S0 FPs (~ 0.1 dex). Does this mean that E+As, many of which are clear merger remnants, settle into a relaxed state on a short timescale? Or is it possible that the correlation is the result of a selection effect? Our selection of galaxies with strong Hδ absorption tends to choose galaxies with stronger bursts and/or the younger ages; therefore it is possible that our sample represents only a certain part of the FP, i.e., near the exclusion zone. To address this issue, a larger sample of E+As covering a wider range of Hδ strengths is required.

[1]This excludes EA01AB, 07, 17 and 18 which do not have a measured σ_{old}.

Using the best fit FP parameters, M/L for E+As can be expressed as

$$M/L \propto M^{0.1} r_e^{0.4}, \tag{3.8}$$

compared with $M/L \propto M^{0.24} r_e^{0.02}$ for E/S0s. Unlike in the E/S0 FP, where M/L is a function mostly of mass, M/L for E+As depends on the effective radius as well as the mass of the system. E+As with smaller effective radii have smaller M/L, possibly resulting from a stronger burst and/or shorter time elapsed since the starburst. Because M/L is proportional to $(r_e \langle I_e \rangle)^{-1}$ at a fixed velocity dispersion, one might expect that a smaller r_e would lead to a larger M/L, but the observed trend is the opposite. Therefore, the surface brightness of E+As must increase faster than the mass or size of the galaxy decreases. This inference is consistent with the observed KR (Figure 3.10), in which $\langle \mu_e \rangle$ deviates further from the E/S0 relation for E+As with small effective radii.

If M/L does indeed vary among E+As, then one might expect a correlation between the deviation of M/L from E/S0s and the color of the galaxy. In Figure 3.13, we plot $\Delta M/L$ against $(B - R)$ color, and against other parameters (mass, r_e, Sérsic n, and σ_{old}). We find a strong correlation between $\Delta M/L$ and color, but no significant correlation with n or σ. A Spearman rank test shows that only $(B - R)$ color correlates with $\Delta M/L$ at a significance level higher than 99.5% for both the r and B bands. We conclude that the tilt, i.e., the variation of M/L within the E+A FP, does reflect a real variation of the stellar population. E+As with smaller effective radii have younger stellar populations, on average, and therefore, smaller M/L.

The remaining question is what does the small r_e physically represent? Does it indicate that the intrinsic size of the galaxy is small or that there was a strongly concentrated starburst? We compare the effective radii in B and r to address these questions. In blue-core E+As or E+As with the positive color gradients ($\sim$
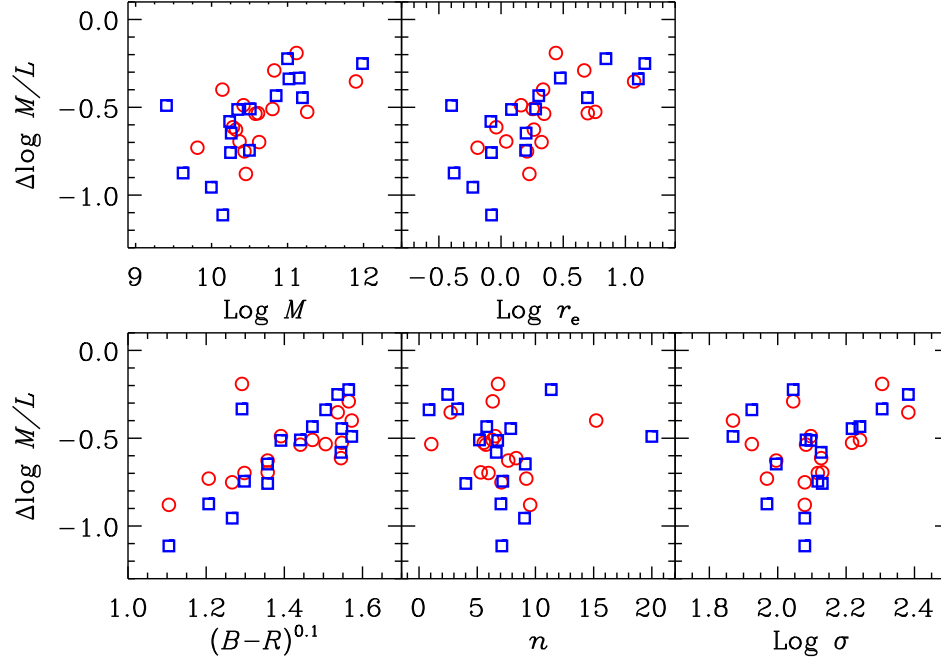
Figure 3.13 — Correlations between the deviation of M/L from E/S0s for individual E+As and the $(B - R)$ color, dynamical mass, Sérsic index n, velocity dispersion of the old stellar population σ_{old}, and the effective radius r_e. The squares and circles represent parameters from the B and R bands, respectively. $\Delta M/L$ is tightly correlated with $(B-R)$ color, but not with n or σ. We conclude that the tilt, i.e. the variation of M/L along the E+A FP, is mostly due to stellar population variations. E+As with smaller effective radii have younger stellar populations, on average, and therefore smaller M/L.

75% of E+As), the effective radius tends to be smaller in the B band ($r_{e\mathrm{B}}$) than in the r band ($r_{e\mathrm{R}}$). In these galaxies, it is likely that $r_{e\mathrm{B}}$ will eventually become close to $r_{e\mathrm{R}}$ as the light from the young stars in the central region fades and the color gradients flatten. However, most galaxies have fairly small differences, $|\log r_{e\mathrm{B}} - \log r_{e\mathrm{R}}| < 0.30$, which is clearly not enough to produce the tilt observed over two orders of magnitude in effective radius.

To further test whether intrinsically small galaxies have smaller M/L's, we re-

peat the orthogonal fitting, but this time exclude galaxies with $|\log r_{eB} - \log r_{eR}| >$ 0.15, i.e., for which the two effective radii differ by more than 25%.[2] For this subsample, the color gradients are moderately flat and there is little dust, so strong evolution in the effective radius due to stellar evolution is unlikely. The fitting of this subsample results in the same FP slope as for the full sample, implying that intrinsically small and therefore less massive galaxies have smaller M/L ratios.

Blue-core galaxies analogous to our blue core E+As (§4.2) are found among early-type galaxies at high-z (van Dokkum & Ellis, 2003; Treu et al., 2005), and their rest-frame B-band M/L is estimated to be much smaller (roughly $4\times$) than that of normal E/S0 galaxies at the same epoch. As a cautionary note, we examine how the difference between the blue and red r_e affects the measurement of M/L , especially for blue core galaxies. When we use the blue r_e to derive M/L for our blue core E+As, we find that M/L can be biased low by a factor of 1.25 to 5.5 relative to that derived using the red r_e.

3.5.3.3   Will E+As Evolve into E/S0s?

In summary, the scaling relations of E+As demonstrate that their stellar populations are currently different from those of E/S0s. This conclusion is drawn from the FP parameters (σ, r_e and μ_e) in one photometric band, and therefore is derived independently from our spectroscopic knowledge that E+A galaxies have significant A-type populations. The surprising finding is that among E+As, the variation of stellar populations is closely tied to the structural parameters, i.e., E+As follow their own scaling relationships such that smaller or less massive galaxies have a smaller M/L. Such a trend arises naturally within a merger scenario, where low mass galaxies (the progenitors of low-mass E+As) have higher

---

[2]We boost the statistics of this test by combining the B and R band sample assuming the same FPs parameters for both bands (see §3.5.3.2).

gas fractions (Young & Scoville, 1991) and could produce relatively larger populations of young stars.

Will E+As fade onto the fundamental plane of E/S0 galaxies after a few Gyr? This question is difficult to answer fully due to the complex interplay between galaxy's dynamical evolution and the evolution of its stellar populations. However, if we ignore the dynamical evolution, we can estimate the amount of fading using a stellar population synthesis model (Bruzual & Charlot, 2003, BC03). We adopt a simple star formation history for the E+As: a single instantaneous starburst on top of an underlying 10 Gyr old single burst population. Both populations have Salpeter IMFs and solar metallicities.

The largest uncertainties in determining the amount of fading and the time required for settling onto the E/S0 FP are the unknown post-burst age (the time elapsed since the burst) and burst strength (the fraction of the stellar mass produced during the starburst). Because we are unable to break the degeneracy between post-burst age and burst-strength for this sample (see, however, Yang et al. 2008, in prep.), we test whether the required fading time is reasonable for the galaxies whose post-burst ages and burst strengths are consistent with the FP offset (1.42 ± 0.36 mag in Gunn r). For various post-burst ages and burst fractions in Figure 3.14, we calculate how much the galaxies should fade and how long it will take from the given post-burst age until their $(B - R)$ colors agree with that of a 10 Gyr old simple stellar population, i.e., until they become E/S0s. The lined region in Figure 3.14 shows the post-burst ages and burst fractions that would satisfy the E+A selection criteria adopted by Zabludoff et al. (average Balmer equivalent width $\langle H\beta\gamma\delta \rangle > 5.5$Å). The shaded region represents those galaxies that will fade by $\Delta M_r = 1.42 \ (\pm 0.36)$ mag until their $(B - R)$ colors match the 10 Gyr old population i.e., those E+As whose M/L's are consistent with the observed FP offsets.
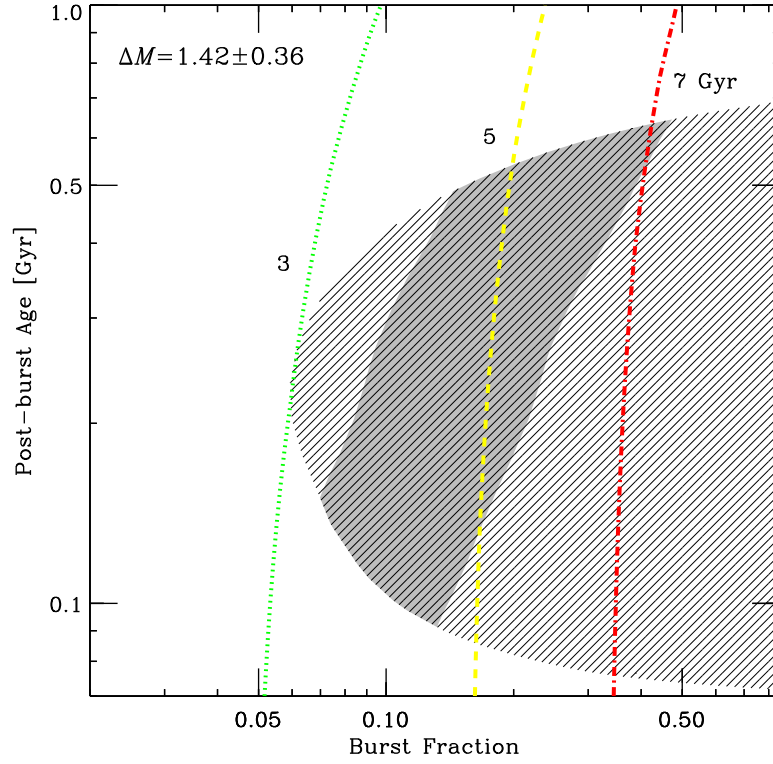
Figure 3.14 — Time required for E+As to fade until their $(B - R)$ colors agree with that of 10 Gyr old simple stellar population as a function of burst fraction and post-burst age. From left to right, the contours represent fading times of 3, 5 and 7 Gyr, respectively. The lined region represents galaxies that would be classified as E+As according to the Zabludoff et al. (1996) selection criteria (average Balmer equivalent width $\langle H\beta\gamma\delta \rangle >$ 5.5Å). The shaded region shows galaxies that will fade by their observed offsets from the E/S0 fundamental plane ($\Delta M_r = 1.42 \pm 0.36$ mag) for the given burst fraction and post-burst age. This fading time lies between 3 and 7 Gyr, indicating that E+As with reasonable post-burst ages (100 – 700 Myr) and burst fractions (7 – 50%) can evolve into E/S0s within ~ 5 Gyr.

This shaded region illustrates the degeneracy between the post-burst ages and burst strength: old/strong and young/weak bursts both explain the observed FP

offsets. We also show the required fading time (3, 5, and 7 Gyr) with contours. The shaded region falls between 3 and 7 Gyr, indicating that E+A galaxies with reasonable post-burst ages ($100 - 700$ Myr) and burst fractions ($7 - 50\%$) will settle onto the E/S0 FP after ~ 5 Gyr.

3.6 Young Star Clusters

The properties of star cluster systems in early type galaxies, e.g., the color bimodality, provide important clues for how the host galaxies formed and how they assembled their stellar content over time (see the recent review by Brodie & Strader, 2006). If many or all E+A galaxies result from galaxy-galaxy close interactions or mergers, as suggested here and in previous work (Zabludoff et al., 1996; Yang et al., 2004, 2006; Blake et al., 2004; Tran et al., 2003, 2004; Goto, 2005), and evolve into E/S0s, as we argue in this paper, the photometric properties of their cluster systems should be consistent, to within evolutionary corrections, with those of early types. In the WFPC2 sample, we discovered young star clusters around four E+As[3] (Yang et al., 2004). These clusters are much brighter than Galactic globular clusters and have blue colors consistent with ages estimated roughly from the E+A galaxy spectra ($\lesssim$ Gyr). Our new ACS observations of the remaining LCRS E+As also reveal a number of point-like sources surrounding the galaxies. In this section, we first present the evidence that these are newly-formed star clusters, then investigate whether their colors and luminosities are consistent with being created concurrently with the burst that generated the young stars in the E+As, and finally test whether these cluster systems can evolve into the globular cluster systems of present-day E/S0s.

---

[3]EA01A, 02, 03, 04

3.6.1 Detection and Photometry of Cluster Candidates

To detect cluster candidates, we use SExtractor (Bertin & Arnouts, 1996) on both the original and model-subtracted residual R band images (Fig. 3.2). After testing various selection criteria and visually inspecting the detected point sources, we require that cluster candidates have at least 4 adjacent pixels whose flux in each pixel is at least $3\sigma_{\mathrm{sky}}$ larger than the local sky value, where σ_{sky} is the root mean square (rms) of the local sky values estimated using a background mesh size of 4–8 pixels in SExtractor. We use the residual images to find compact sources within the galaxies, where the rapidly varying galaxy surface brightness prevents the reliable detection of sources in the original images. We choose to lower the detection threshold to 2.5 σ_{sky} for the residual images, because σ_{sky} is inflated by the residual galaxy light. From this initial source list, objects with an apparent magnitude $m_R < 22$, elongation $\varepsilon > 1.7$, and isophotal area $A > 36$ pixels are rejected as possible foreground stars or background galaxies.

Because clusters are expected to be unresolved at the distance of our E+A galaxies (~ 100 pc per pixel at $z \sim 0.1$), contamination from background galaxies, foreground stars, hot pixels, and residual cosmic-rays could be problematic. Therefore, we run a statistical test to determine whether there is an excess of compact sources near each E+A. First, we build a control sample of cluster-like sources from the entire *ACS* field ($\sim 200'' \times 200''$) outside of a 20 kpc radius from the E+A using the same selection criteria. Then we calculate the distribution of the number of the sources within circular beams of 20 kpc projected radius at random positions in the *ACS* field outside a 20 kpc radius from the E+As. If there are significantly more cluster candidates within the 20 kpc beam centered on the E+A than in the random beams, then it is likely that these are true compact objects associated with the E+A. We test various beam sizes, e.g., fixed angular size
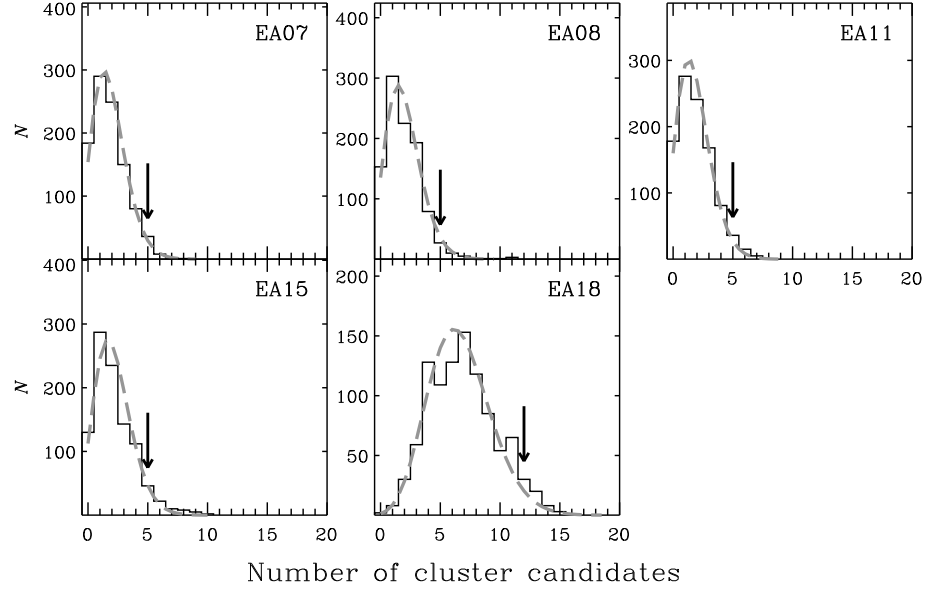
Figure 3.15 — Distribution of the number of point sources in random beams sampling the *ACS* fields of the five E+As (EA07, 08, 11, 15, 18) with a significant ($> 90\%$ confidence level) excess of surrounding sources. In each field, the beam size corresponds to a 20 kpc radius at the E+A's redshift. In each panel, arrows represent the number of cluster candidates within this radius centered on the E+A. The overlayed dashed line is the Poisson distribution.

versus physical size, and find that our conclusions are insensitive to this choice.

Five E+As (EA07, 08, 11, 15, 18) have an excess of associated point sources at a confidence level greater than 90%. We show the number of cluster candidates found near the E+As relative to the distribution found within random beams in Figure 3.15. Because of the post-starburst nature of E+As and the merger signatures clearly seen in EA07, 11, and 18, it is likely that these sources are the newly formed star clusters often found in on-going mergers (The Antennae; Whitmore & Schweizer, 1995) and merger remnants (NGC7272; Whitmore et al., 1993).

To test whether the colors and luminosities of these cluster candidates are

consistent with a merger origin and with evolution into the globular cluster populations of E/S0s, we measure aperture magnitudes in the B and R band images. Because many cluster candidates are located within the galaxy, where there is a rapidly varying effective background, obtaining reliable photometry is difficult. We first subtract the background galaxy light by fitting 7th order polynomials to the background, excluding the cluster itself, within a 11×11 pixel box centered on the point source. We then add a flat background that has the same mean as the fitted background to preserve the noise properties. Finally, we measure magnitudes within a 2 pixel radius. Because the uncertainties in the measured magnitudes and colors transfer directly to those in the derived ages, we estimate photometric errors using artificial cluster tests. We place one thousand model star clusters with known brightness into the relevant parts of the images and repeat our procedure. We find that if the model cluster is detected, the magnitude error due to the background subtraction is nearly insensitive to the underlying average sky value and depends mostly on the brightness of the cluster. Typically, the magnitude uncertainty is ∼0.25 mag down to m_R = 26.5.

3.6.2 Luminosity Functions and Ages of the Star Clusters

In Figure 3.16, we present the luminosity functions (LFs) of cluster candidates in the four E+As (EA01A, 07, 15, 18) that have more than five clusters with measurable colors ($\sigma_{B-R} < 0.35$ mag) within a 30 kpc radius[4]. The LFs of Milky Way globular clusters (Harris, 1996) and clusters in a merging galaxy (NGC 3597; Carlson et al., 1999) are also shown in the top panel for comparison. The thick solid lines and the shaded histograms represent all E+A cluster candidates within 30 kpc and only those with measured colors, respectively. The detected clus-

---

[4]We adopt a 20 kpc radius for the random beam test to determine if cluster candidates exist, but we analyze all cluster candidates within a 30 kpc radius to include as many cluster candidates as possible.

ters in the four E+As are generally much brighter than Galactic globular clusters ($M_R \lesssim -11$), but consistent with the bright end of the NGC3597 cluster LF, suggesting that these compact point sources are a population of star clusters formed during the starburst.

More interesting is that the bright end of the LFs becomes fainter as the EA number increases, i.e., as the host E+A becomes redder. Furthermore, we are able to detect a cluster population more often in E+As with smaller EA number. We can reject with ~90% confidence that the distribution of E+As with cluster populations (EA01A, 02, 03, 04, 07, 08, 11, 15, 18) is random. All nine of these E+As exhibit tidal features or disturbed morphologies (§A.1). These trends suggest that the newly-formed young star cluster systems fade or disrupt as the merger remnant ages and morphologically relaxes. If E+As evolve into E/S0s, we expect these cluster systems to become part of the globular cluster systems of E/S0s.

To pursue these suggestions, we determine the ages of individual clusters by comparing the cluster colors with predictions from stellar population synthesis models. In Figure 3.17, we show the $(B - R)$ evolution for star clusters derived from a BC03 model and the colors of the star clusters found in three E+As (EA07, 15, 18). We also reproduce Figure 10 from Yang et al. (2004) for the clusters in EA01A for completeness. To avoid uncertainties in the *K*-correction and the magnitude transformation due to the unknown SED, we calculate the redshifted $(B_{435}-R_{625})$ color evolution using the spectra provided by the BC03 stellar synthesis model. We assume an instantaneous stellar population with a Salpeter initial mass function (IMF) over stellar masses ranging from 1 to 100 $M_\odot$ and solar metallicity. On the model tracks in Figure 3.17, we plot the observed cluster colors and the possible age ranges due to the photometric errors (shaded region). We include only clusters with color uncertainties less than 0.35 mag. The ages of
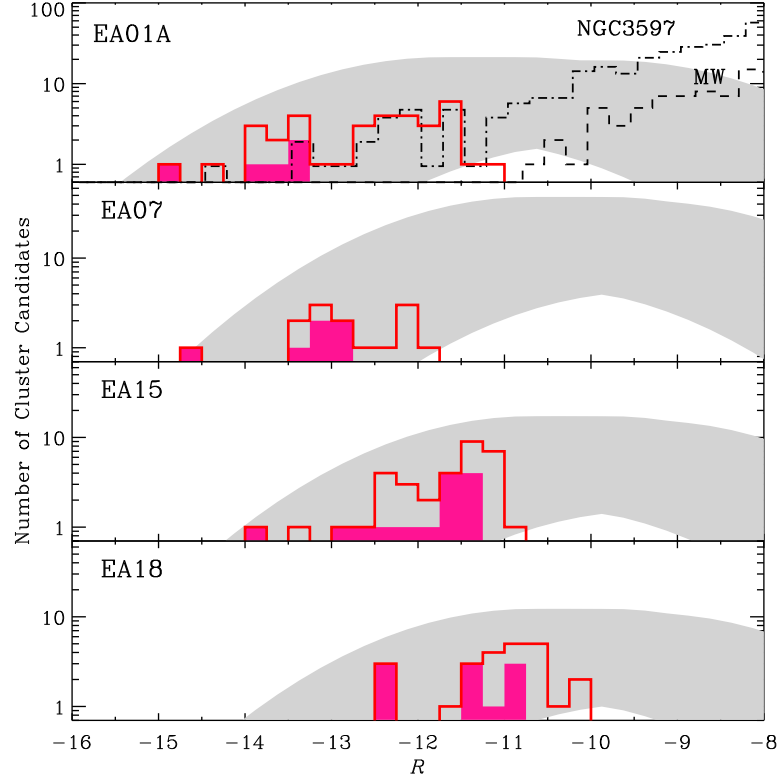
Figure 3.16 — Cluster luminosity functions for the four E+As (EA01, 07, 15, 18) that have more than five clusters with measurable colors. The bluest (and perhaps youngest) galaxy is at the top, the reddest galaxy at the bottom. The solid lines are the LFs for the cluster candidates projected within 30 kpc of the host galaxy. These LFs are incomplete fainter than about the middle of their range. The shaded histograms are for the clusters with measured colors. The LFs of Galactic GCs and the merging galaxy NGC3597 are represented with dashed and dot-dashed lines, respectively. The clusters in the E+As are much brighter than the Galactic globular clusters ($M_R \lesssim -11$) but consistent with the bright end of the NGC3597 cluster LF, suggesting that these compact point sources are the population of star clusters formed during the starburst. The luminosity of the brightest clusters decreases as the color of the host galaxy reddens, suggesting a fading trend with age. The shaded regions are the globular cluster LFs of E/S0s that are evolved backward to the epoch of the E+A phase. The LFs of the cluster candidates fall in the shaded region, indicating that they could evolve into the globular cluster population of early-type galaxies.
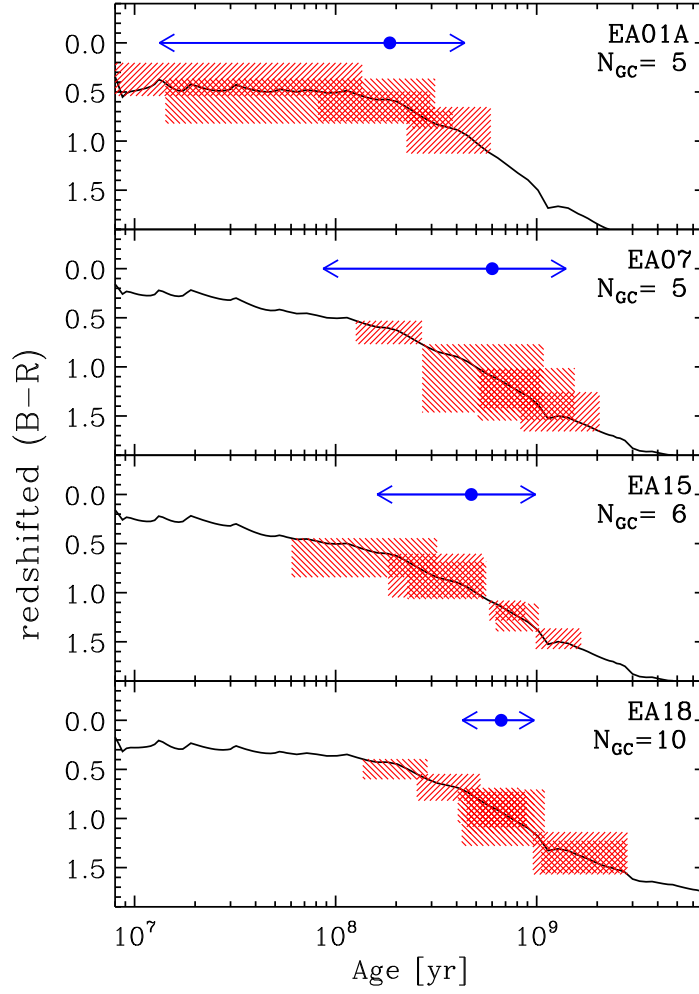
Figure 3.17 — Evolution of the redshifted $(B - R)$ colors of star clusters derived from BC03 and the cluster colors from the four E+As (EA01, 07, 15, 18) in Figure 3.16. For the model track, we assume an instantaneous stellar population with a Salpeter IMF, masses ranging from 1 to 100 $M_\odot$, and solar metallicity. On the model track, we show the measured cluster colors and the possible range of ages due to the photometric errors (shaded region). Only the clusters with color uncertainties less than 0.35 mag are included in the age determination. The ages of clusters derived from their colors are consistent with our expectations from the E+A galaxy spectra: older than ~10 Myr (the lack of the emission lines due to the massive OB stars), but younger than $\sim$ Gyr (the presence of strong Balmer lines due to the A stars). The arrows represent the estimated post-burst age (time elapsed since the starburst) using the methods described in §3.6.2. Cluster ages become older as the EA number increases, i.e., as the host E+A becomes redder.

individual clusters are consistent with what one expects from the E+A spectra: older than ~10 Myr (the lack of emission lines associated with massive OB stars) but younger than ~ Gyr (the presence of strong Balmer lines due to A stars).

To use the clusters to derive the time since the starburst, when the majority of the clusters and the young galactic stars formed, we apply a statistical test assuming that all star clusters formed during a single burst and therefore that their spread in observed color arises only from measurement errors. Details of the post-burst age estimation and statistical tests of the coeval assumption are described in Appendix B. We show the post-burst age inferred from the clusters as horizontal bars in Figure 3.17. EA01A, 07, 15, and 18 have post-burst age ranges of [10 Myr, 450 Myr], [100 Myr, 1.5 Gyr], [150 Myr, 1 Gyr], and [400 Myr, 1 Gyr], respectively, corresponding to the 95% confidence level. Note that it may be possible to break the long-standing degeneracy between the burst strength and the time elapsed since the starburst by using individual cluster ages, because these systems are much simpler than the composite population of the host galaxies. However, small number statistics and low S/N in the color measurements do not allow us to put tighter constraints on the post-burst ages at this time.

The evolution of the cluster LFs is consistent with the model predictions. While the uncertainties are fairly large, the derived post-burst ages are consistent with the E+A spectra and tend to increase with EA number, suggesting that the EA numbers *are* roughly consistent with a sequence of post-burst ages. In Figure 3.18, we show that the evolution of the bright magnitude limit of the cluster LF and the post-burst ages (derived from the cluster colors) are consistent with the fading of a uniform cluster mass function.

3.6.3 Evolution of the Cluster Population

The remaining question is whether these young cluster candidates can evolve into a significant part of the globular cluster systems of present-day E/S0s. Specifically, are the current numbers of clusters in E+As consistent with the globular cluster luminosity function (GCLFs) of E/S0s? It has been proposed that the metal-rich GCs in giant ellipticals formed during mergers of gas-rich spirals, producing the bimodality of the GC subpopulations (Ashman & Zepf, 1992). Indeed, many young GCs have been found in mergers (e.g., Whitmore et al., 1993), and Goudfrooij et al. (2004) demonstrated that the LF of intermediate-age ($\sim$3 Gyr) GCs in NGC1316 can evolve dynamically into the red metal-rich cluster populations that are ubiquitous in E/S0s. Unfortunately, due to low S/N in the color measurements and the small number statistics of our cluster candidates, it is difficult to predict the evolution of the individual cluster systems in our sample. Instead, we "predict" the cluster LFs of E+As under the assumption that they are indeed the progenitors of the E/S0 cluster population.

First, we assume the following form of the GCLFs, i.e., the number of GCs per unit magnitude:

$$\phi(M_R) = \frac{f_{\mathrm{MR}}}{\sqrt{2\pi}\sigma} \frac{S_N}{10^{0.4(M_V+15)}} \exp[\frac{-(M_R - M_0)^2}{2\sigma^2}], \qquad (3.9)$$

where M_V is the total V-band magnitude of the host galaxy, M_0 and σ are the turnover magnitude and the dispersion of the Gaussian function, S_N is the specific frequency given by $S_N \equiv N_{\mathrm{GC}} \cdot 10^{0.4(M_V+15)}$ (Harris & van den Bergh, 1981), and f_{MR} is the fraction of metal-rich "red" clusters. Harris (2001) found that $\langle S_N \rangle$ = 3.6$\pm$0.5, $M_0 = -7.4\pm0.15$ mag in the V-band and $\sigma = 1.4\pm0.03$ for local elliptical galaxies ($M_V \lesssim -18$).

Second, to evolve this GCLF backward to the E+A epoch, we calculate the fading of the turnover magnitude between an age corresponding to the E+A clusters
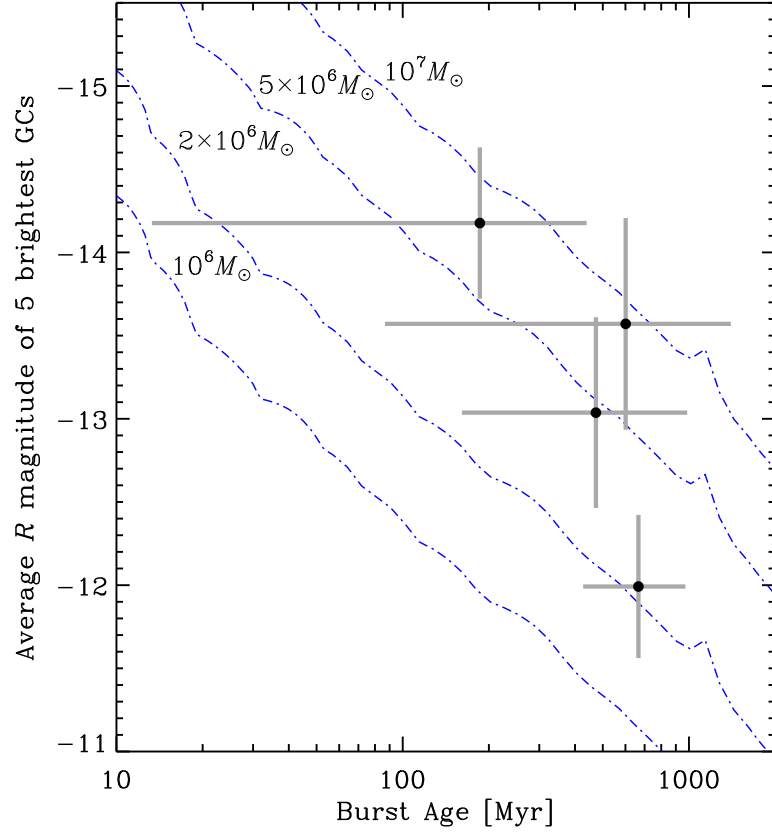
Figure 3.18 — Evolution of the bright end of the star cluster LFs in the four E+As (EA01A, 07, 15, 18) in Figures 3.16 and 3.17. We show the relation between the average luminosity of the five brightest clusters in each E+A and the post-burst age shown in Figure 3.17. Dot-dashed lines represent BC03 model tracks for simple stellar populations (SSPs) with different cluster masses (1, 2, 5 and $10 \times 10^6 \, M_\odot$). The observed fading of the cluster LFs is consistent with the color-derived post-burst ages.

and that corresponding to E/S0 GCs, assuming that E/S0 GCs are $5 - 10$ Gyr old. For solar metallicity and a Salpeter IMF, a BC03 model predicts ~ 2 mag of fading between 1 Gyr and 10 Gyr. Note that these derived LFs will be lower limits because we consider only photometric evolution. For host galaxy luminosities, we adopt $M_V = M_V^{\mathrm{E+A}} + (1.3 \pm 0.73)$, as measured from the scaling relationships.

The "predicted" GCLFs taking into account all possible errors mentioned above are consistent with the observed E+A cluster LFs (Figure 3.16). The most uncertain parameter is the age difference between the clusters in E+As and in E/S0s due to the fast luminosity evolution around 1 Gyr. We use ages of 100 – 500 Myr and 500 – 1000 Myr for EA01A and the other E+As, respectively. We vary f_{MR} between $\frac{1}{3}$ and $\frac{2}{3}$. Most of our observed LFs fall within the uncertainties (shaded regions), indicating that the number of clusters observed does not violate the constraint derived from the GCLFs of the present-day E/S0s. While it is highly uncertain how many clusters in E+As will survive and how much they will contribute to the metal-rich GCs in E/S0s, we conclude that it is at least possible that young star clusters in E+As can evolve into the globular cluster systems of E/S0s.

3.7   Conclusions

We study the detailed morphologies of 21 E+A galaxies using high resolution *HST/ACS* and *WFPC2* images to investigate into what E+A galaxies will evolve after their young stellar populations fade away in a few Gyr. Our findings are:

1. The morphologies of E+As are extremely diverse, ranging across trainwrecks, barred galaxies, and blue-cores to relaxed disky galaxies. Most of these galaxies lie in the field, well outside of rich clusters, and at least 11 (55%) have tidal or other disturbed features. Our sample includes one binary E+A system, in which both E+As are tidally disturbed and interacting with each other. These results support the picture in which galaxy-galaxy tidal interactions or mergers are responsible for triggering the E+A phase in many cases.

2. E+As are bulge-dominated systems (median bulge fraction $B/T = 0.59$) and their light is highly concentrated (Sérsic index $n \gtrsim 5$). When dust is negligible (at

least 67% of the time), E+As have high concentration indices ($C \gtrsim 4.3$) consistent with those of spheroids, but considerably larger asymmetry indices ($A \gtrsim 0.04$) than ellipticals due to structures within a few r_e that presumably arise from the starburst and/or recent merger. Thus E+As would be morphologically classified as early-type galaxies once these disturbances relax and the low surface brightness tidal features dissipate or fade.

3. The color morphologies of E+As are as diverse as their structural morphologies. A large fraction (70%) have positive color gradients (bluer toward center), indicating that their young stellar populations are more concentrated than their older populations. We demonstrate that evolution can invert these gradients into the negative gradients typical of E/S0s if the inner parts of E+As have become more metal enriched than the outer parts due to the centralized star formation.

4. Six E+As (30%) exhibit compact (0.4–1.4 kpc) blue cores, which might be the local analogs of the high-z elliptical blue-cores (Menanteau et al., 2001). We discovered LINERs in three of these blue-core E+As (Yang et al., 2006), and the relationship between LINERs and blue-cores could be an important clue to what stops the star formation in E+A galaxies.

5. E+As stand apart from the E/S0 fundamental plane (FP) in the edge-on projection, implying that the stellar populations of E+As are different from that of E/S0s. E+As have, on average, a *M/L* that is 3.8 times smaller than that of E/S0s. The tilt of the E+A FP indicates that the variation of the stellar populations among E+As is closely tied to their structural parameters, i.e., E+As follow their own scaling relationships such that smaller or less massive galaxies have smaller *M/L*. Such a trend arises naturally within a merger scenario, where low mass galaxies (the progenitors of low-mass E+As) have higher gas fractions (Young & Scoville, 1991) and could produce relatively larger populations of young stars.

6. We find a population of unresolved compact sources in at least nine E+A galaxies (45%). The colors and luminosities of these young star cluster candidates are consistent with the ages inferred from the E+A spectra (0.01 − 1 Gyr). The bright end of the cluster luminosity function fades as the host galaxy becomes redder, suggesting that the newly-formed young star clusters age in parallel to their host. This interpretation is confirmed by the color evolution of the cluster systems.

We have now examined the full set of E+As from the Las Campanas Redshift Survey and so have representative results for local E+A galaxies. We have used high spatial resolution images to probe their detailed morphologies. We find that their properties are either consistent with those of E/S0s or, if left to evolve passively, will become like those of early-types. The morphologies, color profiles, scaling relations, and young star clusters suggest that E+As galaxies are caught in the act of transforming from late-type to early-type galaxies.

Table 3.1.   Properties of E+A Galaxies

ID[a]	R.A. (J2000)	Dec. (J2000)	z[a]	Scale (kpc/″)	$\sigma_{\rm old}$[b] (km s^{-1})	SFR ($M_\odot$ yr^{-1})	H I mass ($10^9\ M_\odot$)	Morphology
EA01A	11 01 19.05	−12 10 17.8	0.07463	1.42	35^{+39}_{-35}	$< 0.12 \pm 0.07$[c]	7.7 ± 0.4[f]	tidal-feature, companion, cluster
EA01B	11 01 18.39	−12 10 14.1	0.07463	1.42	$\cdots$	$< 0.07 \pm 0.03$[c]	$\cdots$	tidal-feature, companion, LINER
EA02	02 17 39.88	−44 32 47.2	0.09873	1.82	202^{+17}_{-16}	< 4.4 [d]	< 3.4[f]	tidal-feature, dust?, cluster
EA03	12 09 5.54	−12 22 35.8	0.08109	1.53	120^{+22}_{-20}	< 1.7 [e]	< 4.2[f]	tidal-feature, cluster
EA04	04 00 0.34	−44 35 15.8	0.10122	1.86	131^{+9}_{-9}	< 3.2 [d]	< 2.3[f]	disturbed, dust?, cluster
EA05	01 58 1.52	−44 37 14.0	0.11731	2.12	120^{+7}_{-8}	$\cdots$	$\cdots$	bar, blue-core
EA06	11 53 55.59	−03 10 36.3	0.08850	1.65	23^{+1}_{-23}	$< 0.10 \pm 0.03$[c]	$\cdots$	dust, blue-core, LINER
EA07	22 41 9.75	−38 34 34.9	0.11413	2.07	241^{+11}_{-12}	$\cdots$	$\cdots$	tidal-feature, dust, cluster
EA08	14 32 3.23	−12 57 33.1	0.11222	2.04	99^{+8}_{-11}	< 1.8 [e]	$\cdots$	tidal-feature, cluster
EA09	01 17 38.28	−41 34 24.6	0.06513	1.25	74^{+134}_{-5}	< 1.3 [e]	$\cdots$	blue-core
EA10	02 11 42.96	−44 07 40.2	0.10493	1.92	121^{+7}_{-8}	$\cdots$	$\cdots$	tidal-feature, companion
EA11	01 14 49.65	−41 22 31.8	0.12167	2.19	174^{+12}_{-11}	< 9.6 [d]	< 5.3[f]	disturbed, companion, cluster
EA12	12 05 59.79	−02 54 32.4	0.09713	1.80	111^{+17}_{-18}	7.9 [e]	$\cdots$	tidal-feature, companion, dust
EA13	11 19 52.44	−12 52 39.6	0.09572	1.77	165^{+10}_{-9}	< 2.1 [e]	$\cdots$	tidal-feature, companion, dust
EA14	13 57 1.68	−12 26 48.2	0.07046	1.34	135^{+10}_{-10}	< 1.5 [e]	$\cdots$	bar, blue-core
EA15	14 40 44.26	−06 39 52.3	0.11381	2.07	125^{+9}_{-10}	$< 0.05 \pm 0.02$[c]	$\cdots$	cluster
EA16	12 19 55.69	−06 14 1.0	0.07642	1.45	93^{+7}_{-8}	$< 0.05 \pm 0.02$[c]	$\cdots$	blue-core, LINER
EA17	10 13 52.40	−02 55 47.2	0.06090	1.18	23^{+1}_{-23}	$< 0.06 \pm 0.03$[c]	< 2.9[g]	dust, blue-core, LINER
EA18	00 22 46.79	−41 33 35.8	0.05985	1.16	23^{+4}_{-23}	< 1.2 [e]	2.0 ± 0.3[g]	disturbed, dust, cluster
EA19	02 07 49.45	−45 20 51.1	0.06400	1.23	84^{+18}_{-34}	2.7 [e]	< 1.2[g]	dust
EA21	11 15 24.96	−06 45 13.8	0.09944	1.84	134^{+7}_{-9}	< 1.7 [e]	$\cdots$	bar

[a] E+A IDs and redshifts from Zabludoff et al. (1996).

[b] Velocity dispersion of the old stellar population from Norton et al. (2001). The entries with $\sigma = 23$ km s^{-1} are the upper limits.

[c] SFR from Hα luminosity (Yang et al., 2006) using the relation, SFR ($M_\odot$ yr^{-1}) = $L_{\rm H\alpha}$ /1.27 $\times$ 10^{41} ergs s^{-1} (Kennicutt, 1998).

[d] SFR from the radio-continuum (Chang et al., 2001) using the relation, SFR ($M_\odot$ yr^{-1}) = 5.9 $\times$ 10^{-22} $L_{\rm 1.4GHz}$ (W Hz^{-1}) (Yun et al., 2001). Corrected for the cosmological parameters adopted in this paper. Note that we do not adopt the SFRs derived from the gas surface densities, which are highly uncertain.

[e] SFR from the radio-continuum (Miller & Owen, 2001). Same as footnote d.

[f] H I mass from Chang et al. (2001). Corrected for the cosmological parameters adopted in this paper.

[g] H I mass from Buyle et al. (2006).

Table 3.2.   Magnitude Transformation

TCOL	SCOL	c_0	c_1	c_2
$B-B_{439}$	$B_{439}-R_{702}$	-0.001	-0.029	-0.033
$B-B_{435}$	$B_{435}-R_{625}$	0.008	-0.048	-0.023
$r-R_{702}$	$B_{439}-R_{702}$	0.496	0.014	0.023
$r-R_{625}$	$B_{435}-R_{625}$	0.406	-0.084	0.016
$B_{435}-R_{625}$	$B_{439}-R_{702}$	-0.107	0.938	-0.033
$B_{435}^{0.1}-R_{625}^{0.1}$	$B_{439}^{0.1}-R_{702}^{0.1}$	-0.030	0.857	-0.009

Table 3.3.   Concentrations and Asymmetries

ID	$r(\eta = 0.2)$	$C(R)$	$A(R)^{[a]}$	m_B	m_R
	(arcsec)			$(r < 2r_p)$	$(r < 2r_p)$
EA01A	6.75 ± 0.06	3.10 ± 0.01	0.17	17.09 ± 0.30	16.77 ± 0.01
EA01B	1.28 ± 0.02	4.28 ± 0.02	0.08	17.44 ± 0.02	16.03 ± 0.01
EA02	3.94 ± 0.05	4.96 ± 0.01	0.09	17.79 ± 0.04	16.24 ± 0.01
EA03	2.35 ± 0.06	5.07 ± 0.02	0.07	16.76 ± 0.05	15.35 ± 0.01
EA04	3.24 ± 0.06	4.81 ± 0.01	0.11	17.36 ± 0.01	15.77 ± 0.01
EA05	1.31 ± 0.18	4.54 ± 0.17	0.05	18.65 ± 0.02	16.99 ± 0.06
EA06	0.52 ± 0.01	3.40 ± 0.03	0.08	18.67 ± 0.01	17.41 ± 0.01
EA07	6.93 ± 0.07	3.94 ± 0.01	0.15	16.91 ± 0.01	15.30 ± 0.01
EA08	2.44 ± 0.05	4.71 ± 0.01	0.05	18.78 ± 0.01	17.27 ± 0.01
EA09	2.56 ± 0.08	4.47 ± 0.01	0.11	19.01 ± 0.01	17.55 ± 0.01
EA10	2.18 ± 0.06	4.57 ± 0.02	0.05	18.39 ± 0.01	16.91 ± 0.01
EA11	1.94 ± 0.11	4.90 ± 0.04	0.07	18.79 ± 0.02	17.22 ± 0.01
EA12	4.33 ± 0.04	4.09 ± 0.01	0.14	18.44 ± 0.01	16.84 ± 0.01
EA13	6.45 ± 0.13	4.74 ± 0.01	0.27	17.62 ± 0.01	16.00 ± 0.01
EA14	0.83 ± 0.03	3.64 ± 0.05	0.03	18.05 ± 0.01	16.69 ± 0.01
EA15	1.67 ± 0.05	4.45 ± 0.02	0.04	19.02 ± 0.01	17.50 ± 0.01
EA16	0.63 ± 0.06	3.84 ± 0.15	0.04	18.47 ± 0.02	17.30 ± 0.04
EA17	2.84 ± 0.05	5.04 ± 0.01	0.08	18.58 ± 0.01	17.16 ± 0.01
EA18	2.92 ± 0.05	3.73 ± 0.01	0.19	17.81 ± 0.01	16.37 ± 0.01
EA19	4.43 ± 0.03	2.95 ± 0.01	0.10	18.06 ± 0.01	16.66 ± 0.01
EA21	1.22 ± 0.17	4.64 ± 0.18	0.04	18.85 ± 0.04	17.26 ± 0.05

[a]Typical errors for A are $\sigma(A)/A \simeq 0.015$.

Table 3.4.   de Vaucouleurs and Sérsic Profile Fit (R_{702} or R_{625} bands)

	$r^{1/4}$-Law					Sérsic $r^{1/n}$-Law					
ID	r_e	μ_e	q [a]	c [a]	χ^2_ν	r_e	μ_e	n	q [a]	c [a]	χ^2_ν
	(kpc)	(mag arcsec^{-2})	(b/a)			(kpc)	(mag arcsec^{-2})		(b/a)		
EA01B	$1.08^{+0.07}_{-0.01}$	$17.86^{+0.12}_{-0.02}$	0.70	-0.04	2.88	$1.35^{+0.40}_{-0.04}$	$18.39^{+0.55}_{-0.05}$	$5.39^{+0.99}_{-0.05}$	0.68	-0.06	2.53
EA02	$2.76^{+0.17}_{-0.01}$	$19.83^{+0.11}_{-0.05}$	0.73	0.15	1.51	$5.85^{+2.01}_{-0.01}$	$21.41^{+0.57}_{-0.35}$	$6.79^{+0.76}_{-0.48}$	0.75	0.34	1.43
EA03	$1.69^{+0.09}_{-0.01}$	$18.32^{+0.10}_{-0.05}$	0.97	-0.04	2.26	$4.99^{+1.03}_{-0.22}$	$20.65^{+0.37}_{-0.22}$	$9.55^{+0.54}_{-0.37}$	0.98	-0.04	1.50
EA04	$2.12^{+0.11}_{-0.01}$	$18.92^{+0.10}_{-0.03}$	0.97	0.01	1.42	$3.07^{+0.37}_{-0.01}$	$19.76^{+0.23}_{-0.11}$	$5.97^{+0.29}_{-0.17}$	0.98	-0.02	1.31
EA05	$1.62^{+0.05}_{-0.01}$	$18.57^{+0.07}_{-0.05}$	0.61	-0.10	1.37	$2.93^{+0.82}_{-0.01}$	$19.91^{+0.51}_{-0.24}$	$7.08^{+0.89}_{-0.41}$	0.62	-0.06	1.30
EA06	$0.43^{+0.01}_{-0.01}$	$17.07^{+0.01}_{-0.04}$	0.86	-0.05	0.70	$0.46^{+0.01}_{-0.01}$	$17.25^{+0.05}_{-0.07}$	$4.60^{+0.12}_{-0.21}$	0.86	-0.05	0.69
EA07	$11.75^{+0.19}_{-0.01}$	$21.27^{+0.02}_{-0.05}$	0.74	0.07	1.27	$7.97^{+0.35}_{-0.01}$	$20.44^{+0.08}_{-0.08}$	$2.72^{+0.11}_{-0.09}$	0.75	0.07	1.12
EA08	$1.84^{+0.05}_{-0.01}$	$19.58^{+0.04}_{-0.02}$	0.89	0.07	0.99	$4.00^{+0.73}_{-0.01}$	$21.25^{+0.32}_{-0.19}$	$7.67^{+0.52}_{-0.36}$	0.89	0.08	0.85
EA09	$2.18^{+0.08}_{-0.01}$	$20.86^{+0.05}_{-0.05}$	0.52	-0.37	1.61	$20.92^{+12.12}_{-0.01}$	$25.58^{+0.86}_{-1.34}$	$15.22^{+1.56}_{-2.55}$	0.52	-0.37	1.39
EA10	$2.22^{+0.03}_{-0.01}$	$19.73^{+0.02}_{-0.05}$	0.81	0.05	0.83	$3.28^{+0.70}_{-0.20}$	$20.57^{+0.41}_{-0.20}$	$5.74^{+1.00}_{-0.31}$	0.81	0.04	0.75
EA11	$1.80^{+0.04}_{-0.01}$	$18.92^{+0.04}_{-0.15}$	0.53	0.14	1.16	$2.88^{+0.44}_{-0.01}$	$19.97^{+0.29}_{-0.15}$	$6.31^{+0.94}_{-0.24}$	0.53	0.13	1.06
EA12	$4.67^{+0.25}_{-0.01}$	$21.47^{+0.07}_{-0.10}$	0.81	1.13	1.29	$9.14^{+2.40}_{-0.33}$	$22.83^{+0.42}_{-0.33}$	$6.33^{+0.56}_{-0.40}$	0.81	1.25	1.22
EA13	$5.72^{+0.28}_{-0.01}$	$20.50^{+0.07}_{-0.07}$	0.55	0.22	0.94	$8.52^{+2.41}_{-0.01}$	$21.35^{+0.47}_{-0.35}$	$5.56^{+0.72}_{-0.48}$	0.54	0.17	0.90
EA14	$1.10^{+0.01}_{-0.01}$	$18.23^{+0.00}_{-0.03}$	0.57	0.18	1.68	$1.44^{+0.01}_{-0.01}$	$18.83^{+0.01}_{-0.11}$	$5.30^{+0.04}_{-0.17}$	0.56	0.20	1.58
EA15	$1.45^{+0.01}_{-0.01}$	$19.23^{+0.00}_{-0.07}$	0.91	-0.07	0.83	$2.38^{+0.09}_{-0.01}$	$20.34^{+0.08}_{-0.30}$	$6.54^{+0.23}_{-0.51}$	0.91	-0.07	0.75
EA16	$0.65^{+0.01}_{-0.01}$	$18.04^{+0.01}_{-0.02}$	0.83	0.05	1.25	$1.71^{+0.13}_{-0.01}$	$20.18^{+0.15}_{-0.31}$	$9.22^{+0.33}_{-0.70}$	0.81	0.07	0.84
EA17	$1.35^{+0.07}_{-0.01}$	$20.02^{+0.08}_{-0.03}$	0.65	-0.13	1.28	$5.16^{+3.89}_{-0.01}$	$22.82^{+1.10}_{-0.50}$	$10.44^{+2.44}_{-0.86}$	0.64	-0.11	0.96
EA18	$3.17^{+0.03}_{-0.01}$	$20.57^{+0.01}_{-0.06}$	0.50	-0.27	1.66	$2.24^{+0.04}_{-0.01}$	$19.76^{+0.04}_{-0.08}$	$2.60^{+0.06}_{-0.09}$	0.49	-0.29	1.42
EA19	$4.98^{+0.18}_{-0.08}$	$21.41^{+0.05}_{-0.08}$	0.43	-0.14	1.65	$3.22^{+0.04}_{-0.01}$	$20.16^{+0.03}_{-0.02}$	$1.06^{+0.03}_{-0.02}$	0.40	-0.10	1.06
EA21	$0.92^{+0.01}_{-0.01}$	$18.20^{+0.02}_{-0.03}$	0.72	0.21	1.28	$2.20^{+0.33}_{-0.01}$	$20.09^{+0.28}_{-0.31}$	$8.35^{+0.60}_{-0.60}$	0.70	0.19	1.04

Note. — EA01A is excluded because it is so irregular.

[a] Typical errors for q and c are ~ 0.01.

Table 3.5.　Bulge-Disk Decomposition (R_{702} and R_{625} bands)

ID	r_e (kpc)	μ_e (mag arcsec^{-2})	q [a] (b/a)	c [a]	r_d (kpc)	μ_d (mag arcsec^{-2})	q [a] (b/a)	c [a]	B/T	χ^2_ν
			$r^{1/4}$-Bulge				Disk			
EA01B	$0.73^{+0.01}_{-0.01}$	$17.35^{+0.01}_{-0.04}$	0.75	−0.06	$2.38^{+0.23}_{-0.07}$	$19.35^{+0.13}_{-0.07}$	0.39	1.21	$0.78^{+0.01}_{-0.03}$	2.40
EA03	$0.71^{+0.01}_{-0.01}$	$16.94^{+0.03}_{-0.04}$	0.93	0.09	$3.60^{+0.17}_{-0.01}$	$19.19^{+0.07}_{-0.17}$	0.88	0.04	$0.54^{+0.01}_{-0.02}$	1.57
EA04	$1.11^{+0.01}_{-0.01}$	$17.93^{+0.02}_{-0.08}$	0.87	0.08	$3.40^{+0.11}_{-0.01}$	$19.30^{+0.06}_{-0.19}$	0.72	0.32	$0.61^{+0.01}_{-0.03}$	1.24
EA05	$1.12^{+0.04}_{-0.01}$	$17.96^{+0.05}_{-0.07}$	0.57	−0.15	$4.35^{+0.98}_{-0.01}$	$20.59^{+0.32}_{-0.30}$	0.77	−0.38	$0.68^{+0.02}_{-0.05}$	1.30
EA06	$0.40^{+0.01}_{-0.01}$	$16.94^{+0.05}_{-0.03}$	0.85	−0.05	$4.82^{+4.05}_{-0.01}$	$22.49^{+0.79}_{-0.22}$	0.55	0.84	$0.85^{+0.04}_{-0.09}$	0.67
EA07 [b]	$11.59^{+0.48}_{-0.01}$	$21.43^{+0.03}_{-0.07}$	0.69	0.17	$3.35^{+0.63}_{-0.01}$	$19.25^{+0.03}_{-0.24}$	0.82	−0.50	$0.85^{+0.02}_{-0.11}$	1.09
EA08	$0.59^{+0.03}_{-0.01}$	$17.93^{+0.08}_{-0.00}$	0.89	−0.03	$2.16^{+0.11}_{-0.01}$	$19.24^{+0.10}_{-0.00}$	0.90	0.25	$0.45^{+0.01}_{-0.01}$	0.82
EA09	$0.06^{+0.01}_{-0.01}$	$15.64^{+0.09}_{-0.04}$	0.98	−0.81	$1.45^{+0.02}_{-0.01}$	$18.71^{+0.02}_{-0.00}$	0.41	−0.21	$0.16^{+0.01}_{-0.01}$	0.84
EA10	$1.16^{+0.05}_{-0.01}$	$18.90^{+0.05}_{-0.56}$	0.85	0.17	$3.13^{+0.18}_{-0.01}$	$19.98^{+0.15}_{-0.66}$	0.68	−0.12	$0.64^{+0.01}_{-0.12}$	0.74
EA11	$1.06^{+0.03}_{-0.01}$	$18.00^{+0.05}_{-0.20}$	0.42	0.47	$3.24^{+0.36}_{-0.01}$	$20.10^{+0.17}_{-0.05}$	0.95	−0.68	$0.61^{+0.01}_{-0.02}$	0.92
EA12 [b]	$1.49^{+0.16}_{-0.01}$	$19.74^{+0.10}_{-0.05}$	0.65	−0.48	$3.88^{+0.56}_{-0.01}$	$19.82^{+0.19}_{-0.03}$	0.69	−0.56	$0.36^{+0.04}_{-0.01}$	1.04
EA13	$1.95^{+0.33}_{-0.01}$	$19.24^{+0.19}_{-0.25}$	0.61	0.10	$5.07^{+0.61}_{-0.01}$	$19.43^{+0.27}_{-0.24}$	0.43	0.07	$0.47^{+0.05}_{-0.05}$	0.83
EA14	$0.75^{+0.01}_{-0.01}$	$17.62^{+0.00}_{-0.03}$	0.55	0.10	$2.93^{+0.05}_{-0.01}$	$19.88^{+0.04}_{-0.07}$	0.40	0.33	$0.71^{+0.01}_{-0.01}$	1.36
EA15	$0.47^{+0.01}_{-0.01}$	$17.68^{+0.01}_{-0.15}$	0.92	0.02	$1.57^{+0.01}_{-0.01}$	$18.76^{+0.01}_{-0.12}$	0.90	−0.11	$0.48^{+0.01}_{-0.02}$	0.73
EA16	$0.34^{+0.01}_{-0.01}$	$17.03^{+0.05}_{-0.02}$	0.81	0.02	$2.21^{+0.09}_{-0.01}$	$20.02^{+0.08}_{-0.05}$	0.81	0.14	$0.57^{+0.01}_{-0.01}$	0.72
EA17	$0.25^{+0.01}_{-0.01}$	$17.48^{+0.02}_{-0.37}$	0.69	−0.15	$1.62^{+0.03}_{-0.01}$	$19.36^{+0.03}_{-0.11}$	0.58	0.06	$0.35^{+0.01}_{-0.03}$	0.78
EA18 [b]	$2.93^{+0.02}_{-0.01}$	$20.59^{+0.00}_{-0.05}$	0.52	−0.30	$0.63^{+0.01}_{-0.01}$	$18.64^{+0.06}_{-0.00}$	1.00	−0.95	$0.91^{+0.01}_{-0.01}$	1.24
EA21	$0.56^{+0.01}_{-0.01}$	$17.41^{+0.03}_{-0.03}$	0.70	0.33	$4.19^{+0.32}_{-0.01}$	$20.60^{+0.10}_{-0.10}$	0.65	−0.23	$0.59^{+0.02}_{-0.02}$	0.93

Note. — EA01A, EA02 and EA19 are excluded from the bulge-disk decomposition because the GALFIT program fit does not converge.

[a] Typical errors for q and c are ~ 0.01.

[b] E+As with unreliable bulge-disk decompositions.

Table 3.6.   Color Gradients

ID	$\frac{d(B-R)}{d\log r}$ (mag dex^{-1})	$\log R_{\rm break}$ (kpc)	$\left.\frac{d(B-R)}{d\log r}\right|_{\rm in}$ (mag dex^{-1})	$\left.\frac{d(B-R)}{d\log r}\right|_{\rm out}$ (mag dex^{-1})	Morphology[a]
EA01B	0.13 ± 0.01	$\cdots$	$\cdots$	$\cdots$	P
EA02	0.00 ± 0.03	0.03 ± 0.03	-0.25 ± 0.04	0.38 ± 0.05	N,D
EA03	0.20 ± 0.01	$\cdots$	$\cdots$	$\cdots$	P
EA04	-0.00 ± 0.01	0.01 ± 0.05	0.07 ± 0.01	-0.20 ± 0.03	N,D
EA05	0.44 ± 0.05	-0.37 ± 0.02	0.95 ± 0.07	0.27 ± 0.02	P,BC
EA06	0.44 ± 0.03	0.13 ± 0.02	0.60 ± 0.02	-0.05 ± 0.05	P,BC,D
EA07	-0.16 ± 0.02	0.28 ± 0.03	-0.46 ± 0.03	-0.02 ± 0.01	N,D
EA08	0.01 ± 0.01	0.62 ± 0.03	-0.04 ± 0.01	0.48 ± 0.11	P
EA09	0.06 ± 0.04	-0.38 ± 0.01	1.02 ± 0.05	-0.18 ± 0.01	P,BC
EA10	0.08 ± 0.01	0.66 ± 0.03	0.06 ± 0.01	0.63 ± 0.09	P
EA11	0.17 ± 0.04	0.13 ± 0.03	-0.09 ± 0.03	0.43 ± 0.03	F
EA12	-0.31 ± 0.05	0.08 ± 0.02	0.34 ± 0.04	-0.68 ± 0.03	N,D
EA13	0.08 ± 0.02	-0.11 ± 0.03	0.33 ± 0.02	-0.02 ± 0.01	F,D
EA14	0.29 ± 0.03	0.13 ± 0.01	0.75 ± 0.02	0.08 ± 0.02	P,BC
EA15	0.12 ± 0.01	$\cdots$	$\cdots$	$\cdots$	P
EA16	0.45 ± 0.02	0.07 ± 0.02	0.63 ± 0.02	0.28 ± 0.02	P,BC
EA17	0.18 ± 0.02	-0.43 ± 0.03	0.72 ± 0.06	0.10 ± 0.01	P,BC,D
EA18	0.06 ± 0.02	-0.15 ± 0.04	0.40 ± 0.04	-0.10 ± 0.02	F,D
EA19	-0.25 ± 0.02	0.46 ± 0.03	-0.37 ± 0.02	0.23 ± 0.06	N,D
EA21	0.09 ± 0.01	0.13 ± 0.09	0.15 ± 0.02	0.04 ± 0.02	F

Note. — Because a single linear fit is not the best representation of most color profiles, the statistical uncertainties are always too small and unrealistic. Therefore, we calculate bootstrap uncertainties.

[a] Morphology of the color profile: N(negative), P(positive), BC(blue-core), F(flat or variable), D(dust)

CHAPTER 4

E+A GALAXIES WITH BLUE CORES: ACTIVE GALAXIES IN TRANSITION

4.1   Introduction

The strong correlation between black hole mass and galaxy bulge velocity disper-
sion ($M_\bullet - \sigma_B$; Ferrarese & Merritt, 2000; Gebhardt et al., 2000) suggests one of two
things. Either early-type galaxies do not arise from dissipative mergers or there is
a connection — perhaps causal — between the small-scale physics of black hole
(BH) growth and the large-scale physics that organizes the host galaxy morphol-
ogy, kinematics, and stellar populations during and after the merger. Given the
observational evidence that gas-rich mergers do occur and that at least some pro-
duce pressure-supported, bulge-dominated remnants, it remains to understand
how the processes that drive the evolution of the smallest and largest galactic
scales are related.

   A key to resolving this question is to identify galaxies undergoing large-scale
transitions via mergers and to consider the properties of their cores. On-going
mergers are too complicated to provide clear answers, while their likely rem-
nants are too far removed from the merger event. E+A galaxies, which have
post-starburst spectra, frequent tidal features, and the kinematic and morpholog-
ical signatures of early type galaxies (Zabludoff et al., 1996; Norton et al., 2001;
Chang et al., 2001; Yang et al., 2004), are true transitional objects and thus plau-
sible test cases. In this *Letter*, we explore whether there is evidence for a central
BH/AGN in nearby E+As, and, if so, whether the core is consistent with those of
early-type galaxies and evolving in concert with the galaxy as a whole.
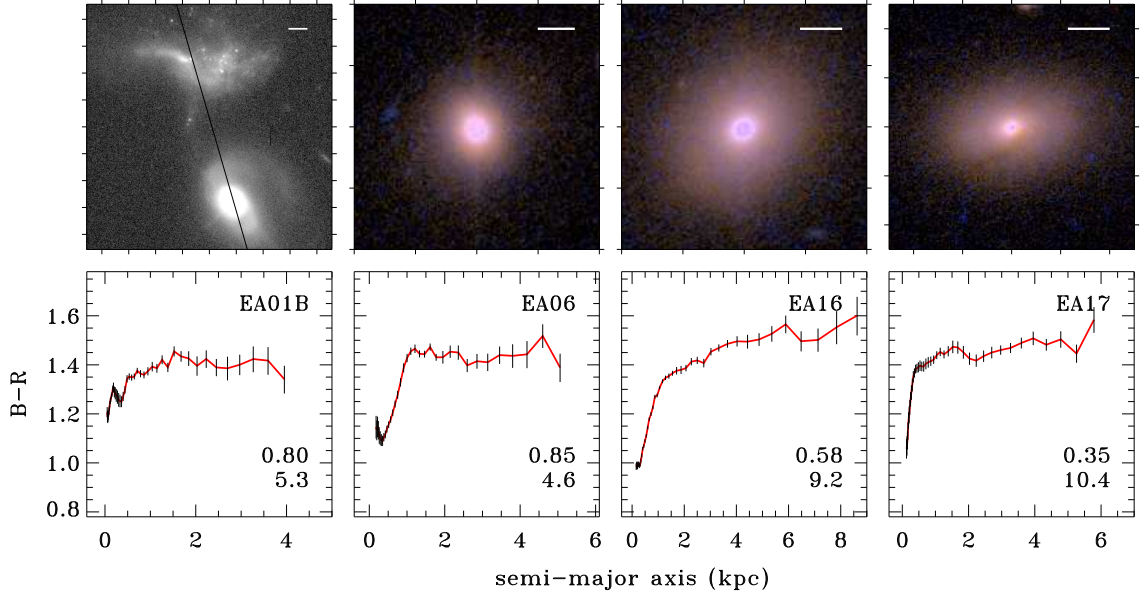
Figure 4.1 — (*Top panels*) Two-color composite images of four E+A galaxies with blue cores. We adopt a color scheme employing the arcsinh stretch from Lupton et al. (2004). We bound each image with 2 arcsec tickmarks and include a 2 kpc horizontal scalebar. The leftmost panel shows the newly-discovered binary E+A system, EA01A (up) and EA01B, the blue-core galaxy (below), with the long-slit orientation. (*Bottom panels*) $(B-R)$ color profiles of four E+A galaxies with blue cores. We note the bulge fractions (bulge-to-total light) and Sérsic indices n (from a single Sérsic $r^{1/n}$ profile fit) derived from the GALFIT algorithm (Peng et al., 2002). The spheroid-dominated morphologies and post-starburst spectra are consistent with these galaxies being in transition from late- to early-types.

4.2 Data: Imaging and Spectroscopy

Our sample is a subset of the 20 nearby ($0.06 < z < 0.12$) E+As (defined to have strong Balmer absorption lines, $\langle H\beta\gamma\delta \rangle > 5.5$ Å, but little or no [O II] emission, EW[O II] < 2.5 Å) in the Las Campanas Redshift Survey (Zabludoff et al., 1996). Initial inspection of our *HST* WFPC2 and ACS B and R images[1] reveals at least

six galaxies with bright, blue, almost stellar-like cores (Yang et al., 2008). In Fig. 4.1, we show the color profiles for three of these galaxies (EA06, EA16, EA17) and for another blue-core galaxy (EA01B) that was observed serendipitously. EA01B is the disturbed companion galaxy of EA01A (originally EA1 in Zabludoff et al., 1996) that we have now determined spectroscopically to lie at the same redshift as EA01A and also to have an E+A spectrum. The EA01A-B system is the first known binary E+A system and provides additional evidence that the E+A phase of galaxy evolution is triggered by galaxy-galaxy interactions. The central blue core of each galaxy has $\Delta(B-R) \simeq 0.3$ with respect to the outer galaxy and a characteristic size of 1 kpc.

With the exception of the blue cores, the morphologies of these galaxies are consistent with elliptical/S0 galaxies (EA01B, EA06, EA16) or early spiral galaxies (EA17).

The blue cores, while too faint to extract independently from models of the underlying galaxy light, raise the possibility of a central AGN (e.g., O'Connell et al., 2005) or of a luminous, compact star cluster (e.g., Colina et al., 2002). We therefore obtained long-slit spectra of the four blue-core E+As (and EA01A) with the Inamori Magellan Areal Camera and Spectrograph (IMACS) on the Magellan Baade 6.5 meter telescope between April 3 and 5, 2005. We used the 300 line mm^{-1} grism and $0.7''$ wide slit, which resulted in a dispersion of 1.34 Å pixel^{-1} and a spectral resolution of ~ 4.2 Å over the wavelength range 4000-8000 Å. We took three 600s or 900s exposures for each galaxy to remove the cosmic rays. The frames were processed and flux-calibrated in the standard manner with IRAF. The following analysis uses one-dimensional spectra extracted from a $0.7'' \times 2.0''$ aperture. No X-ray data are yet available for these sources to help discriminate

---

[1](B, R) corresponds to (F435W, F625W) for the ACS imaging (EA06, EA16, and EA17) and to (F439W, F702W) for the WFPC2 imaging (EA01), respectively.
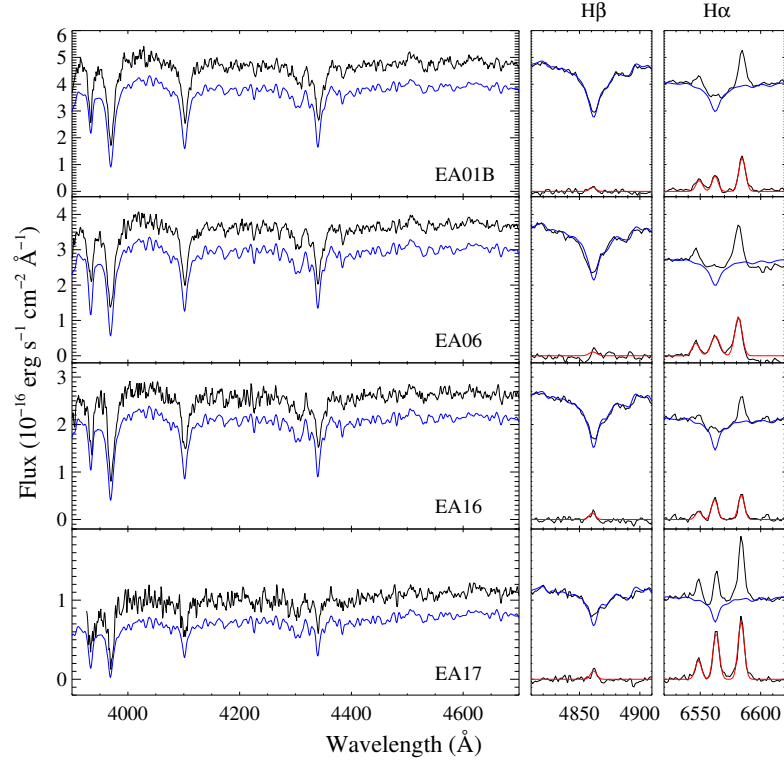
Figure 4.2 — Examples of our continuum and line fits. The leftmost panel shows the data (dark) and the best fit continuum model (light, offset for clarity). The two panels on the right zoom in on the Hβ and Hα lines. The upper lines show the data (dark) and the continuum model (light). The lower lines show the continuum subtracted spectrum (dark) and our fit to the nebular lines (light). All three panels have the same vertical scaling.

between the possible origins of the blue cores.

4.3 Nebular Diagnostics of Nuclear Activity

Optical nebular emission lines provide key diagnostics of the state of the interstellar medium and the source of ionization (AGN or hot stars). Measuring these lines presents a particular challenge in E+As because they are weak (by definition) and superposed on a complex stellar continuum. Conventional continuum subtraction techniques are inadequate, especially for the Balmer emission lines, which can be swallowed by 5 Å or more of stellar absorption. Instead, we fit a stellar population model to the continuum following Tremonti et al. (2006). We use a library of template spectra drawn from the stellar population models of Bruzual & Charlot (2003), which have a spectral resolution of ~ 3 Å. We use templates spanning a range of ages (1, 10, 25, 50, 100, 250, 500, 750 Myr, 1, 1.5, 3, 6, 13 Gyr) and metallicities (0.4 $Z_\odot$, 1 $Z_\odot$, 2.5 $Z_\odot$). To construct the best fitting model, we perform a non-negative least squares fit with dust attenuation modeled as an additional free parameter.

After subtracting the best-fitting stellar population model of the continuum, we fit the nebular emission lines. Because we are interested in recovering very weak nebular features, we adopt a special strategy: we fit all the emission lines with Gaussians simultaneously, requiring that the Balmer lines (Hγ, Hβ, Hα) have the same line width and velocity offset, and likewise for the forbidden lines ([O III] $\lambda\lambda 4959, 5007$, [N II] $\lambda\lambda 6548, 6584$, [S II] $\lambda\lambda 6717, 6731$). This procedure minimizes the number of free parameters and allows the stronger lines to constrain the weaker ones. The measured Hα emission line equivalent widths range from 1 to 5 Å for Hα, and from 0.2 to 1.2 Å for Hβ. Measurements of lines this weak are only possible because of the high S/N of the spectra (10 - 40 per pixel) and our continuum subtraction techniques[2]. We show examples of our continuum and

line fits in Figure 4.2.

To obtain error estimates for the line fluxes that include errors in the continuum subtraction, we adopt a bootstrap approach. For each spectrum, we take the difference between the continuum and the data as a measure of the error. We randomly re-sample the errors in bins of 500 Å, add them to the model of the continuum and nebular lines, and fit the resultant spectrum with our code. We do this 1000 times per galaxy, and use the spread in the measured emission lines as our estimate of the error. The technique does not address possible systematic errors in the stellar population models. Therefore, we perform an identical fitting procedure, substituting the synthetic spectra of González-Delgado et al. (2005) for the empirical ones of Bruzual & Charlot (2003). The resulting differences in line fluxes are small in EA01A, EA01B, and EA17, but exceed the random errors in EA06 and EA16 (see Fig. 4.3).

The weak nebular emission lines extracted from our spectra provide a key AGN diagnostic heretofore unavailable for most E+As. Following Baldwin et al. (1981) and Veilleux & Osterbrock (1987), we plot the flux ratios, [O III] $\lambda5007/$Hβ versus [N II] $\lambda6584/$Hα, in Figure 4.3 (widely referred to as the BPT diagram). For comparison, we plot 254,548 emission line galaxies from the Sloan Digital Sky Survey (SDSS) Data Release 4. The SDSS data form two distinct and remarkably narrow sequences in this plot, the first corresponding to gas ionized by massive, main-sequence stars (the star forming sequence), the second to gas ionized by other means (the Seyfert/LINER sequence). Kewley et al. (2001) theoretically calibrate a limit (dashed curve in Fig. 4.3) above which galaxies cannot be explained by any possible combination of parameters in a standard star forming model. Kauffmann et al. (2003) use SDSS data to empirically calibrate a limit that more

---

[2]The Tremonti et al. (2006) code allows the line amplitudes to be negative or positive, hence there is no overall bias towards detecting lines in emission.

closely adheres to the star forming galaxy locus (solid curve in Fig. 4.3).

Our E+As occupy an interesting part of the BPT plot. EA01A falls squarely on the locus of star forming galaxies, suggesting that there is minor star formation that was undetected previously due to dilution by light from larger radii. In contrast, the other four sources lie well above the star forming locus, even considering the uncertainties. Kauffmann et al. (2003) quantify the position of AGN in the BPT plot using a polar scheme centered at the point where the AGN leave the star forming galaxy locus. Galaxies are characterized by their distance D from the origin and by an angle Φ, which is zero along the positive [O III]/Hβ axis and increases clockwise. Our four blue-core E+As have $D = 1 - 1.1$ and $\Phi = 30°$-$46°$. Kauffmann et al. (2003) classify such galaxies as LINERs.

The nature of LINERs (Heckman, 1980) remains a puzzle. LINERs may be low-luminosity AGN (LLAGN) arising from low-rate or low radiative efficiency accretion onto super-massive black holes (Halpern & Steiner, 1983; Ferland & Netzer, 1983), or they may be the product of other mechanisms (see Filippenko, 2003, and references therein) such as photoionization by young clusters during the Wolf-Rayet phase (Barth & Shields, 2000). For example, a 4 Myr old star cluster was identified as the dominant ionizing source of the LINER nucleus in NGC 4303 (Colina et al., 2002), but subsequent Chandra imaging revealed a hard X-ray point source indicative of an AGN (Jiménez-Bailón et al., 2003). In the nuclei of our E+As, the Balmer absorption lines constrain the mass fraction of < 10 Myr old stars to be less than 0.1%, ruling out a major contribution from young stars.

A more plausible alternative to ionization by an AGN is ionization by planetary nebula nuclei that appear in the late-phase evolution of intermediate mass stars. (Indeed, some LINER galaxies have significant intermediate-age stellar

populations (Cid Fernandes et al., 2004; González Delgado et al., 2004).) However, PNe nuclei are inefficient producers of Hα photons (Taniguchi et al., 2000), and the intermediate age stellar mass required to generate the Hα luminosities of our nuclear spectra (a few $\times 10^{39}$ erg s^{-1}) is large ($\sim 10^9$ M$_\odot$ in the slit aperture). While such large masses are not ruled out, a LLAGN provides a more natural explanation. Indeed, many LINERs have nuclear activity difficult to explain via stellar processes: compact flat-spectrum radio cores or jets, X-ray point sources with power-law spectra, and broad Balmer emission (Ho, 2004, and references therein). Maoz et al. (2005) found that 80% of LINERs with compact UV cores show significant variability, strongly linking LINERs to AGNs. Thus, the LINER spectra in our E+As are *likely* signposts of weak AGN activity, but we acknowledge that intermediate mass stars may provide an alternate or additional source of gas ionization.

4.4   Discussion

Using spectral diagnostics, we discover LINERs in the centers of four E+A galaxies with blue cores. These LINERs have low luminosities similar to those in many nearby early-type galaxies (Ho et al., 1997). The existence of LINERs in E+As, which are typically post-merger, post-starburst, and bulge-dominated galaxies, is more evidence that E+As will evolve into early-type galaxies.

If these LINERs are low-luminosity AGN, *i.e.*, powered by black holes, a more interesting aspect of our discovery is the apparently simultaneous end of star formation and significant BH growth. If we estimate the AGN bolometric luminosity from the [O III] luminosity (Heckman et al., 2004), and the BH mass and associated Eddington luminosity from the $M_\bullet - \sigma_B$ relation (Ferrarese & Merritt, 2000; Gebhardt et al., 2000) and Norton et al.'s (2001) velocity dispersion,

the black holes in these E+A's are currently radiating at only 0.1 - 0.5 % of their theoretical maximum luminosity. Thus any period of strong AGN activity and significant BH growth, as might occur during the gas-rich merger (Sanders et al., 1988), has now ended. The same is true for the star formation: after experiencing a burst within the last Gyr, these galaxies are now forming stars at rates of less than $0.01 - 0.08$ M$_\odot$ yr^{-1} (derived from the measured Hα luminosities assuming SFR (M$_\odot$ yr^{-1}) = $L_{\mathrm{H}\alpha}$/ 1.27×10^{41}ergs s^{-1}; Kennicutt, 1998).

These results have implications for the intersection of the small-scale physics associated with BH evolution and the large-scale physics that determines the properties of the host galaxy's bulge. The coherence of the $M_\bullet - \sigma_B$ relation (Ferrarese & Merritt, 2000; Gebhardt et al., 2000) requires that these small- and large-scale processes are connected, either causally or through a third process, particularly in systems where $M_\bullet$ or σ_B is changing by large factors in a short time. If these LINERs are LLAGNs that represent the end of BH growth, and the E+A phase marks the point at which the galactic bulge, enhanced via the galaxy-galaxy merger and resulting starburst, stops growing, the study of E+As will provide unique insights into the origin of this relation.

If the cores of these E+As do harbor LLAGN, are the AGN really fading? Kauffmann et al. (2003) find that powerful AGNs (Seyferts with large D and $\Phi < 25°$) lie in massive early-type galaxies with young stellar populations, whereas weak AGNs (pure LINERs with large D and $\Phi > 25°$) inhabit normal early-type galaxies. Given that the blue core E+As are evolving from late- to early-type galaxies through the post-starburst phase, it is quite possible that their AGNs are also in transition (or fading) from the strong (Seyfert) to the weak (LINER) AGNs. Finding Seyfert nuclei among the youngest E+As would confirm this conjecture, but our sample is presently too small for this type of search.

Is the apparent relationship between the small-scale (LLAGN-sized) and large-scale (bulge-sized) physics in E+A galaxies causal? Recent numerical simulations including BHs suggest that collisions between galaxies trigger an inflow of gas that causes a strong circumnuclear starburst *and* fuels BH accretion. A powerful quasar outflow removes the gas from the inner region of the merger remnant, quenching the star formation on a relatively short timescale (~1 Gyr; Springel et al., 2005a,b). These models ultimately produce elliptical galaxies within a few Gyr and, unlike past simulations without AGN-feedback (Mihos & Hernquist, 1994, 1996), effectively predict a true E+A phase in which the merger remnant has no lingering star formation. It is possible, though not proved, that the LINERs in our blue core E+As are the relic (fading) AGNs that once caused the truncation of star formation in these post-starburst galaxies. If so, their presence suggests a path by which early-type galaxies arrive on the $M_\bullet - \sigma_B$ relation and also solves the long-standing puzzle of what mechanism during the merger ends the star formation in E+As.

What is the occurrence of LINER spectra in the general post-starburst galaxy population? In recent work, Yan et al. (2006) investigate the emission line properties of a large sample of galaxies drawn from the SDSS. They find that AGN are characterized by large [OII]/Hα EW ratios and conclude that post-starburst samples defined with an [OII] EW cut (such as ours) will be biased against AGN. However, our high S/N spectroscopy reveals that even E+As with negligible emission (1-5 Å at Hα) have line ratios characteristic of AGN. Yan et al. (2006) are able to use the BPT diagram (i.e., our Figure 3) to classify only 40% of their post-starburst sample owing to the weakness of the emission lines. Of the galaxies they can classify, $\sim 90\%$ harbor AGN. They suggest that many of the weaker-lined objects may have LINER-like spectra, which is consistent with our results.

A final puzzle is the nature of the blue cores, which first led us to investigate these galaxies. While our ground-based spectral resolution is not ideal for addressing this question, the low emission line luminosity of our LINERs and the lack of broad emission lines suggest that the blue light is not from an AGN continuum. It may instead arise from a (fading) circumnuclear starburst, which grew in concert with the nuclear activity. Blue cores are common in early-type galaxies at higher redshift ($z \gtrsim 0.5$), when field spheroids were assembling. For example, 30% of the morphologically-selected elliptical galaxies in the Hubble Deep Field North have color inhomogeneities, mostly due to blue cores (Menanteau et al., 2001). Treu et al. (2005) find that $\sim 15\%$ (2/14) of blue-core spheroids in the Great Observatories Origins Deep Survey North (GOODS-N) field have X-ray detections ($L_X > 10^{42}$ ergs s^{-1}), suggesting the presence of AGN. Our blue-core, LINER E+As may be local examples of a phenomenon common at high redshift.

4.5 Conclusions

We identify four E+A galaxies with blue cores, which are revealed by our follow-up spectroscopy to have LINER spectra. The existence of LINERs, similar to those in elliptical galaxies, is more evidence that E+A galaxies, with their post-starburst spectra, post-merger, gas-poor, bulge-dominated morphologies, and pressure-supported kinematics (e.g., Norton et al., 2001; Chang et al., 2001; Yang et al., 2004), evolve into normal early-types. More interestingly, if LINERs are low-luminosity AGN, their presence in E+As suggests that any rapid growth phase of the central AGN has ended in rough concert with the star formation and therefore that the evolution of the black hole is tied to that of the galactic bulge. What is not clear from our work is whether the coupling between AGN and bulge evolution is causal, as is suggested by some theoretical models incorporating AGN

feedback (Springel et al., 2005a,b). The study of a large sample of E+As, including an investigation of any correlation between AGN strength and the time elapsed since the starburst, could provide a test of the AGN-feedback hypothesis, as those models predict that the black hole accretion rate peaks shortly after the starburst and declines quickly as the merger remnant ages.
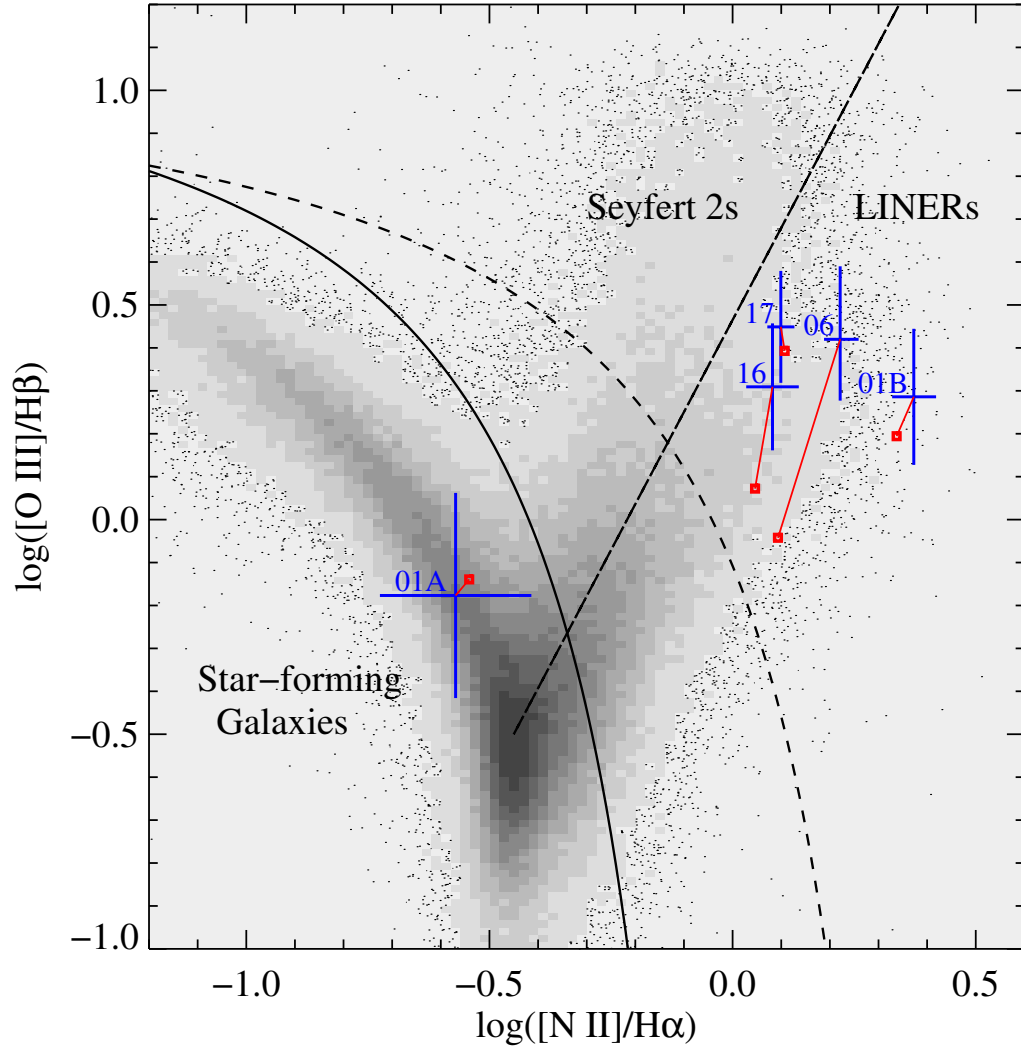
Figure 4.3 — AGN diagnostic diagram. The greyscale shows the locus of SDSS galaxies. The dashed curve is the AGN division theoretically calibrated by Kewley et al. (2001); the solid curve is the empirical division suggested by Kauffmann et al. (2003). The diagonal dashed line denotes $\Phi = 25°$, the Kauffmann et al. division between Seyfert 2s and LINERs. The points with error bars indicate our E+A sample, fit with the Bruzual & Charlot (2003) models. The square points show the effect of fitting the continuum with the models of González-Delgado et al. (2005) and are an indication of the systematic error in the measurements.

CHAPTER 5

PROBING GALAXY FORMATION WITH HE II COOLING LINES

5.1 Introduction

Galaxies grow partly by accretion of gas from the surrounding intergalactic medium and partly by mergers with other galaxies. Observational studies of galaxy assembly have focused primarily on merger rates, which can be measured indirectly by counting close pairs and merger remnants. However, all the mass that enters the galaxy population ultimately does so by accretion — mergers can only redistribute this mass from smaller systems to larger systems. Furthermore, numerical simulations predict that even large galaxies grow primarily by smooth gas accretion rather than by cannibalism of smaller objects (Murali et al., 2002; Kereš et al., 2005). Gas shock-heated to the virial temperature of a typical dark matter halo would radiate most of its acquired gravitational energy in the soft X-ray continuum, making individual sources very difficult to detect, especially at high redshift. However, Fardal et al. (2001, hereafter F01) show that much of the gas that enters galaxies in hydrodynamic cosmological simulations never heats to high temperatures at all, and that it therefore channels a substantial fraction of its cooling radiation into atomic emission lines, especially H I Lyα. F01 and Haiman, Spaans, & Quataert (2000) suggested that extended "Lyα blobs" (e.g., Keel et al., 1999; Steidel et al., 2000; Francis et al., 2001; Matsuda et al., 2004; Dey et al., 2005), with typical sizes of $10 - 20''$ and line luminosities $L_{\mathrm{Ly}\alpha} \sim 10^{44}$ ergs s^{-1}, might be signatures of cooling radiation from forming galaxies. Furlanetto et al. (2005) have also investigated predictions for Lyα cooling radiation from forming galaxies in hydrodynamic simulations.

In this paper, we investigate other aspects of cooling radiation from form-

ing galaxies, in particular the potentially detectable radiation in the He II $\lambda 304$ ("Lyα") and He II $\lambda 1640$ ("Hα") lines of singly ionized helium. While challenging, the successful detection He II line emission would complement H I Lyα measurements in at least three ways. First, because H I and He II line cooling rates peak at different temperatures ($T \sim 10^{4.3}$ K vs. $T \sim 10^5$ K), measurements of both lines could constrain the physical conditions of the emitting gas. Recent theoretical studies imply that "cold mode" accretion, in which the maximum gas temperature is well below the halo virial temperature, is a ubiquitous and fundamental feature of galaxy formation (F01; Katz et al. 2003; Birnboim & Dekel 2003; Kereš et al. 2005; Dekel & Birnboim 2006), a view anticipated by the early analytical work of Binney (1977). Simultaneous measurements of He II and H I emission from different types of galaxies could eventually test detailed predictions for the temperature distribution of cooling gas.

The second advantage of the He II $\lambda 1640$ line is that it should be optically thin, allowing a straightforward interpretation of the observed emission in terms of the spatial distribution and kinematics of the cooling gas. In contrast, the radiative transfer effects on the H I Lyα emission from accreting gas are more complicated, an issue that we will investigate in future work (J. Kollmeier et al., in preparation; see also Cantalupo et al. 2005).

Third, the different temperature dependence and absence of radiative transfer effects in He II lines could help distinguish cooling radiation from alternative explanations of "Lyα blobs," such as emission from collisionally ionized gas in galactic superwinds (Taniguchi & Shioya, 2000) or from gas photoionized by young stellar populations. For example, only the lowest metallicity stars ($\log Z/Z_\odot \lesssim -5.3$) have hard enough spectra to ionize He II to He III , so stellar photoionization will generally not produce He II line emission.

It is possible that He II cooling emission from forming galaxies at high red-shift has already been detected. One such example is the broad He II λ1640 line in the composite spectrum of Lyman break galaxies (LBGs) from Shapley et al. (2003). The composite He II line shows a rather broad line width (FWHM$\sim$ 1500 km s^{-1}), which is a possible signature of Wolf-Rayet stars. However, it is difficult to reproduce the strength of the He II line via stellar population models with reasonable parameters (Shapley et al., 2003). We show in this paper that the He II cooling emission around individual galaxies is detectable, which suggests it might be fruitful to search for He II λ1640 cooling emission in the outer parts of individual LBG's.

The next section describes our simulations and the radiative cooling mechanisms that lead to H I λ1216, He II λ1640, and He II λ304 line emission. We present H I λ1216 and He II λ1640 cooling maps in §5.3.1 and discuss the properties of the cooling radiation sources in §5.3.2. In §5.3.3, we examine the detectability of the three major cooling lines in the far ultraviolet and optical and discuss the best observational strategies. In §5.4, we discuss mechanisms other than gravitational cooling radiation that can generate extended Lyα emission and describe how the He II cooling line might help us discriminate among those mechanisms. We summarize our conclusions in §5.5.

5.2 Simulations and Cooling Radiation

We use Parallel TreeSPH simulations (Davé, Dubinski, & Hernquist, 1997) including the effects of radiative cooling, star formation, thermal feedback, and a spatially uniform metagalactic photoionizing background. We analyze two simulations: one with a cubic volume of $11.111\ h^{-1}$ Mpc (comoving) on a side and a spatial resolution of $1.75\ h^{-1}$ kpc (comoving; equivalent Plummer softening), the

other with a cubic volume of $22.222\ h^{-1}$ Mpc on a side and $3.5\ h^{-1}$ kpc resolution. Hereafter, we refer to these two simulations as the 11 Mpc and 22 Mpc simulations, respectively. The simulations consist of 128^3 dark matter particles and 128^3 gas particles, giving a mass resolution of $m_{\mathrm{SPH}} = 1.3 \times 10^7 M_\odot$ and $m_{\mathrm{dark}} = 10^8 M_\odot$ for the 11 Mpc simulation, and $m_{\mathrm{SPH}} = 1.1 \times 10^8 M_\odot$ and $m_{\mathrm{dark}} = 7.9 \times 10^8 M_\odot$ for the 22 Mpc simulation. We adopt a ΛCDM cosmology with the parameters $\Omega_{\mathrm{M}} = 0.4$, $\Omega_\Lambda = 0.6$, $\Omega_b h^2 = 0.02$, and $H_0 = 65$ km s^{-1} Mpc^{-1}. In our calculation of cooling emission lines, we basically follow the radiative cooling processes described in Katz, Weinberg, & Hernquist (1996, hereafter KWH). Here, we briefly summarize the cooling processes that can contribute to line emission.

The four underlying assumptions of radiative cooling are: primordial composition, ionization equilibrium, an optically thin gas, and a spatially uniform radiation field. In the simulations, we adopt $X = 0.76$ and $Y = 0.24$, where X and Y are the hydrogen and helium abundance by mass. The abundances of each ionic species (H^0, H$^+$, He^0, He$^+$, He^{++}) are solely determined by assuming that the primordial plasma is optically thin and in ionization equilibrium (but not in thermal equilibrium). The functional forms of the temperature-dependent recombination rates, collisional ionization rates, collisional excitation rates, and the rate equations are given in §3 of KWH and the tables therein. The uniform photoionizing UV background is taken from Haardt & Madau (1996).

In the next section, we describe the Lyα and He II cooling curves under the optically thin gas assumption, the assumption used in our simulations. However, in the high density regime, a gas cloud becomes dense enough to shield the central part of itself from the UV background, i.e., becomes self-shielded. Therefore, the actual emissivity of this self-shielded (or condensed phase) gas is highly uncertain. We discuss below how to treat this phase of the IGM to derive
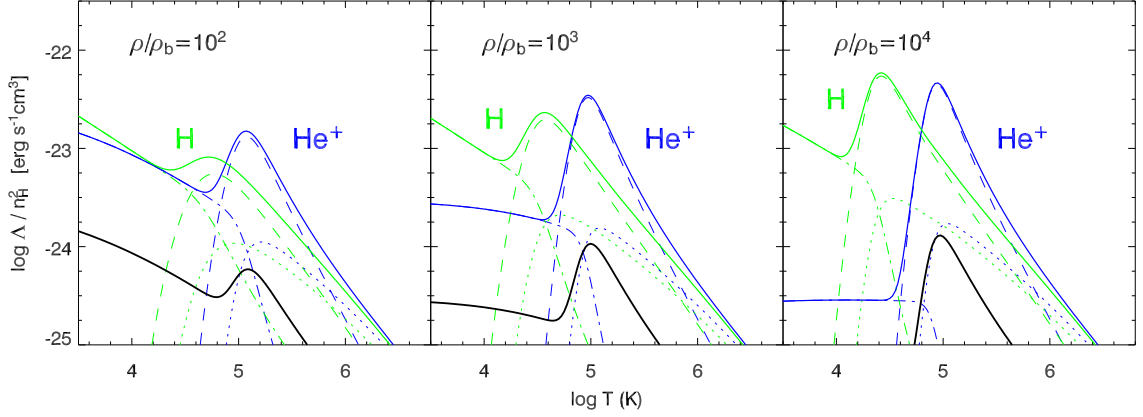
Figure 5.1 — Normalized line emissivity $\log \Lambda / n_{\mathrm{H}}^2$ as a function of temperature for a primordial plasma at densities $\rho / \bar{\rho}_b = 10^2$, 10^3, and 10^4 (*from left to right*) in the presence of a UV ionizing background at $z = 3$. In each panel, the dashed lines represent the collisional excitation cooling rates. The dot-dashed lines and dotted lines denote the recombination rates owing to photoionization and the collisional ionization, respectively. The solid lines represent the total line cooling rates of hydrogen and helium. The bold solid lines below the He II cooling curves represent the He II $\lambda 1640$ line emissivity. Compared with H I, the cooling rates of He II owing to the UV ionizing background become significantly weaker as the gas density increases.

better estimates of the cooling radiation. Once we generate the Lyα and He II cooling emissivities, the cooling radiation is determined by how many gas particles populate a certain range of temperature and density, where we appeal to the high-resolution cosmological simulations mentioned above.

5.2.1 Cooling Curves

Among the various radiative cooling processes, only two can produce H I Lyα (1216Å), He II Lyα (340Å), and He II Balmer α (1640Å) photons: the recombination cascades of a free electron and the collisional excitation of a bound electron to an excited state followed by radiative decay. The dominant cooling mechanism

is the collisional excitation of neutral hydrogen and singly ionized helium, which have their peaks at temperatures of $T \sim 10^{4.3}$ K and $\sim 10^5$ K, respectively. Figure 5.1 shows the H I $\lambda 1216$ and He II $\lambda 304$ emissivities for gas of different densities in ionization equilibrium in the presence of a metagalactic photoionizing background. The dashed lines represent the collisional excitation cooling lines of neutral hydrogen and singly ionized helium. The dot-dashed lines and dotted lines denote the recombination lines for these two species due to photoionization and collisional ionization, respectively. The solid lines represent the total Lyα cooling rates of hydrogen and helium. Below $T \sim 10^4$ K, collisions with free electrons are not energetic enough to raise bound electrons to upper levels or to ionize the neutral hydrogen, so the collisional cooling rate of hydrogen drops quickly below this temperature. For singly ionized helium, the collisional cooling rate drops to virtually zero below $T \sim 10^{4.6}$ K. Therefore, below $T \sim 10^4$ K, photoionization by the background UV spectrum (heating) and the following recombination (cooling) is the dominant source for cooling line emission of the primordial plasma.

In the presence of photoionization, the cooling curve depends on the density as shown in Figure 5.1, because the equilibrium abundances of each species depend on the density. While the collisional ionization rate per unit volume scales as n_{H}^2, the photoionization rate per volume is proportional to only n_{H}. In low density gas ($\rho/\bar{\rho}_b \lesssim 10^2$), a significant fraction of H I and He II is photoionized and their abundances are mainly determined by the photoionization process, so the collisional excitation feature is relatively weak. As the gas density increases ($\rho/\bar{\rho}_b \approx 10^3 - 10^4$), however, collisional excitation becomes more important and the cooling curves approach pure collisional equilibrium, the so-called coronal equilibrium. The notable difference between the cooling curves of hydrogen and singly ionized helium is that the cooling rates of He II owing to photoionization

become significantly weaker as the gas density increases. If we assume that the medium is optically thin to the ionizing background — i.e., not self-shielded — hydrogen is almost fully ionized over the entire temperature range even at high densities, but ∼90% of the helium is in a singly ionized state below $T \sim 10^{4.8}$ K at high densities. Thus the assumption that the gas is optically thin everywhere is roughly valid for the calculation of the He II line fluxes, while it is poor for hydrogen. The correction for the self-shielding of hydrogen will be discussed in the next section.

We estimate the He II $\lambda 1640$ flux from the He II $\lambda 304$ flux by considering the ratio of He II $\lambda 1640$ to He II $\lambda 304$ in the recombination cascades and in the collisional excitations, respectively. The thick solid lines below the He II cooling curves in Figure 5.1 represent our estimate of the He II $\lambda 1640$ line emissivity. Below $T \sim 10^5$ K, the optical depth of He II $\lambda 304$ is so large that case-B recombination is a good approximation. Even though the Lyα optical depth is extremely large, the population of the $2p$ and $2s$ states is always much smaller than that of the $1s$ state, because the de-excitation time for level transitions is very short ($A_{2p1s} \approx 10^{10} s^{-1}$). One might be concerned whether the population of the $2s$ state is large because of the forbidden transition ($2s \rightarrow 1s$), but the two photon decay process is fast enough to de-populate $2s$ electrons ($A_{2s1s} \simeq 8.22 Z^6 s^{-1}$). Therefore, Balmer lines are always optically thin. We adopt $F_{1640}^{\rm rec}/F_{304}^{\rm rec} \simeq 10\%$ by extrapolating the case-B values of Storey & Hummer (1995) to the low density limit. For collisional excitation, we estimate the He II $\lambda 1640$ flux using

$$\frac{F_{1640}^{\rm coll}}{F_{304}^{\rm coll}} \simeq \frac{C_{1s3s} + C_{1s3p} + C_{1s3d}}{C_{1s2p} + C_{1s3s} + C_{1s3d}} \frac{h\nu_{1640}}{h\nu_{304}}, \tag{5.1}$$

where C_{ij} is the collisional excitation rate from the i to the j state. We adopt the C_{ij}'s from Aggarwal et al. (1992). $F_{1640}^{\rm coll}/F_{304}^{\rm coll}$ is roughly $2 - 4\%$ in the temperature range of $10^5 < T < 10^{5.7}$ where He II $\lambda 304$ collisional excitation cooling is

dominant. In summary, the He II $\lambda 1640$ flux is calculated by

$$\varepsilon_{\text{He\,II }\lambda 1640} = f_{\text{rec}} n_e n_{\text{He}^{++}} \alpha_{\text{He}^+}^{\text{rec}} h\nu_{\text{Ly}\alpha} + f_{\text{coll}} n_e n_{\text{He}^+} C_{12} h\nu_{\text{Ly}\alpha}, \qquad (5.2)$$

where $\alpha_{\text{He}^+}^{\text{rec}}$ is the recombination rate into $n \geqslant 2$ states of He II, and by assuming $f_{\text{rec}} \approx 10\%$ and $f_{\text{coll}} \approx 2 - 4\%$.

5.2.2 Self-shielding Correction

A major difference between our work and that of Fardal et al. (2001) is that our simulations include a uniform UV background radiation field (see also Furlanetto et al., 2005). However, because even state-of-art cosmological simulations like ours do not include radiative transfer, the self-shielded phase of the gas at high column densities is not treated properly. When the gas is heated to high temperature ($T \sim 10^5 - 10^6$ K) by falling into the forming galaxy's halo, the gas is mostly ionized, so it is reasonable to assume that the gas is optically thin to the uniform UV background. Subsequently, when the gas cloud starts losing its thermal energy via cooling radiation, its neutral column density becomes sufficiently high that the metagalactic UV radiation cannot penetrate the surrounding gas, and the cloud becomes self-shielded.

Once the supply of ionizing photons is shut off, what happens to the self-shielded high column density clouds? First, the ionization states will achieve collisional ionization equilibrium, where the emissivity is determined solely by collisional ionization and collisional excitation. Second, because the cooling emissivity is boosted by these processes, the self-shielded cloud will cool more rapidly to $T \sim 10^4$ K than in the presence of heating by ionizing photons. Below this temperature, the subsequent cooling is dominated by metal lines (if there are metals). Stars ultimately form from this cold gas.

Because our simulations do not include the time evolution of the self-shielded

gas or metal-line cooling, it is not clear how long the gas particles stay in the self-shielded phase and emit in collisional ionization equilibrium. The Lyα emissivities shown in Figure 5.1 become unreliable in this self-shielded regime. Thus we apply a *pseudo* self-shielding correction to the high density gas particles to correct their emissivities. This correction is not rigorous; to properly calculate the emissivity of the self-shielded phase of the IGM, one should incorporate a radiative transfer calculation that includes non-uniform and anisotropic UV radiation fields. A different prescription for the self-shielded phase is definitely possible. For example, Furlanetto et al. (2005) consider two extreme cases: 1) adopting zero emissivity and 2) using the collisional ionization equilibrium emissivity for the self-shielded phase. Our self-shielding correction scenario described below lies between these two extremes.

To apply the self-shielding correction, we first define the "local" optical depth for each gas particle, $\tau_{\text{local}}(\nu) = \sum_i n_i \sigma_i(\nu) (\alpha l)$, where n_i and σ_i are the number densities and the photoionization cross sections of each species (H^0, He^0, He^+), respectively. The "local" size of the gas cloud l — the length that corresponds to the volume that the gas particle would occupy in space — is defined as $(m_{\text{gas}}/\rho)^{1/3}$. [1] For each gas particle, the UV background spectrum $J(\nu)$ is attenuated using this local optical depth, i.e. $J(\nu)e^{-\tau(\nu)}$, and new photoionization/heating rates and equilibrium number densities are calculated. We then determine a new $\tau_{\text{local}}(\nu)$ from these values and iterate this procedure until the photoionization rates and the optical depths converge. We use these final ioniza-

---

[1]Clumping inside a gas particle and/or among gas particles could be approximated using a free parameter α such that αl represents the effective geometrical edge-to-center distance of the gas cloud. For example, $\alpha_{\text{sphere}} = (3/4\pi)^{1/3}$ is given for a single spherical gas cloud, whereas $\alpha = 2$ corresponds to the clumping of $(\alpha/\alpha_{\text{sphere}})^3 \simeq 34$ gas particles. The value of α should vary from one particle to another, but we adopt $\alpha = 1$ throughout the paper as a fiducial value. The over-density where the self-shielding occurs also depends on the choice of the edge-to-center distance αl (and on the redshift). However, we find that the effects of adopting $\alpha = 0.5 - 2.0$ are insignificant.
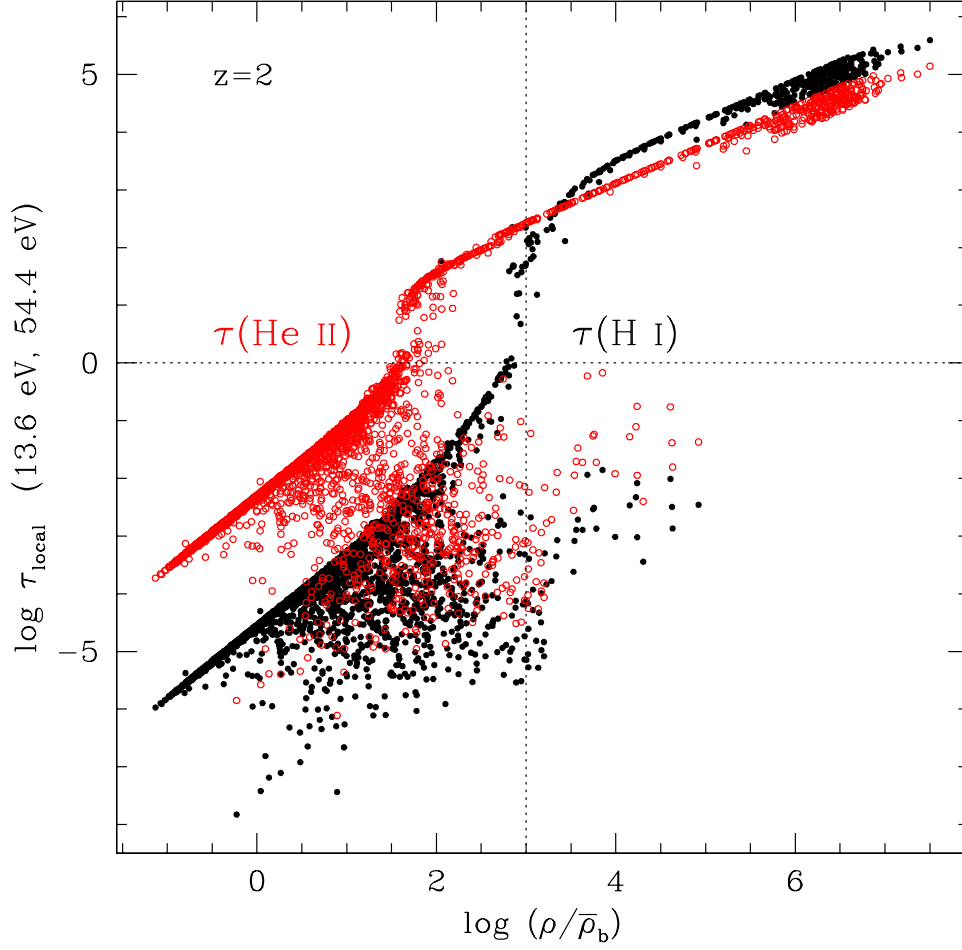
Figure 5.2 — The local optical depth of each gas particle as a function of over-density at $z = 2$. Solid and open circles indicate the optical depth at the H I (13.6 eV) and He II (54.4 eV) ionization edges, respectively. The horizontal and vertical lines represent $\tau = 1$ and $\rho/\bar{\rho}_b \simeq 10^3$, respectively. Note that H I optical depth increases abruptly at $\rho/\bar{\rho}_b \simeq 10^3$ and the gas becomes self-shielded.

tion/heating rates to calculate the Lyα and He II emissivity of each gas particle. This modified emissivity for each gas particle is what we will refer to as the *self-shielding correction case*.

In Figure 5.2, we show the local optical depths of each gas particle in the fi-

nal equilibrium state as a function of over-density. For the 22 Mpc simulation at $z = 2$, we show τ(H I) and τ(He II), the optical depth at the H I (13.6 eV) and He II (54.4 eV) ionization edges, respectively. As indicated by the dotted lines, the H I optical depth increases abruptly from $\tau \simeq 1$ to $\tau = 10 - 100$ at $\rho/\bar{\rho}_b = 10^3$. Therefore, the optically thin UV background assumption is valid below $\rho/\bar{\rho}_b = 10^3$, but the gas becomes self-shielded quickly above this over-density. Because the transition from the optically thin case to the self-shielded phase occurs abruptly, we also consider the emissivity of a *condensed phase cut* case as the most conservative for the cooling radiation. There we set the emissivity of the self-shielded gas particles to zero.

Hence, in the following analyses, we consider three possibilities. First is the *optically thin case* that assumes a spatially uniform UV background for every gas particle. Second is the *self-shielding corrected case* described above that uses an attenuated UV background for each gas particle appropriate for the local optical depth. Third is the *condensed phase cut case* where we set the emissivity of gas with $\log T < 4.5$ and $\rho/\bar{\rho}_b > 10^3$ to zero. We emphasize again that while none of these possibilities are rigorously correct, they range from the most optimistic (1) to the most conservative case (3). Note again that case (1) is appropriate for He II, but the full range of cases should be considered for H I.

5.3   Results

5.3.1   Cooling Maps

We generate H I $\lambda 1216$ and He II $\lambda 1640$ cooling maps at $z = 2$ and 3 by applying our line emissivities to each pixel element and integrating them along the line of sight. The temperature and density of each volume element is computed using the usual SPH smoothing kernels, and the abundances of ionic species are cal-

culated from these smoothed quantities. The thickness of the 11 Mpc simulation along the line of sight is $\Delta z \simeq 0.013$ and 0.019 for $z = 2$ and 3, respectively. We convert these cooling maps into surface brightness maps using our adopted cosmology. Figure 5.3 shows the H I $\lambda 1216$ and He II $\lambda 1640$ cooling maps for the 11 Mpc simulation at $z = 3$. We show the cooling maps for the condensed phase cut case to represent the most conservative prediction. The left panels show a part ($^1/_4 \times {}^1/_4$) of our simulation where the filamentary structure of the IGM — the so-called "cosmic web" — is evident. In the middle panels, we show the brightest region (also the most over-dense region for $z = 3$) at a finer pixel scale ($\sim 1.5 \; h^{-1}$ kpc per pixel; half of the spatial resolution of our simulation). The right panels show the cooling maps convolved with a $0{.}''5$ FWHM Gaussian filter to mimic a typical ground-based observation.

As shown in Figure 5.3, the Lyα cooling emission from the IGM is somewhat extended above a surface brightness threshold of 10^{-18} ergs s^{-1} cm^{-2} arcsec^{-2} (the current limit of ground-based detections), whereas the He II emission will be seen almost as a point source. We will refer to these extended Lyα cooling sources in our simulations as Lyα blobs hereafter. In the cooling maps, we include only Lyα emission from the IGM, not from star formation (i.e. from photoionization caused by massive stars followed by recombination). However, we find a compact group of stars and/or star-forming particles, i.e., galaxies, at the center of each Lyα blob. Therefore, what we would actually observe are galaxies (or Lyα emitters if dust absorption is negligible) embedded within the Lyα blobs.

The most uncertain factor in generating the cooling maps is how much the self-shielded gas contributes to the emission. To quantify this factor globally in the simulations, we consider the H I $\lambda 1216$ and He II $\lambda 1640$ luminosity-weighted temperature and density plots for the optically thin (optimistic) case in Figure
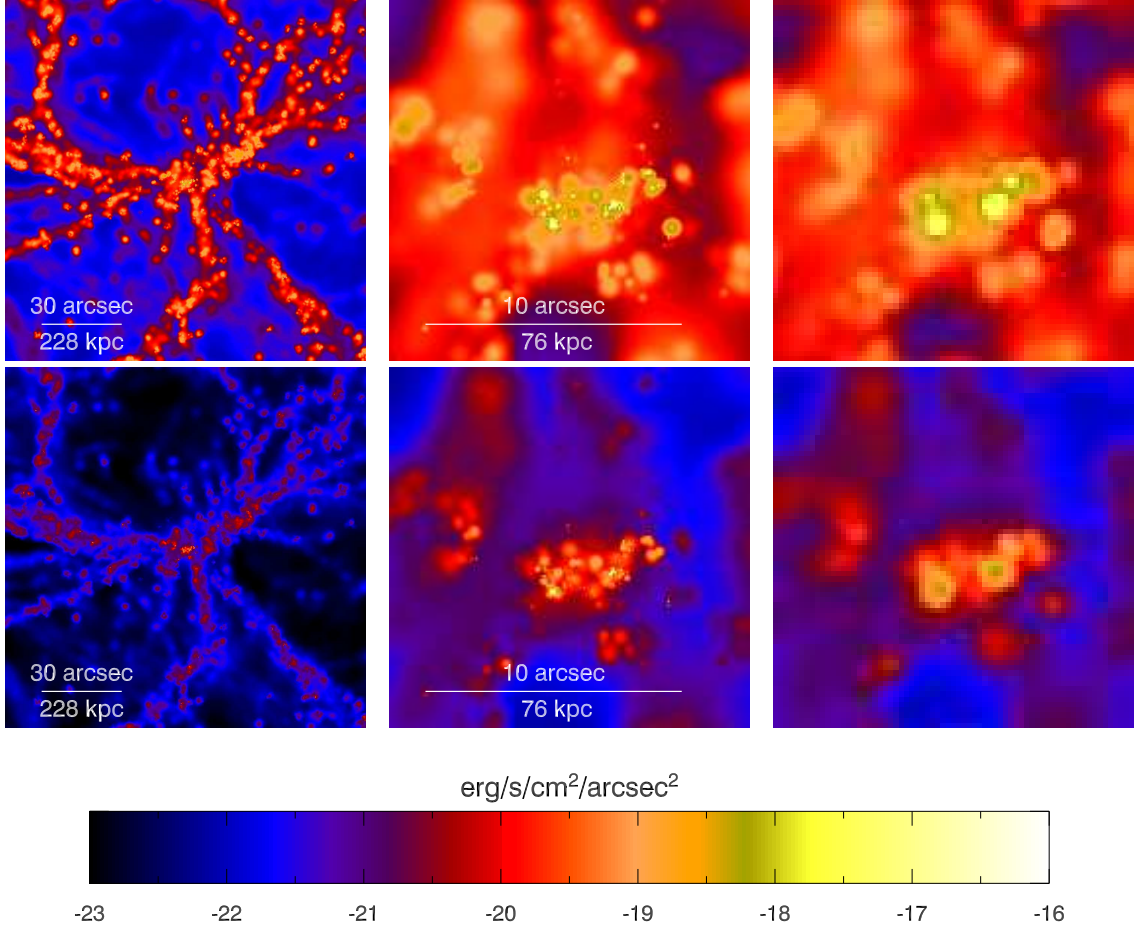
Figure 5.3 — H I $\lambda 1216$ (*top*) and He II $\lambda 1640$ (*bottom*) cooling maps for the 11 Mpc simulation at $z = 3$. The line of sight depth is $\Delta z \simeq 0.019$. The left panels show a part ($^1/_4 \times {}^1/_4$) of our simulation, the middle panels show the brightest region at a finer pixel scale ($\sim 1.5\ h^{-1}$ kpc per pixel), and the right panels show the cooling maps convolved with a $0\rlap{.}''5$ FWHM Gaussian filter to mimic a typical ground-based observation (re-binned to $0\rlap{.}''2$ per pixel). Note that we include Lyα and He II emission from the IGM assuming that the emissivity of the condensed phase is zero, the most conservative case. The Lyα cooling radiation from the gas around the forming galaxies will be observed as a diffuse and extended blob above $\sim 10^{-18}$ ergs s^{-1} cm^{-2} arcsec^{-2}, the current flux limit of ground-based detections ($R = 100$), whereas He II will be almost point source-like at current detection limits.
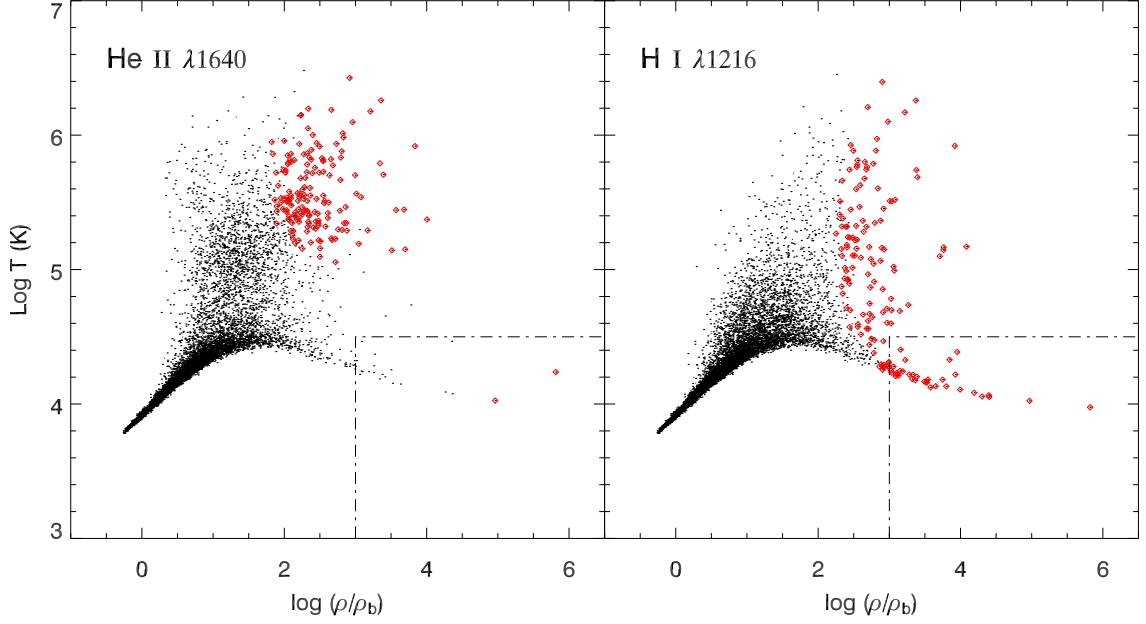
Figure 5.4 — "Luminosity-weighted" phase diagram for 100×100 lines of sight through the simulation at $z = 3$ for He II $\lambda 1640$ (*left*) and H I $\lambda 1216$ (*right*). The diamonds indicate the lines of sight that have He II $\lambda 1640$ or H I $\lambda 1216$ surface brightnesses larger than 10^{-19} ergs s^{-1} cm^{-2} arcsec^{-2}. The condensed phase of the IGM ($T < 10^{4.5}$ and $\rho/\bar{\rho}_b > 10^3$) is represented by the dot-dashed lines. The brightest He II $\lambda 1640$ blobs occupy a specific range of temperature ($10^5 < T < 10^6$) and density ($10^2 < \rho/\bar{\rho}_b < 10^3$), while the brightest H I $\lambda 1216$ blobs tend to come from the high density gas. Thus the H I $\lambda 1216$ cooling map is greatly affected by the condensed phase of the IGM. To be conservative, we thus exclude the condensed phase gas particles in generating the cooling maps (Fig. 5.3).

5.4. To make these phase diagrams, we extract temperature and density profiles for 100×100 evenly-spaced lines of sight, apply our emissivities to each radial bin, and integrate the temperatures and densities with the H I $\lambda 1216$ and He II $\lambda 1640$ luminosities as weighting factors. Thus each diagram represents the phases that we could actually probe by observing each line. In each phase dia-

gram, the condensed phase of the IGM is delineated by dot-dashed lines. The sharp edge of the condensed phase at $T \sim 10^4$ K arises from the lack of metal-line cooling in our simulations. The diamonds in Figure 5.4 indicate the lines of sight that have He II $\lambda1640$ or H I $\lambda1216$ surface brightnesses larger than 10^{-19} ergs s^{-1} cm^{-2} arcsec^{-2}. Most He II $\lambda1640$ emission comes from a specific range of temperature ($10^5 < T < 10^6$) and density ($10^2 < \rho/\bar{\rho}_b < 10^3$) that is remote from the condensed phase, whereas the brightest H I $\lambda1216$ blobs have significant amounts of condensed phase gas. Because self-shielding becomes important in the condensed phase, we exclude this phase in calculating the cooling maps (in Fig. 5.3) to produce our most conservative predictions. As we expected, this cutoff does not affect the He II cooling maps seriously, but does affect the H I $\lambda1216$ cooling map dramatically, as gas particles with $T < 10^{4.5}$ K cannot contribute to He II collisional excitation cooling but only to H I collisional excitation cooling. Therefore, our predictions for the He II $\lambda1640$ cooling radiation are far more robust than for H I $\lambda1216$.

The next factor that could modify the Lyα cooling maps is the radiative transfer of Lyα photons, which could alter the shapes and surface brightness profiles of the blobs substantially. Both the H I $\lambda1216$ and He II $\lambda304$ photons produced in the optically thick medium will be transported to the outer region by resonant scattering until the optical depth becomes smaller than $\tau \sim 2/3$. Lyα photons escape eventually by scattering into the optically thin damping wing in the frequency domain, unless they are extinguished by dust. We expect that the IGM at $z \sim 3$ contains little dust and that the cooling emission from the IGM is sufficiently far from the star-forming regions since we exclude the high density gas particles in our condensed phase cut case. Therefore, the net effect of the resonant scattering in the spatial and frequency domains is to smooth the surface bright-

ness out to the last scattering surfaces. For example, Fardal et al. (2001) resorted to resonant scattering to explain the observed size of the Steidel blobs. However, owing to the complicated structure of the density and to turbulent velocity fields, it is difficult to predict how much radiative transfer blurs the surface brightness of the cooling blob. The large bulk motions will especially affect the transfer of Lyα photons. Depending on the optical depth and velocity field, photons can often undergo very little spatial diffusion and just random walk in velocity space until they reach a frequency where the optical depth is ~ 1 (Zheng & Miralda-Escudé, 2002). A Monte Carlo Lyα radiative transfer calculation would be an ideal tool to make more realistic spatial and frequency maps of Lyα cooling radiation (Zheng & Miralda-Escudé, 2002; Kollmeier et al., 2005). In Figure 5.5, we show the profiles of density, temperature, velocity, and H I and He II emissivity for a line of sight toward a typical Lyα blob to illustrate the complicated structure of these quantities. Because we do *not* take into account these radiative transfer effects in our cooling maps, the H I $\lambda 1216$ cooling map (the upper middle panel in Figure 5.3) should be smoothed to better represent reality. In contrast, because most He II resides in the ground state, making the IGM optically thin to the He II $\lambda 1640$ line, our He II cooling maps should be accurate.

Besides gravitational cooling and photoionization caused by the UV background, supernova feedback is another energy source included in our simulations. When stars form in the simulations, supernova feedback energy is deposited into the surrounding gas in the form of heat. Thermal energy deposited into dense, rapidly cooling gas is quickly radiated away, so feedback contributes somewhat to the cooling emission. However, we find that our density-temperature cutoff for the condensed phase effectively removes all the star-forming gas particles at each time step. Because the supernova thermal input is directly propor-
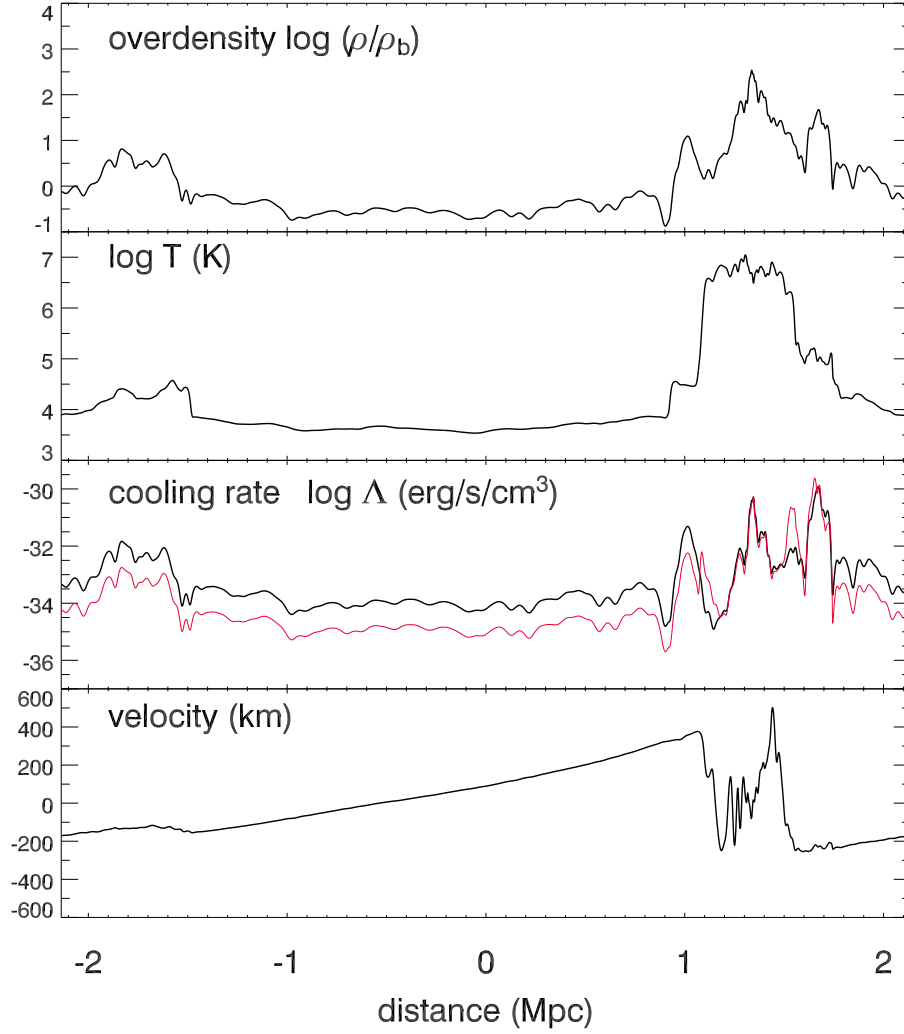
Figure 5.5 — Profiles of density, temperature, H I $\lambda 1216$ (*bold*) and He II $\lambda 1640$ (*light*) cooling rates, and velocity for a line of sight. Owing to the complicated structure of the density and the turbulent velocity fields, it is difficult to predict how much the radiative transfer blurs the surface brightness of Lyα cooling blobs. However, because the IGM is optically thin to He II, our He II cooling maps (Fig. 5.3) should be accurate.

tional to the star formation rate, our cooling maps without the condensed phase should not be seriously contaminated by supernova feedback energy. Thus the cooling maps in Figure 5.3 with the condensed phase removed are still robust lower limits of the flux from the gravitational cooling. Fardal et al. (2001) also show that while the re-radiated supernova energy dominates at lower luminosity, gravitational cooling becomes the dominant source as the mass and luminosity increase.

5.3.2 Properties of Cooling Sources

To study the properties of individual H I $\lambda 1216$ and He II $\lambda 1640$ sources like the ones shown in the cooling maps, we identify discrete groups of gas particles associated with individual dark matter halos and then calculate the total Lyα and He II $\lambda 1640$ luminosities for these sources. To find the dark matter halos, we apply a friends-of-friends algorithm with a linking length that is 0.25 times the mean inter-particle separation. We count a gas particle as a member of the source, i.e. blob, associated with the dark matter halo if the distance from the potential center is less than the virial radius of the halo. We then add the Lyα and He II $\lambda 1640$ luminosities of the particles to obtain the total cooling luminosities of the blob. We restrict our analysis to blobs with more than 64 gas particles and 64 dark matter particles to mitigate numerical resolution effects. Thus the smallest halo in the 22 Mpc simulation has a gas mass of $M_{\mathrm{gas}} = 6.3 \times 10^9 M_\odot$ and dark matter mass of $M_{\mathrm{dark}} = 5.0 \times 10^{10} M_\odot$. These masses decrease to $M_{\mathrm{gas}} = 8.5 \times 10^8 M_\odot$ and $M_{\mathrm{dark}} = 6.8 \times 10^9 M_\odot$ in the 11 Mpc simulation.

H I $\lambda 1216$ and He II $\lambda 1640$ cooling luminosities show tight correlations with halo mass and star formation rate (Fig. 5.6). The open squares, crosses and circles represent the luminosities for the three different emissivities discussed in §5.2.2: the optically thin case, the self-shielding correction case, and the condensed phase

cut cases, respectively. The correlations are as one would expect: the more massive a galaxy is, the more gas accretes onto the galaxy, resulting in more cooling radiation and a higher star formation rate. The distribution of cooling luminosity is continuous, and we do not find any evidence that extended Lyα or He II emission originates only from high-mass systems or high density regions.

The solid line in the upper panel in Figure 5.6 indicates the Lyα emission due to recombination from stellar ionizing photons. We assume a conversion factor of $f_{\mathrm{Ly}\alpha} = 2.44 \times 10^{42}$ ergs s^{-1} for a 1 $M_\odot$ yr^{-1} star formation rate with no dust absorption, no escaping ionizing photons, a Salpeter IMF, and solar metallicity. Under these assumptions the Lyα emission from star formation in galaxies always dominates the Lyα emission from the surrounding IGM, even in the (most optimistic) optically thin case. This result is consistent with the predictions of Fardal et al. (2001) and Furlanetto et al. (2005). [2] The strong correlation between the Lyα cooling rate in the optically thin case (squares) and the star formation rate results from the fact that the gas in the condensed phase tends to satisfy the star formation criteria of the simulation and is likely to form stars in the next time step. In contrast, the He II emission caused by star formation is quite uncertain because only extremely low metallicity ($Z < 10^{-5}$) stars can emit the hard ionizing photons necessary to ionize He II. However, star formation at $z = 2 - 3$ is unlikely to be dominated by Population III or extremely low metallicity stars. Unlike for Lyα, the contribution of star formation to He II must be negligible. We discuss this point in more detail in §5.4.

Figure 5.7 shows the Lyα and He II luminosity functions (LFs) for the three emissivity cases at $z = 2$ and 3. The LFs include emission only from the IGM.

---

[2]In contrast, we do not find the trend of Fardal et al. (2001) in which Lyα from cooling radiation dominates the Lyα from star formation in more massive systems. We suspect that this difference is a consequence of including a photoionizing background in the simulation analyzed here.
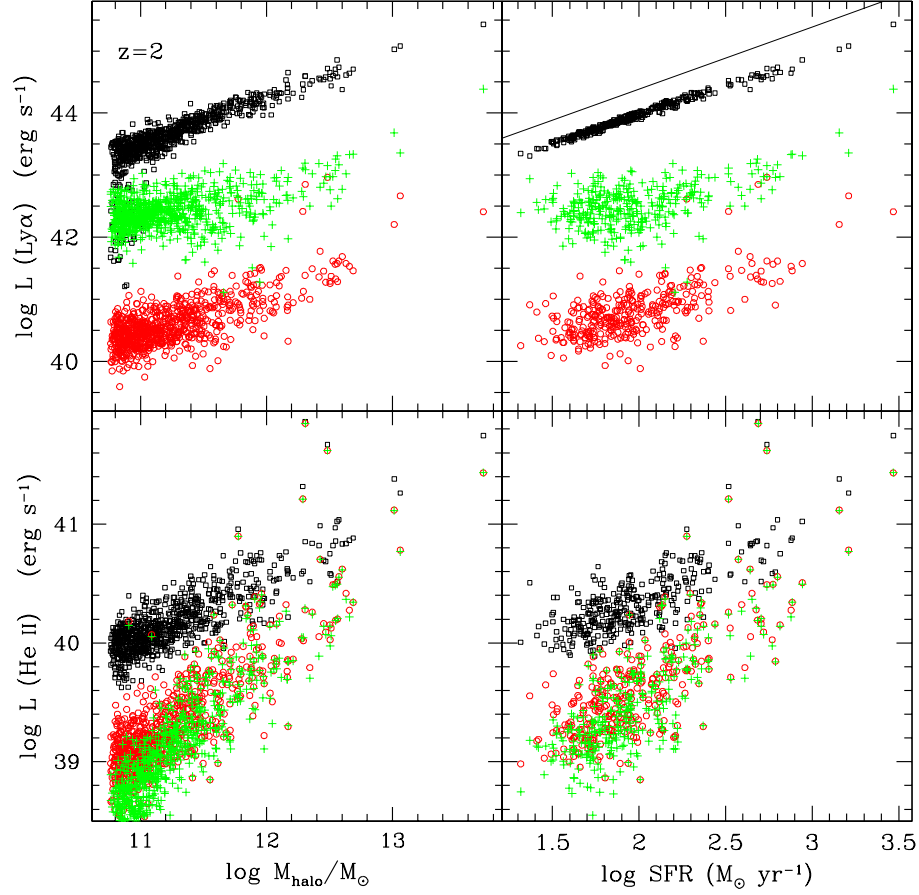
Figure 5.6 — Lyα and He II luminosity as a function of the halo viral mass and the star formation rate in the 22 Mpc simulation at $z = 2$. The open squares, crosses and circles represent the three different emissivity predictions: the optically thin case, the self-shielding correction case, and the condensed phase cut case, respectively. In the right panels, we plot only blobs with a baryonic (star + gas) mass larger than 200 m_{SPH}. Below this mass limit, the derived star formation rates are not reliable owing to our limited resolution. As discussed in the text, Lyα luminosity changes dramatically depending on the prescription used for the self-shielded phase. The correlations between the cooling luminosity, halo mass, and SFR are as one generally expects: the more massive a galaxy is, the more gas accretes onto the galaxy, resulting in more cooling radiation and a higher star formation rate. The solid line in the upper right panel represents the Lyα emission expected from star formation, assuming a conversion factor, $f_{Ly\alpha} = 2.44 \times 10^{42}$ ergs s^{-1}, for a $1 M_\odot$ yr^{-1} star formation rate with no dust absorption, no escaping ionizing photons, a Salpeter IMF, and solar metallicity. Note that under these assumptions the Lyα emission from star formation always dominates the cooling emission from the surrounding IGM.

The solid, dashed, and dot-dashed lines represent the optically thin, the self-shielding correction, and the condensed phase cut cases, respectively. The horizontal dotted lines indicate the number density of one halo in the simulation volume. Note that the distributions extend to brighter blobs as we increase the simulation volume because the larger simulations contain higher mass systems. Note also that the Lyα luminosity function is very sensitive to the assumed emissivities, whereas the He II $\lambda1640$ cooling luminosity depends much less on the treatment of the self-shielded or condensed phase of the IGM. This large variation of the Lyα luminosity is consistent with the results of Furlanetto et al. (2005).

5.3.3 Detectability and Observational Strategy

To estimate the detectability of cooling emission from the extended sources, we convert the rest-frame cooling maps at $z = 2$ and 3 into observed surface brightness maps and rebin them with a pixel scale of $0\farcs5 \times 0\farcs5$ to mimic the independent resolution elements of ground-based observations (Fig. 5.3). Figure 5.8 shows the surface brightness distributions of the rebinned cooling maps at $z = 2$ and 3, assuming the conservative condensed phase cut case. Note that the distributions depend strongly on the size of the bins in the surface brightness maps, because the bright, small-scale structures are smoothed out by binning. We express each surface brightness distribution in terms of the number of binned pixels per co-moving volume and also the number of pixels per square arcmin if one were to observe through a $R = 100$ narrow band filter. The projected angular extents of the 11 Mpc simulation at $z = 2$ and 3 are $11.4'$ and $9.4'$, respectively. The depth of the 11 Mpc simulation is $\Delta z \simeq 0.013$ and 0.019 for $z = 2$ and 3, respectively.

Deep, wide-field ($\sim 30' \times 30'$), narrow-band ($R > 100$) imaging is an effective way to detect cooling radiation, because sky noise dominates in this low surface brightness range. For example, the average sky background at 6500Å on the
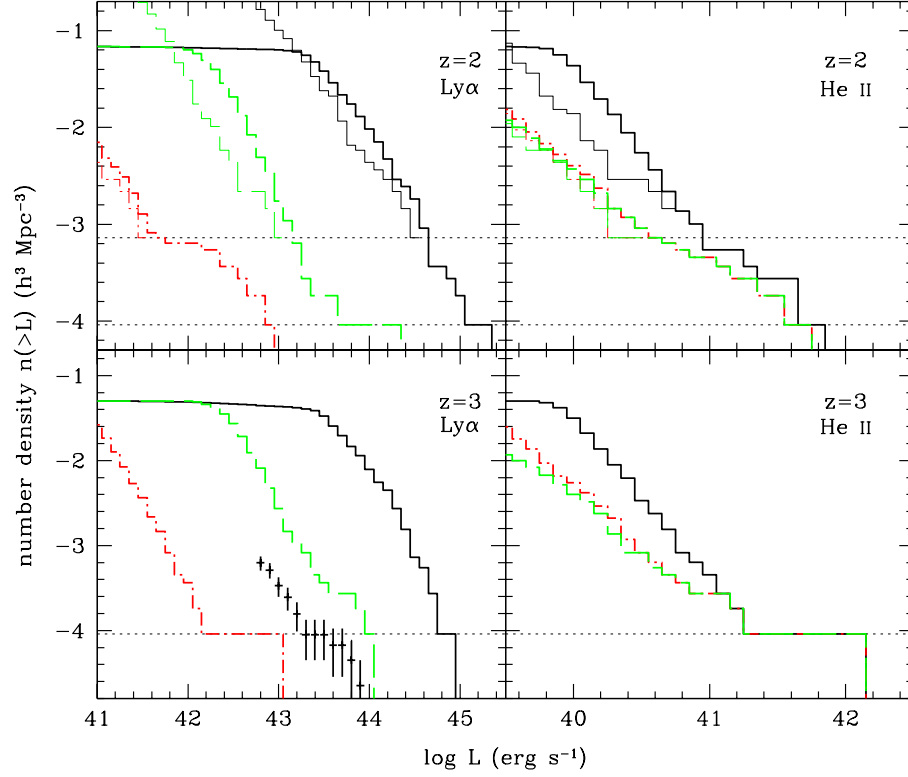
Figure 5.7 — Luminosity functions of Lyα and He II λ1640 cooling radiation at $z = 2$ (*upper*) and 3 (*lower*). The solid, dashed, and dot-dashed lines represent the optically thin, the self-shielding correction, and the condensed phase cut cases, respectively. In the upper panels, for each emissivity case, the LFs from the 11 and 22 Mpc simulations are denoted with light and bold lines, respectively. The horizontal dotted lines indicate the number density of one halo in the 11 Mpc and 22 Mpc simulations. Note that the 22 Mpc results extend to higher luminosity than the 11 Mpc results, and that even the larger simulation may underestimate the density of high luminosity systems. In the lower panels, we show only results from the 22 Mpc simulation. For comparison, we show the LF of the Subaru Lyα blob sample (the crosses; Matsuda et al., 2004). The Subaru Lyα blobs could arise from a variety of mechanisms (see text), including cooling radiation. It is suggestive, however, that their LF lies between our predictions for the self-shielding correction and condensed phase cut cases. Note also that the Lyα LF is very sensitive to the assumed emissivities, whereas the He II λ1640 cooling luminosity depends much less on the treatment of the self-shielded or condensed phase of the IGM.

ground is $\sim 10^{-17}$ ergs s^{-1} cm^{-2} arcsec^{-2} Å^{-1}, comparable to our estimates for the brightest blobs. In Figure 5.8, we show the $5\,\sigma$ detection limits for typical $R = 100$ narrow band imaging with an 8m-class telescope and for $R = 1000$ imaging with a hypothetical 30m telescope. We assume a peak system throughput of $\sim 35\%$, a Mauna Kea sky background (for the 50% dark condition), and a 30-hour exposure time. We estimate the signal-to-noise ratios for one binned pixel ($0''\!.5 \times 0''\!.5$), which corresponds to $\gtrsim 2 \times 2$ instrumental pixels in ground-based CCD detectors.

5.3.3.1 H I λ1216

We predict that H I λ1216 cooling emission from the brightest blobs at $z = 2$ and 3 is detectable by 6-8m class telescopes with moderate resolving power ($R = 100$). The limiting sensitivity of current surveys for high-z Lyα emitters is $\sim 10^{-18}$ ergs s^{-1} cm^{-2} (e.g., Malhotra & Rhoads, 2004, and references therein). It is encouraging that even our most conservative predictions suggest that the Lyα blobs arising from gravitational cooling radiation are detectable with a reasonable amount of telescope time.

The Lyα surface brightness of the largest system in our $z = 3$ simulation ($M_{\mathrm{halo}} \sim 6.5 \times 10^{12} h^{-1} M_{\odot}$), corresponding to the brightest blob in Figure 5.3, is consistent with the *mean* surface brightnesses of the Lyα blobs of the Matsuda et al. (2004) sample (represented with small vertical bars in the Figure 5.8). Note that our predicted Lyα blob luminosities depend on the different emissivities for the self-shielded phase and/or the exact location of our density-temperature cut of the condensed phase. Though the surface brightnesses of the predicted and observed blobs are consistent, the *luminosity* of our brightest Lyα blob is fainter than that of observed blobs (see Fig. 5.7), possibly because of our conservative assumptions for the self-shielded phase.
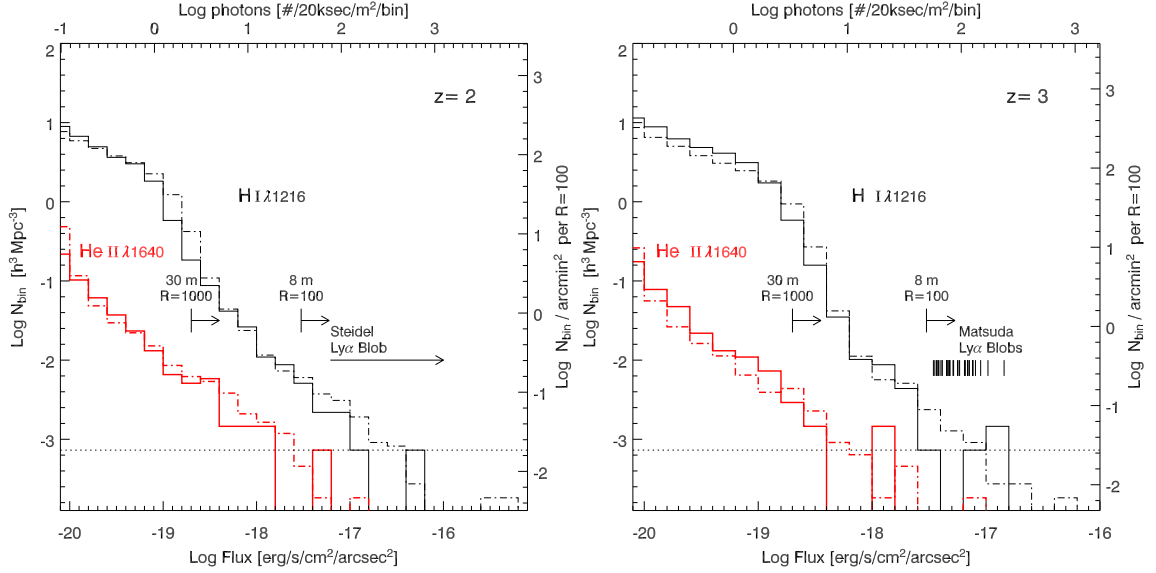
Figure 5.8 — Distributions of surface brightnesses in the cooling maps for the IGM at $z = 2$ and 3. Bold and light solid lines represent the surface brightness histograms of rebinned ($0''\!\!.5 \times 0''\!\!.5$) pixels for He II $\lambda 1640$ and H I $\lambda 1216$, respectively, in the 11 Mpc simulation. We show the $\mathrm{S/N} > 5$ detection limits for a 30-hour observation with an 8-meter telescope and $R = 100$ narrow-band filter, and with a 30-meter telescope and $R = 1000$ filter. The right y-axis represents the number of binned pixels per square arcminute per the redshift width for the $R = 100$ filter. The dotted lines at the bottom of each panel indicate one detection in the simulation. The dot-dashed lines represent the surface brightness distributions for the 22 Mpc simulation. Detection of the brightest H I $\lambda 1216$ and He II $\lambda 1640$ blobs at $z = 2$ and 3 is possible with deep narrow-band imaging on a 6-8 meter class telescope. Note that the larger simulation extends the bright tail of the surface brightness distribution. Even larger simulation volumes might therefore predict still brighter, thus more easily detectable, systems.

5.3.3.2   He II $\lambda 1640$

A pixel-by-pixel comparison of the H I $\lambda 1216$ and He II $\lambda 1640$ cooling maps reveals that, without the condensed phase, the He II $\lambda 1640$ flux is always $\gtrsim$

$10\times$ fainter than that of H I $\lambda1216$. The He II $\lambda1640$ emission could be $1000\times$ fainter than Lyα in the optically thin case, i.e., the most optimistic Lyα prediction. Nonetheless, detection of the He II $\lambda1640$ cooling line from $z = 2$ sources is clearly feasible with 6-8 meter class telescopes, and even possible at $z = 3$. Though the number statistics of bright blobs are limited by the relatively small volume of our simulations, we expect one source in the 11 Mpc simulation and six sources in the 22 Mpc simulation at $z = 2$ with areas of $\gtrsim 0\rlap{.}''5 \times 0\rlap{.}''5$ above the surface brightness detection threshold of $\sim 5 \times 10^{-18}$ ergs s^{-1} cm^{-2} arcsec^{-2} ($R = 100$ arrow in Figure 8). Thus the space density of the sources from which we could detect not only Lyα but also He II $\lambda1640$ emission with narrow band imaging corresponds to a comoving number density of $\sim 5 - 7 \times 10^{-4}$ h^3 Mpc^{-3} or ~ 0.02 arcmin^{-2} per $R = 100$ filter ($\Delta z = 0.03$; $\Delta\lambda \simeq 49$Å for He II $\lambda1640$).

If we consider the larger survey volume typically accessible by modern narrow band imagers, we could expect better survey efficiency than that described above. Because cosmological simulations do not contain power on scales larger than their finite sizes, the largest objects in the simulation are typically underestimated in number and size. For example, the luminosity functions and surface brightness distributions in Figs. 5.7 and 5.8 extend their bright limits as the volume of the simulation increases. Therefore, one might expect that the detection of even brighter blobs by surveying more volume. For example, many current wide-field imagers and spectrographs have half degree field of views, so it is possible to survey a volume ~ 17 times larger than encompassed by our 11 Mpc simulation at $z = 2$ (or a volume $\sim$ twice that of the 22 Mpc simulation). Therefore, if we naïvely extrapolate the number of detectable He II sources in our 11 Mpc and 22 Mpc simulations, then 17 (±17) and 13 (±5) He II sources would be detected, respectively. The numbers within parentheses indicate Poisson errors.

Our results predict that bright He II sources are always bright Lyα cooling blobs. Observationally, the difficulties in searching for He II cooling sources could be eased (1) by pursuing narrow-band Lyα imaging first, detecting Lyα blobs, and looking for He II $\lambda 1640$ emission in those blobs with follow-up observations, or (2) by adopting a combined multislit spectroscopy + narrow-band filter approach (Martin & Sawicki, 2004; Tran et al., 2004) to identify Lyα blobs (which can then be targeted for He II).

The latter technique is potentially quite effective despite the faint surface brightness of the Lyα and He II blobs. This technique employs multiple parallel long slits with a narrow band filter that limits the observed spectral range to a few hundred angstroms and, by dispersing the sky background, achieves better sensitivity than narrow-band imaging alone. In the sense that this technique trades off survey volume (or sky coverage) to go deeper in flux, it is about as efficient as simple narrow band imaging for surveys of Lyα emitters, which are not as extended as Lyα blobs. However, the multi-slit window technique is superior to narrow band imaging for low surface brightness objects like the Lyα and He II blobs discussed here. It has the further advantages that 1) it provides the spectral and kinematic data necessary to distinguish the origins of blob emission (§5.4) and 2) it enables us to exclude contaminating emission lines, such as Hα, Hβ, [O III], and [O II], from nearby star-forming galaxies by measuring the line shapes (e.g. line asymmetries and line doublets) and blueward continuum. If this technique is employed with large field-of-view imagers, the survey volume covered by the multiple slits is still reasonably large ($\sim 10\%$ of the whole field of view).

It is possible to search for He II cooling radiation at lower redshifts than $z \sim 2 - 3$. For example, $z \approx 1.5$ is the lowest redshift at which He II $\lambda 1640$ still lies at an optical wavelength ($\lambda_{obs} \approx 4100$ Å). Because metal abundances in the IGM

do not change very much over $z \sim 2 - 4$ (Schaye et al., 2003), it is unlikely that our basic assumption of a primordial composition (§5.2) is violated seriously at $z \approx 1.5$. Any blind search for He II $\lambda 1640$ blobs at $z = 1.5 - 2$ will be contaminated by H I Lyα emission from $z \approx 3$ sources if only one emission line is identified in the spectrum. In this case, the blob's redshift could be further constrained by obtaining a redshift for the galaxy it surrounds.

He II $\lambda 1640$ cooling radiation at very low redshifts ($z \lesssim 0.5$) is potentially detectable in the ultraviolet using UV satellites or *HST*. For example, Furlanetto et al. (2003) show that detection of the bright cores of H I $\lambda 1216$ emission from $z \lesssim 0.5$ sources is feasible with deep wide-field UV imaging, e.g. with *The Galaxy Evolution Explorer* (GALEX) or the proposed *Space Ultraviolet-Visible Observatory* (SUVO; Shull et al., 1999). Because H I $\lambda 1216$ and He II $\lambda 1640$ trace different phases of the gas, as shown in Figure 5.4, combined observations of these two lines, e.g., of their morphologies and line ratios, would probe different phases of the IGM.

5.3.3.3   He II $\lambda 304$

In contrast to H I $\lambda 1216$ and He II $\lambda 1640$, He II $\lambda 304$ photons redshifted to wavelengths shorter than the photoionization edge of H I and He I (912Å and 504Å, respectively) can be absorbed by neutral hydrogen and neutral helium. Even if they escape the blobs, He II $\lambda 304$ photons are removed from the line of sight owing to cumulative absorption by the intervening neutral IGM, including the Lyα forest and damped Lyα systems. We estimate the transmission of He II $\lambda 304$ through the intervening IGM using Monte Carlo simulations as described in Møller & Jakobsen (1990) with the updated statistics of Lyman forest and Lyman limit systems (i.e., number density evolution and column density distribution) from Jakobsen (1998). For the emitters at $z = 3$, we find that the transmission factor averaged

over all lines of sight is $\sim 12\%$ and that 67% (76%) of the sightlines will have transmission lower than 1% (10%). Therefore, though the He II $\lambda 304$ emissivity is roughly $10\times$ higher than that of He II $\lambda 1640$ (Fig. 5.1 in §5.2.1), we expect the He II $\lambda 304$ cooling map to be fainter than that of He II $\lambda 1640$ in most cases and to vary strongly from sightline to sightline. [3]

He II $\lambda 304$ photons can also be destroyed by the H I and He I inside the blobs, because He II $\lambda 304$ photons experience a large number of scatterings before escaping. The destruction probability by H I and He I atoms per scattering is given by

$$\epsilon = \frac{n_{\mathrm{HI}}\sigma_{\mathrm{HI}} + n_{\mathrm{HeI}}\sigma_{\mathrm{HeI}}}{n_{\mathrm{HI}}\sigma_{\mathrm{HI}} + n_{\mathrm{HeI}}\sigma_{\mathrm{HeI}} + n_{\mathrm{HeII}}\sigma_{\mathrm{Ly\alpha}}}, \tag{5.3}$$

where σ_{HI} and σ_{HeI} are the photoionization cross sections of H I and He I at 304 Å, respectively, and $\sigma_{\mathrm{Ly\alpha}}$ is the integrated scattering cross section of He II $\lambda 304$. The abundances of H I and He I atoms are smaller than for He II, and their photoionization cross sections are also much smaller than the resonant cross section of He II $\lambda 304$ by a factor of $\lesssim 2\times 10^{-5}$. We estimate that the destruction probability is $\epsilon \gtrsim 5 \times 10^{-8}$ at a temperature of $T \sim 10^{4.8}$ without applying the self-shielding correction. In the self-shielded regions where more neutral hydrogen can reside, this probability rises. Thus the escape probability of a He II $\lambda 304$ photon from a blob is $f_{\mathrm{IGM}} \simeq (1 - \epsilon)^{N_\tau}$, where $N_\tau \simeq \tau^2$ is the number of scatterings required to escape the blob, if it is approximated by an optically thick slab. For example, we obtain $f_{\mathrm{IGM}} \simeq 0.7\%$ for $\tau_{\mathrm{HeII}} = 10^4$. Therefore, we cannot ignore the absorption by H I and He I atoms in the high density gas. However, the number of scatterings N_τ is very difficult to estimate correctly because of the complex density and velocity structure of the blob, unless one carries out full 3-D hydro-radiative transfer calculations (which are beyond the scope of this paper). For certain ge-

---

[3]If one sightline does not have any Lyman limit or damped Lyα systems, it will have $\sim$87% transmission on average due only to Lyman forest systems.

ometries and velocity fields, bulk motions of the gas will help the He II $\lambda 304$ photons escape the blob with fewer scatterings (e.g., Zheng & Miralda-Escudé, 2002).

Owing to intervening absorption and the destruction inside the blobs, He II $\lambda 304$ is the most uncertain cooling line we consider. Although He II $\lambda 304$ is diminished significantly by the intervening IGM, if the escape fraction from the IGM is significant ($f_{\rm IGM} \simeq 1$), the detection of He II $\lambda 304$ may not be out of question with a large aperture UV/optical optimized space telescope (e.g., SUVO; Shull et al., 1999). An advantage of observing He II $\lambda 304$ in the far ultraviolet in space is that the sky background is very low ($\sim 10^{-23}$ ergs s^{-1} cm^{-2} arcsec^{-2} Å^{-1} at 1250 Å) compared to the optical ($\sim 10^{-18}$ ergs s^{-1} cm^{-2} arcsec^{-2} Å^{-1} at 6500 Å), except for the geocoronal emission lines (e.g., Lyα 1216 Å and O I 1304 Å). Thus, if these geocoronal emission lines could be eliminated with blocking filters or by adopting an L2 orbit, the direct detection of He II $\lambda 304$ is feasible. In this case, the detector noise — especially the dark current — will dominate. Recent developments in UV detector technology are very promising, so the possibility of studying these blobs at those wavelengths remains open.

5.4 Discussion

Until now, we have only considered the cooling radiation from gas that is losing its gravitational energy, falling into a galaxy-sized dark halo, and ultimately forming stars. Photoionization by these stars is another possible heating source for the blobs. Starburst-driven superwinds or AGNs, which are not included in our simulations, are other potential blob energy sources (e.g., see the discussions in Steidel et al., 2000; Matsuda et al., 2004). Although the radiation from gas heated by these feedback processes is not generally termed "cooling radia-

tion", the energy injected into the surrounding gas can also be released through line emission. Thus our estimates for cooling emission might be lower limits for the actual fluxes in the cooling lines. In this section, we assess whether other H I $\lambda1216$ and He II $\lambda1640$ sources overwhelm our gravitational cooling signals and then discuss how to discriminate among these other possible mechanisms in order to use H I $\lambda1216$ and He II $\lambda1640$ cooling lines to study gas infall into galaxies.

5.4.1   Photoionization by Stellar Populations

UV photons from massive stars in a galaxy or blob ionize the surrounding interstellar medium, and the recombination lines from these nebulae could contribute to the Lyα and He II line fluxes. Generally, the recombination line luminosity is proportional to the star formation rate (SFR) and is given by

$$L_{\text{line}} = e^{-\tau_{\text{dust}}} (1 - f_{\text{esc}}) f_{\text{IGM}} f_{\text{line}} \left(\frac{\text{SFR}}{M_\odot \text{yr}^{-1}} \right), \qquad (5.4)$$

where τ_{dust} is the dust optical depth for the ionizing continuum in the interstellar medium (ISM), f_{esc} is the fraction of ionizing photons that escape the star-forming galaxy, f_{IGM} is the fraction of photons that escape the surrounding IGM, and f_{line} is the conversion factor from the SFR to the line luminosity in ergs s^{-1}. This SFR conversion factor depends on the metallicity, initial mass function (IMF), and evolutionary history of the stars in the blobs (e.g., a lower metallicity and a top heavy IMF produce more ionizing photons and thus more recombination line photons).

[4]

---

[4]Note that the equation (5.4) does *not* take into account the dust absorption of Lyα photons by ISM after Lyα photons escape from the H II region. When the H I optical depth in the ISM is high enough, Lyα photons will experience a large number of resonant scatterings before escaping the galaxy. These scatterings will increase the effective dust optical depth and destroy Lyα photons preferentially. However, the actual optical depth is likely to strongly depend on the kinematics of neutral gas and the geometry of the galaxy, which are hard to quantify.

The conversion factor for H I $\lambda 1216$, f_{1216}, is large enough to make it difficult to distinguish the cooling lines (of IGM origin) from the recombination-induced lines (of ISM origin). For example, Schaerer (2003) finds $f_{1216} = 2.44 \times 10^{42}$ ergs s^{-1} for a constant star formation history, solar metallicity, and a Salpeter IMF with a mass range of $1 - 100\ M_\odot$. Thus for a SFR $= 10\ M_\odot$ yr^{-1}, $f_{\rm esc} \simeq 0.1$, $e^{-\tau_{\rm dust}} \simeq 0.1$, and $f_{\rm IGM} \simeq 1$, we obtain the observed flux, $F_{1216} \simeq 2.9 \times 10^{-17}$ ergs cm^{-2} s^{-1}, due to the stars in a Lyα blob at $z = 3$, which is comparable to the surface brightness of the brightest blobs in our simulations (see §5.3.3 for the blob luminosity functions). Therefore, the contamination of the H I $\lambda 1216$ line by stars is not negligible, unless the Lyα photons from star-forming regions are heavily absorbed by a dusty ISM (e.g., in highly obscured sub-millimeter galaxies or Lyman break galaxies with the damped Lyα absorption). Because Lyα cooling radiation is produced sufficiently far from the star-forming region and thus should be less susceptible to dust attenuation than the Lyα emission from the stellar populations, it might be possible to isolate extended Lyα cooling radiation in these galaxies. However, in the case that Lyα photons emitted by stars escape the galaxy (e.g., Lyα emitters), it will be challenging to distinguish the Lyα cooling radiation from the Lyα produced by the stellar populations unless the various parameters such as $f_{\rm esc}$, $f_{\rm IGM}$, and SFR are fully constrained.

In contrast, He II $\lambda 1640$ emission appears to be limited to very small metallicities ($\log(Z/Z_\odot) \lesssim -5.3$) and Population III objects, because stars of solar or subsolar metallicities emit few if any He II ionizing photons (Bromm, Kudritzki, & Loeb, 2001; Schaerer, 2003; Tumlinson, Shull, & Venkatesan, 2003). Using He II $\lambda 1640$ to detect the first hard-ionizing sources such as metal-free stellar populations, the first miniquasars, or even stellar populations before the reionization epoch has been proposed (e.g., Tumlinson, Giroux, & Shull, 2001; Oh, Haiman,

& Rees, 2001; Barton et al., 2004). In this paper, we take advantage of this fact to discount the contributions of stellar populations to the He II $\lambda 1640$ cooling line. Even for $Z = 10^{-5}$, $f_{1640} = 1.82 \times 10^{40}$ ergs s^{-1} ($\simeq 6 \times 10^{-4} f_{1216}$) for an extremely top heavy IMF containing only stars in the range $50 - 500\ M_\odot$. For the same assumptions used in the Lyα calculation above, we obtain an observed flux of $F_{1640} \simeq 2.2 \times 10^{-19}$ ergs cm^{-2} s^{-1} from the blob stars at $z = 3$, an order of magnitude below the brightest He II $\lambda 1640$ blobs in our simulations. Therefore, it is very unlikely that the He II $\lambda 1640$ photons originating from stars contaminate the gravitational cooling emission, unless significant numbers of metal-free stellar populations are forming. Thus He II $\lambda 1640$ cooling radiation is much less contaminated than H I $\lambda 1216$ by recombination lines originating from star-forming galaxies.

The only caveat is the possibility of He II $\lambda 1640$ emission arising not from stars directly, but from the hot, dense stellar winds of Wolf-Rayet (W-R) stars, the descendants of O stars with masses of $M > 20 - 30\ M_\odot$. W-R populations formed in an instantaneous starburst at high redshifts would not seriously contaminate the He II $\lambda 1640$ cooling radiation, because W-R stars are very short-lived ($\lesssim 3$ Myr) and their number relative to O stars (W-R/O) drops as the metallicity decreases below solar. In the case of continuous star formation, a stellar population synthesis model (Starburst99; Leitherer et al., 1999) predicts that the maximum number of W-R stars is reached ~ 10 Myr after the initial burst. Using the He II $\lambda 1640$ luminosity of a W-R star (Schaerer & Vacca, 1998) and the number evolution of W-R stars from Starburst99 under the assumptions of a Salpeter IMF ($1 - 100\ M_\odot$), sub-solar metallicity ($Z \leqslant 0.4 Z_\odot$), and a massive SFR of 100 $M_\odot$ yr^{-1} over at least 10 Myr, we estimate the He II $\lambda 1640$ line luminosity due to W-R stellar winds to be $\lesssim 10^{42}$ ergs s^{-1}. Although this He II $\lambda 1640$ luminosity is comparable to the pre-
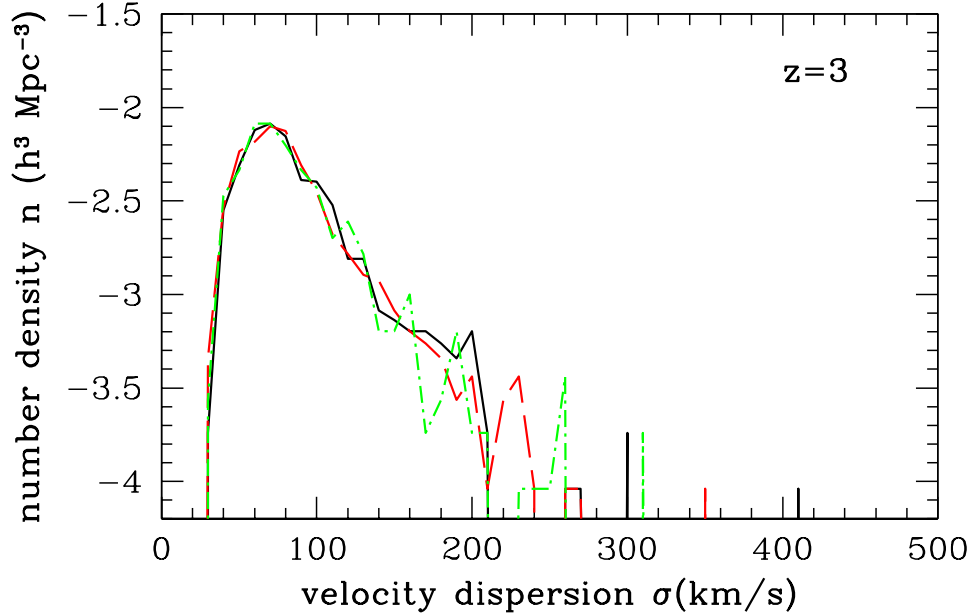
Figure 5.9 — Distribution of He II $\lambda1640$ flux-weighted velocity dispersion of the gas particles associated with individual dark matter halos. The different lines represent the velocity dispersions in the x, y, and z directions. Note that the velocity dispersion due to gas accretion is less than 400 km s^{-1}, in contrast to the typical galactic wind speed of $\sim$ 400-800 km s^{-1} (Heckman et al., 2000). Thus the width of the optically thin He II $\lambda1640$ line could be used as a diagnostic to discriminate between the galactic wind and the gravitational cooling hypotheses for powering Lyα blobs.

dicted He II cooling radiation, it is possible to discriminate between the two He II $\lambda1640$ sources in individual objects because the emission from W-R winds should be much broader (e.g. $\sim$ 1000 km s^{-1}; see Fig. 5.9 in §5.4.3, which is relevant here even though it is presented in the context of the galactic superwind scenario).

One way to test our predictions in this section is to look more closely at the He II $\lambda1640$ emission associated with high redshift star-forming galaxies, i.e., the Lyman break galaxies (LBGs) with vigorous star formation rates. Shapley

et al. (2003) show that composite spectra of LBGs have very broad (FWHM $\sim$ 1500 km s^{-1}) He II $\lambda 1640$ profiles regardless of their Lyα emission strength. While they attribute the He II features to W-R stellar winds, those authors have difficulty reproducing the strength of the He II lines using stellar population synthesis models with reasonable parameters. Because of this inconsistency, we speculate that some fraction of the He II features may come from the cooling of gas falling into these galaxies along line of sight. It would be worthwhile to obtain high signal-to-noise spectra of individual LBG's and their surroundings to see if the He II line is present, especially outside the galaxy, and relatively narrow.

5.4.2 Photoionization by AGNs

AGNs inside the star-forming regions of blobs could photoionize the surrounding gas and generate He II $\lambda 1640$ as well as H I $\lambda 1216$ emission. The predicted size (a few arcseconds) and surface brightness ($\sim 10^{-18} - 10^{-16}$ ergs s^{-1} cm^{-2} arcsec^{-2}) of an extended Lyα blob enshrouding a quasar are consistent with the observed quantities (Haiman & Rees, 2001).

How many AGN-powered sources might we expect in a Lyα/He II blob survey? Unfortunately, it appears that there is no easy way to predict Lyα/He II luminosity from the surrounding IGM, because we do not know how much neutral IGM is distributed around the AGN. Therefore we take a conservative approach to estimate the number of the AGN-powered sources. First, we establish a simplistic relationship between the induced Lyα (or He II) blob luminosity and the X-ray luminosity of the AGN, then we estimate the number of AGN-powered blobs based on the known hard X-ray luminosity function of AGN at $z = 2 - 3$. If there are not many relative to the number of blobs powered by gravitational cooling radiation, then we could conclude that they are unlikely to complicate the interpretation of extended Lyα/He II sources.

We assume that all the ionizing photons from an AGN with a simple power-law spectrum, $L_\nu = L_0(\nu/\nu_0)^\alpha$, are absorbed by the surrounding medium and re-emitted as recombination lines. The line (Lyα or He II) luminosity of the surrounding blob is then given by:

$$L_{\text{line}} = c_{\text{line}}Q = c_{\text{line}} \int_{\nu_{LL}}^{\infty} \frac{L_0}{h\nu} \left(\frac{\nu}{\nu_0}\right)^\alpha, \tag{5.5}$$

where Q is the number of ionizing photons emitted per unit time, ν_{LL} is the frequency of the Lyman limits for the hydrogen and He II ($h\nu_{LL} = 13.6$ eV and 54.4 eV, respectively), and the line emission coefficient c_{line} in ergs is the energy of the line photon emitted for each H I or He II ionizing photon. For case-B recombination with an electron temperature of $T_e = 30,000$K and an electron number density of $n_e = 100$ cm^{-3}, we obtain $c_{1216} = 1.04 \times 10^{-11}$ and $c_{1640} = 5.67 \times 10^{-12}$ ergs (c.f. Schaerer, 2003). We adopt a spectral index $\alpha = -1.8$ for the extreme UV (Telfer et al., 2002) and assume that this α is valid even in the X-ray. The hard X-ray luminosity of AGN (L_X) is simply given by the integration of L_ν between 2 keV and 8 keV.

Once the Lyα (or He II) luminosity is monotonically linked with the AGN X-ray luminosity, we estimate the number density of AGN-powered sources from the hard X-ray luminosity function (e.g., Barger et al., 2003; Cowie et al., 2003). To power a blob with $L_{\text{Ly}\alpha} = 10^{43}$ ergs s^{-1}, an AGN must have $L_X \gtrsim 10^{41.8}$ ergs s^{-1}, which would generate a He II blob with $L_{\text{He II}} \gtrsim 10^{41.7}$ ergs s^{-1}. Around the required X-ray luminosity, Cowie et al. (2003) derive the number density of X-ray selected AGNs regardless of their optical AGN signatures to be $1.3 \times 10^{-5} \lesssim \Phi(L_X > 10^{42} \text{ ergs s}^{-1}) \ll 1.4 \times 10^{-4} \text{ Mpc}^{-3}$ at $2 < z < 4$. The extreme upper limit was determined by assigning all the unidentified sources in the survey to $2 < z < 4$ and is thus very conservative. For the brightest cooling sources in our simulations (Fig. 5.7), we find $\Phi(L_{\text{Ly}\alpha} \gtrsim 10^{43}) \sim 3 \times 10^{-5} \text{ Mpc}^{-3}$ and $\sim 9 \times 10^{-4}$

Mpc^{-3} for the condensed phase cut and the self-shielding correction cases, respectively. [5] Note again that our assumption that all the ionizing photons from all AGNs are absorbed to produce Lyα/He II photons is very conservative and that we are clearly over-predicting the number of AGN-powered blobs. However, even under this conservative assumption the number density of AGN-powered sources is only marginally comparable to the number density of cooling sources in our simulations. Therefore, at present, we conclude simply that a survey for extended Lyα and He II cooling radiation is not likely to be swamped by AGN-powered sources.

The above arguments are statistical, whereas distinguishing gravitational cooling radiation from the emission of AGN-photoionized gas for an *individual* source requires a multi-wavelength approach. It is therefore useful to target fields with a large amount of ancillary data (e.g., deep broad-band or X-ray imaging) to make an unambiguous detection of a true He II cooling blob. First, searching for the C IV (1549 Å) emission line in the optical spectrum of the source is a good way to identify an AGN (e.g., Keel et al., 1999). The composite spectra of optically selected quasars show bright C IV lines, but much fainter He II lines (Telfer et al., 2002). The recently discovered Lyα blob associated with a luminous mid-infrared source (Dey et al., 2005) shows unusually strong He II $\lambda1640$ lines *and* C IV lines in a localized region near the center of nebula, suggesting that this Lyα blob is powered, at least in part, by an obscured AGN. On the other hand, the absence of a C IV line in a spectrum with strong He II emission might indicate gravitational cooling gas like that in our simulations. As we discuss in the next section, the kinematics of the He II line can further constrain the origin of the He II emission. Second, if the AGN is heavily obscured, deep X-ray imaging of $\sim$ Msec will pro-

---

[5]The number density of Lyα blobs (of unknown origin(s)) from the Subaru survey (Matsuda et al., 2004) lies between these two cases.

vide the most direct probe, because X-rays from the AGN can penetrate the large column densities of gas and dust.

5.4.3 Superwinds

Alternatively, Taniguchi & Shioya (2000) suggest that galactic superwinds driven by starbursts could power the extended Lyα blobs. In this scenario, the collective kinetic energy of multiple supernovae is deposited into the surrounding gas, producing a super-bubble filled with hot and high-pressure gas. If the mechanical energy overcomes the gravitational potential of the galaxies, this metal-enriched gas blows out into the surrounding primordial IGM and evolves into superwinds.

While the luminosity and sizes of the observed blobs are roughly consistent with the predictions of simple wind models, the mechanism to convert the mechanical energy into Lyα emission is not clear. Using a fast-shock model, Francis et al. (2001) show that if the shocks are radiative, the emission from the excited gas in the shock itself and the photoionized precursor region in front of the shock can explain the observed Lyα surface brightness of the blobs. For example, if we adopt the fiducial model of the pre-run shock grids from Allen et al. (2004) (MAPPINGS code by Dopita & Sutherland, 1996) with a shock velocity of $700 \mathrm{\ km \ s^{-1}}$, a number density of $10^{-2} \mathrm{\ cm^{-3}}$, a magnetic parameter of $B/\sqrt{n} = 2\mu\mathrm{G \ cm^{3/2}}$, and solar metallicity, then the Lyα and He II $\lambda1640$ emissivity from the shock + precursor region will be ~ 0.04 and $0.002 \mathrm{\ ergs \ s^{-1} \ cm^{-2}}$, respectively. If the shock is perpendicular to our line of sight, we would expect surface brightnesses of $F_{\mathrm{Ly}\alpha} \sim 3 \times 10^{-18}$ and $F_{\mathrm{He II}} \sim 1.5 \times 10^{-19} \mathrm{\ ergs \ s^{-1} \ cm^{-2} \ arcsec^{-2}}$ at $z = 3$. This Lyα surface brightness is roughly consistent with the observed mean surface brightness of Lyα blobs (Matsuda et al., 2004), but is an underestimate if we consider that Lyα emission can be suppressed by various factors such as self-absorption and that the density of the IGM is possibly lower than the assumed density. If

the IGM in the preshock region is composed of neutral primordial gas, the UV photons produced in the post-shock plasma will ionize the preshock region, and the lack of an effective cooling mechanism other than the atomic hydrogen and helium lines can boost the Lyα and He II $\lambda1640$ line emissivities significantly. However, the low metallicity shock grid is not currently available, and the density of the IGM in the preshock region and the effect of mixing between the metal-enriched winds and the pristine IGM are quite uncertain. Thus it is difficult to predict how much mechanical energy is released through the Lyα or He II $\lambda1640$ lines in the superwind model.

One important feature of the superwind shock model is that it also predicts many UV diagnostic lines (e.g., C IV $\lambda1549$) that have been used to study the energetics of the narrow-line region in AGNs. The debate about the origin of the Lyα blobs arises mainly because Lyα is not a good diagnostic line to discriminate between AGN photoionization and superwind shock-excitation owing to its sensitivity to resonant scattering and obscuration by dust. Ideally, line ratios (e.g., He II/C IV, once detected) could be used to discriminate among the different mechanisms.

The kinematics of the blob is potentially another test of the superwind hypothesis, because of the expected bipolar outflow motion of the expanding shell. For example, Ohyama et al. (2003) claim that Blob 1 of Steidel et al. (2000) shows both blueshifted and redshifted components ($\sim \pm3000$ km s^{-1}) in the central region, and they attribute these profiles to the expanding bipolar motion of a shocked shell driven by a superwind. On the other hand, using integral field spectrograph data, Bower et al. (2004) argue that Blob 1 has chaotic velocity structures that can be explained by the interaction of slowly rising buoyant material with cooling gas in the cluster potential, and that a powerful collimated outflow alone

appears inconsistent with the lack of velocity shear across the blob.

We show the He II $\lambda 1640$ luminosity-weighted velocity dispersions of the gas particles associated with individual blobs in Figure 5.9. The effect of Hubble expansion and peculiar motion is included in the velocity dispersion calculations but the thermal broadening for each gas particle is not. Most halos have velocity dispersions smaller than ~ 400 km s^{-1}, compared to the typical superwind speed of several hundreds to a 1000 km s^{-1} (e.g., Heckman et al., 2000; Pettini et al., 2001). For the superwind case, because the observed Lyα emission comes mainly from the shock between the outflow from a galaxy and the surrounding pristine IGM, we expect the He II emission to be as extended as the observed Lyα emission. Therefore, if we observe a spatially resolved Lyα *and* He II emitting blob, and its velocity dispersion is larger than 400 km s^{-1}, it is possible to exclude cooling radiation as the source of that blob. Note that there would be no ambiguities in measuring the size and line broadening because He II $\lambda 1640$ is optically thin. Thus He II $\lambda 1640$ is a finer tool than H I $\lambda 1216$ to study the kinematic properties of Lyα blobs.

5.5 Conclusions

In this paper, we use high resolution cosmological simulations to study the gravitational cooling lines arising from gas accreted by forming galaxies. Because baryons must radiate thermal energy to join a galaxy and form stars, accreting gas produces extended H I $\lambda 1216$ emission (a "Lyα blob") surrounding the galaxy. We also expect cooling lines from singly ionized helium such as He II $\lambda 1640$ to be present within Lyα blobs. We investigate whether three major atomic cooling lines, H I $\lambda 1216$, He II $\lambda 1640$, and He II $\lambda 304$ are observable in the FUV and optical. We discuss the best observational strategies to search for cooling sources

and how to distinguish them from other possible mechanisms for producing Lyα blobs. Our principal findings are:

1. H I $\lambda 1216$ and He II $\lambda 1640$ (He II Balmer α) cooling emission at $z = 2 - 3$ are potentially detectable with deep narrow band imaging and/or spectroscopy from the ground. He II $\lambda 304$ will be unreachable until a large aperture UV space telescope (e.g. SUVO; Shull et al., 1999) is available.

2. While our predictions for the strength of the H I $\lambda 1216$ emission line depend strongly on how to handle the self-shielded gas, our predictions for the He II $\lambda 1640$ line are rather robust owing to the negligible emissivity of He II for the self-shielded IGM below $T \sim 10^{4.5}$ K.

3. Although He II $\lambda 1640$ cooling emission is fainter than Lyα by at least a factor of 10 and, unlike Lyα blobs, might not be resolved spatially with current observational facilities, it is more suitable to study gas accretion in the galaxy formation process because it is optically thin, less sensitive to the UV background, and less contaminated by recombination lines from star-forming galaxies.

4. To use the H I $\lambda 1216$ and He II $\lambda 1640$ cooling lines to constrain galaxy formation models, we first need to exclude the other possible mechanisms for producing Lyα blobs. First, because He II $\lambda 1640$ emission from stars is limited to stars with very low metallicities ($\log(Z/Z_{\odot}) \lesssim -5.3$) and Population III objects, its detection, unlike Lyα, cannot be caused by stellar populations. Second, the kinematics of the He II $\lambda 1640$ line can distinguish gravitational cooling radiation from a scenario in which starburst-driven superwinds power Lyα blobs, because the He II line width from cooling gas is narrower ($\sigma < 400 \, \mathrm{kms}^{-1}$) than the typical wind speeds (which are factors of several higher). Third, if some fraction of the He II emitting blobs are powered by AGN, additional diagnostics such as the C IV line and/or X-ray emission can be used to discriminate gravitationally cooling

blobs from those powered, at least in part, by AGN.

CHAPTER 6

EXTENDED LYα NEBULAE AT $z \simeq 2.3$:

AN EXTREMELY RARE AND STRONGLY CLUSTERED POPULATION?

6.1   Introduction

The recent discovery of extended Lyα nebulae, the so-called Lyα blobs, may ultimately provide clues to how galaxies formed in early Universe ($z \sim 2 - 5$). The most luminous Lyα blobs have been discovered mostly by deep narrow-band imaging surveys and have typical sizes of $\sim 10''$ (~ 100 kpc) and Lyα luminosities of $\sim 10^{44}$ ergs s^{-1} (e.g., Keel et al., 1999; Steidel et al., 2000; Francis et al., 2001; Palunas et al., 2004; Dey et al., 2005; Smith & Jarvis, 2007). However, what powers the blobs and what they will evolve into remains a mystery. To begin to answer these questions, we need first to constrain their basic properties, including how common they are, how they are spatially distributed, and how diverse their possible power sources may be.

Despite intense interest, these characteristics, for even the brightest Lyα blobs, are poorly constrained due to the absence of an appropriate sample. Giant, luminous blobs (Steidel et al., 2000) appear to be rare (Saito et al., 2006) at $z = 3 - 5$, so an efficient, large-volume survey is required to detect any. Furthermore, the survey must be blind to be representative of blob statistics and must include ancillary data (in the X-ray, other optical bands, etc.) to better constrain possible sources of blob emission. To date most Lyα blobs have been discovered by targeting two previously known over-dense regions (Steidel et al., 2000; Francis et al., 2001; Palunas et al., 2004; Matsuda et al., 2004). Matsuda et al. (2004) discovered 33 additional Lyα blobs in the proto-cluster region at $z = 3.1$ where the two giant Steidel et al. blobs reside, and spectroscopic follow-up confirms that the

blobs are located in three filamentary structures traced by compact Lyα-emitting galaxies (Matsuda et al., 2005). Palunas et al. (2004) report that four Lyα blobs are associated with an over-dense region of Lyα emitters around the galaxy cluster J2142-4420 at $z = 2.38$. The first and only study of the environment of a Lyα blob found without any prior knowledge of its surroundings (Dey et al., 2005) shows it to lie in a $3\times$ over-dense region traced by Lyα-emitting galaxies (Prescott et al., 2008). Although these results suggest that bright Lyα blobs occupy higher density regions, we still lack an unbiased, statistical measurement of how frequent and clustered they truly are.

The origin of the blobs' Lyα emission is similarly murky. Proposed mechanisms include gravitational cooling radiation from accreting gas (Haiman, Spaans, & Quataert, 2000; Fardal et al., 2001), galactic superwinds driven by a starburst (Taniguchi & Shioya, 2000), photo-ionization by extended star formation (Matsuda et al., 2007), and a hidden AGN (Haiman & Rees, 2001). Smith & Jarvis (2007) report the discovery of a giant Lyα blob that appears to have cooling origin, while others suggest that blobs are experiencing outflows (Wilman et al., 2005) or are static (Verhamme et al., 2006). It is also not clear what central sources the blobs harbor, e.g., what fraction of those central sources contain AGN? These ambiguities arise from the optically-thick nature of the Lyα line (cf. Yang et al., 2006), which clouds the interpretation of the blob kinematics, and from the lack of multi-wavelength data, which, were it available for a representative blob sample, could reveal the nature of any central sources.

To obtain a unbiased sample of bright Lyα blobs ideal for determining their properties and, ultimately, for resolving the origin of their extended emission, we are conducting a blind, wide-field, narrow-band imaging survey for the brightest ($L_{\mathrm{Ly}\alpha} \gtrsim 10^{44}$ ergs s^{-1}) and most extended ($A_{iso} \gtrsim 50\,\square''$) objects, similar to those

originally found by Steidel et al. (2000). To date, only five such blobs have been discovered among several surveys (Steidel et al., 2000; Francis et al., 2001; Dey et al., 2005; Smith & Jarvis, 2007). We select the NOAO Deep Wide Field Survey (NDWFS) Boötes and Cetus fields (Jannuzi & Dey, 1999), as well as the Cosmic Evolution Survey (COSMOS) field (Scoville et al., 2007) as our targets, given the complementary, multi-wavelength data available for these fields. We choose $z = 2.3$ as our survey redshift so that the optically thin Hα $\lambda6563$ emission line from the surrounding gas falls in a relatively clean region of the *NIR* sky spectrum. The comparison between Hα and Lyα, as well as analysis of other lines including [O II] $\lambda3727$, [O III] $\lambda5007$, and C IV, will enable us in future papers to study the kinematics of the surrounding gas in more detail (Dijkstra et al., 2006) and to better constrain the nature of any central sources.

In this paper, we present the initial results from our Lyα blob survey in the NOAO Deep Wide Field Survey (NDWFS) Boötes field. In §6.2, we describe our narrow-band imaging survey design, observations, and selection of Lyα blob candidates. In §6.3, we present the first results from the survey and its spectroscopic follow-up. We also discuss the number density and environment of the Lyα blobs in comparison with previous studies. In §6.4, we summarize the results. Throughout this paper, we adopt cosmological parameters: $H_0 = 70\,h_{70}\,\mathrm{km\,s^{-1}\,Mpc^{-1}}$, $\Omega_{\mathrm{M}} = 0.3$, and $\Omega_{\Lambda} = 0.7$. All magnitudes are in the AB system (Oke, 1974).

6.2 Observations

6.2.1 Survey Design

Using the 90Prime one-degree field imager (Williams et al., 2004) mounted on the Steward Observatory Bok 2.3m telescope on Kitt Peak, we carry out our narrow-band imaging survey with a custom narrow-band filter (hereafter *NB* 403 or *NB*

). This narrow-band filter has a central wavelength of $\lambda_c \approx 4030\text{Å}$, designed for selecting Lyα-emitting sources at $z \approx 2.3$, and a band-width of $\Delta\lambda_{\mathrm{FWHM}} \approx 45\text{Å}$ that provides a line of sight depth of $\Delta z \simeq 0.037$ corresponding to 46.8 h_{70}^{-1} Mpc at $z = 2.3$ in the comoving frame. The 90Prime camera consists of a mosaic of four $4\text{k} \times 4\text{k}$ blue sensitive CCDs with a plate scale of $0\farcs45$ per pixel. The detector field-of-view is ~ 0.8 deg^2 after accounting for cosmetic defects in two of the CCDs. This wide field-of-view is ideal for our survey as the large area coverage compensates for the narrowness of the filter, producing a survey comparable in volume to the largest intermediate band filter survey (Saito et al., 2006).

To date, we have finished narrow-band imaging observations with a total sky coverage of ~ 12 deg^2 in three fields where extensive ancillary data sets are publicly available: the NOAO Deep Wide Field Survey Boötes and Cetus fields (ND-WFS; Jannuzi & Dey, 1999) and the Cosmic Evolution Survey field (COSMOS; Scoville et al., 2007). In this paper, we present the initial results from the survey within the NDWFS Boötes region centered at $\alpha = 14^{\mathrm{h}}\ 32^{\mathrm{m}}\ 05\fs7$, $\delta = +34°\ 16'\ 47\farcs5$ (J2000). We carried out these observations from April to June 2007 over 16 dark nights. Figure 6.1 shows our sky coverage overlayed with the NDWFS field layout. After excluding regions with artifacts and bright stars, we achieve a total sky coverage of 4.82 deg^2. Although the exposure times range from 6 to 20 hours, all the Lyα blobs in our final sample would have been detected even in the shallowest sub-fields (§6.2.2). The sky coverage corresponds to a comoving survey volume of $2.1 \times 10^6\ h_{70}^{-3}$ Mpc^3, which is $\sim 16\times$ larger than the area covered by the deepest narrow-band Lyα blob survey to date (Matsuda et al., 2004).

We reduce the data with the IRAF *mscred* mosaic data reduction package (Valdes, 1998). The data are corrected for cross-talk between amplifiers, bias-subtracted, and dark-subtracted. For flat-fielding, we use twilight flats together
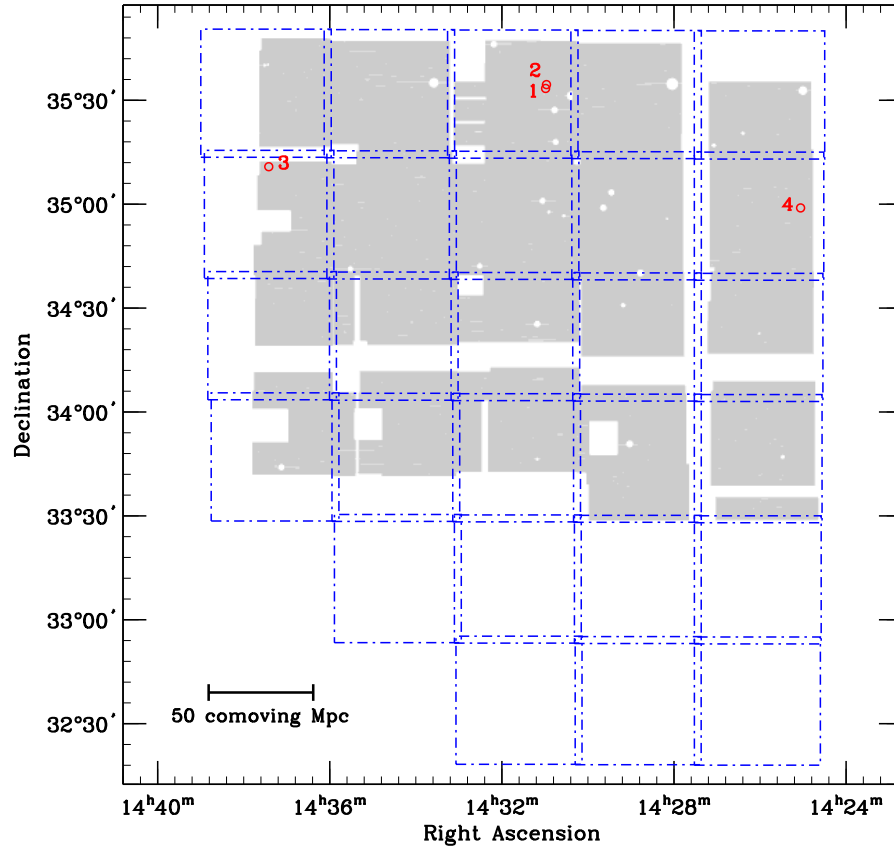
Figure 6.1 — Sky coverage of our narrow-band imaging survey for Lyα blobs within the NOAO Deep Wide Field Survey (NDWFS) Boötes field. The shaded region represents the area covered in our Bok 2.3m + *NB* 403 filter survey, and the dot-dashed lines represent the sub-fields of the NDWFS. The gaps in the sky coverage are due to the large gaps between the 90Prime CCDs and a large trap in one of the CCDs. The total sky coverage is 4.82 deg^2, excluding bright stars and artifacts, making our survey one of the widest FOV, narrow-band imaging surveys to date. The four circles represent the Lyα blobs that we have discovered (see §6.3.2 for details). None are radio-loud. The easternmost and westernmost blobs are detected in X-rays, while the the pair of blobs in the upper middle region is not.

with night-sky flats, which are median-combined from object frames without the bright stars each night. Satellite trails, CCD edges, bad pixels, and saturated pixels are masked. The astrometry is calibrated with the USNO-B1.0 catalog (Monet et al., 2003) using the IRAF *ccmap* task. The images are scaled using common stars in each frame and stacked to remove cosmic rays. Finally, the images are transformed into the same world coordinate systems as the NDWFS B_W band images, which are resampled with a coarse 90Prime pixel scale ($0\rlap{.}''45$ pixel^{-1}). We observed 3–5 spectro-photometric standard stars in each night to derive extinction coefficients and zero points for the *NB* 403 magnitudes. The major drawback is the poor seeing, which, in the final combined images, ranges from $1\rlap{.}''5$ to $2''$ with a median of $1\rlap{.}''7$. However, as we discuss in §6.2.2, the seeing does not impact our ability to identify the blobs with sizes greater than $25\,\square''$.

To identify blob candidates requires that we subtract the continuum emission within the *NB* 403 bandpass. We estimate the continuum using archival, deep, broad-band B_W images from the NOAO Deep Wide Field Survey data set ($B_W RIJK$; Jannuzi & Dey, 1999). The wide B_W filter ($\lambda_c \approx 4135$Å and $\Delta\lambda \approx 1278$Å) encompasses our *NB* 403 filter near the central wavelength. The 5-σ limiting magnitude of the B_W images is ~ 26.6 mag for a $2''$ diameter aperture. The seeing of the NDWFS B_W images ranges from $0\rlap{.}''8$ to $1\rlap{.}''47$ with a median of $1\rlap{.}''2$. A total of 20 NDWFS tiles cover our narrow-band imaging fields as shown Figure 6.1.

6.2.2   Selection of Lyα Blob Candidates

To find Lyα blob candidates, we construct photometric catalogs in the *NB* 403 and B_W bands using SExtractor (Bertin & Arnouts, 1996). Because our narrow-band images are much shallower and typically have worse seeing than the broad-band images, we make "detection" images (*NB* $+B_W$) by adding the *NB* 403 and B_W images after scaling them according to their signal-to-noise ratios (S/N). After
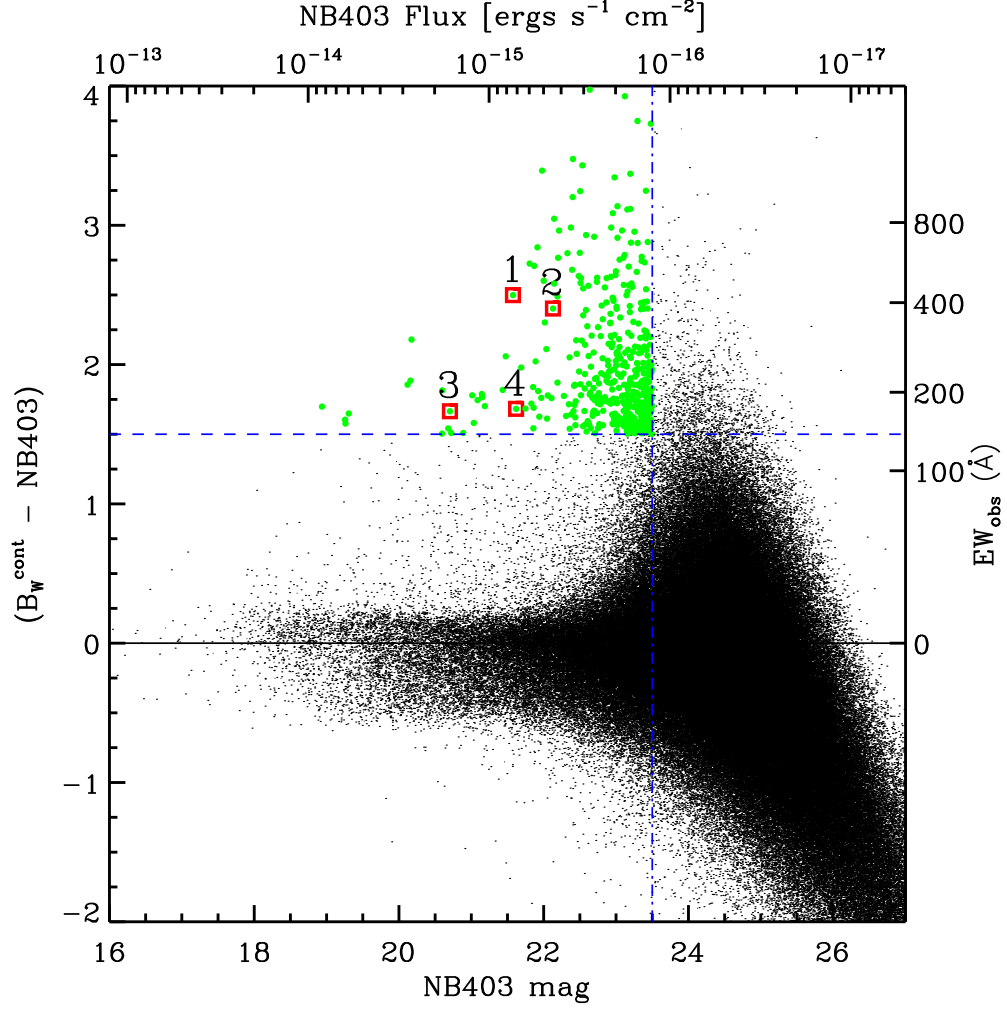
Figure 6.2 — The ($B_{\mathrm{W}}^{cont} - NB\,403$) color-magnitude diagram for all sources detected in either the B_{W} and NB images within the Boötes survey field. Right and top axes show the corresponding equivalent widths in the observed frame and NB fluxes, respectively. The sharp boundary at $NB\,403 \gtrsim 24.0$ is due to sources detected only in the B_{W} band. We select line-emission objects with the criteria $NB\ < 23.5$ (dot-dashed line) and $B_{\mathrm{W}}^{cont} - NB > 1.5$ (dashed line; $EW_{\mathrm{obs}} > 140$Å). Squares represent the final Lyα blob candidates (see Fig.6.3).

identifying sources in the "detection" images that have least 5 pixels that are 1.5σ above the local sky, we run SExtractor in double-image mode on the NB 403 and B_W images with these detection images. In other words, we first find the sources in the detection images and then obtain photometry at their position in the NB 403 and B_W images to make two separate (narrow- and broad-band) catalogs. We adopt Kron-like elliptical aperture magnitudes (i.e., MAG_AUTO in SExtractor) to derive photometric properties. Our use of the "detection" images ensures that 1) all the sources detected in either the NB or B_W band are included in our catalog and 2) the elliptical apertures determined by the more extended sources in (NB $+B_W$) are large enough to include all the light from both the NB and B_W images. This last point is critical because we do not attempt to match the seeing between the two bands at this stage.

The selection of Lyα blob candidates from the NB and B_W photometry catalogs consists of two steps: 1) selection for line (hopefully, Lyα) emitting objects with large line equivalent widths and 2) selection for spatially extended objects with a larger angular extent in line emission than in the broad-band.

First, we choose candidates by requiring that they are detected above the completeness limits of the NB 403 images (NB 403 $<$ 23.5 mag).[1] We also require that candidates have observed-frame equivalent widths larger than 140Å ($EW_\mathrm{rest} > 42$Å) corresponding to $B_W^{cont} - NB > 1.5$ (vertical and horizontal lines in Fig. 6.2). Candidates must be extended (SExtractor CLASS_STAR > 0.95 in *both* the NB and B_W bands). There are a total of ~ 450 objects over 4.82 deg^2 satisfying these criteria. Because most of the Lyα blobs ($\sim$30/35) discovered by Matsuda et al. (2004) have $EW_\mathrm{obs} \gtrsim 200$Å ($EW_\mathrm{rest} > 50$Å), our selection criteria would include them if blob properties remain the same between $z = 2.3$ and 3.1.

---

[1]The completeness limit varies by ± 0.5 mag depending on the sub-field due to seeing variations and different exposure times. However, our final blob sample does not depend on the choice

We estimate the continuum flux density, f^λ_{cont}, and continuum-subtracted line flux, F_{line}, of these objects using the following relations:

$$f^\lambda_{cont} = \frac{F_B - F_{NB}}{\Delta\lambda_B - \Delta\lambda_{NB}}$$

$$F_{line} = F_{NB} - f^\lambda_{cont}\Delta\lambda_{NB},$$

(6.1)

where F_B and F_{NB} are the total flux in each filter derived from the B_W and NB 403 magnitudes, respectively. $\Delta\lambda_B$ and $\Delta\lambda_{NB}$ represent the band-widths of the B_W and NB filters, respectively. Figure 6.2 shows the $(B^{cont}_W - NB)$ color excess as a function of NB magnitude for all objects detected in either the NB and B_W bands within our survey area. Here, B^{cont}_W represents the broad-band continuum magnitude corrected for the emission line: $B^{cont}_W = -2.5\log f^\nu_{cont} - 48.6$.

At our survey redshift, the only possible interlopers are nearby [O II] λ3727 emitters at $z \approx 0.08$. However, such objects rarely have equivalent widths larger than 100Å in the rest frame (Hogg et al., 1998). Therefore, the contamination of our $z = 2.3$ Lyα source catalog by nearby star forming galaxies is expected to be minimal. Even if we reduce our selection limit to $EW_{\rm obs} \gtrsim 65$Å, we end up with the same final Lyα blob sample and none of our conclusions in this paper change.

Second, we identify those line-emission selected objects that are more spatially extended in Lyα than their continuum counterparts (Fig. 6.3).[2] We measure the spatial extents of the Lyα emission in the continuum-subtracted images. After registering the NB 403 and B_W images at the sub-pixel level and matching their seeing, we construct continuum-subtracted NB 403 images by applying the relations in Eq. (6.2) in 2–D. We measure the isophotal area of the emission region by running SExtractor with a threshold of 5×10^{-18} ergs s^{-1} cm^{-2} arcsec^{-2}. This measurement threshold is $\sim 2.3\times$ higher than that adopted by Matsuda et al. (2004), but because our survey redshift ($z = 2.3$) is lower than theirs ($z = 3.1$), we gain

of completeness limit because all the blobs are at least ~ 1.5 mag brighter than this cut (§6.3).
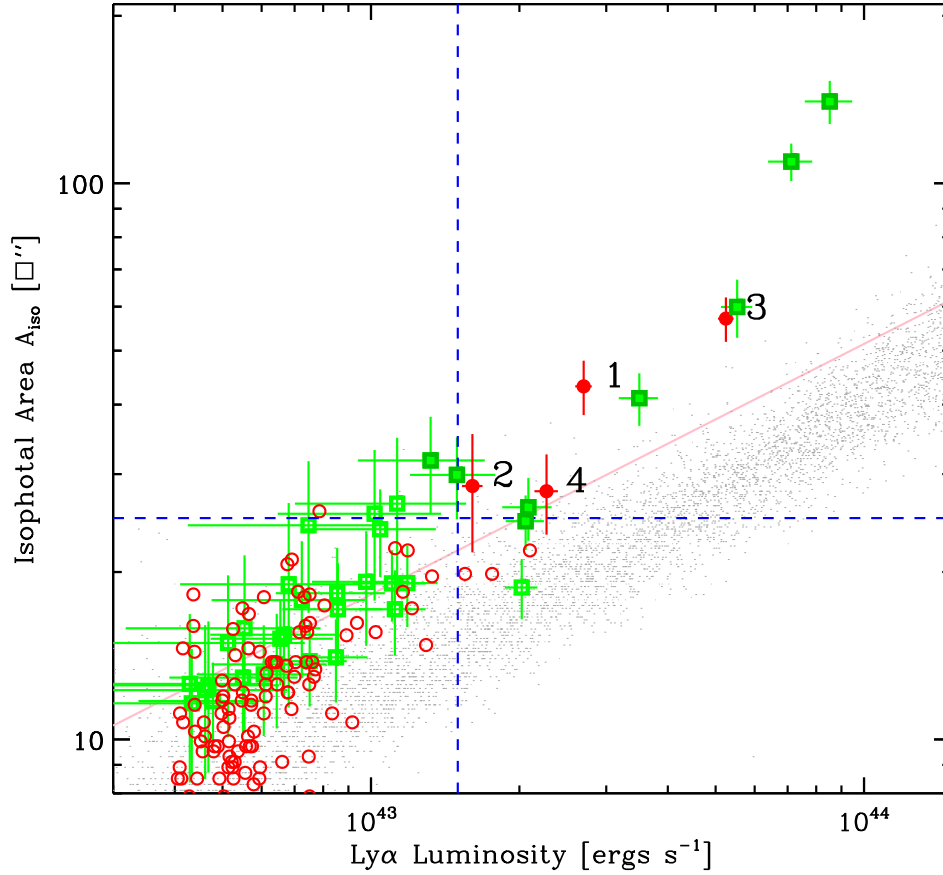
Figure 6.3 — Distribution of isophotal areas and Lyα luminosities of Lyα-emitting sources (circles) selected with the first criteria (Fig. 6.2). The horizontal and vertical dashed lines represent the selection criteria for the final Lyα blob candidate sample: $A_{iso} > 25\,\square''$ and $L(\mathrm{Ly}\alpha) > 1.5 \times 10^{43}$ ergs s^{-1}, respectively. Gray dots represent the A_{iso}–$L_{\mathrm{Ly}\alpha}$ relation for simulated point sources. Note that our four final blob candidates (filled circles) are located well above this relation (the solid line represents the upper 2σ limit), indicating that they are extended sources despite the poor seeing. Simulated point sources mix with extended Lyα-emitting sources below our selection limits on A_{iso} and $L_{\mathrm{Ly}\alpha}$, making it difficult to distinguish blobs from point sources there. The squares represent the predicted sizes and Lyα luminosities of the 35 Matsuda et al. (2004) blobs were they observed with our observational set-up at $z = 2.3$. Our final blob candidate selection criteria (dashed lines) would find $6 - 8$ (filled squares) of the brightest and largest Matsuda et al. (2004) Lyα blobs (see §6.3.3).

a factor of ~ 2.4 in surface brightness. Although this measurement threshold is comparable to the rms noise of the continuum-subtracted $NB\,403$ images ($\sim 0.5 - 1 \times 10^{-17}$ ergs s^{-1} cm^{-2} arcsec^{-2} depending on the field), we are still able to measure the sizes over this measurement limit because the bright central parts of the objects were already detected with high S/Ns.

One of the potential problems in detecting a blob is the contamination of our extended Lyα candidate sample by point sources, especially given the poor seeing of the narrow-band images. To quantify this effect, we first place artificial point-sources with a range of luminosities ($L_{\mathrm{Ly\alpha}} = 10^{42} - 10^{45}$ ergs s^{-1}) into the sky regions over the whole NDWFS field and measure their sizes and fluxes in the same manner as for the extended sources. We then determine isophotal area and line luminosity limits above which extended and point sources can be differentiated.

Figure 6.3 shows the distribution of the angular sizes and line luminosities of the 185 Lyα-emitting candidates assuming that they are all located at $z = 2.3$. The open and filled circles represent the line-emitting objects selected using the line-emission criteria (Fig. 6.2), and the gray dots show the relation between the sizes and brightnesses for the artificial point sources. As final blob candidates, we select objects with isophotal areas larger than $25\,\square''$ and line luminosities brighter than 1.5×10^{43} ergs s^{-1}. Below these limits, extended and point sources mix, and the sizes of blobs cannot be measured reliably as explained below.

Because the chosen isophotal threshold is comparable to the rms sky noise, we test how reliably we can measure the spatial extent of the blob candidates. We cut out a small (51$\times$51 pixels) section around each blob candidate from the

---

[2]Saito et al. (2006) selected spatially extended objects by requiring the FWHM in their intermediate-band to be larger than that in the broad-band image, but the large seeing difference between our $NB\,403$ images ($\sim 1''\!.7$) and the NDWFS B_{W} images ($\sim 1''\!.2$) prevents us from adopting this approach.
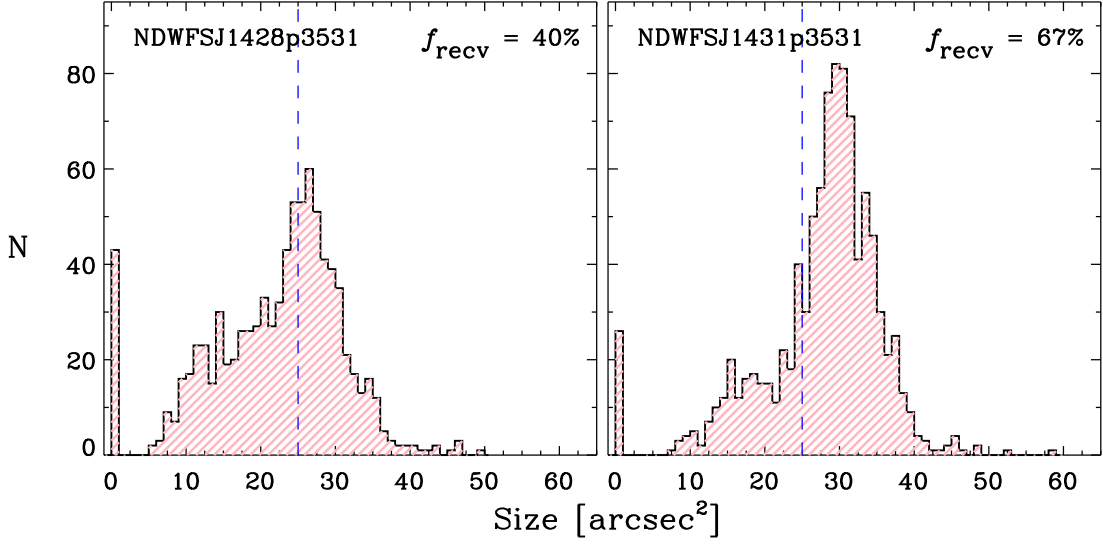
Figure 6.4 — An example of recovery test for the faintest blob (blob 2) in our final sample. We show the distribution of the recovered isophotal area for two NDWFS sub-fields for illustrative purposes. This blob is actually located in the NDWFSJ1431+3531 sub-field (*right*) and has the worst recovery fraction ($f_{\rm recv}$) in the NDWFSJ1428+3531 sub-field (*left*). The bins with zero size indicate non-detections. The vertical dashed line represents our selection criteria for blob size ($25\,\square''$).

($NB - B_{\rm W}$) image, filter it with a smoothing kernel,[3] place each postage stamp into $300 - 1000$ empty sky regions in each of the 20 NDWFS sub-fields in Figure 6.1, and extract the sources with SExtractor in the same way as for the real data. Then we check how often and accurately their sizes are recovered from these simulated images. This procedure tests how the detectability of a given blob candidate changes across the fields due to the seeing and exposure time variations.

Figure 6.4 shows an example of this recovery test for the faintest blob in our final sample (blob 2, see §6.3). We show the distribution of the recovered isopho-

---

[3]We use a 3×3 pixel convolution mask with a FWHM = 2 pixel, which is a default kernel in SExtractor.

tal sizes of the artificial blob for two sub-fields. While most ($\gtrsim$95%) of time, the artificial blob is detected, its size is measured with a large spread because of non-uniform sky background noise. We adopt this spread of the recovered size distributions as the error in the blob size, A_{iso}.

A recovery fraction of a blob (f_{recv}) in a sub-field is defined as the fraction of time that the artificial blob is recovered with a size larger than 25 $\square''$. These recovery fractions are averaged over the whole field to obtain the final recovery fraction of the blob for this survey. The size error becomes comparable to the measured size below our sample selection criteria and the recovery fraction drops from $\gtrsim$90% to $\sim$50% at the selection boundary for the brightest blob candidates. The recovery fractions are used to correct the incompleteness of our survey in calculating the blob number density in §6.3.3.

6.3 Results and Discussion

The selection criteria, $EW_{\mathrm{obs}} > 140$Å, $A_{iso} > 25 \square''$, and $L(\mathrm{Ly}\alpha) > 1.5 \times 10^{43}\,\mathrm{ergs\,s^{-1}}$, yield four extended Ly$\alpha$ candidates at $z = 2.3$ with sizes of $28 - 57 \square''$, Lyα luminosities of $1.6 - 5.3 \times 10^{43}\,\mathrm{ergs\,s^{-1}}$, and EW_{obs} of $\sim 170 - 420$Å (Table 6.1). Figure 6.5 shows the $NB\,403$, B_{W}, and continuum-subtracted ($NB - B_{\mathrm{W}}$) images for these candidates. Except for Blob 4, which appears to have more than two continuum counterparts, we are able to identify single host galaxies in the B_{W} bands for the other three blob candidates. Although these continuum sources are barely resolved in B_{W}, the line-emission regions are extended over ~ 5–$10''$ in the ($NB - B_{\mathrm{W}}$) images. We also show the locations of the blob candidates on the sky in Figure 6.1. Because blobs 1 and 2 are separated by only $70''$ (~ 550 physical kpc at $z = 2.3$), they are shown in the same panel in Figure 6.5.
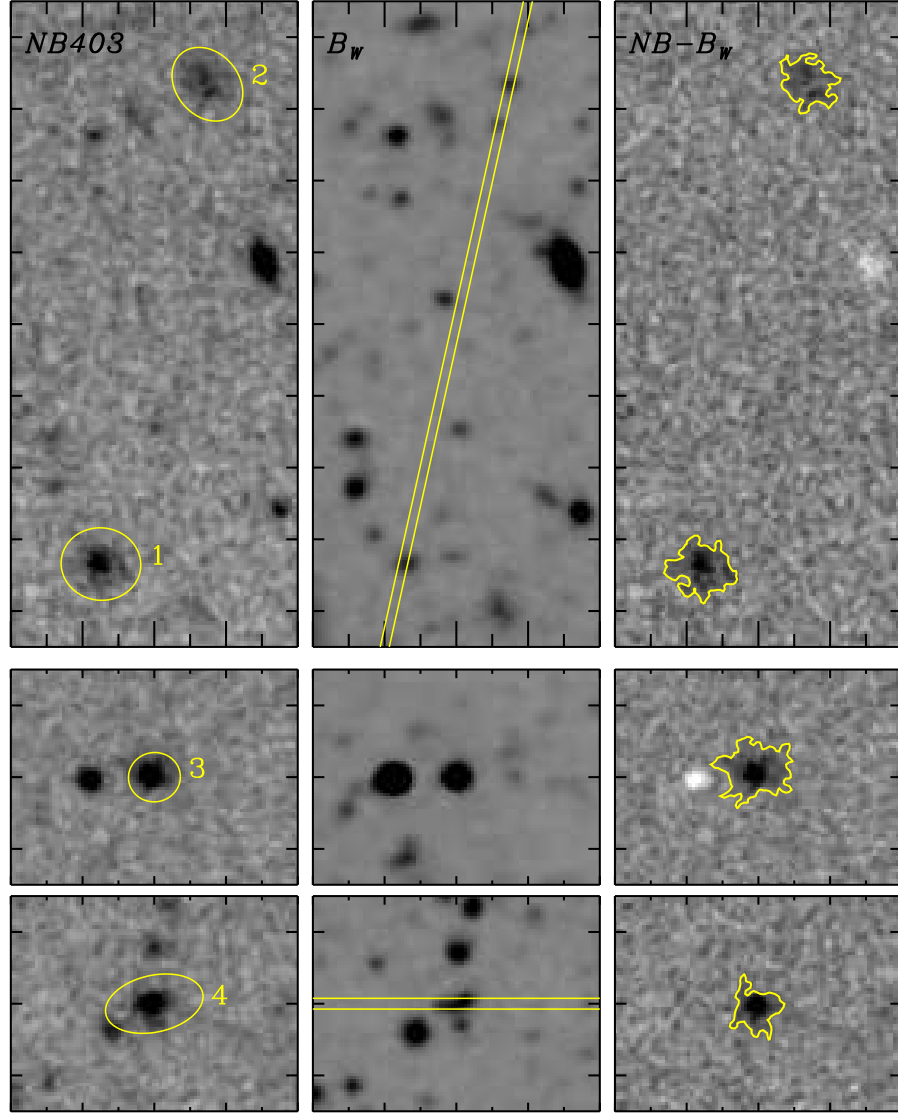
Figure 6.5 — Images of the four Lyα blob candidates. From left to right are the NB 403, NDWFS B_W, and continuum-subtracted ($NB - B_W$) images. The ticks are spaced every $10''$, which corresponds to ~ 82 physical kpc at $z = 2.3$. The elliptical apertures used for photometry and blob identification are shown in the left panels. The B_W images are smoothed to match the seeing of the NB images. In the right panels, the contours represent the surface brightness limit of 5×10^{-18} ergs s^{-1} cm^{-2} arcsec^{-2}, within which we determine the blob sizes. The location of the $1.5''$-wide slit used for spectroscopic follow-up with the 6.5m MMT is shown for blobs 1, 2, and 3 in the B_W image. We spectroscopically confirm that all four blobs lie at $z = 2.3$ (Fig. 6.6). Blobs 3 and 4 are broad-line QSOs that are both detected in X-rays [$L_X(2-7 \, \text{keV}) = 1.6 - 4.1 \times 10^{44}$ ergs s^{-1}]. None of the blobs are radio-loud.

6.3.1 Spectroscopic Confirmation

We spectroscopically confirm the redshifts of all four blob candidates using spectra taken with the 6.5m "Multiple Mirror" Telescope (MMT) Blue Channel Spectrograph and an existing optical spectrum from the AGN and Galaxy Evolution Survey (AGES; Kochanek et al. in prep., Cool et al., 2006). For blobs 1, 2 and 4, we obtained low-resolution long-slit spectra on UT 2008 February 13, April 29, and June 7. We used the 500 gpm grating with a $1''5 \times 180''$ slit, which provides a dispersion of 1.2Å per pixel and a spectral resolution of 5.4Å over the wavelength range 3400 − 6400Å (1000 − 1900Å in the rest frame). Because blobs 1 and 2 are separated by only $\sim 70''$, we observed them simultaneously for a total of 6 hours with the slit position (P.A. = $-12.1°$) shown in Figure 6.5. Blob 4 is the most ambiguous object in our sample as its continuum counterpart is not clear due to the blending in the B_W image. Therefore, we put a slit at P.A. = $90.0°$ to include all the continuum components seen in the B_W band images. The spectra were reduced, extracted, and flux-calibrated in the standard manner with `IRAF`.

The MMT spectra confirm that blobs 1, 2 and 4 are indeed $z = 2.3$ Lyα blobs. We show the extracted spectra of these three blobs in Figure 6.6. In each case, there is an emission line at $\simeq 4030$Å, which agrees well with the central wavelength of the *NB* 403 filter. For blobs 1 and 2, there are no other emission lines over the entire wavelength range, which covers the redshifted [O II] $\lambda 3727$, Hβ $\lambda 4868$, and [O III] $\lambda 5007$ lines from any $z = 0.08$ star-forming galaxies. The Lyα lines have large velocity widths of ~ 900 and 1250 km s^{-1}, and observed-frame equivalent widths of ~ 150Å and 190Å, respectively. The broad line profile and the absence of other emission features in blobs 1 and 2 indicate that the emission line is Lyα. The stellar continuum of blobs 1 and 2 bears a strong resemblance to the UV spectra of Lyman break galaxies (e.g., Shapley et al., 2003). Notably, there

is no evidence of broad emission at the wavelengths of Si IV and C IVC, so the presence of an unobscured AGN is ruled out with confidence. A detailed analysis of the continuum and spectral features of these blobs will be presented in a future paper. For blob 4, we identify two continuum sources, an [O II] emitter at $z \simeq 0.266$ and a QSO that produces broad Lyα and C IV lines at $z \simeq 2.32$. The Lyα line has a velocity width of ~ 950 km s^{-1} and an observed-frame equivalent width of ~ 85Å. Note that the EWs measured from the long-slit spectra are lower than those estimated from the narrow-band imaging due to slit-loss.

For blob 3, we obtain a spectrum from AGES, which has extensive optical spectroscopy for all the X-ray detected galaxies with $I_{AB} \lesssim 22.0$ mag in the Boötes field. This spectrum shows that blob 3 is at $z = 2.32$ and contains a QSO with strong, broad Lyα emission (Figure 6.6). Blob 3 is perhaps similar to the diffuse Lyα halos associated with some QSOs (e.g., Bunker et al., 2003; Weidinger et al., 2005).

6.3.2 Multi-Wavelength Properties of Confirmed Lyα Blobs

Are any of the four blobs associated with strong radio or X-ray sources? None is detected in the VLA FIRST survey (White et al., 1997) at 1.4 GHz at the detection limit of 1 mJy. Assuming a power-law spectral energy distribution of $S(\nu) \propto \nu^{-0.8}$, this limit corresponds to a rest-frame 1.4 GHz luminosity density of 3.2×10^{32} ergs s^{-1}Hz^{-1}, which is $\sim$ two orders of magnitude fainter than the powerful radio galaxies associated with Lyα halos (e.g., Reuland et al., 2003). However, in X-rays, the properties of these blobs vary wildly. Blobs 3 and 4, whose optical spectra have broad QSO lines, are detected in the *Chandra* XBoötes survey (Kenter et al., 2005; Brand et al., 2006) with $L(2\text{--}7\,\text{keV}) = 1.6 - 4.1 \times 10^{44}$ ergs s^{-1}. Blobs 1 and 2 are not detected at a similar depth and have upper limits of $L(2\text{--}7\,\text{keV})$ < 0.63 and 0.18×10^{44} ergs s^{-1}, respectively. Therefore, at least two of the blobs
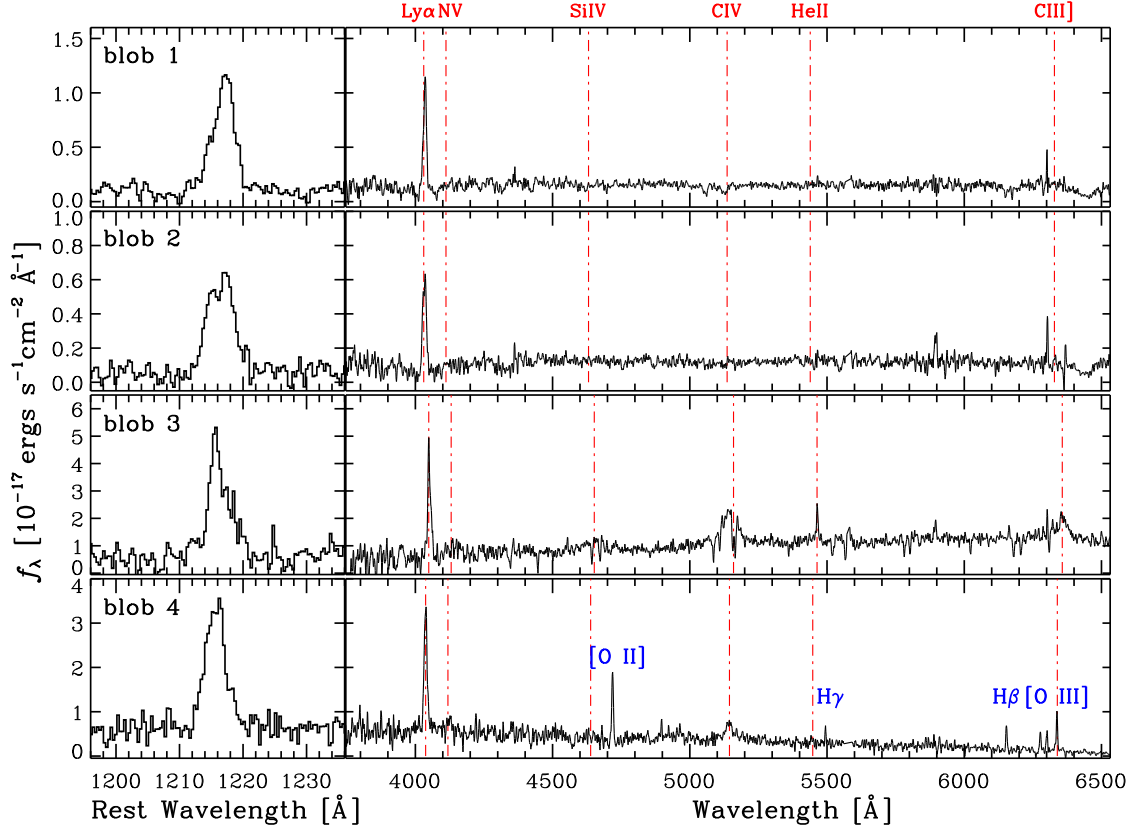
Figure 6.6 — Extracted 1D spectra for four blobs from 6.5m MMT long-slit spectroscopy (blobs 1, 2, and 4) and the AGN and Galaxy Evolution Survey (blob 3; Kochanek et al. in prep.). For blobs 1 and 2, there is no other emission line visible up to 6500 Å. The broad Lyα profiles and the absence of other emission lines indicate that blob 1 and 2 are true Lyα blobs. These two blobs have almost the same redshifts ($z = 2.316$) within $\delta z \simeq 0.001$. Their spectra do not show any AGN signatures (e.g., C IV $\lambda 1549$). Neither of these blobs is X-ray-detected (§6.3.2). Blobs 3 and 4 show other broad emission lines (e.g., C IV $\lambda 1549$ and/or C III] $\lambda 1909$), indicating that these blobs host QSOs. Unlike blobs 1 and 2, these blobs are X-ray detected [L_X(2–8 keV) = $1.6 - 4.1 \times 10^{44}$ ergs s^{-1}]. Because of the blending in the B_W images, the blob 4 spectrum contains an interloper, an [O II] emitter at $z \simeq 0.266$ (Hγ, Hβ, and [O III] lines).

(50%) are associated with AGN. Table 6.1 lists the optical and X-ray properties of the four blobs.

It is unknown what powers the copious Lyα emission of blobs. Previous observational studies suggest diverse mechanisms, e.g., a central AGN (Dey et al., 2005), galactic superwind (e.g., Wilman et al., 2005), extended star formation (Matsuda et al., 2007), and cooling radiation (Nilsson et al., 2006; Smith & Jarvis, 2007; Smith et al., 2008), yet there is no smoking gun. Due to its blind strategy, large volume, follow-up optical spectroscopy, and overlap with wide *Chandra* X-ray imaging coverage, our work here is the first to place unbiased limits on the fraction of blobs with luminous AGN (50%). The *diversity* of the blob optical and X-ray properties is also interesting, suggesting that AGN like those detected in half the blobs are not necessary to power the others.

6.3.3 Rarity of Lyα Blobs

Our survey indicates that extended Lyα nebulae are extremely rare at a redshift of 2.3. Based on the completeness (recovery) test in §6.2.2, we estimate the number of Lyα blobs within the survey volume as $N = \sum_i 1/f_{\mathrm{recv}}^i$, where f_{recv}^i is the recovery fraction (Table 6.1). The discovery of only four Lyα blobs over 4.82 deg^2 yields a number density of $3.2 \pm 1.2 \times 10^{-6}\ h_{70}^3\,\mathrm{Mpc}^{-3}$ for blobs with $A_{iso} > 25\,\square''$ and $L(\mathrm{Ly}\alpha) > 1.5 \times 10^{43}\ \mathrm{ergs\,s}^{-1}$. Note that this number density is comparable to those of galaxy clusters in the nearby and high-z Universe, $n \sim 10^{-5} - 10^{-6}$ $h_{70}^3\,\mathrm{Mpc}^{-3}$(e.g., Bahcall et al., 2003; Papovich, 2008). Because our survey fails to find blobs as bright ($L_{\mathrm{Ly}\alpha} \gtrsim 10^{44}\ \mathrm{ergs\,s}^{-1}$) and large ($A_{iso} \gtrsim 150\,\square''$) as the brightest and largest in the Steidel et al. (2000) sample (their Blobs 1 and 2), we conclude that the Steidel et al. (2000) blobs are even rarer objects with a number density of $n \lesssim 0.5 \times 10^{-6}\ h_{70}^3\,\mathrm{Mpc}^{-3}$.

To compare our blob number density with those from previous surveys (Mat-

suda et al., 2004; Saito et al., 2006), we determine how many of the Matsuda et al. (2004) blobs would be detected in our survey if they were located at $z = 2.3$. Using the continuum subtracted NB_{corr} images of the 35 blobs from Matsuda et al. (2004), we scale the blob surface brightnesses and sizes to $z = 2.3$ according to the adopted cosmology and assuming that their physical sizes and Lyα luminosities do not change from $z = 3.1$ to 2.3. These images are convolved with Gaussian kernels to match our poor seeing, rebinned to the 90Prime pixel scale, and given Poisson noise. We do not account for the difference between the filter ($NB\,403$ vs. $NB\,497$) band-widths, because the resolving power of two filters is similar. We place the simulated images into our continuum-subtracted $NB\,403$ images and measure their sizes and luminosities in the same way as described in §6.2.2. We repeat this process 500–1000 times to derive the range of recovered luminosities and sizes.

We show the distribution of sizes and Lyα luminosities ($A_{iso} - L_{\mathrm{Ly}\alpha}$) in Figure 6.3. Based on this test, we expect that $6 - 8$ of the 35 Matsuda et al. (2004) blobs are detectable given our luminosity-size criteria.[4] Considering the recovery rate of each Matsuda blob, which is $\sim100\%$ for $L(\mathrm{Ly}\alpha) > 5 \times 10^{43}$ and drops to $\sim 50\%$ at our selection boundary, we expect to detect on average ~ 6.0 of their blobs with our survey criteria. Once we factor in the difference between our survey volume and Matsuda et al.'s, we should have detected $\sim$98 blobs — not four — provided that the blob number density at $z = 3.1$ and 2.3, and between the two survey fields, is the same.

The comparison of our results with those of Saito et al. (2006) is more difficult because we do not have high S/N measurements of their blob surface bright-

---

[4]In the detectability simulation, the average values of extracted A_{iso} and $L_{\mathrm{Ly}\alpha}$ for six Matsuda et al. (2004) blobs (their LAB 1, 2, 3, 4, 8, 10) satisfy our selection criteria. Two other blobs (their LAB 6 and 15) are located on our selection boundary, but satisfy the selection criteria more than 50% of the time in the simulation.

ness profiles. Therefore, we estimate the blob number density for $L(\text{Ly}\alpha) \gtrsim 1.5$ $\times 10^{43}\,\text{ergs s}^{-1}$ from the brightest bin in their Figure 13. We consider the resulting number density of $\sim 6.7 \times 10^{-6}\ h_{70}^3\,\text{Mpc}^{-3}$ an upper limit at $z = 3\text{–}5$, given that some fraction of their blobs might not have been detected with our survey criteria.

We show the number density of Lyα blobs from the different samples and at different redshifts in Figure 6.7. Open and filled squares represent the number density estimates from our survey with and without the two X-ray detected blobs. For the Matsuda et al. sample, we show both the measured number density and that scaled down to compensate for the known over-density of the SSA22 field ($\delta \sim 6$; Steidel et al., 2000). For Saito et al.'s survey, we show the upper-limit discussed above and the redshift range (horizontal error bar). We also show a lower limit on the number density at $z = 6.595$ derived from the recent discovery of a Lyα blob in the Subaru/XMM-Newton Deep Survey field (Ouchi et al., 2008).

At face value, Lyα blobs within the $z = 3.1$ proto-cluster from the Matsuda et al. (2004) survey are $\sim 20 - 30$ times more numerous than blobs in our blind field survey. Even if we account for the galaxy over-density in the proto-cluster, the blob number density in our survey is still by a factor of 3 lower, suggesting that extended Lyα emission is closely related to (or enhanced by) a clustered environment. However, we cannot rule out that this discrepancy might reflect real evolution between $z = 2.3$ and 3.1.

6.3.4 A Close Pair of Lyα Blobs

One of our most interesting results is the discovery of the pair of blobs (1 and 2) separated by only 70$''$, which corresponds to $\sim$550 physical kpc at $z = 2.3$. To estimate how unlikely it is to find two blobs within 70$''$ of each other, we calculate the expected number of galaxy pairs assuming that the spatial distribution of Lyα
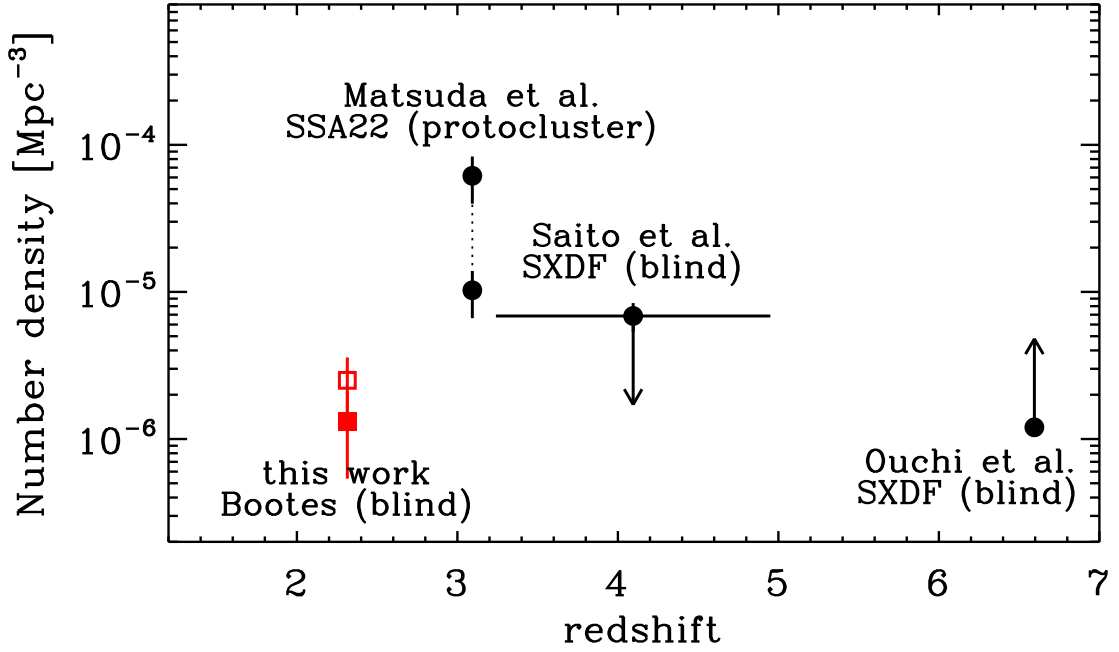
Figure 6.7 — Number density of Lyα blobs at different redshifts. Open and filled squares represent the number density from our narrow-band imaging survey at $z = 2.3$ for the blobs with and without X-ray detections, respectively. We also show two number density estimates for the blobs in Matsuda et al. (2004), with or without correction for the over-density of the SSA22 proto-cluster region. For blobs at higher redshifts, we show only upper ($3 < z < 5$; Saito et al., 2006) and lower limits ($z = 6.595$ Ouchi et al., 2008).

blobs can be represented by a two-point correlation function, $\xi(r, z) = [r/r_0(z)]^{-\gamma}$, where $r_0(z)$ is the scale length of galaxy clustering at the redshift z. By project-ing this correlation function onto the sky (Limber, 1953), we derive the angular correlation function $\omega(\theta)$, which measures the excess probability above random of finding a galaxy at an angle θ from another galaxy. For a given power-law cor-relation function, one can derive $\omega(\theta) = A_\omega \theta^{1-\gamma}$ (Peebles, 1980; Efstathiou et al., 1991) such that

$$A_\omega = H_\gamma \int r_0^\gamma(z)\, d_C^{1-\gamma}(z) \left[\frac{dN}{dz}\right]^2 \frac{H(z)}{c} dz \left[\int \frac{dN}{dz} dz\right]^{-2}, \qquad (6.2)$$

where $d_C(z)$ is comoving distance at z, dN/dz is the number of galaxies per unit redshift interval, $H(z)$ is the Hubble parameter at z, and $H_\gamma = \sqrt{\pi}\Gamma[(\gamma - 1)/2]/\Gamma(\gamma/2)$. We adopt dN/dz as a top-hat function for our survey redshift interval and assume a fiducial value of $\gamma = 1.8$.

From this angular correlation function, we estimate the number of galaxy pairs within θ_p using:

$$N_p(< \theta_p) = \int_0^{\theta_p} \frac{1}{2}N(N-1)[1 + \omega(\theta)]\frac{2\pi\theta d\theta}{\Omega}, \tag{6.3}$$

where Ω is the survey area, and N is the number of blobs found in our survey. For the typical galaxy correlation length, $r_0 \sim 7$ Mpc in the comoving frame (e.g., Maddox et al., 1990), we predict a negligible pair count, $N_p \simeq 0.005$. The expected number of close pairs does not increase dramatically as the correlation length increases. Even for the correlation length of the richest galaxy clusters, $r_0 \sim 30$ Mpc (e.g., Bahcall et al., 2003; Papovich, 2008) for redshifts out to $z \sim 1.5$, only $N_p \simeq 0.05$ pairs are expected. Therefore, we conclude that the observed close pair of Lyα blobs is unlikely to occur for a reasonable range of clustering strengths if we assume that the two Lyα blobs belong to individual dark matter halos.

Increasing the size of our blob sample (Yang et al. 2008, in prep.) will better constrain the clustering of Lyα blobs. For the time being, it is intriguing that we do discover a close pair. Our MMT spectra confirm that the two blobs have almost the same redshifts within $\delta z \simeq 0.001$ and a corresponding line-of-sight separation of $\delta r \simeq 360$ physical kpc assuming no peculiar velocity. The similarity of their redshifts, as well as their small separation on the sky (corresponding to 550 physical kpc), leads us to speculate that these two blobs might lie within a single dark matter halo, i.e., within a massive proto-group or cluster of galaxies. (Note that the analytic ΛCDM model predicts a virial radius (r_{200}) of 430 kpc at $z = 2.3$ for a dark matter halo with a mass of $10^{14}\,M_\odot$ (Mo & White, 2002).) Previous studies

also suggest that Lyα blobs are phenomena that favor dense environments (Matsuda et al., 2005; Prescott et al., 2008). This hypothesis could be tested by using a deeper narrow-band imaging survey to characterize the environment of this blob pair with the spatial distribution of fainter, smaller blobs and/or faint, compact Lyα emitters.

6.4 Conclusion

In this paper, we present initial results from our blind, wide-field, narrow-band imaging survey in the NOAO Deep Wide Field Survey Boötes field to constrain the number density, environment, and multi-wavelength properties of extended Lyα nebulae ("Lyα blobs") at $z = 2.3$. After searching over 4.82 deg^2, we discover four Lyα blobs with $L_{\rm Ly\alpha} = 1.6 - 5.3 \times 10^{43}$ ergs s^{-1}, isophotal areas of $28 - 57\,\square''$, and broad Lyα line profiles ($\Delta v = 900 - 1250$ km s^{-1}). We confirm the redshifts of all four blobs spectroscopically. In contrast with the extended Lyα halos associated with high-z radio galaxies, none of our four blobs are radio-loud. The X-ray luminosities and optical spectra of these blobs are diverse. Two blobs (3 and 4) are X-ray-detected with $L_X(2-7\,{\rm keV}) = 2$–4×10^{44} ergs s^{-1} and have broad optical emission lines (C IV and C III]) characteristic of AGN, implying that 50% of our sample blobs are associated with strong AGN. The other 50% of blobs (1 and 2) are not X-ray or optically-detected as AGN down to similar limits, suggesting that AGN like those in blobs 3 and 4 are not necessary to power them. The number density of the four blobs is $\sim 3 \times 10^{-6}\ h_{70}^3$ Mpc^{-3}, comparable to that of galaxy clusters at similar redshifts and $3\times$ lower than that found in the SSA22 proto-cluster at $z = 3.1$, even after accounting for the over-density of that region. The two X-ray undetected blobs (1 and 2) are separated by only 70$''$ (550 physical kpc) and have almost identical redshifts (corresponding to $\lesssim 360$ physical kpc

along the line-of-sight), suggesting that they are part of the same system. Given the rarity of the blobs and our discovery of a close pair, we speculate that blobs occupy the highest density regions and thus may be precursors of today's rich cluster galaxies.

Table 6.1. Properties of Lyα Blobs

ID	R.A. (J2000)	Dec. (J2000)	z	$L(\text{Ly}\alpha)$ $(10^{43}\,\text{ergs s}^{-1})$	Size $(\square'')$	f_{recv}	EW_{obs} (Å)	$L(\text{2-7keV})$[a] $(10^{44}\,\text{ergs s}^{-1})$	NDWFS Name	NDWFS magnitudes[b]			
										Bw	R	I	K
Blob 1	14 30 59.0	+35 33 24.7	2.3186	2.70 ± 0.10	43 ± 4.8	0.91	422 ± 20.8	$\lesssim 0.63$[c]	NDWFS J143059.0+353324	23.63	22.91	22.69	$\cdots$
Blob 2	14 30 57.8	+35 34 31.6	2.3178	1.61 ± 0.08	29 ± 6.9	0.34	383 ± 22.2	$\lesssim 0.18$[c]	NDWFS J143057.8+353431	24.05	22.92	22.53	$\cdots$
Blob 3	14 37 25.1	+35 10 48.8	2.3321	5.25 ± 0.19	57 ± 5.2	0.97	171 ± 7.3	4.11 ± 1.86	NDWFS J143725.0+351048	22.11	20.67	19.93	16.74
Blob 4	14 25 03.5	+34 58 55.1	2.3211	2.27 ± 0.12	28 ± 4.6	0.58	174 ± 10.4	1.63 ± 1.40	NDWFS J142503.4+345854[d]	23.06	23.70	22.13	$\cdots$
									NDWFS J142503.3+345855[d]	$\cdots$	23.66	23.24	$\cdots$

[a] X-ray luminosities are derived from the observed flux in the 0.5–2 keV band assuming a power-law spectrum with $\Gamma = 1.7$ and a Galactic absorption $N_{\text{H}} = 1 \times 10^{20}\,\text{cm}^{-1}$.

[b] Vega magnitudes from the NDWFS DR3 catalog.

[c] The upper limits are derived from the combined Chandra ACIS-I images (Obs-ID 3608,6993).

[d] It is not clear which of two galaxies is associated with the blob 4 and the X-ray source.

CHAPTER 7

CONCLUSIONS AND FUTURE DIRECTIONS

The goal of this thesis has been to study two samples of galaxies that represent two important modes of galaxy formation and evolution — post-starburst, or E+A, galaxies are markers for the role of galaxy-galaxy mergers and the so-called Lyα blobs may represent the early acquisition of baryons by galaxies. In this chapter, we summarize the main results of this thesis and discuss the issues that we plan to follow-up in the future.

7.1 Constructing a Detailed Timeline for E/S0 Evolution

In Chapters 2 and 3, we sought to understand what triggers the starbursts in E+A galaxies and whether their morphological features are consistent with a transition from gas-rich and star-forming to gas-poor and passively-evolving as the result of galaxy-galaxy interactions. We showed that the morphologies of E+As are extremely diverse, ranging across train-wrecks, barred galaxies, and blue-cores to relaxed disky galaxies, and that at least half of galaxies have tidal or other disturbed features caused by recent galaxy-galaxy tidal interactions or mergers. Given that E+As are currently bulge-dominated systems (median bulge fraction B/T = 0.59) and their light is highly concentrated (Sérsic index $n \gtrsim 5$), E+As would be morphologically classified as early-type galaxies once these disturbances relax and the low surface brightness tidal features dissipate or fade. While large fraction (70%) have positive color gradients (bluer toward center), indicating that their young stellar populations are more concentrated than their older populations, we demonstrate that evolution can invert these gradients into the negative gradients typical of E/S0s if the inner parts of E+As have become more

metal enriched than the outer parts due to the centralized star formation. E+As stand apart from the E/S0 fundamental plane (FP) in the edge-on projection, implying that the stellar populations of E+As are different from that of E/S0s. E+As have, on average, a *M/L* that is 3.8 times smaller than that of E/S0s. The tilt of the E+A FP indicates that the variation of the stellar populations among E+As is closely tied to their structural parameters, i.e., E+As follow their own scaling relationships such that smaller or less massive galaxies have smaller *M/L*. Such a trend arises naturally within a merger scenario, where low mass galaxies (the progenitors of low-mass E+As) have higher gas fractions (Young & Scoville, 1991) and could produce relatively larger populations of young stars. We discovered a population of unresolved compact sources in at least nine E+A galaxies (45%). The colors and luminosities of these young star cluster candidates are consistent with the ages inferred from the E+A spectra (0.01 − 1 Gyr). The bright end of the cluster luminosity function fades as the host galaxy becomes redder, suggesting that the newly-formed young star clusters age in parallel to their host. This interpretation is confirmed by the color evolution of the cluster systems.

In Chapter 4, we identified LINER spectra in four E+As that have compact blue cores. The existence of LINERs, similar to those in elliptical galaxies, is more evidence that E+A galaxies evolve into normal early-types. Furthermore, their presence in E+As suggests that any rapid growth phase of the central AGN has ended in rough concert with the star formation and therefore that the evolution of the black hole is tied to that of the galactic bulge. With the strong wind signatures found in high-z post-starburst (Tremonti et al., 2007), our discovery of LINERs in local E+As has prompted us to consider the possibility that AGN feedback might be responsible for the quenching of the star formation in E+A galaxies. Therefore, we are currently pursuing a spectroscopic program to identify possible outflow

signatures in local E+A galaxies.

FUTURE DIRECTIONS.

Although this thesis work has shown that E+A galaxies are progenitors of red sequence galaxies, we still need map their baryonic components over time to complete the merger-driven galaxy evolution picture.

First, what happens to the dust and molecular gas during mergers? E+As are evolving from objects that are dust- and gas-rich objects to those that are not. It is not known whether these components are consumed or expelled as these galaxies age. Second, how does the nuclear activity, and, more specifically, the AGN accretion rate, change as the merger remnant ages? While $\sim 70\%$ of post-starburst galaxies have LINERs or Seyferts from the optical AGN diagnostic diagram, it is difficult to measure the accretion rate without high-resolution X-ray images. Third, while we are the first to discover the newly-formed star clusters in post-starburst galaxies, it is still not clear how many clusters will survive disruption and contribute to the present-day globular cluster systems of E/S0's. With a new UV-optical age-dating technique, we plan to track the evolution of all these baryonic components over time in a sample of post-starburst galaxies observed by the Sloan Digital Sky Survey (SDSS) and GALEX UV satellite. Our team has been awarded *Spitzer/HST/Chandra* observations of a subset of these galaxies. We are obtaining complementary CO observations with the Heinrich Hertz Telescope.

7.2 Searching for Galaxies Forming via Gas Accretion

In Chapter 5, we used high resolution cosmological simulations to study hydrogen and helium gravitational cooling radiation from gas accretion by young galaxies. We showed that observing optically thin emission lines, such as He II

$\lambda 1640$ and Hα, from the cooling gas are required to understand the nature of Lyα blobs. In Chapter 6, we presented initial results from our blind, wide-field, narrow-band imaging survey in the NOAO Deep Wide Field Survey Boötes field to constrain the number density, environment, and multi-wavelength properties of extended Lyα nebulae ("Lyα blobs") at $z = 2.3$. After searching over 4.82 deg^2, we discover four Lyα blobs with $L_{\mathrm{Ly}\alpha} = 1.6 - 5.3 \times 10^{43}$ ergs s^{-1}, isophotal areas of $28 - 57 \,\square''$, and broad Lyα line profiles ($\Delta v = 900 - 1250$ km s^{-1}). We confirmed the redshifts of all four blobs spectroscopically. In contrast with the extended Lyα halos associated with high-z radio galaxies, none of our four blobs are radio-loud. The X-ray luminosities and optical spectra of these blobs are diverse. Two blobs are X-ray-detected with $L_X(2-7$ keV$) = 2$–4×10^{44} ergs s^{-1} and have broad optical emission lines (C IV and C III]) characteristic of AGN, implying that 50% of our sample blobs are associated with strong AGN. The other 50% of blobs are not X-ray or optically-detected as AGN down to similar limits. The number density of the four blobs is $\sim 3 \times 10^{-6} \, h_{70}^3 \, \mathrm{Mpc}^{-3}$, comparable to that of galaxy clusters at similar redshifts and $3\times$ lower than that found in the SSA22 proto-cluster at $z = 3.1$, even after accounting for the over-density of that region. The two X-ray undetected blobs are separated by only 70$''$ (550 physical kpc) and have almost identical redshifts (corresponding to $\lesssim 360$ physical kpc along the line-of-sight), suggesting that they are part of the same system. Given the rarity of the blobs and our discovery of a close pair, we speculate that blobs occupy the highest density regions and thus may be precursors of today's rich cluster galaxies.

FUTURE DIRECTIONS.

With this thesis work, we completed the first stage of our two-stage program, i.e., the narrow-band imaging search for a new, large, environmentally-unbiased sample of Lyα blobs that is well-suited for ultimately resolving their

nature. While the discovery of a close pair of blobs provided a hint that Lyα blobs reside in over-dense regions, increasing the size of our sample from the total surveyed area ($\sim$12 $\square^\circ$) will better constrain their number density and environment in the near term. In addition to the four Lyα blobs discovered in the wide-field survey presented in Chapter 6, our deeper narrow-band surveys in the CDFS, CDFN, and COSMOS fields uncover $\sim$ 14 blobs only in the CDFS field (see Table 1.1). This strong field-to-field variation of the Lyα blob population supports our claim that they are extremely rare, clustered objects specific to the highest density regions. We will carry out a detailed analysis of the clustering of these Lyα blobs and compact Lyα emitters.

Now we plan to follow-up this unique blob sample in order to determine whether Lyα blobs truly represent the galaxies forming via gas accretion. The most straightforward way to uncover the nature of Lyα blobs is to study spectroscopically the kinematics of their extended Lyα-emitting gas. Is the gas falling into the embedded galaxy or outflowing into the IGM? The detection of gas infall or outflow would be direct and exciting evidence for either gas accretion or for AGN/starburst driven galactic winds, respectively. This approach is problematic for most known Lyα blobs (those with $z \gtrsim 3$), because only their Lyα line is accessible from the ground. As discussed in Chapter 5, Lyα is a resonant line and typically optically thick in the surrounding IGM, thus its interpretation has been ambiguous. Therefore, we plan to study the kinematics of blob gas using hydrogen Hα $\lambda6563$, which is not seriously altered by radiative transfer effects and is accessible from the ground in the NIR K-band (Fig. 1.1). As a result, its kinematics reflects the true underlying velocity field. *All* infall models predict that the optically thick Lyα emission line must be blueshifted with respect to the center of the optically thin Hα line, whereas outflows will redshift the Lyα line (Dijkstra

et al., 2006). Our ground-based optical and NIR spectroscopic measurements of Lyα and Hα in our blobs have just begun, with newly awarded Magellan/MagE and VLT/SINFONI time.

An alternative approach is to study what powers the Lyα emitting gas, i.e., the energetics of Lyα blobs, by counting all ionizing sources within or around the extended Lyα emission and comparing that energy budget with the observed Lyα luminosity. If one can exclude possible energy sources, such as AGN and star formation, the remaining Lyα luminosity is attributable to cooling radiation (e.g., Nilsson et al., 2006; Smith & Jarvis, 2007; Smith et al., 2008). This approach requires both high spatial resolution *HST* imaging to resolve UV ionizing sources within the blobs and multi-wavelength data (X-ray to radio) to reliably detect AGN. Our newly found Lyα blob sample in the Extended Chandra Deep Field South is ideal for this approach. Using *HST* archival data (GOODS-S and GEMS) with exhaustive ancillary data from X-ray to radio wavelengths, we will characterize any sources embedded in ~ 14 new Lyα blobs and ~ 250 compact Lyα emitters.

APPENDIX A

DETAILED MORPHOLOGIES OF E+A GALAXIES

High resolution *HST* images enable us to identify a wealth of small and large scale features. For example, the low surface brightness tidal features, small companion galaxies, blue cores, bars, and even point-like, newly-formed star clusters are essential clues in understanding the causes and end-products of the E+A phase. In this appendix, we describe the qualitative morphologies of 21 E+A galaxies. Given that our E+A sample was selected using uniform spectroscopic criteria (large Balmer absorption and no [O II] emission), it is striking that the morphologies of E+A galaxies are so diverse.

A.1   Tidal Features and Disturbed Morphologies

Eight E+As (EA01AB, 02, 03, 07, 08, 10, 12, 13) show clear tidal features indicative of recent galaxy-galaxy interactions. These features include tidal tails that extend over a few tens of kpc and bridges that connect apparent companions. In addition to these dramatic large-scale tidal features, another three (EA04, 11, 18) exhibit disturbed morphologies such as shell-like structures (EA04 and EA11) and highly irregular isophotes (EA18). We conclude that the fraction of E+A galaxies with readily identifiable, i.e., brighter than our detection limit ($\mu_R < 25.1 \pm 0.5$ mag arcsec^{-2}), merger/interaction signatures is $\sim 55\%$ (± 15).

Since Zabludoff et al. (1996) first claimed galaxy-galaxy interactions/mergers as the main mechanism for E+A formation, other studies using larger samples of E+As have reached similar conclusions. For example, Blake et al. (2004) found that $\sim$13% of E+As selected from the 2dFGRS, using the same spectroscopic criteria as was done for the LCRS sample, show tidal features or disturbed mor-

phologies. Goto (2005) found that $\sim$30% of his sample shows tidal features. The higher merger fraction that we report here is almost certainly due to the improved sensitivity and higher resolution of *HST* imaging rather than intrinsic differences among E+A samples. For example, the low surface brightness features seen in EA08 and the shell-like structure in EA04 would not be detected in typical ground-based imaging.

Do merger features correlate with increasing EA numbers (i.e., increasing D_{4000}), which is likely to correlate with the mean stellar age of the galaxy? We find tidal features more often among E+As with smaller EA numbers. The distribution of EA numbers for E+As with tidal features is not random at the $\sim$90% confidence level. Because the duration of the E+A phase ($\sim$ Gyr) is longer than the dynamical relaxation time of the merger, we expect this correlation if EA numbers constitute a rough age sequence.

A.2   Companion Galaxies

Among the 11 E+As with interaction/merger signatures, five (EA01AB, 10, 11, 12, 13) have companion galaxies within $\sim$ 30 kpc that appear to be interacting with the E+A. The EA01AB system is spectroscopically confirmed (Yang et al., 2006), but the others may only be projected companions. For example, EA15's companion (R.A. = 14:40:45.2, DEC. = $-$06:39:53), which we also observed in our slit, is at a different redshift. The properties of the projected companion galaxies are as diverse as those of the E+As. They range from almost 1:3 mergers (EA01AB) to apparent 1:75 minor mergers (EA10) as judged from the relative R band fluxes. Are the interactions with these companion galaxies responsible for the starburst in E+As that ended $\lesssim$ Gyr ago? If these apparent on-going interactions produce the E+A spectra, then there was a close interaction $\lesssim$ Gyr ago,

and we are now witnessing a subsequent passage. Therefore, a wide range of merger configurations may cause the E+A phenomenon. Alternatively, another interaction/trigger produces the E+A spectra, and the current interactions are solely by chance. Larger surveys including redshift measurements of the companion galaxies will help to resolve this issue. Conversely, not all interactions lead to E+A's. Yagi et al. (2006) present a spectroscopically confirmed interacting E+A system where one galaxy is an E+A, but the other has neither current star formation nor post-starburst signatures.

A.3   Dust Features

Seven E+As (EA06, 07, 12, 13, 17, 18, 19) show dust features, such as lanes and filamentary structures, in the two-color composites or the residual images. In the WFPC2 sample, we also suspect that EA02 and EA04 might have dust from their irregular residual images, but the shallow B_{439} images prohibit us from confirming it. Signatures of dust, although typically fairly minor, are present in over a third (33–43%) of our E+As.

There have been suggestions that star-forming galaxies could be disguised as E+A galaxies due to obscuration by dust (Smail et al., 1999). However, this is not an issue for the E+As in this sample. As discussed in §3.4, only three E+As (EA07, 12, 19) have color profiles seriously affected by dust lanes [$\Delta(B - R) \gtrsim 0.5$]. Furthermore, radio continuum emission is detected from only two of the dusty E+As (EA12 and 19) with inferred star formation rates (SFR) of 5.9 and 2.2 $M_{\odot}$ yr^{-1}, respectively (Miller & Owen, 2001). EA07 was not observed in the radio. We conclude that the contamination rate due to the E+A selection criteria adopted by Zabludoff et al. (1996), which employs the average Balmer line strength and [O II], is less than 15% (see also Blake et al., 2004; Goto, 2004).

A.4   Barred Galaxies

Only three E+As galaxies (EA05, 14, 21) exhibit clear signs of bars in the residual images, while two other E+As (EA11 and EA19) have elongated residuals that suggest the presence of a bar. Because there is no model profile for the bar component, we fit these galaxies as well as possible using the various model GAL-FIT components. Because introducing too many free components makes it impossible to interpret the components physically (Peng et al., 2002), we use only three-component models, each with a combination of two Sérsic profiles and one exponential disk profile. We show the best-fit model profiles in Figure 3.3 for the barred E+A galaxies. The bars appear to be fit reasonably well with a steep ($n < 0.8$) and flat ($q \sim 0.5$) component.

APPENDIX B

POST-BURST AGE DETERMINATION

The ages of the young star cluster populations in E+A galaxies could be used to break the degeneracy between the burst strength and the time elapsed since the starburst, because a simple stellar population (SSP) is an excellent approximation for the star clusters and therefore no additional assumptions are required to model the underlying old stellar populations. To derive the time since the starburst (post-burst age), when the majority of the detected clusters and young stars formed, we use a statistical test and the simple assumption that all star clusters formed during a single burst. Therefore, we assume that their spread in colors is due entirely to color measurement errors. For each post-burst age, we draw a thousand sets of N cluster colors, each scattered according to a Gaussian error distribution described by the measurement error σ_{err}^i, where N is the number of cluster candidates found in each E+A. These simulated colors are compared to the distributions of observed colors. We determine the fraction of sets that are statistically indistinguishable from the observations using the two sample K-S test. If the fraction of acceptable sets is less than 5%, we reject that model age as the time since the starburst.

Next we test whether the key assumptions in determining the post-burst ages — 1) the Gaussian distribution of observed colors and 2) the single age cluster population — are statistically acceptable. First, we consider whether the assumption that the measured cluster colors are randomly distributed according to a Gaussian is realistic. Due to small number statistics in each galaxy, it is not possible to test this assumption for the clusters in each galaxy. Therefore, we apply the following test to all clusters discovered in the five E+As (EA07, 08, 11, 15,

18). For each E+A, we calculate the deviation of each cluster color from the median color of the sample in terms of its measurement error, $\delta_i = (C_i - C_{med})/\sigma^i_{err}$, where C_i and C_{med} are the measured color of the cluster and the median color of clusters in the given E+A, and σ^i_{err} is the error in each cluster color including uncertainties in background subtraction. We examine the distribution of δ_i's. If the δ_i's follow a Gaussian distribution with zero mean and a standard deviation of unity, our assumption of Gaussian distributed errors can be justified. If not, e.g., if the δ_i's show a skewed or flat distribution, their measured colors could be seriously affected by the other factors. In Figure B.1, we show the distribution of δ_i's. The histogram is marginally consistent with a Gaussian distribution with unit standard deviation ($\sigma_{\text{fit}} = 1.34$), therefore we conclude that there is no strong evidence against this assumption.

Second, we test the validity of the assumption that all of the detected star clusters formed during a single instantaneous burst. We generate a thousand sets of simulated cluster colors with an age spread of Δt. Gaussian random errors with a dispersion corresponding to the measurement errors σ^i_{err} are added to the simulated colors. Now we calculate the δ_i's using these simulated sets of cluster colors and compare the width σ_{fit} of the δ_i distribution with the observed value $\sigma_{\text{fit}} = 1.34$. If the observed σ_{fit} is significantly different from the distribution of σ_{fit}, then we reject the given Δt. We find that $\Delta t < 0.1$ Gyr is rejected at the 95% confidence level. However, the small number statistics and low S/N of the color measurements do not allow us to constrain the upper limits of the burst durations. Therefore, the instantaneous burst assumption might not be strictly true, and the burst duration should be at least longer than 100 Myr. On the other hand, using an E+A galaxy sample selected from the Sloan Digital Sky Survey, Yang et al. (2008) show that the timescale over which star formation ends
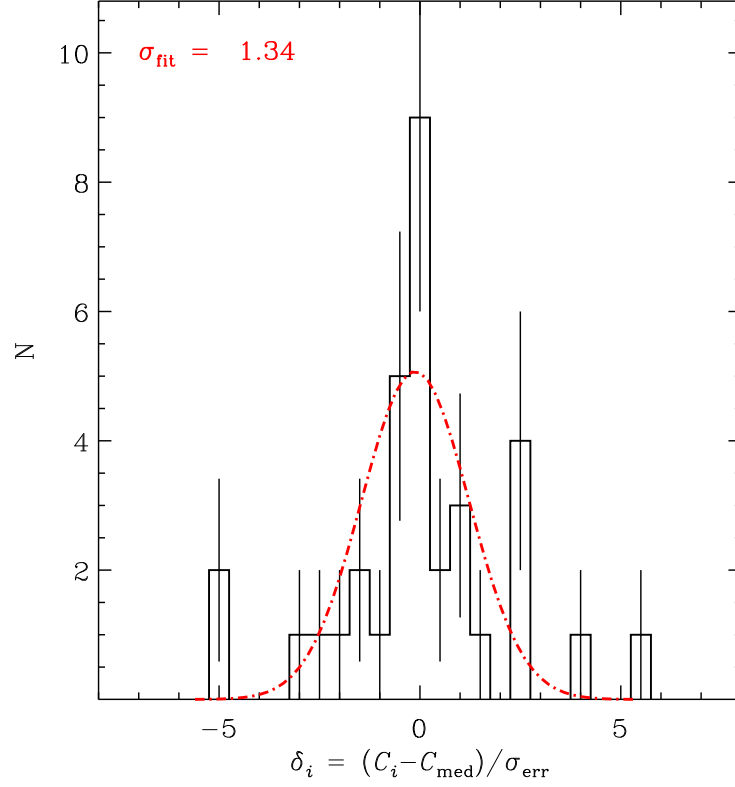
Figure B.1 The composite distribution of $\delta_i = (C_i - C_{med})/\sigma_{err}^i$ from five *ACS* E+As with cluster candidates. The histogram is marginally consistent with a Gaussian with $\sigma = 1$. There is no strong indication against our assumption of Gaussian-distributed uncertainties.

tends to be smaller than ~ 200 Myr, and larger burst durations (several hundred Myr) would wipe out the correlations that we find among post-burst ages, global E+A colors (i.e., EA number), and the bright end of the star cluster luminosity function. Therefore, we argue that the single burst age approximation is valid to within a few hundred Myr.

REFERENCES

Abazajian, K., et al. 2004, AJ, 128, 502

Abraham, R. G., Valdes, F., Yee, H. K. C., & van den Bergh, S. 1994, ApJ, 432, 75

Abraham, R. G., Tanvir, N. R., Santiago, B. X., Ellis, R. S., Glazebrook, K., & van den Bergh, S. 1996, MNRAS, 279, L47

Adelman-McCarthy, J. K., et al. 2007, ApJS, 172, 634

Aggarwal, K. M., Callaway, J., Kingston, A. E., & Unnikrishnan, K. 1992, ApJS, 80, 473

Allen et al., 2004, in preparation.

Ashman, K. M. & Zepf, S. E. 1992, ApJ, 384, 50

Avni, Y. 1976, ApJ, 210, 642

Bahcall, N. A., Dong, F., Hao, L., Bode, P., Annis, J., Gunn, J. E., & Schneider, D. P. 2003, ApJ, 599, 814

Baldwin, J. A., Phillips, M. M., & Terlevich, R. 1981, PASP, 93, 5

Balogh, M. L., Navarro, J. F., & Morris, S. L. 2000, ApJ, 540, 113

Balogh, M. L., Miller, C., Nichol, R., Zabludoff, A., & Goto, T. 2005, MNRAS, 360, 587

Barger, A. J., Aragon-Salamanca, A., Ellis, R. S., Couch, W. J., Smail, I., & Sharples, R. M. 1996, MNRAS, 279, 1

Barger, A. J., et al. 2003, AJ, 126, 632

Barnes, J. E. 1988, ApJ, 331, 699

Barnes, J. E. & Hernquist, L. 1996, ApJ, 471, 115

Bartholomew, L. J., Rose, J. A., Gaba, A. E., & Caldwell, N. 2001, AJ, 122, 2913

Barth, A. J., & Shields, J. C. 2000, PASP, 112, 753

Barton, E. J., Davé, R., Smith, J. T., Papovich, C., Hernquist, L., & Springel, V. 2004, ApJL, 604, L1

Bekki, K., Couch, W. J., Shioya, Y., & Vazdekis, A. 2005, MNRAS, 359, 949

Bell, E. F., McIntosh, D. H., Katz, N., & Weinberg, M. D. 2003, ApJS, 149, 289

Bender, R., Burstein, D., & Faber, S. M. 1992, ApJ, 399, 462

Bendo, G. J. & Barnes, J. E. 2000, MNRAS, 316, 315

Bernardi, M., et al. 2003, AJ, 125, 1866

Bershady, M. A., Jangren, A., & Conselice, C. J. 2000, AJ, 119, 2645

Bertin, E. & Arnouts, S. 1996, A&AS, 117, 393

Bica, E., Alloin, D., & Schmidt, A. 1990, MNRAS, 242, 241

Binney, J. 1977, ApJ, 215, 483

Birnboim, Y. & Dekel, A. 2003, MNRAS, 345, 349

Blake, C., et al. 2004, MNRAS, 355, 713

Blanton, M. R., et al. 2001, AJ, 121, 2358

Blanton, M. R., et al. 2003, ApJ, 594, 186

Blanton, M. R., et al. 2003, AJ, 125, 2348

Bower, R. G., et al. 2004, MNRAS, 351, 63

Brand, K., et al. 2006, ApJ, 641, 140

Brodie, J. P., & Strader, J. 2006, ARA&A, 44, 193

Bromm, V., Kudritzki, R. P., & Loeb, A. 2001, ApJ, 552, 464

Bruzual, G. & Charlot, S., MNRAS, 344, 1000

Bunker, A., Smith, J., Spinrad, H., Stern, D., & Warren, S. 2003, Ap&SS, 284, 357

Butcher, H. & Oemler, A. 1978, ApJ, 219, 18

Buyle, P., Michielsen, D., De Rijcke, S., Pisano, D. J., Dejonghe, H., & Freeman, K. 2006, ArXiv Astrophysics e-prints, arXiv:astro-ph/0604563

Caldwell, N., Rose, J. A., Franx, M., & Leonardi, A. J. 1996, AJ, 111, 78

Caldwell, N., Rose, J. A., & Dendy, K. 1999, AJ, 117, 140

Calzetti, D., Armus, L., Bohlin, R. C., Kinney, A. L., Koornneef, J., & Storchi-Bergmann, T. 2000, ApJ, 533, 682

Cantalupo, S., Porciani, C., Lilly, S. J., & Miniati, F. 2005, ApJ, in press, astro-ph/0504015

Carlson, M. N. et al. 1999, AJ, 117, 1700

Chang, T., van Gorkom, J. H., Zabludoff, A. I., Zaritsky, D., & Mihos, J. C. 2001, AJ, 121, 1965

Charlot, S., & Silk, J. 1994, ApJ, 432, 453

Cid Fernandes, R., et al. 2004, ApJ, 605, 105

Cole, S., et al. 2001, MNRAS, 326, 255

Colina, L., Gonzalez Delgado, R., Mas-Hesse, J. M., & Leitherer, C. 2002, ApJ, 579, 545

Conselice, C. J., Bershady, M. A., & Jangren, A. 2000, ApJ, 529, 886

Cool, R. J., et al. 2006, AJ, 132, 823

Couch, W. J. & Sharples, R. M. 1987, MNRAS, 229, 423

Cowie, L. L., Barger, A. J., Bautz, M. W., Brandt, W. N., & Garmire, G. P. 2003, ApJL, 584, L57

Davé, R., Dubinski, J., & Hernquist, L. 1997, New Astronomy, 2, 277

Davé, R. et al. 2001, ApJ, 552, 473

Dekel, A., & Birnboim, Y. 2006, MNRAS, 368, 2

Dey, A., et al. 2005, ApJ, 629, 654

Dijkstra, M., Haiman, Z., & Spaans, M. 2006, ApJ, 649, 37

Djorgovski, S., & Davis, M. 1987, ApJ, 313, 59

Dopita, M. A. & Sutherland, R. S. 1996, ApJS, 102, 161

Dressler, A. 1987, ApJ, 317, 1

Dressler, A., Smail, I., Poggianti, B. M., Butcher, H., Couch, W. J., Ellis, R. S., & Oemler, A. J. 1999, ApJS, 122, 51

Dressler, A. & Gunn, J. E. 1983, ApJ, 270, 7

Efstathiou, G., Bernstein, G., Tyson, J. A., Katz, N., & Guhathakurta, P. 1991, ApJL, 380, L47

Eisenstein, D. J., et al. 2003, ApJ, 585, 694

Faber, S. M., Tremaine, S., Ajhar, E. A., Byun, Y., Dressler, A., Gebhardt, K., Grillmair, C., Kormendy, J., Lauer, T. R., & Richstone, D. 1997, AJ, 114, 1771

Faber, S. M., et al. 2007, ApJ, 665, 265

Faber, S. M., & Jackson, R. E. 1976, ApJ, 204, 668

Fardal, M. A., Katz, N., Gardner, J. P., Hernquist, L., Weinberg, D. H., & Davé, R. 2001, ApJ, 562, 605

Ferland, G. J., & Netzer, H. 1983, ApJ, 264, 105

Ferrarese, L., & Merritt, D. 2000, ApJL, 539, L9

Filippenko, A. V. 2003, in Active Galactic Nuclei: from Central Engine to Host Galaxy, ed. S. Collin, F. Combes, & I. Shlosman (San Francisco: ASP), 387

Francis, P. J., et al. 2001, ApJ, 554, 1001

Franx, M. 1993, ApJL, 407, L5

Franx, M., Illingworth, G., & Heckman, T. 1989, AJ, 98, 538

Frei, Z., Guhathakurta, P., Gunn, J. E., & Tyson, J. A. 1996, AJ, 111, 174

Fukugita, M., Shimasaku, K., & Oshawa, T. 1995, PASP, 107, 945

Furlanetto, S. R., Schaye, J., Springel, V., & Hernquist, L. 2003, ApJL, 599, L1

Furlanetto, S. R., Schaye, J., Springel, V., & Hernquist, L. 2005, ApJ, 622, 7

Galaz, G. 2000, AJ, 119, 2118

Gebhardt, K., et al. 2000, ApJL, 539, L13

González Delgado, R. M. et al. 2004, ApJ, 605, 127

Gonzalez-Delgado, R. M., Cervino, M., Martins, L. P., Leitherer, C., & Hauschildt, P. H. 2005, MNRAS, 357, 945

Gordon, K. D., Clayton, G. C., Misselt, K. A., Landolt, A. U., & Wolff, M. J. 2003, ApJ, 594, 279

Goto, T. 2004, A&A, 427, 125

Goto, T. 2005, MNRAS, 357, 937

Goto, T. 2007, MNRAS, 381, 187

Goto, T., et al. 2003, PASJ, 55, 771

Goudfrooij, P., Gilmore, D., Whitmore, B. C., & Schweizer, F. 2004, ApJL, 613, L121

Graham, A. W. 2002, MNRAS, 334, 859

Graham, A. W., Erwin, P., Caon, N., & Trujillo, I. 2001, ApJL, 563, L11

Gunn, J. E., & Gott, J. R. I. 1972, ApJ, 176, 1

Gunn, J. E. & Stryker, L. L. 1983, ApJS, 52, 121

Haardt, F. & Madau, P. 1996, ApJ, 461, 20

Haiman, Z., & Rees, M. J. 2001, ApJ, 556, 87

Haiman, Z., Spaans, M., & Quataert, E. 2000, ApJL, 537, L5

Halpern, J. P., & Steiner, J. E. 1983, ApJL, 269, L37

Hamabe, M., & Kormendy, J. 1987, IAU Symp. 127: Structure and Dynamics of Elliptical Galaxies, 127, 379

Harris, W. E. 1996, AJ, 112, 1487

Harris, W. E. 2001, Saas-Fee Advanced Course 28: Star Clusters, 223

Harris, J., Calzetti, D., Gallagher, J. S., Conselice, C. J., & Smith, D. A. 2001, AJ, 122, 3046

Harris, W. E., & van den Bergh, S. 1981, AJ, 86, 1627

Heckman, T. M., 1980, A&A, 87, 152

Heckman, T. M., Lehnert, M. D., Strickland, D. K., & Armus, L. 2000, ApJS, 129, 493

Heckman, T. M., Kauffmann, G., Brinchmann, J., Charlot, S., Tremonti, C., & White, S. D. M. 2004, ApJ, 613, 109

Hernquist, L. & Mihos, J. C. 1995, ApJ, 448, 41

Hibbard, J. E. & Vacca, W. D. 1997, AJ, 114, 1741

Ho, L. C., 2004, in Carnegie Observatories Astrophysics Series, Vol 1: Coevolution of Black Holes and Galaxies, ed. L. C. Ho, (Cambridge: Cambridge Univ. Press)

Ho, L. C., Filippenko, A. V., & Sargent, W. L. W. 1997, ApJ, 487, 568

Hogg, D. W., Cohen, J. G., Blandford, R., & Pahre, M. A. 1998, ApJ, 504, 622

Hogg, D. W., Masjedi, M., Berlind, A. A., Blanton, M. R., Quintero, A. D., & Brinkmann, J. 2006, ApJ, 650, 763

Holtzman, J. A. et al. 1992, AJ, 103, 691

Holtzman, J. A., Burrows, C. J., Casertano, S., Hester, J. J., Trauger, J. T., Watson, A. M., & Worthey, G. 1995, PASP, 107, 1065

Jakobsen, P. 1998, A&A, 335, 876

Jannuzi, B. T., & Dey, A. 1999, Photometric Redshifts and the Detection of High Redshift Galaxies, 191, 111

Jedrzejewski, R. I. 1987, MNRAS, 226, 747

Jiménez-Bailón, E. et al. 2003, ApJ, 593, 127

Jørgensen, I., Franx, M., & Kjaergaard, P. 1996, MNRAS, 280, 167

Katz, N., Keres, D., Dave, R., & Weinberg, D. H. 2003, ASSL Vol. 281: The IGM/Galaxy Connection. The Distribution of Baryons at z=0, 185

Katz, N., Weinberg, D. H., & Hernquist, L. 1996, ApJS, 105, 19

Kauffmann, G. et al. 2003, MNRAS, 346, 1055

Kaviraj, S., Kirkby, L. A., Silk, J., & Sarzi, M. 2007, MNRAS, 382, 960

Keel, W. C., Cohen, S. H., Windhorst, R. A., & Waddington, I. 1999, AJ, 118, 2547

Kelson, D. D., Illingworth, G. D., van Dokkum, P. G., & Franx, M. 2000, ApJ, 531, 137

Kelson, D. D., Illingworth, G. D., van Dokkum, P. G., & Franx, M. 2000, ApJ, 531, 184

Kennicutt, R. C. 1998, ARA&A, 36, 189

Kent, S. M. 1985, ApJS, 59, 115

Kenter, A., et al. 2005, ApJS, 161, 9

Kereš, D., Katz, N., Weinberg, D. H., & Davé, R. 2005, MNRAS, 363, 2

Kewley, L. J., Dopita, M. A., Sutherland, R. S., Heisler, C. A., & Trevena, J. 2001, ApJ, 556, 121

King, I. R. 1966, AJ, 71, 64

Kobayashi, C. 2004, MNRAS, 347, 740

Kollmeier et al., 2005, in preparation.

Kormendy, J. 1977, ApJ, 218, 333

Kornreich, D. A., Lovelace, R. V. E., & Haynes, M. P. 2002, ApJ, 580, 705

Krist, J. & Hook, R. 1999, The TinyTim User's Guide(Baltimore: STSCI)

Lauer, T. R., Ajhar, E. A., Byun, Y.-I., Dressler, A., Faber, S. M., Grillmair, C., Kormendy, J., Richstone, D., & Tremaine, S. 1995, AJ, 110, 2622

Lauer, T. R., Faber, S. M., Ajhar, E. A., Grillmair, C. J., & Scowen, P. A. 1998, AJ, 116, 2263

Lee, J. H., Lee, M. G., & Hwang, H. S. 2006, ApJ, 650, 148

Leitherer, C., et al. 1999, ApJS, 123, 3

Leitherer, C. et al. 1999, ApJS, 123, 3

Leonardi, A. J. & Rose, J. A. 1996, AJ, 111, 182

Levine, S. E. & Sparke, L. S. 1998, ApJL, 496, L13

Limber, D. N. 1953, ApJ, 117, 134

Liu, C. T., Hooper, E. J., O'Neil, K., Thompson, D., Wolf, M., & Lisker, T. 2007, ApJ, 658, 249

Liu, C. T., & Green, R. F. 1996, ApJL, 458, L63

Lotz, J. M., Primack, J., & Madau, P. 2004, AJ, 128, 163

Lotz, J. M., et al. 2008, ApJ, 672, 177

Lucy, L. B. 1974, AJ, 79, 745

Lupton, R., Blanton, M. R., Fekete, G., Hogg, D. W., O'Mullane, W., Szalay, A., & Wherry, N. 2004, PASP, 116, 133

Maddox, S. J., Efstathiou, G., Sutherland, W. J., & Loveday, J. 1990, MNRAS, 242, 43P

Malhotra, S., & Rhoads, J. E. 2004, ApJL, 617, L5

Maoz, D., Nagar, N. M., Falcke, H., & Wilson, A. W. 2005, ApJ, 625, 699

Martin, D. C., et al. 2005, ApJL, 619, L1

Martin, C. L., & Sawicki, M. 2004, ApJ, 603, 414

Matsuda, Y., et al. 2004, AJ, 128, 569

Matsuda, Y., et al. 2005, ApJL, 634, L125

Matsuda, Y., Iono, D., Ohta, K., Yamada, T., Kawabe, R., Hayashino, T., Peck, A. B., & Petitpas, G. R. 2007, ApJ, 667, 667

Menanteau, F., Abraham, R. G., & Ellis, R. S. 2001, MNRAS, 322, 1

Menanteau, F., et al. 2004, ApJ, 612, 202

Mihos, J. C. 1995, ApJL, 438, L75

Mihos, J. C., & Hernquist, L. 1994, ApJL, 425, L13

Mihos, J. C., & Hernquist, L. 1994, ApJ, 427, 112

Mihos, J. C. & Hernquist, L. 1994, ApJL, 431, L9

Mihos, J. C. & Hernquist, L. 1996, ApJ, 464, 641

Miller, N. A. & Owen, F. N. 2001, ApJL, 554, L25

Mo, H. J., & White, S. D. M. 2002, MNRAS, 336, 112

Møller, P. & Jakobsen, P. 1990, A&A, 228, 299

Monet, D. G., et al. 2003, AJ, 125, 984

Morrissey, P., et al. 2005, ApJL, 619, L7

Morrissey, P., et al. 2007, ApJS, 173, 682

Moustakas, J., & Kennicutt, R. C., Jr. 2006, ApJS, 164, 81

Murali, C., Katz, N., Hernquist, L., Weinberg, D. H., & Davé, R. 2002, ApJ, 571, 1

Naab, T. 2000, Ph.D. thesis

Nilsson, K. K., Fynbo, J. P. U., Møller, P., Sommer-Larsen, J., & Ledoux, C. 2006, A&A, 452, L23

Norton, S. A., Gebhardt, K., Zabludoff, A. I., & Zaritsky, D. 2001, ApJ, 557, 150

Nugent, P., Kim, A., & Perlmutter, S. 2002, PASP, 114, 803

O'Connell, R. W. et al. 2005, ApJ, 635, 305

Oh, S. P., Haiman, Z., & Rees, M. J. 2001, ApJ, 553, 73

Ohyama, Y., et al. 2003, ApJL, 591, L9

Oke, J. B. 1974, ApJS, 27, 21

Ouchi, M., et al. 2008, ArXiv e-prints, 807, arXiv:0807.4174

Pahre, M. A., Djorgovski, S. G., & de Carvalho, R. R. 1998, AJ, 116, 1591

Palunas, P., Teplitz, H. I., Francis, P. J., Williger, G. M., & Woodgate, B. E. 2004, ApJ, 602, 545

Papovich, C. 2008, ApJ, 676, 206

Peebles, P. J. E. 1980, The Large-Scale Structure of the Universe, (Princeton: Princeton University Press)

Peletier, R. F., Davies, R. L., Illingworth, G. D., Davis, L. E., & Cawson, M. 1990, AJ, 100, 1091

Peng, C. Y., Ho, L. C., Impey, C. D., & Rix, H. 2002, AJ, 124, 266

Petrosian, V. 1976, ApJL, 209, L1

Pettini, M., Shapley, A. E., Steidel, C. C., Cuby, J., Dickinson, M., Moorwood, A. F. M., Adelberger, K. L., & Giavalisco, M. 2001, ApJ, 554, 981

Poggianti, B. M., Smail, I., Dressler, A., Couch, W. J., Barger, A. J., Butcher, H., Ellis, R. S., & Oemler, A. J. 1999, ApJ, 518, 576

Pracy, M. B., Couch, W. J., Blake, C., Bekki, K., Harrison, C., Colless, M., Kuntschner, H., & de Propris, R. 2005, MNRAS, 359, 1421

Prescott, M. K. M., Kashikawa, N., Dey, A., & Matsuda, Y. 2008, ArXiv e-prints, 803, arXiv:0803.4230

Quintero, A. D., et al. 2004, ApJ, 602, 190

Reuland, M., et al. 2003, ApJ, 592, 755

Richardson, W. H. 1972, J. Opt. Soc. A., 62, 5

Rix, H. & Zaritsky, D. 1995, ApJ, 447, 82

Rose, J. A., Gaba, A. E., Caldwell, N., & Chaboyer, B. 2001, AJ, 121, 793

Rothberg, B., & Joseph, R. D. 2006, AJ, 131, 185

Rudnick, G. & Rix, H. 1998, AJ, 116, 1163

Saito, T., Shimasaku, K., Okamura, S., Ouchi, M., Akiyama, M., & Yoshida, M. 2006, ApJ, 648, 54

Salim, S., et al. 2005, ApJL, 619, L39

Salim, S., et al. 2007, ArXiv e-prints, 704, arXiv:0704.3611

Salpeter, E. E. 1955, ApJ, 121, 161

Sanders, D. B., Soifer, B. T., Elias, J. H., Madore, B. F., Matthews, K., Neugebauer, G., & Scoville, N. Z. 1988, ApJ, 325, 74

Schade, D., Lilly, S. J., Crampton, D., Hammer, F., Le Fevre, O., & Tresse, L. 1995, ApJL, 451, L1

Schaerer, D. 2003, A&A, 397, 527

Schaerer, D., & Vacca, W. D. 1998, ApJ, 497, 618

Schaye, J., Aguirre, A., Kim, T., Theuns, T., Rauch, M., & Sargent, W. L. W. 2003, ApJ, 596, 768

Schlegel, D. J., Finkbeiner, D. P., & Davis, M. 1998, ApJ, 500, 525

Scoville, N., et al. 2007, ApJS, 172, 1

Shapley, A. E., Steidel, C. C., Pettini, M., & Adelberger, K. L. 2003, ApJ, 588, 65

Shectman, S. A., Landy, S. D., Oemler, A., Tucker, D. L., Lin, H., Kirshner, R. P., & Schechter, P. L. 1996, ApJ, 470, 172

Shull et al, 1999, UVOWG White Paper: "The Emergence of the Modern Universe: Tracing the Cosmic Web", astro-ph/9907101

Sirianni, M., et al. 2005, PASP, 117, 1049

Smail, I., Morrison, G., Gray, M. E., Owen, F. N., Ivison, R. J., Kneib, J.-P., & Ellis, R. S. 1999, ApJ, 525, 609

Smith, D. J. B., Jarvis, M. J., Lacy, M., & Martínez-Sansigre, A. 2008, ArXiv e-prints, 806, arXiv:0806.4384

Smith, D. J. B., & Jarvis, M. J. 2007, MNRAS, 378, L49

Springel, V., Di Matteo, T., & Hernquist, L. 2005, MNRAS, 361, 776

Springel, V., Di Matteo, T., & Hernquist, L. 2005, ApJL, 620, L79

Steidel, C. C., Adelberger, K. L., Shapley, A. E., Pettini, M., Dickinson, M., & Giavalisco, M. 2000, ApJ, 532, 170

Storey, P. J. & Hummer, D. G. 1995, MNRAS, 272, 41

Strauss, M. A., et al. 2002, AJ, 124, 1810

Tacconi, L. J., Genzel, R., Lutz, D., Rigopoulou, D., Baker, A. J., Iserlohe, C., & Tecza, M. 2002, ApJ, 580, 73

Tamura, N., Kobayashi, C., Arimoto, N., Kodama, T., & Ohta, K. 2000, AJ, 119, 2134

Taniguchi, Y., Shioya, Y., & Murayama, T. 2000, AJ, 120, 1265

Taniguchi, Y. & Shioya, Y. 2000, ApJL, 532, L13

Telfer, R. C., Zheng, W., Kriss, G. A., & Davidsen, A. F. 2002, ApJ, 565, 773

Toomre, A. 1977, in "The Evolution of Galaxies and Stellar Populations", eds. B. Tinsley and R.B. Larson (New Haven: Yale Univ.), p. 401

Toomre, A., & Toomre, J. 1972, ApJ, 178, 623

Tran, K.-V. H., Franx, M., Illingworth, G., Kelson, D. D., & van Dokkum, P. 2003, ApJ, 599, 865

Tran, K. H., Lilly, S. J., Crampton, D., & Brodwin, M. 2004, ApJL, 612, L89

Tran, K.-V. H., Franx, M., Illingworth, G. D., van Dokkum, P., Kelson, D. D., & Magee, D. 2004, ApJ, 609, 683

Tremonti, C. A., et al. 2004, ApJ, 613, 898

Tremonti, C. A., Brinchmann, J., Seibert, M., Bradley, L. 2006, in prep.

Tremonti, C. A., Moustakas, J., & Diamond-Stanic, A. M. 2007, ApJL, 663, L77

Treu, T., et al. 2005, ApJ, 633, 174

Treu, T., Koopmans, L. V., Bolton, A. S., Burles, S., & Moustakas, L. A. 2006, ApJ, 640, 662

Tumlinson, J., Giroux, M. L., & Shull, J. M. 2001, ApJL, 550, L1

Tumlinson, J., Shull, J. M., & Venkatesan, A. 2003, ApJ, 584, 608

Valdes, F. G. 1998, Astronomical Data Analysis Software and Systems VII, 145, 53

van Dokkum, P. G. 2001, PASP, 113, 1420

van Dokkum, P. G., & Ellis, R. S. 2003, ApJL, 592, L53

Veilleux, S., & Osterbrock, D. E. 1987, ApJS, 63, 295

Verhamme, A., Schaerer, D., & Maselli, A. 2006, A&A, 460, 397

Weidinger, M., Møller, P., Fynbo, J. P. U., & Thomsen, B. 2005, A&A, 436, 825

White, R. L., Becker, R. H., Helfand, D. J., & Gregg, M. D. 1997, ApJ, 475, 479

Whitmore, B. C., Schweizer, F., Leitherer, C., Borne, K., & Robert, C. 1993, AJ, 106, 1354

Whitmore, B. C., & Schweizer, F. 1995, AJ, 109, 960

Williams, G. G., Olszewski, E., Lesser, M. P., & Burge, J. H. 2004, Proc. SPIE, 5492, 787

Wilman, R. J., Gerssen, J., Bower, R. G., Morris, S. L., Bacon, R., de Zeeuw, P. T., & Davies, R. L. 2005, Nature, 436, 227

Wise, M. W., & Silva, D. R. 1996, ApJ, 461, 155

Yagi, M., Goto, T., & Hattori, T. 2006, ApJ, 642, 152

Yamauchi, C., & Goto, T. 2005, MNRAS, 359, 1557

Yan, R., Newman, J. A., Faber, S. M., Konidaris, N., Koo, D., & Davis, M. 2006, ApJ, 648, 281

Yan, R., et al. 2008, ArXiv e-prints, 805, arXiv:0805.0004

Yang, Y., Zabludoff, A. I., Zaritsky, D., Lauer, T. R., & Mihos, J. C. 2004, ApJ, 607, 258

Yang, Y., Zabludoff, A. I., Davé, R., Eisenstein, D. J., Pinto, P. A., Katz, N., Weinberg, D. H., & Barton, E. J. 2006, ApJ, 640, 539

Yang, Y., Tremonti, C. A., Zabludoff, A. I., & Zaritsky, D. 2006, ApJL, 646, L33

Yang, Y., Zabludoff, A. I., Zaritsky, D., & Mihos, J. C. 2008, ApJ, in press.

Young, J. S., & Scoville, N. Z. 1991, ARA&A, 29, 581

Yun, M. S., Reddy, N. A., & Condon, J. J. 2001, ApJ, 554, 803

Zabludoff, A. I., Zaritsky, D., Lin, H., Tucker, D., Hashimoto, Y., Shectman, S. A., Oemler, A., & Kirshner, R. P. 1996, ApJ, 466, 104

Zaritsky, D., Gonzalez, A. H., & Zabludoff, A. I. 2006, ApJ, 638,725

Zaritsky, D. & Rix, H. 1997, ApJ, 477, 118

Zheng, Z., & Miralda-Escudé, J. 2002, ApJ, 578, 33